Lecture Notes in Physics

699

J.-P. Rozelot
(Ed.)

Solar and Heliospheric Origins of Weather Phenomena

Lecture Notes in Physics

The Lecture Notes in Physics

The series Lecture Notes in Physics (LNP), founded in 1969, reports new developments in physics research and teaching – quickly and informally, but with a high quality and the explicit aim to summarize and communicate current knowledge in an accessible way. Books published in this series are conceived as bridging material between advanced graduate textbooks and the forefront of research to serve the following purposes:

• to be a compact and modern up-to-date source of reference on a well-defined topic;
• to serve as an accessible introduction to the field to postgraduate students and nonspecialist researchers from related areas;
• to be a source of advanced teaching material for specialized seminars, courses and schools.

Both monographs and multi-author volumes will be considered for publication. Edited volumes should, however, consist of a very limited number of contributions only. Proceedings will not be considered for LNP.

Volumes published in LNP are disseminated both in print and in electronic formats, the electronic archive is available at springerlink.com. The series content is indexed, abstracted and referenced by many abstracting and information services, bibliographic networks, subscription agencies, library networks, and consortia.

Proposals should be sent to a member of the Editorial Board, or directly to the managing editor at Springer:

Dr. Christian Caron
Springer Heidelberg
Physics Editorial Department I
Tiergartenstrasse 17
69121 Heidelberg/Germany
christian.caron@springer.com

Jean-Pierre Rozelot (Ed.)

Solar and Heliospheric Origins of Space Weather Phenomena

Springer

Editor

Jean-Pierre Rozelot
Observatoire de la Côte d′Azur
Département CERGA
Avenue Copernic
06130 Grasse, France
E-mail: rozelot@obs-azur.fr

J.-P. Rozelot, *Solar and Heliospheric Origins of Space Weather Phenomena*, Lect. Notes Phys. 699 (Springer, Berlin Heidelberg 2006), DOI 10.1007/b11429173

Library of Congress Control Number: 2006924825

ISSN 0075-8450
ISBN-10 3-540-33758-X Springer Berlin Heidelberg New York
ISBN-13 978-3-540-33758-4 Springer Berlin Heidelberg New York

Typesetting: by the authors and techbooks using a Springer LaTeX macro package
Cover design: *design & production* GmbH, Heidelberg

Printed on acid-free paper SPIN: 11429173 54/techbooks 5 4 3 2 1 0

Contents

List of Contributors

Guy Artzner
IAS BT 121
91405 Orsay Cedex, France
Guy.artzner@ias.u-psud.fr

Jean-Louis Bougeret
Observatoire de Paris-Meudon
LESIA
5, place Jules Janssen
92195 Meudon
Cedex, France
bougeret@obspm.fr

Sébastien Bourdarie
ONERA-CERT/DESP BP 4025
2, Avenue Edouard Belin
31055 Toulouse Cedex 4, France
Sebastien.Bourdarie@onecert.fr

Pierre Carrega
UFR "Espaces et Cultures"
98 bd E. Herriot
06204 Nice cedex 3, France
Carrega@nice.fr

Arnaud Claret
CEA-Saclay Service d'Astrophysique
91191 Gif/Yvette Cedex, France
Aclaret@cea.fr

Vesna Ducic
IPGP
Dpt Géophysique Spatiale et Planétaire
4, avenue de Neptune
94107 Saint Maur des Fossés Cedex
France
ducic@ipgp.jussieu.fr

Witt Thierry de Dudok
LPCE - CNRS
3A. Av. de la Recherche Scientifique
45071 Orleans cedex 2, France
ddwit@cnrs-orleans.fr

Monique Fulconis
Observatoire de la Côte d'Azur
Site de Nice
BP 4229
06304 Nice cedex 04, France
monik@laposte.fr

Annie Ginibre
Campus d'Orsay
Laboratoire Aimé Cotton, Bt 505
91405 Orsay cedex, France
annie.Ginibre@lac.u-psud.fr

Alexis Glover
ESA/ESTEC Postbus 299
Keplerlaan 12200 AG
Noordwijk, The Netherlands
alexi.glover@esa.int

Jocelyne Gosselin
DR 20 - CNRS
250, Av. Albert Einstein
06130 Valbonne, France
Gosselin@dr20.cnrs.fr

Michel Herse
SA - CNRS BP 3
91 371 Verrières-le-Buisson, France
michel.herse@aerov.jussieu.fr

Karine Issautier
Observatoire de Paris LESIA
Place Jules Janssen
92195 Meudon cedex, France
karine.issautier@obspm.fr

Chantal Lathuilliere
Laboratoire de Planétologie de Grenoble
Bâtiment D de Physique, BP 53
38041 Grenoble Cedex 9, France
Chantal.Lathuillere@obs.ujf-grenoble.fr

Sandrine Lefebvre
Service d'Astrophysique
SAp/DAPNIA/DSM CEA Saclay
L'Orme des Merisiers Bat. 709
91191 Gif Sur Yvette Cedex
France
(on leave from OCA-GEMINI)
sandrine.lefebvre@cea.fr

François Lefeuvre
CNRS Labo de Phys. et Chimie de l'Environnement
3A. Av. de la Recherche Scientifique
45071 Orleans cedex 2, France
Jnicoull@cnrs-orleans.fr

Jean Lilensten
Laboratoire de Planétologie de Grenoble
(Observatoire des Sciences de l'Univers)
Bâtiment D de Physique
B.P. 53
38041 Grenoble cedex 9, France
Jean.Lilensten@planeto.obs.ujf-grenoble.fr

Aurélie Marchaudon
CETP
4, avenue de Neptune
94107 Saint Maur des Fossés cedex, France
am@mssl.ucl.ac.uk

Emilie Martin
Ciel et Espace
75014 Paris, France
e.martin@cieletespace.fr

Michel Menvielle
CETP
4, avenue de Neptune
94100 Saint Maur, France
michel.menvielle@cetp.ipsl.fr

Koryo Okumura
CEA Saclay CNRS-URA 2052
"Plasma, Gravitation, Cosmologie"
Bt 709
91191 Gif sur Yvette cedex, France
Koryo.okumura@cea.fr

Fernando Pereira
LPCE/CNRS 34, avenue de la Recherche Scientifique
45071 Orléans cedex 02, France
pereiras@cnrs-orleans.fr

Monique Pick
Observatoire de Paris-Meudon
5, place Jules Janssen
92195 Meudon-cedex, France
Pick@obspm.fr

Fabrice Portier-Fozzani
Research Center for Astronomy and Applied Mathematics
14 Aganostopoulou Street
10673 Athènes
Grèce, France
fabrice.3dsun@free.fr

Jean-Pierre Rozelot
Observatoire de la Côte d'Azur
Départment Gemini
Av. Copernic, 06130 Grasse, France
rozelot@obs-azur.fr

Cyril Simon
LPGP, Bt D de Physique
BP 53
38041 Grenoble cedex 9, France
Cyril.simonsen@yahoo.fr

Claude Thirriot
ENSEEIHT 2, rue Charles Camichel
31000 Toulouse, France
thirriot@enseeiht.fr

Introduction

J.P. Rozelot

1 The CNRS Solar Astrophysics Schools

This book is the third one edited by Springer in this collection (*Lecture Notes in Physics*) and devoted to the transcription of main lectures delivered during CNRS summer schools.

These Solar Astrophysics Schools held each year in Saint-Pierre d'Oléron (France) since 1996 have progressively acquired a high-standard international quality mainly due to the excellence of the lectures that are given. A dedicated topic is each time chosen to investigate specific points at the top of progress (such as chaos and fractals in solar cycle activity, attractors reconstruction, and chaos measurement from signal analysis,[1] transport and conversion of energy in the heliosphere,[2] new avenues for astronomical data analysis,[3] physics of the Earth's climate and the Sun's surface and subsurface: investigating shape and irradiance[4]). This VIIth School was dedicated to Space Weather, a subject today in full expansion.

The Oléron summer schools bring together scientists and postdoctoral students to discuss current topics in solar astrophysics, to evolve new projects, and to set up new cooperations that can efficiently be carried out afterward. The school is sponsored by the French CNRS Agency (*Formation permanente*) and is open for about 30 to 45 people. No more than seven to eight invited lectures are given as an overview of the newest investigations and results on the chosen topic. This does not exclude that students and other colleagues working in the specific field have the possibility to present and discuss their projects and results in the workshop meetings.

[1] See also LNP 590, 2002, D. Benest & C. Froeschlé, eds.
[2] LNP 553, 2000, J.P. Rozelot ed.
[3] Journal de Physique IV, 2002, 12, J.P. Rozelot & A. Bijaoui eds.
[4] LNP 599, 2003, J.P. Rozelot ed.

J.P. Rozelot: *Introduction*, Lect. Notes Phys. **699**, 1–4 (2006)
DOI 10.1007/3-540-33759-8_1

The excellent site, a small island, sunny most of the time, the quietness of the place and the beautiful small flourished villages have, no doubt, something to do with the fact that people enjoy coming there.

The organizers warmly thank the Springer editions for their help, their efficiency, and sometimes for their patience...

I wish to express my thanks to all invited speakers and to all participants and I hope the readers of this book will find the same pleasure in reading it as the writers had in composing their lectures.

2 A New Field of Solar Physics?

This book takes an excursion through Space Weather, a topic in full scientific growth and still in progress for its growing impact in an international context where competition remains severe.

Authors conceived this book by approaching Space Weather by its main contributor: the Sun and the Solar wind. This method explains the title of the book, as the reader will find here more an overview of the solar physics behind Space Weather, with solar and heliosphere emphasis, than a description of the wide range of technological systems that are influenced or impacted through Space Weather occurrences. As a matter of fact, from a pure scientific point of view, Space Weather aims at setting operational numerical tools to forecast and quantify the solar activity events, to model their responses on the Earth magnetosphere, ionosphere, and thermosphere and then, to study their consequences on our technological societies, in space and on the ground.

The most important social and economic aspects of Space Weather are related to being aware of and possibly avoiding the consequences on spacecrafts systems, on launchers, on manned space flights, on communications, on electrical power systems, etc., and allowing for preventive measures to be taken. As the principal subjects that were tackled during the School, were mainly

- the definition of Space Weather,
- the solar signatures that precede the coronal mass ejections (CME), and the observations, principally in the radio frequency field,
- the transfer mechanisms in the interplanetary space of these ejecta, mostly through the solar wind,
- and the consequences on the upper layers of the Earth's atmosphere,

this book will follow the same lines. In the first chapter, an attempt to clarify the various concepts, Space Weather, Space Climate, Space Physics is made, as they are related to the general term of Sun–Earth links. A particular emphasis is put on sunspot forecasting, which plays a key role in Space Weather, but for which we are still rather ignorant on how the previsions can be done. The second chapter underlines the central role of the solar irradiance in all wavelengths and mainly in the UV part of the spectrum. The third chapter fully analyzes the role of the radiation belts. Such finding naturally leads to a

detailed study of the space environment and of the effects that it induces on space vehicles and astronauts. Then, it is given some background and updated observations on the structure of the solar wind and some theoretical issues, which are both fundamental to understand stellar wind and transport of the energy in a collisionless plasma. At last, the importance of radio observations for understanding the Sun–Earth system is reported.

We still miss a basic scientific knowledge to fully understand the mechanisms through which huge quantity of solar matter is ejected and how this material is transferred into the interplanetary space. However the various satellites located on the route (e.g., SOHO at the Lagrange point, UARS in the high Earth's atmosphere, WIND, etc.) gather data when they "see" the passing disturbance. And it is from the successive transformations of the ejecta that one can determine the physical parameters. We will point out the need to monitor accurate data series (or indexes) the most homogeneous as possible, over long time periods, to forecast the behavior of the solar–terrestrial system.

This book does not answer all the questions listed here (and they are not all asserted) but focuses on some particular aspects and try to show why it is important, from a physical point of view, to solve some of the crucial above-mentioned questions.

At last, it must be emphasized that a new European program (lead by one of us) has been set up within the COST framework (European Co-operation in the field of Scientific and Technical Research, see http://cost724.obs.ujf-grenoble.fr/) the objectives of which are to develop the science underpinning Space Weather applications, as well as exploring methods to provide a comprehensive range of Space Weather services to a variety of users, based on the modeling and the monitoring of the Sun–Earth system.

Some General References

Space Weather: public scientific documents. Available at: http://lpce.cnrs-orleans.fr/fr/meteo/meteo1–3.htm
ESA Space Weather Study, Alcatel Consortium: http://esa-spaceweather.net/spweather/esa_-initiatives/spweatherstudies/ALC/WP2100-V2.2.pdf
ESA Space Weather: http://esa-spaceweather.net/
Space Weather Today: http://www.windows.ucar.edu/spaceweather/
Space Weather Center: http://www.spaceweathercenter.org/
Space Environment Center: http://www.sec.noaa.gov/
C. Lathuillère, M. Menvielle, J. Lilensten, T. Amari, S.M. Radicella: Annales Geophys. **20** (2000), 1081–1104.

"Space Weather Quarterly" a digest from AGU'S Space Weather: "The International Journal of Research an Applications".
J. Lilensten, J. Bornarel: *Space Weather, Environment and Societies*, selected and edited by Grenoble Sciences, supported by COST (Springer, 2006) 242 p.

Advances in Understanding Elements of the Sun–Earth Links

Jean-Pierre Rozelot[1] and Sandrine Lefebvre[2]

[1] OCA (Observatoire de la Côte d'Azur), GEMINI Dpt, Av. Copernic, 06 130 GRASSE, France
jean-pierre.rozelot@obs-azur.fr

[2] Service d'Astrophysique SAp/DAPNIA/DSM CEA Saclay, L'Orme des Merisiers Bat. 709, 91191 Gif Sur Yvette Cedex (on leave from OCA-GEMINI)
sandrine.lefebvre@cea.fr

Abstract. The study of the Sun–Earth connections is a science in full effervescence, as much as for the physical problems that arise as for its growing impact on our societies. This last case is illustrated by the emergence of a new field of research called *Space Weather*. The launch of this new concept (translated in French by *météorologie de l'espace*) deserves to be clarified in spite of a great number of articles and books devoted to this question. In this chapter we will not extensively describe what Space Weather is, but we will only emphasize some appropriate definitions and other main notions. We will first establish a clear distinction between Space Weather and Sun–Earth connections (and Space physics). In a next section, we will briefly review the Sun as a variable star (in the Space Weather context). Then we will underline the necessity to better predict solar cycles showing the physical difficulties for such an exercise, leading to the extreme complexity for forecasting specific events of high energy. We will succinctly describe the question of risks. At last we will conclude by giving some imprints for future works.

1 Introduction

Most of the energy arriving on the Earth comes from the Sun, and the remainder comes from cosmic galactic rays.[1] It is thus usual to consider that the Sun's light and heat have to contribute to the warming of the surface of the continents, of the upper meters of the oceans, and of the atmosphere. Such ideas are not new and the fact that the Sun is one of the main sources of heat and life has indeed a long history. As far as one goes back into Antiquity, men gave a dominating place to the Sun for the organization of their daily life. Accordingly, agriculture was dictated by the rhythm of seasons: see, for

[1] We will not consider here the galactic rays whose influence on the cloud cover was shown very recently and for which effects are at the base of profitable studies (see the first paper on the question by Svensmark and Friis-Christensen [1]).

J.P. Rozelot and S. Lefebvre: *Advances in Understanding Elements of the Sun–Earth Links*, Lect. Notes Phys. **699**, 5–24 (2006)
DOI 10.1007/3-540-33759-8_2

example, how the Egyptians were anxious in awaiting the return of the floods of the river Nile and their concern to predict them in the most accurate way.[2] Progressively humanity started to look up to the Sun less as a "god" and more as an object of science. We are always impressed by this heritage, and we recognize today on physical grounds, that the solar energy is at the basis of weather variations, maybe also at the basis of climatic changes.[3]

If all the relations of cause to effects are still very poorly known, it nonetheless remains that weather conditions influence human activities on a large panel, such as the choice of an air route for the civil aviation, the choice of a routing for a sailing ship race,[4] the best choice for a harvest time, etc. It is known that this solar energy is the engine of the convective movements of the air masses: finally they contribute to the fact that the weather, in a given place of the globe, is more or less dry or more or less rainy, more or less cold or warm. It is known that this energy is variable with time, but curiously, meteorologists do not yet take into account the solar variability in short-term modeling. However, it can be seen from these brief considerations that it is essential to predict weather with a good reliability for the continuation of ground human economic activities to be able. This is also true now for space activities as it is known that solar eruptions may have a tremendous impact on satellites.

Understanding the complicated chain that links the solar variable output to the complex physical state of the Earth's atmosphere is still a challenge to physicists (Fig. 1). It is not possible yet to manage it completely, although some parts of the puzzle begin to be assembled. By contrast, it is possible to analyze the effects of the outflow of solar material on human technologies, on the ground or in space. These effects are numerous and varied: corruption of informatics aboard satellites, electronic failures, interruption in telecommunications, deterioration of technical systems on Earth, and hazards to astronauts or aircraft pilots. It is thus essential to be able to predict how a tremendous release of energy traveling from the Sun to our atmosphere may endanger human life (in space) and our technological systems (in space and on the ground). Such predictions are far from being achieved.

2 Space Weather Versus Solar–Terrestrial Links

The study of the Sun–Earth connections is a science in full effervescence, as well as for the physical problems that are raised as for its growing impact on

[2] A recent study [2] showed that floods of the river Nile may have followed the rhythm of the solar cycle.

[3] Note that Climate is different from Weather: briefly speaking the climatic signal is the slowly variable component contained in the meteorological data analyzed over longer time ranges (see further).

[4] See, for example, the non-stop solo Vendée Globe race around the world by Ellen MacArthur, for which meteorological previsions were crucial.

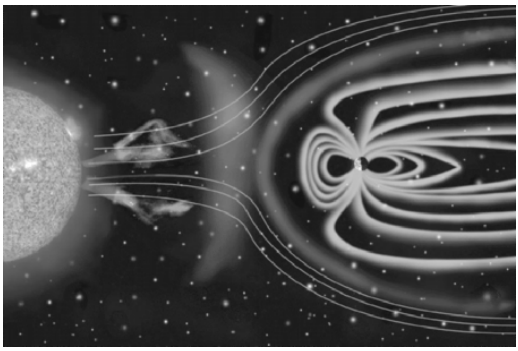

Fig. 1. A popular representation of the Sun–Earth connections

our societies. This last case is illustrated by the emergence of a new field of research called "Space Weather." The launch of this new concept (translated in French by "météorologie de l'espace"[5]) deserves to be clarified in spite of a great number of papers and books devoted to this question. Weather first induces a brief temporal idea: *weather* is the state of the environment at a given time and place; it may be quiet or violent. Weather is currently associated with local parameters such as temperature, pressure, hygrometry, or wind speed. On Earth, prior to the satellite era, such data have been widely recorded and were used, and still are, in meteorological reports. They have been used as time series for correlative studies with solar phenomena, and accompanied by a lot of skepticism among scientists due to a lack of physical mechanisms to account for these correlations. By contrast, *climate* refers to the long term, using data spanning more than one century and even more. Nowadays, climatic studies use a large variety of data other than "pure meteorological" parameters, such as cloud cover, albedo, extension of polar caps, tree leaves abundance, etc. Using the word "weather" must not be minimized. It must refer to specific conditions occurring in space, locally, and for which timescales are of the order of minutes to hours, up to no more than some days (or a few months). Beyond is another field of research.

Sun–Earth connections (in French "Relations Soleil-Terre") refer, on one hand, to the structure of the solar plasma by the magnetic field, and on the other hand to the structure of the magnetospheric plasma by the interplanetary medium. It is important here to stress the Sun's fundamental role in shaping the interplanetary space within the solar system, the region known as the *heliosphere*. The physics of the heliosphere and its interactions with

[5] It is not exactly the same; but as we will see later, meteorology is better appropriate than climatology, as it is written sometimes abusively. Space Climate is another new field of research, devoted to the study of impacts of solar outflows material in the environment of the Earth over long periods of time. The study of Space Climate thus involves both long-term average behavior and variations about those long-term averages [3].

the Earth magnetosphere and ionosphere is the domain of Sun–Earth connections, which can be extended to the interactions of the heliosphere with the magnetosphere and ionosphere of other planets, such as Jupiter (space physics). To conclude, we can say that

- *Sun–Earth connections* deal with the "Physics of the Transport and Energy Conversion in the Heliosphere," whereas, following the definition made by US National Space Weather,
- *Space Weather* may be described as "Conditions on the Sun and in the Solar Wind, magnetosphere, ionosphere and thermosphere that can influence the performance and reliability of space-born and ground-based technological systems and can endanger human life or health."

  Some comments on this last definition can be made at this step. First, man-made pollution of space, such as debris or radio-pollution is not taken into account. Second, the life of a human has never been affected by plasma bursts arriving from the Sun on the Earth.[6] There is no direct reference to unspecified dangers but to impacts on the human activity and the living conditions on ground. At last, the word "meteorology" refers also to an operational system of forecasts. It results that
- *Space Weather* can be defined as "the science aiming at studying the composition and the dynamic of the upper layers of the atmosphere of the Earth (magnetosphere, ionosphere, and thermosphere) the perturbations of which are due to solar events or man-made pollution (such as space debris or radio waves). Effects can endanger human life in space, and may have impacts on the performance and reliability of space-borne and ground-based technological systems, yielding economic upshots on our society."[7]

3 The Sun and the Earth

Sun and Earth form a complex dynamic system that is linked through radiation, particles, and magnetic fields. In principle, a refined study of each component would lead to a better understanding of the complete structure of the atmosphere. In fact, it is rather difficult to separate the role of each component, and the analysis of the global system is very hard to set up. Thus, before building huge models of climatic changes, it is necessary to try to understand how each part of the puzzle can act. There is a growing evidence that the solar variability affects the Earth system in various ways and on multiple timescales resulting in various proxies that can be used to investigate the variability of the Sun (see Fig. 2). On the other hand, as it is certain that

[6] At least during the last century where official recorded data are available.

[7] See other tutorials in http://www.phys.ucalgary.ca/satellites/html/sp_weather.html. A new definition is under consideration by COST 724 "Developing the Scientific Basis for Monitoring, Modeling and Predicting Space Weather": http://cost724.obs.ujf-grenoble.fr/).

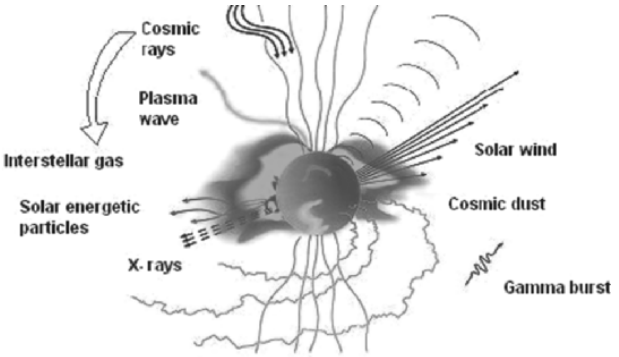

Fig. 2. A schematic view of the various ingredients emitted by the Sun filling the interplanetary space

the Earth's climate is unstable and is changing also on different timescales, it is of interest to get insights into the nature of these changes and how they can be related to solar effects.

The Sun is one of the main drivers for terrestrial climate changes. The Earth's envelope absorbs all radiations from far UV to IR, and the energy is redistributed by the atmospheric and oceanic circulations, and then radiated back to space. To first order, and taking the Earth as a whole, the annual mean incoming solar radiation energy is balanced by the outgoing terrestrial one. Any factor that alters the radiation received from the Sun or lost back to space alters the redistribution of energy within the atmosphere, land, and ocean, and thus can affect the climate. The factors that may have a great influence are divided into two groups: natural and anthropogenic ones. The difficulty is to separate their contributions, and any means to estimate the size of their effects is of decisive importance for a credible assessment of the man-made contribution.

Solar astronomers of the nineteenth century rapidly recognized that strong eruptions, such as solar flares or other intense activity events observed on the Sun, were often followed, minutes later, by disturbances in magnetic instruments on Earth. Large flares and coronal mass ejections often trigger geomagnetic storms; coronal material blown outward from the Sun at speeds exceeding that of the normal quasi-steady solar wind steepens into shocks, which pass by the vicinity of the Earth, interacting with the Earth's magnetosphere and perturbing it. The most common (and spectacular) manifestation of geomagnetic storms is the occurrence of Aurorae Borealis and Aurorae Australis (the so-called Northern and Southern Lights). More disruptive effects include perturbation of radio communications, disruption of power grids, and enhanced orbital decay of low-orbiting satellites. However, in view of their transient character, such events are not believed to induce long-lasting variations in the

climatic system, unless their frequency of occurrence were to change dramatically over extended periods of time.[8]

4 The Sun (in Brief)

For a few years, it has become of common use to say that the Sun is a banal star, a star among thousands or millions of others, although variable. And, to conclude that undoubtedly, the complete knowledge of the physics that allows the solar machine to function will come from the understanding of the mechanisms operating within stars, which are now observed through increasingly complex instruments, like the VLTI.[9] If the Sun is in fact a star, it is all but a trivial case. It is the only star we can examine in sufficient details to learn at the basic underlying atomic physics. It is because we first discovered spots on the solar surface and the differential rotation, it is because we first explore as well the solar interior as the solar corona, that we are able to transfer our knowledge on other stars. Do not reverse the roles! It is also because the Sun permits the life on Earth that the Sun is not a banal star. This proximity allows the Sun to be an extraordinary laboratory where plasma physicists can find natural conditions of temperature, pressure, and magnetic field which do not exist on Earth yet. But, of course, we have greatly enhanced our understanding of the physical properties of the Sun by comparing solar and nonsolar manifestations.

The Sun is located on the main branch of the Hertzprung–Russell diagram, and is of G2 spectral type, class V (dwarf). Its identity card[10] is summarized in Table 1, and typical features are listed in Table 2.

Space missions have changed our view of the Sun in many ways. Two main points emerge among many others: the first one is the unbelievable diversity of the magnetic field and the second concerns the probe of the solar interior. We have learned that the magnetic field is concentrated in small tubes of high field strength, with implications for solar activity, that it plays a crucial role in coronal heating and that reconnection is certainly the primary source of energy release in flares. We have learned a lot on the successive layers that composed the Sun. The core of the Sun itself, under investigation, is rotating at a nearly uniform velocity (at around 435 nHz), or a little more rapidly perhaps. The layer that envelopes this core, up to around $0.7R_{\odot}$, is the radiative zone. Then the convection zone is observed to undergo latitudinal shear (with little radial shear). A thin shallow shear layer separates the two zones, the tachocline,[11] of thickness about $0.05R_{\odot}$ [5]. Because of its intrinsic nature, and because of

[8] P. Charbonneau and O.R. White, 1995, http://www.hao.ucar.edu/public/slides/-conc.html.

[9] Very Large Telescope Interferometer, now operating at Paranal (Chile).

[10] A number of Web sites are dedicated to solar facts and terminology; one can consult, for instance, http://www.hao.ucar.edu/public/slides/intro.html.

[11] From Greek, $\tau\alpha\chi\varnothing\varsigma$, velocity and $\chi\lambda\iota\nu\epsilon$, bend or hill.

Table 1. Some main (and crucial) parameters of the Sun (compiled by the authors)

Mass	$1.9891 \pm 0.0004\ 10^{30}$ kg
Equatorial radius	$6.\ 959\ 917\ 56\ 10^{8}$ m
Polar radius	$6.\ 959\ 843\ 88\ 10^{8}$ m
Mean density	1409 kg m^{-3}
Central density	$9.0\ 10^{4}$ kg m^{-3}
Gravitational acceleration	274.0 m s^{-2}
Rotation of the core	$\Omega_c = 435$ nHz
Rotation of the surface	$\Omega(\theta) = \Omega_{eq}(1 - a_2 \cos^2\theta - a_4 \cos^4\theta)$
(θ is the colatitude)	$\Omega_{eq} = 2.83\ 10^{-6}$ rd/s
	$a_2 = \approx 0.1$ and $a_4 = \approx 0.18$
Minimum distance (Perihelion; January)	$1.4710\ 10^{11}$ m
Maximum distance (Aphelion; July)	$1.5210\ 10^{11}$ m
Irradiance at mean distance (1 AU)	1366 ± 1.3 W m^{-2}
Luminosity	$3.846 \pm 0.05\ 10^{26}$ W
Angular momentum	$1.94 \pm 0.05 \times 10^{48}$ $gcm^{-2}s^{-1}$ (mean value)
Home	Galaxy arm, $\approx$ 30 000 light-years from the center
Age	4.52 ± 0.4 Gyr
Distinctive mark	Covered with spots every 11 years Best period: 10.898 years

its location, in a region of transition between two radically physical different zones (radiative below and convective above), the tachocline is the seat of the most interesting and complex phenomena occurring in the Sun, and the place where the differential rotation starts.

The *photosphere* is the surface of the Sun, of about 150–200 km deep. When speaking of the solar surface, one is not referring to a solid surface, but to a fictitious more or less distorted surface, determined by a gravitational equilibrium. All features (which are of interest for our purpose here), such as sunspots, bright faculae, convective cells, pores, and granules, are observed on the photosphere. In this layer, the solar gas changes from almost complete transparency to complete opacity. Just below the surface, another very thin layer takes place, the *leptocline,*[12] which is a region of steep density gradient determined through the gravitational moment J_2 [6] or recently put in evidence by the helioseismologic f-modes [7].

At last, the Sun emits in the whole spectral range, from very short wavelengths (gamma rays $\approx$0.1 nm) to very long wavelengths (radio, $\approx$1 km). Most part of the radiation is emitted in the visible, mainly through the photosphere, $\approx$40% of the total energy; $\approx$50% are emitted in IR (converted into heat on the upper atmosphere of the Earth) and the $\approx$10% left are emitted in UV, EUV, and X. The total flux of these waves varies slightly with time. Radio

[12] From Greek $\lambda\epsilon\pi\tau\varnothing\varsigma$, thin and $\chi\lambda\iota\nu\epsilon$, bend or hill, as seen in footnote 11.

Table 2. Typical averaged parameters of the Sun (After Démoulin and Klein [4])

	T (K)	n_e (m^{-3})	n_H (m^{-3})	**B** (T)
Photosphere				
Bottom	6,500	8×10^{19}	10^{23}	
Sunspot	4,000	5×10^{18}	4×10^{23}	max 0.3
T min	4,170	3×10^{17}	2×10^{21}	
Chromosphere				
Quiet	10,000	4×10^{16}	5×10^{16}	3×10^{-3}
Plage	10,000	3×10^{17}	4×10^{17}	3×10^{-2}
Corona				
Hole	$\leq 10^6$	1×10^{13}		1×10^{-4}
Active region	4×10^6	1×10^{16}		8×10^{-2}
Quiet	2×10^6	1×10^{14}		1×10^{-3}
Prominence				
	7,000	1×10^{16}	1×10^{17}	1×10^{-3}

Some other typical useful values		
Sunspot length	1×10^7 m	
Granule length	1×10^6 m	
Coronal mass ejections (CME)	1×10^5 s	
Flares		
Main phase	1×10^4 s	
Impulsive phase	3×10^2 s	
Hard X-rays spikes	1×10^{-1} s	
Radio spikes	1×10^{-2} s	
Velocities		
Photospheric motions	0.1 to 1 km s^{-1}	
Particle beams	up to 3×10^5 km s^{-1}	
Solar wind	400 km s^{-1}	min and 800 km s^{-1} max
Jets	few 100 km s^{-1}	

waves are responsible for storms and affect our upper atmosphere (see Pick, this volume).

To quantify the solar energy, the Total Solar Irradiance (TSI) is defined. This quantity has continuously been measured from various spacecrafts platforms (and some rockets) since November 16, 1978 (Fig. 3, upper panel). TSI refers to the total electromagnetic energy received by a unit area per unit of time, at the mean Sun–Earth distance (1 AU). Historically, TSI has been called the *solar constant*[13] by A. Pouillet in 1837. Since then, measurements have been made by a long series of observers up to Abbot, in 1942 [9], and the value was set up as 1.98 ± 0.05 cal min^{-1} cm^{-2} (i.e. 1381 ± 35 W m^{-2}, close to the modern one, 1366 ± 1.3 W m^{-2} [10]. Today, there is irrefutable

[13] Thus the solar constant describes the "average" TSI on the long term.

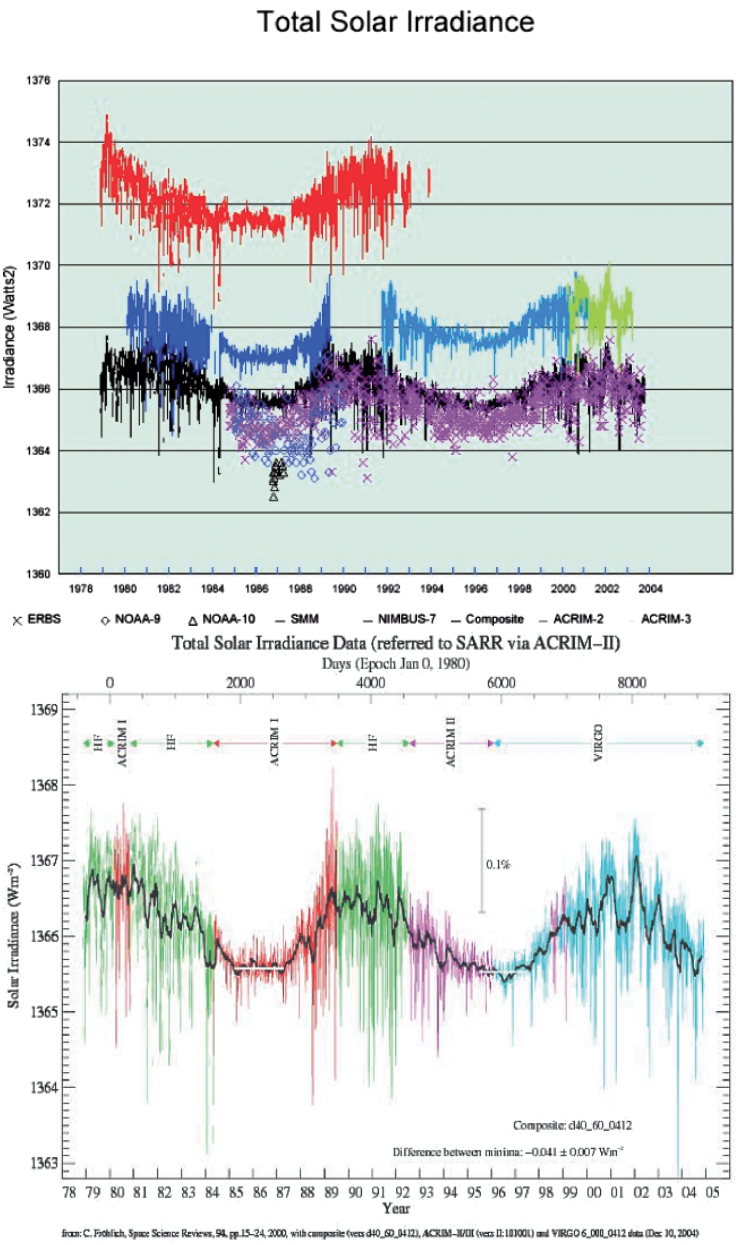

Fig. 3. Various Total Solar Irradiance (TSI) time series measured from space are presented on the upper panel. The composite TSI as daily values plotted in different colors for the different originating experiments is shown on the lower panel (from Fröhlich [8])

evidence of temporal variations of the TSI. Measurements made for 26 years (two and an half solar cycles) show a variability on different timescales, ranging from minutes up to decades, and likely lasting even longer. In spite of the fact that collected data come from different instruments aboard different spacecrafts, it has been possible to construct a homogeneous composite TSI time series, filling the different gaps and adjusted to an initial reference scale. Figure 3 (lower pannel) shows such a composite, details of which can be found in Pap [11]. The most prominent discovery of these space-based TSI measurements is a 0.1% variability over the solar cycle, values being higher during phases of maximum activity (see [11] and many other references herein). This variability reaches a factor of 2 in UV, and thus TSI may play a key role in the upper atmosphere. Wavelengths below 150 nm can be responsible for the ionization of neutral atoms and molecules. The ionization processes occur above 80 km altitude and the produced ionized species form the Earth's ionosphere, embedded in the upper atmospheric layers [12].

The physical causes of these variations still remain a subject of debate. If we know that surface magnetism might be the primary cause [13, 14], we are not sure that other factors would not have to play a role. Among them, a possible one could be temporal variations of the radius of the Sun, others being mainly effective temperature and solar oscillations frequencies. At last, the magnetic fields originating from the tachocline must increase the luminosity so that spots and faculae do not explain the whole observed irradiance variations over the solar cycle [15].

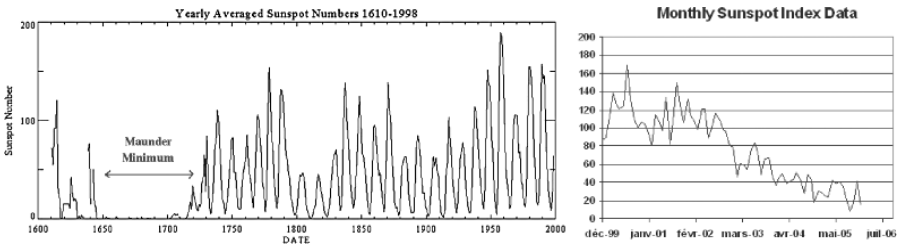

Fig. 4. *Left*: Yearly mean Sunspot Numbers since 1600 (From Usoskin and Mursula [16]). *Right*: Monthly mean Sunspot Numbers since 2000 up to nowadays

5 Sunspots Prediction

The solar activity cycle, as manifested by the 11-years variation in the number of spots and faculae, has been observed systematically since 1749. However, considerable efforts have been made to determine estimates for sunspots before this date, mainly through analysis of old books and records on Astronomy. Sunspots are now available since approximately 1600 AD (Fig. 4) where the

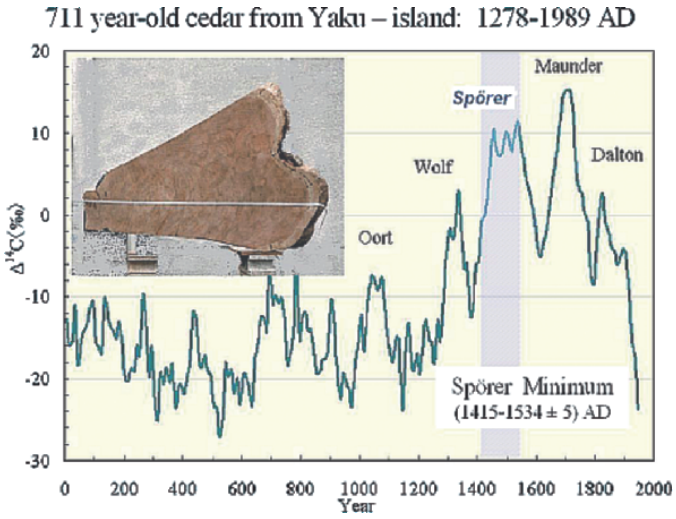

Fig. 5. Analysis of isotope ^{14}C permits to deduce through the Forbush effect, past periods of very low solar activity. The green curve is from Stuiver et al. [17]. The analysis of the tree rings shown in the left upper part has been made by Hiroko Miyahara et al. from the Solar-Terrestrial Environment Laboratory, Nagoya University, Japan. Such episodes were related to climatic conditions on Earth

Maunder Minimum appears, a period of time where the solar activity was practically null. The intensity of the activity cycle, as measured by its peak in the annual mean sunspot count, is not the same from one cycle to another. Inspection of Fig. 4 clearly reveals a modulation of the envelope of the maxima of about 80 years. This period of time is known as the Gleissberg cycle. This period of abnormally low sunspot activity was not a singular event. The analysis of the concentration of the isotope ^{14}C produced in the atmosphere and preserved in tree rings shows a strong anticorrelation with solar activity (Fig. 5). It has been thus possible to go back around 5,000 years. Six episodes of depressed activity and five of elevated activity have been counted, each lasting around 100 years. Such episodes are related to climatic conditions on Earth. It is generally admitted that periods of low solar activity coincide with periods of lower temperature on the Earth (at least for the Northern hemisphere). Due to the elevation of greenhouse gases during the last 50 years, it is hard to find the solar signature again [18].

These notable phases of prolonged minima in solar activity are known as Oort minimum (1010–1050), Wolf minimum (1280–1340), Spörer minimum (1420–1530), Maunder minimum (1645–1715), and Dalton (or Sabine) minimum (1800–1820). The mean peak activity has slowly been increasing since 1700, but, as it will certainly not always increase, it is more likely part of a longer modulation of around 120 years (between a minimum and the next maximum, if one takes into account the evolution of the radius variation over four centuries, see [19]) and around 200 years of cyclicity if one takes into

account a ranging time of about a millenium: a period of 200 ± 20 years seems to be a good average). The next "great" minimum is thus expected for approximately 2015–2045.[14] If such a forecast proved to be exact, **it would be very useful for future space missions, in particular those of long duration, because one would be sure not to be too importuned by violent solar flares**.

A great number of studies have been made to try to model sunspot cycles to make the best possible prediction (or retrospection). Up to now all methods aiming at properly reproducing the observed data fail. The simplest way is to determine periodicities in the solar signal through a Fourier analysis. One can think a priori that about 30 periods, determined over 250 years (i.e., 1749-2000) would lead to a fairly nice reconstruction of the signal. Unfortunately it is not the case and the extrapolation on the next years does not match the observed data. All other methods, such as the method of maximum of entropy, cyclograms, wavelets, and many others, also give poor results. To sum up a subject that has been *à la mode* some 15 years ago, one can say that the failure of the traditional methods indicates

- that the **forecast** is good. For instance, in 2004 it is possible to forecast that the next solar maximum will take place around 2011. However, the **prediction** is poor: inaccuracy on the date, inaccuracy on the estimate of the level of the signal.[15]
- that the **observed** is not enough to deduce the **observable**.

These two statements indicate that the solar cycle is not deterministic in the Laplace sense. Recent works have shown the chaotic deterministic character of the solar cycle with a Lyapunov exponent of around 3–4 years [20]. This exponent is a measure of the divergence of the trajectories in an unstable system. In other words, it means that it would be impossible, in the solar case, to accurately determine the date and the level of intensity of the activity signal more than 3 or 4 years ahead, unless being able to describe the entire mechanisms that govern the physics of the Sun, and this is not the case yet. A large number of techniques (such as described by [21–26], etc) are used to predict the behavior of a sunspot cycle, and its amplitude near and before sunspot minimum or maximum. For instance, relationships have been found between the size of the next cycle maximum and the length of the previous cycle. Waldmeier [27] first suggested an empirical relationship for predicting the sunspot number 5 years after the maximum described by $R_{\max}$:

$$R_5 = (0.29 \pm 0.06) R_{\max} - (11.4 \pm 6.7)$$

Such predictions are made for "smoothed" International Sunspot Numbers. The smoothing is usually over time periods of about a year or more, so both

[14] Note added in proof: Livingston W. and Penn M. recently arrived at the same result: "Sunspot may vanish by 2015". See American Society Proceedings, 2006.

[15] In French, we will say that the *prévision* est bonne, mais que la *prédictibilité* est mauvaise.

the daily and the monthly values for the International Sunspot Number should fluctuate about the predicted numbers. Also note that the "Boulder" numbers reported at http://www.sunspotcycle.com are typically about 35% higher than the International Sunspot Number available at http://sidc.oma.be/-products/ri_hemispheric.

Another indicator of the level of solar activity is the flux of radio emission from the Sun at a wavelength of 10.7 cm (2.8 GHz frequency). This flux has been measured daily since 1947 and current values can be found at http://www.drao.nrc.ca/icarus/www/sol_home.shtml. The radio flux is an important indicator of solar activity because it tends to follow the changes in the solar ultraviolet that influences the Earth's upper atmosphere and ionosphere. Many models of the upper atmosphere use the 10.7 cm flux (F10.7) as input to determine atmospheric densities. Again, another indicator of the solar activity is the Mg II core-to-wing ratio. Mg II is a line formed at 280 nm and is measured continuously since around 1980 by space experiments, such as SUSIM. This index has been introduced because it is a very sensitive indicator of solar activity [28]. The question of to what degree is the Mg II index linearly dependent to the solar UV irradiance is a focus of current research, the aim of which is to better predict irradiance level of activity, both for past reconstruction and for the future.

If other techniques still exist (e.g., through neuronal networks), it can be seen from this discussion, not only all the interest, but also the great difficulties existing, in order to be able to conduct the best forecasts (Fig. 6).

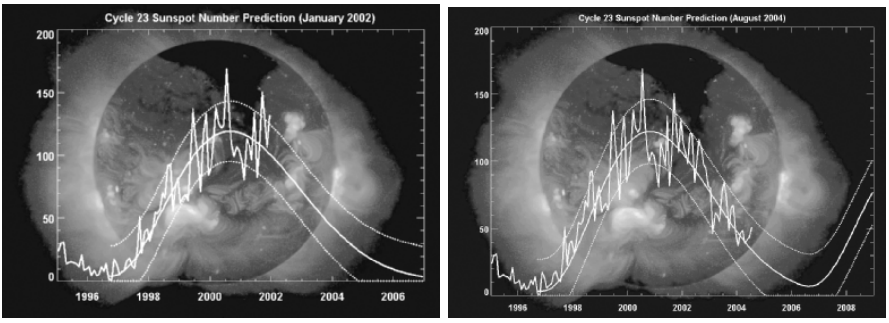

Fig. 6. Prediction of Sunspot numbers. *Left*: the prediction has been made on the basis of the known activity up to January 2002. The minimum is foreseen for April 2006. *Right*: same as before, but the activity is known up to August 2004. The new prediction gives June 2006. This simple figures illustrate the difficulty to forecast sunspot activity more than 3 years in advance. From Hathaway, http://science.msfc.nasa.gov/ssl/pad/solar/images/ssn_predict_l.gif

6 Particle Emission

One common feature to all electromagnetic radiations – from the gamma to the radio ranges of the spectrum – is that photons travel at light speed, covering the distance between the Sun and the Earth (1 AU) in 8 min. By contrast, the particles emitted by the Sun travel at different speeds.

Most of these particles are of low energy, forming a plasma called "solar wind" and traveling in space at an average speed of 400–500 km/s when coming from equatorial regions and 800 km/s elsewhere (see Issautier, this volume). The resulting magnetic fields are not randomly oriented in space but come in more or less two distinct types:

- Closed field lines emerge from the surface, loop up into the atmosphere (chromosphere and corona), and then connect back on the surface; and
- Open field lines stretch out into the interplanetary space and act as pipes for the plasma, usually escaping from flares. The magnetic field and the particles are closely dependent, the field being "frozen" in the plasma. This speed is important to forecast Space Weather because the solar wind takes 2–4 days to reach the Earth: this time lag allows certain precautions to be taken.

One specific form of the solar wind is linked with the solar eruptions. Figure 7 shows such violent features that take place in the vicinity of the surface of the Sun.[16] Enormous quantities of matter can be ejected with a fantastic energy. They have been known for a long time (for instance B. Lyot took a film of such a colossal protuberance in 1947 at the Pic du Midi Observatory) but they have been investigated recently as a main contributor of Space Weather under the name of Coronal Mass Ejection (CME). Such CMEs are higher in mass (billions of tonnes) than the simple particles flow of the solar wind and travel up to three times its velocity, ≈1500 km/s. If interacting the Earth's atmosphere, CMEs induce violent magnetic storms. CMEs contain a large quantity of helium, electrons, and ionized particles, such as iron. As a result there is a large voltage difference between components and currents, which is particularly hazardous for satellites. Moreover, the shock wave on the front edge of the traveling CME is also dangerous for these satellites.

CMEs are associated with protuberances and flares, which are initiated and which develop in the atmosphere of the Sun, the corona. During these eruptions, more energetic particles, reaching sometimes several hundreds MeV, can be ejected from the Sun, forming SPEs (Solar Proton Ejecta). Such events are not only particularly dangerous for electronics onboard satellites

[16] The size of a solar flare is quantified today in an objective way, thanks to the permanent measurements taken in space in the X-rays field. Thus an eruption of X6 size means that total flow coming from the Sun observed at the time of the maximum of the eruption reached the value 6×10^{-4} W/m^2 in the band ranging from 0.1 to 0.8 nm. An eruption giving a flow lower than 10^{-4} is assigned as of M type, a flow lower than 10^{-5} as of C type, then B, then A at each decade below.

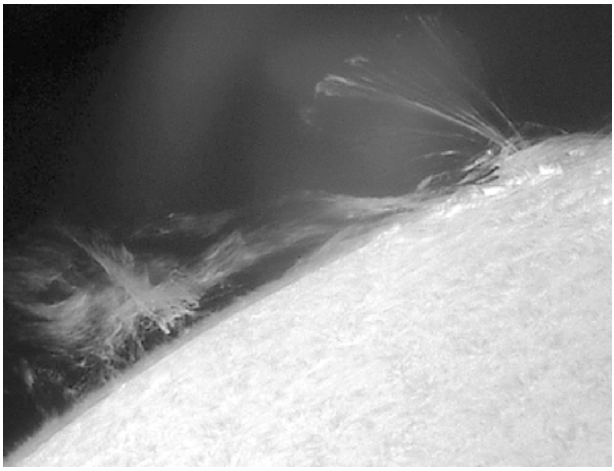

Fig. 7. Eruptions seen at the solar edge. Active regions may produce extremely energetic solar flare activity. For instance, a very large flare occurred at 09:52 UTC on January 17, 2005, when the underlying active region spawned an impressive and very long duration (over 3 h) of a solar X-ray flare of type X3.8. The solar flare produced intense radio emissions across the spectrum. The emissions at 10-cm wavelength were more than 80 times louder than the normal background noise of the Sun, measuring 12,000 sfu! Near-relativistic (traveling near the speed of light) energetic protons from this event began arriving at the Earth near 10:00 UTC and further increased space radiation levels at orbital altitudes. A risk of a category S3 space radiation storm was forecasted being able to give an increased charging related anomalies on orbiting spacecraft. It may also enhance the ambient radiation environment for passengers and crew of commercial airlines operating in high latitude regions. If S3 levels are achieved, a low-level radiation enhancement equivalent to an approximately one chest X-ray may be observed for these personnels (after http://www.spacew.com/astroalert.html)

but may also be dangerous for the health of men in space. SPEs occur in general close to the solar maximum.

As an example, let us briefly describe cycle 22. This cycle started in September 1986, has its minimum in 1986.8 (sunspot number 12.3), its maximum in 1989.6 (sunspot number 158.5), and lasted 9 years and 8 months. The maximum phase of the cycle appeared to end rather abruptly in early 1992 (time rise of 2.8 years), when monthly values of sunspot number dropped significantly (time fall of 6.8 years). The decline of cycle 22 to its minimum in May 1996 was also remarkable because of the lack of major flare activity.[17] However, SPEs were recorded in March 1989, October 1989, and June 1991. On March 13 and 14 occurred one of the largest geomagnetic storms in the

[17] The cycle was less than 10 years in duration – a fair bit shorter than the "traditional" 11 year. However, it is interesting to note that all but one of the last seven cycles have been less than 11 years, cycle 20 being an exception.

last 50 years. The inventory of effects shows a long list of notable features. Power systems in Sweden and Canada failed as large electric currents were induced in power lines and tripped protective relays. On March 13, 1989, in Montreal, Quebec, a few six million people remained deprived of electricity during 9 h following a disturbance which blew up a transformer. The cost for the community and the Hydroquébec Company was particularly high. Increased atmospheric drag, resulting from the expansion of the Earth's outer atmosphere during the disturbance, altered the orbit of many satellites with the result that NASA lost track of some of them for a short period. Satellite navigation systems failed to operate and high frequency (HF) communication systems were also out of action. Aurorae were sighted at quite equatorial latitudes. The southern regions of Australia were under cloud but numerous sightings were made into Queensland and even at Exmouth in Western Australia (which is north of the tropic of Capricorn). June 1991 was the month of the most outstanding solar flare activity of this cycle 22: X-ray detectors on the US GOES satellites that measure output of flares were saturated during five flares over the interval from June 1 to 17 [29].

Note that the first Sun–Earth Connection Event recorded was on September 1, 1859 [3]. It is generally appreciated that the September 1859 solar-terrestrial disturbance, the first recognized Space Weather event, was exceptionally large. Although the correlation between the size of active regions and terrestrial event intensity is rather loose (e.g. [30]), the presence of a major spot group certainly increases the probability of occurrence of strong activity. For example, the largest solar active region during the space age (NOAA/SEC Region 5395; 3500 millionths of a hemisphere) is linked to the notable Space Weather event of March 1989 [31].

Another well-known and well-studied event is the so-called "Bastille day" (Symbol of the end of the French Monarchy) event which occurred on July 14, 2000. A very bright solar flare was visible on the solar disk (see, for instance, http://gse.gi.alaska.edu/bastilleday.html), starting at 10:24 UT. Energetic protons from the flare arrived on the Earth about 15 min after the eruption. The flare coincided with a coronal mass ejection from the Sun, which sent billions of tons of plasma into space traveling at 4 million miles per hour, twice the normal speed. This triggered a category S3 radiation storm.

The release of high energetics electrons (≈30–500 keV) in the solar corona is a subject under progress with the aim to clarify the relationship between the coronal acceleration and the escape of electrons to interplanetary space. Events can be identified, mainly through dedicated satellites (such as $WIND/3P$ experiment). The release time of these electrons could be determined within an uncertainty of a few minutes and can be recorded on large radioheliographs (such as in Nançay, France). Recent findings show that *(i) Electrons detected at the orbit of the Wind spacecraft are released at the time of distinct episodes of electron acceleration in the corona signaled by radio emission. The release may occur at the start of the radio event or up to an hour later; (ii) the most conspicuous examples of delayed electron release oc-*

cur in events associated with complex, long-lasting (>10 min, up to several hours) radio emission. Radio observations suggest that in these cases the earlier accelerated electrons remain confined in the corona or are injected into flux tubes that are not connected to the spacecraft; (iii) type II bursts revealing shock waves in the corona accompany about a third of the events. But the shock waves occur, in general, together with type IV radio signatures due to long-lasting acceleration not related to the shock. With a few exceptions these type IV emissions have a clearer timing relationship with the electron release to space than type II bursts. Thus, the combination of time-extended acceleration at heights 0.5 $R_{\odot}$ *above the photosphere with the injection of electrons into a variety of closed and open magnetic field structures explains the broad variety of timing shown by the radio observations and the in situ measurements* [32]. Such types of observations are essential for the understanding of the release mechanisms of the solar electrons into the interplanetary space.

7 Risks in Space

All solar ejections traveling in space may have consequences at the level of the Earth's orbit and on human activities. These consequences must be analyzed in term of impact: this one can be more or less significant, more or less fatal. This leads to introduce a concept of risk.

But what is a risk in space? How to quantify such a risk? Does a risk require insurance? Is risk mandatory related to a probability concept? What is fatal and what is not? A particular attention must be given to such questions (among others) and from a scientific point of view, we are still in the infancy [33]. First, what can cause a risk in space or on our environment? If we are able to determine the cause, what is the risk? The encounter of "bolides" (asteroids, meteroites, comets) with our planet provokes impacts and the hazard comes from the quantity of material that interacts with the ground, the ocean, or the atmosphere. From historical facts, it seems that Babylonians were already conscious that celestial bodies could fall on Earth. The Chinese emperors tried to decipher the future in the tails of comets or meteors, tails which convey the interaction of the foreign bodies with the Earth's atmosphere. Indeed, we are constantly bombarded by micrometeorites, and fortunately, the effects are not all disastrous for mankind.

The perception of risk is not the same for the public, governments, company managers, and scientists. To be as objective as possible, space environment data must be recorded, processed, validated, and disseminated in an efficient and timely fashion. It is why center's missions are developed and products delivered to customers. Figure 8 shows such an example of data, a free access to them being necessary. Any Space Weather center must be able to give reliable data and reliable forecast. Such centers already exist, such as the NOAA Space Environment Center (SEC) in the United States. In Europe, a new program called "COST 724" has recently been set up to coordinate Space Weather services in Europe [34].

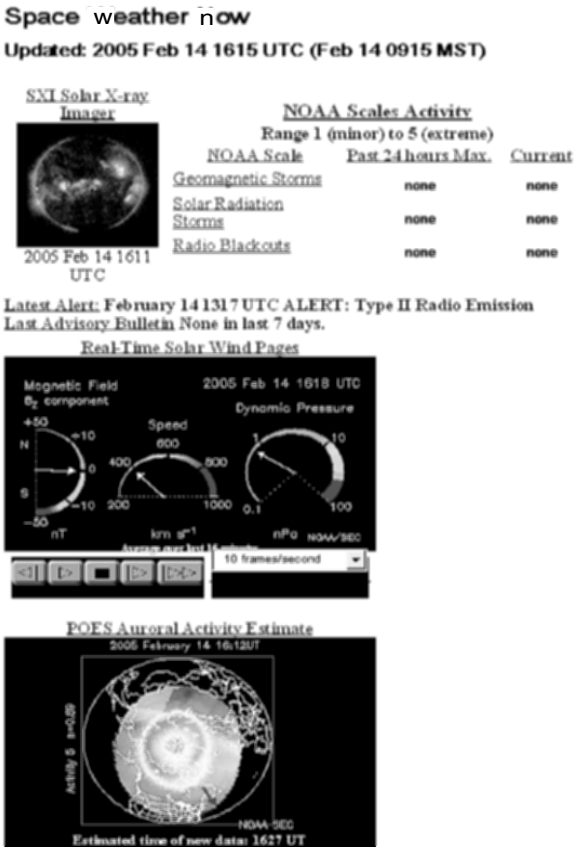

Fig. 8. Example of data delivered from Space Weather Centers

8 Conclusion

Space Weather studies have become important mainly because of the adverse effects on satellites and disruptions in radio communications caused by severe scintillation associated with some of such events occurring in solar–terrestrial system. Anomalies in electron density distribution may also lead to errors in satellite-based navigation.

Substantial progress in moving toward a deep understanding of a great number of questions related to Space Weather has been made recently, refining the questions, displaying them, and answering many parts of them.

To our mind, a clear distinction must be made between "Space Weather," "Space Climate," "Space Physics," and "Sun–Earth connections."

In addition to scientific research to predict space weather, mission centers must be reinforced and developed in the most operational way. Spacecrafts,

which are design to survive the worst conditions, are often overengineered; better models of space environment would lead to reduce cost.

The major era of research, for the next years, is that of constructing models for the solar–terrestrial environment. In addition to the complexity of the problem, which involves MHD, the problem is difficult because of at least three reasons. First, we are still very far from constructing a mathematical model of the Sun. There are still a lot of open questions, such as what trigger flares or why do sunspots occur. Second is the vast interplanetary medium, in which the solar plasma travels, which is not fully understood yet. The third one is the environment of the Earth, the very complex geomagnetosphere, with its many regions and currents. How is a change in one of the domain (for instance in the magnetotail) returned in the others? A comprehensive model, still far from our grasp, is certainly a major problem for physicists in the future.

Last, but not least, the introduction of Space Weather into the *risk management* is far from being unreasonable. Several services of predictions currently produce index of total risks (see the Web site from where Fig. 8 is extracted). Indexes of risk adapted to the needs of users are now currently elaborated. Others require the development of new models that are under consideration. Briefly, one can consider that the integration of the risks related to the space environment in the environmental risks is all the more but an encouraging projection, as it makes it possible to improve the work visibility concerning the ionized environment of the Earth.

Thus Space Weather physics is awaiting new generation of students.

References

1. H. Svensmark, E. Friss-Christensen: J. Atmosph. Sol. Terres. Phys. **59**(11) 1125–1232 (1997)
2. A. Hady: *Historical Events and People in Aeronomy, Geomagnetism and Solar-Terrestrial Physics*, ed by W. Schröder AKGGP/SHGCP, Science ed., Bremen, (G), 211 (2006)
3. E.W. Cliver and L. Svalgaarel: Sol. Phys. **224**, 407 (2004)
4. P. Démoulin, L. Klein: *Structuring of the Solar Plasma*, Lecture Notes in Physics, ed by J.P. Rozelot, L. Klein, J.C. Vial (Springer) pp. 99–135 (2000)
5. J. Schou: Astroph. J. **505**, 390 (1998)
6. S. Godier, J.P. Rozelot: Sol. Phys. **199**, 2, 217–229 (2001)
7. S. Lefebvre, A. Kosovichev, J.P. Rozelot: 2006 ESA SoHo17 proceedings, "10-yrs of SOHO and beyond", 7–12 May 2006, Giardini Naxos (I).
8. C. Fröhlich: Space Sci. Rev. **94**, 15–24 (2000)
9. C.G. Abbot: 1942, Ann. Obs. Smithsonian Inst., **6**, 163
10. G. de Toma, O.R. White, G.A. Chapman, S.R. Walton: Adv. Space Res. **34**, 237 (2004)
11. J.M. Pap: *The Sun's Surface and Subsurface*, Lecture Notes in Physics, 599, ed by Rozelot (Springer, 2003) p. 129

12. D. Fontaine: *Structuring of the Solar Plasma*, Lecture Notes in Physics, ed by J.P. Rozelot, L. Klein, J.C. Vial (Springer, 2000), pp. 137–164
13. N. Krivova, S. Solanki: Astro. Astrophys. **399**, L1–L4 (2003)
14. S. Solanki, N. Krivova: Sol. Phys. **224**, 197 (2004)
15. J.R. Kuhn: Adv. Space Res. **34**, 302 (2004)
16. I.G. Usoskin, K. Mursula: Sol. Phys. **218**, 319 (2003)
17. M. Stuiver, P.J. Reimer, T.F. Braziunas: High-precision radiocarbon age calibration for terrestrial and marine samples, *Radiocarbon* **40**(3), 1127–1151 (1998)
18. J.P. Rozelot, S. Lefebvre: Proceedings of the Solar irradiance variations and Earth's climatic implications, International Workshop on Long Term Changes and Trends in the Atmosphere, 09–14 June 2004, Sozopol, Bulgaria. Published in *Phys. Chem. Earth.*, **31**, 41 (2006)
19. J.P. Rozelot: J. Atmosph. Sol. Terres. Phys. **63**, 375 (2000)
20. J.P. Rozelot: Astro. & Astrophys. **297**, 45 (1995)
21. J. Feynman, S.B. Gabriel: Sol. Phys. **127**, 393 (1990)
22. D.H. Hathaway, R.M. Wilson, E.J. Reichmann: Sol. Phys. **151**, 177 (1994)
23. D.H. Hathaway et al: Sol. Phys. **224**, 5 (2004)
24. K. Mursula, T. Ulich: Geophys. Res. Lett. **25**, 1837–1840 (1998)
25. R. Thompson: Sol. Phys. **148**, 383 (1993)
26. R.M. Wilson, D.H. Hathaway, E.J. Reichmann: J. Geophy. Res. **103**, 17411–17498 (1998)
27. M. Waldmeier: Ergebnisse und Probleme der Sonnenforschung, Geest und Portig., Leipzig (1955).
28. L. Floyd: *The Sun's surface and subsurface*, Lecture Notes in Physics, 599, ed by Rozelot, (Springer, 2003) p. 109
29. R. Thompson: IPS Radio Space Services, Sydney, Australia (1997)
30. E.W. Cliver, N.U. Crooker: Sol. Phys. **145**, 347 (1993)
31. J.K. Allen: In: Proceedings of a Workshop on Satellite Drag, NOAA, Boulder, Co. (1989)
32. K.-L. Klein, S. Krucker, G. Trottet, S. Hoang: Astro. Astrophys. **431**, 1047–1060 (2005)
33. A. Wolfendale: Eur. Rev. **11**, 77–90 (2000)
34. J. Lilensten, T. Clark, A. Belehaki: Space Weather Q. (Summer), 9 (2004)

Some Basic Aspects of the Solar Wind

Karine Issautier

Observatoire de Paris, LESIA, CNRS UMR 8109, 92195 Meudon, France

Abstract. What follows is a compilation of two lectures given during the summer school of Oléron (France) on the solar corona and solar wind. Four decades of ongoing research on these hot topics cannot be summarized here. The scope of this chapter is to give some background and updated observations on the structure of the solar wind and some theoretical issues, which are both fundamental to understand stellar wind and transport of the energy in a collisionless plasma.

1 Introduction

The solar wind is a fully ionized gas; it is a *plasma*, coming from the outer atmosphere of the Sun, the so-called *solar corona*, which expands as a supersonic flow into the interplanetary medium [1]. The first observations indicating that the Sun might be emitting a wind were made by Biermann in 1946 of comet tails [2], which are observed to point away from the Sun when the comet is approaching it. Comets usually exhibit two tails: a dust tail driven by the sunlight pressure and a plasma tail, which points in slightly different directions pushed by the "solar corpuscular radiation" of the Sun. In 1958, E. Parker explained theoretically this particle radiation using a simple fluid model [1], showing that the solar atmosphere is not in equilibrium but must expand into the interplanetary medium as a wind. The existence of this solar wind was debated until it was indeed confirmed by spacecraft Lunik 2 and 3 [3] and continuously observed by Mariner 2 [4].

Because of its proximity, the Sun is an ideal laboratory since in situ and/or remote sensing observations can give major details on our star in particular, and some clues to understand other stars. Dupree in 1996 discussed methods to detect stellar wind from cool stars, as giants or supergiants [5], and gave characteristics of these winds on a color-luminosity diagram (see Fig. 1 of this chapter and Fig. 8 of [5]). Typically, the mass loss rate of cool stars such as the Sun, i.e., the mass lost per second, is around 2.10^{-14} $M_{\rm s}$/year for our Sun, whereas other stars may lose much more material as a wind, three or

K. Issautier: *Some Basic Aspects of the Solar Wind*, Lect. Notes Phys. **699**, 25–52 (2006)
DOI 10.1007/3-540-33759-8_3

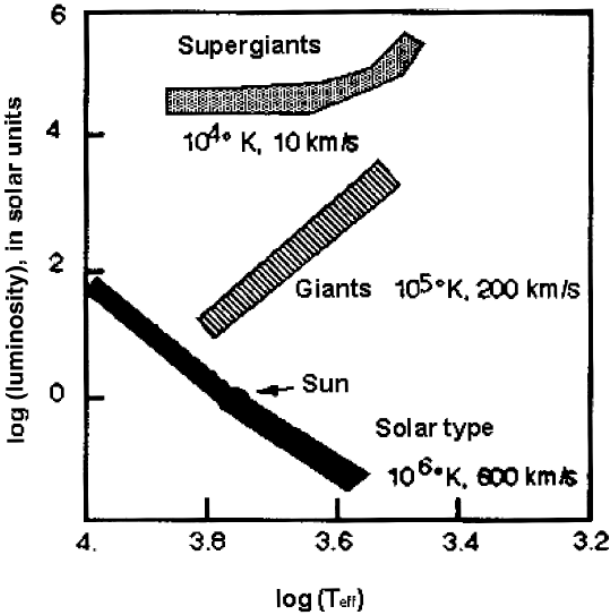

Fig. 1. Schematic color/luminosity diagram. It gives electronic temperature and bulk speed for typical stellar winds. Adapted from [5]

four orders of magnitude more than the Sun. The solar wind is blowing by the Sun and forms a bubble in the interstellar medium, the heliosphere. The wind becomes subsonic after crossing the heliospheric shock. After an intermediate region of subsonic flow through the heliosheath (by analogy to Earth regions) the solar wind reaches an interface, the so-called "heliopause," where the solar wind pressure and the interstellar pressure balance each other [6]. The nature of this boundary is far from being well known since its assumed position, around 100–200 AU from the Sun, has not yet been reached by spacecraft. Voyager 2 should cross the heliopause boundary around 2020 according to some theoretical models [7].

After four decades of extensive observations, the origin and acceleration of the solar wind are still not fully understood. During a total eclipse of the Sun (or using coronagraphs), the solar surface is masked by the Moon, showing the outer atmosphere of the Sun; the solar corona exhibits different visible structures with different spatial and temporal scales, as polar plumes rising from the polar regions of the Sun suggesting a global magnetic field, or polar coronal holes seen in soft X-rays as dark regions on images from the Yohkoh spacecraft. For example, such regions can be seen in Fig. 2. The solar atmosphere contains different layers. The photosphere, which is the visible "surface" of the Sun, is 500 km thick, and can be seen as a dark body with a temperature of approximately 5800 K. Then, the chromosphere from the height of

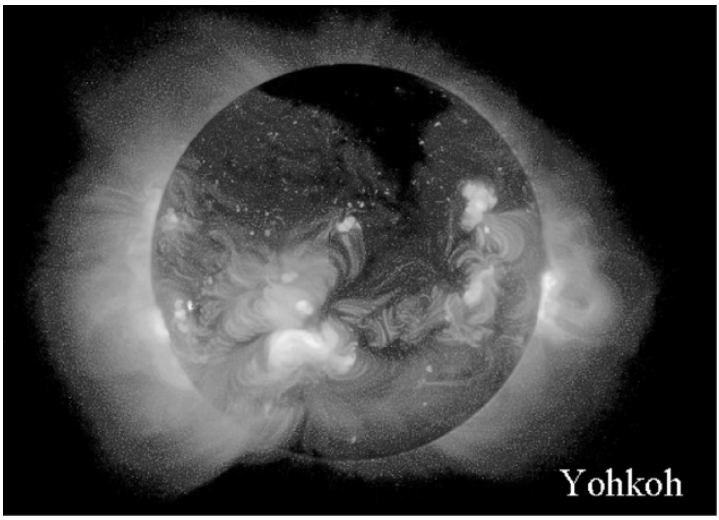

Fig. 2. X-ray emission of the corona from Yohkoh. Different structures are observed: for example, polar coronal hole (dark zone) and active regions (bright zone). (Courtesy of Yohkoh Images)

500 to 2000 km shows a rise of temperature from approximately 4200 K to approximately 10^5 K respectively. The corona and the chromosphere are separated by a layer hundreds of kilometer thick, the transition region, where the temperature dramatically rises to reach 1 or 2 million degrees. This unexpected behavior in contradiction with the second thermodynamic principle is still unexplained. Plot of temperature and density measurements obtained in the coronaand in the solar windis shown in Fig. 3. One can see quite a good agreement between the density measurements made by Soho in the corona and in the solar wind. We can also note that the electron temperature variation forms a plateau low in the corona and, higher up, decreases to match the solar wind data at 1 AU.

In 1942, the Swedish astronomer B. Edlen showed that some unknown corona spectral lines were indeed those of familiar atoms [9], such as iron, nickel, and calcium, but highly ionized. This requires the temperatures of the corona to be extremely high, around 1 or 2 million degrees. Even if the photosphere contained enough energy to heat the corona, we would not fully understand how this energy could be transported across the chromosphere and the transition region. The heating of the solar corona is still an important unsolved problem of solar physics.

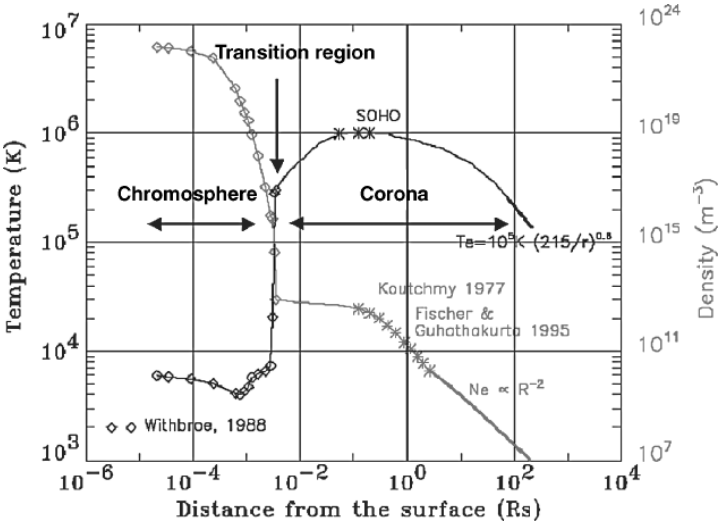

Fig. 3. Profiles of the electron density and temperature observed from remote-sensing measurements in the transition region, and the corona. From [8]

.

2 The Inner Heliosphere Over a Solar Cycle

The hot corona expands radially into interplanetary space and forms the solar wind. The solar magnetic field lines are dragged away by the wind because of its high conductivity and follow the motion of the wind ([10, 11]). The magnetic field is "frozen" in the plasma since the plasma pressure is much larger than the magnetic pressure (magnitude of $\mathbf{B}$ is around $5nT$ at the Earth's orbit). The field lines are anchored in the photosphere and form the Archimedian spiral due to the solar rotation [1].

2.1 Measuring the Key Parameters of the Solar Wind

To better understand the Sun, a major step would be to fly a probe as close as possible to our star. However, it is still not possible due to the very high price of such mission for only a few hours of data. Up to now, measuring the key parameters of the corona can be done with optical techniques from spacecraft in the neighborhood of the Earth since part of solar energy is lost by radiative processes. In addition, to characterize the features of the solar wind, in situ probes can give us some clues.

The Corona

The SKYLAB mission [12] gave the temperature up to nearly 1 MK, but these data were limited because of the poor spectral resolution and to the low intensities in coronal holes. The SOlar and Heliospheric Observatory (SOHO) was

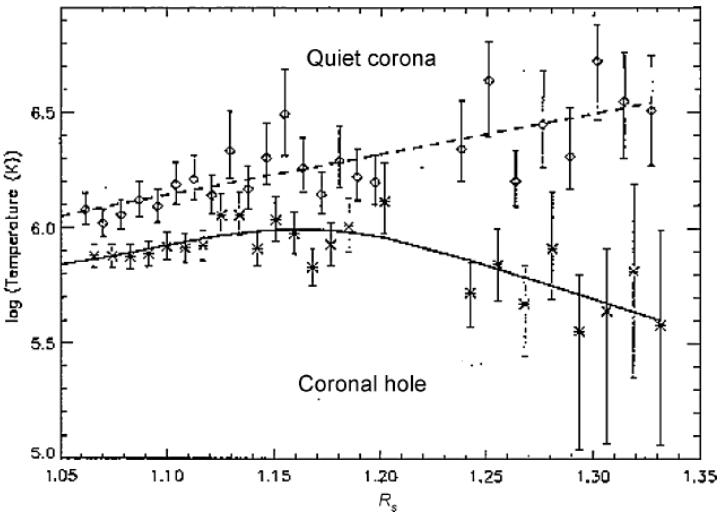

Fig. 4. Electron temperature profile in a polar coronal hole and quiet Sun region from SOHO. From [13]

able to determine a reliable electron temperature profile above a large polar coronal hole and in quiet coronal regions. Using the two SOHO spectrometers CDS (Coronal Diagnostics Spectrometer) and SUMER (Solar Ultraviolet Measurements of Emitted Radiation), electron temperatures have been measured as a function of height above the limb in a polar coronal hole [13] from the line ratio 1032 A/173 A in oxygen VI. Electron temperature profiles in a polar coronal hole and in quiet regions of the Sun are displayed in Fig. 4. Temperatures of around 0.8 MK are found close to the limb, rising to a maximum of less than 1 MK at 1.15 R_s, then falling to around 0.4 MK at 1.3 R_s. However, Ko et al. [14] deduced values of the order 1.5 MK at 1.5 R_s, which are significantly different from the SOHO results. Besides, observations from the Solar Wind Ion Composition Spectrometer (SWICS) instrument on Ulysses, during the south polar pass, have been used to derive the "freezing-in" temperatures in the solar wind. The charge–state ratio of O^{7+}/O^{6+} is a proxy for the coronal temperature [15, 16]. Summarized profiles of temperature are given in the review paper of [17].

Looking at the Sun with a line of sight perpendicular to the general magnetic field will give information on the solar speed on the basis of the Doppler dimming O VI 1032/1037 resonance lines, which affects the absorption profile of the ray, the intensity of the emission profile being related to the radial velocity of the plasma. Recently in 2000, Giordanno et al. enlightened the profile of the outflow speed of the oxygen ions [18], using the Ultraviolet Coronograph Spectrometer (UVCS) in the corona from 1.5 to 4 R_s, which reaches 300 km/s above 2.1 R_s. This is evidence for ion acceleration primarily near 1.6–2.1 R_s

for fast solar wind. The authors also showed that, beyond 1.8 R_s the velocity distribution of the oxygen is highly anisotropic, which may be evidence that the heating process is operating preferentially in the direction perpendicular to the magnetic field.

The Solar Wind

After the pioneer mission of Mariner 2 in the solar wind four decades ago [4], many other successful missions like Helios, Ulysses, Wind, ACE provided extensive measurements of in situ solar wind parameters, which are important to improve our understanding of this medium and to relate the interplanetary observations to the solar ones. Accurate measurements of the electron density and temperature are key elements to improve our knowledge on the energy transport in the solar wind. Electrostatic analyzers gave the first clear proof of the existence of the wind. Particle properties are deduced from measurements of electrons and ions velocity distribution functions with high time resolution, generally combining electrostatic analyzers and particle detectors. From these observations, moments are derived [19, 20]. During each spin period of the spacecraft, the full solid angle is covered and the two- and three-dimensional spectra are returned depending on the telemetry rate. However, these quantities are polluted at low energies by photoelectrons emitted by the spacecraft body due to solar UV light and spacecraft potential, which itself depends on the electron density and temperature of the plasma requiring difficult corrections [21]. Recently, a new calibration technique was been applied on Wind spacecraft. Using two different on board instruments [22] and taking advantage of their high resolution, corrected solar wind parameters are then obtained.

Although these effects can cause difficulties in the measurement of the electron plasma distributions,[1] electrostatic analyzers yield the basic knowledge of the solar wind properties. In situ observations of solar wind electrons show that their distribution contains three components: the core, the halo, and the strahl. Core electrons, i.e., electrons with a speed smaller than the thermal speed, are characterized by a bi-Maxwellian with an anisotropy at 1 AU of $T_{//}/T_{\perp} \sim 1$ to 1.5. Halo electrons form a suprathermal tail of the total electron distribution. At the orbit of the Earth, the density ratio of the halo electrons to those of the core is $N_{\mathrm{halo}}/N_{\mathrm{core}} \sim 0.05$ while their temperature ratio is $T_{\mathrm{halo}}/T_{\mathrm{core}} \sim 6$. The third population, which is not always present, is the strahl. It is a sharply field-aligned beam, where the electron energy is comparable or higher to that of the halo electrons [23].

Another technique makes use of a radio receiver and of a pair of wire antennas to deduce electron plasma parameters. It was initiated in early 1970s on the ISEE-3 mission [24]. The concept is equivalent to that of an antenna

[1] Ion measurements are far less sensitive to photoelectron and spacecraft potential effects due to the significantly higher ion kinetic energies compared to photoelectron and spacecraft energies.

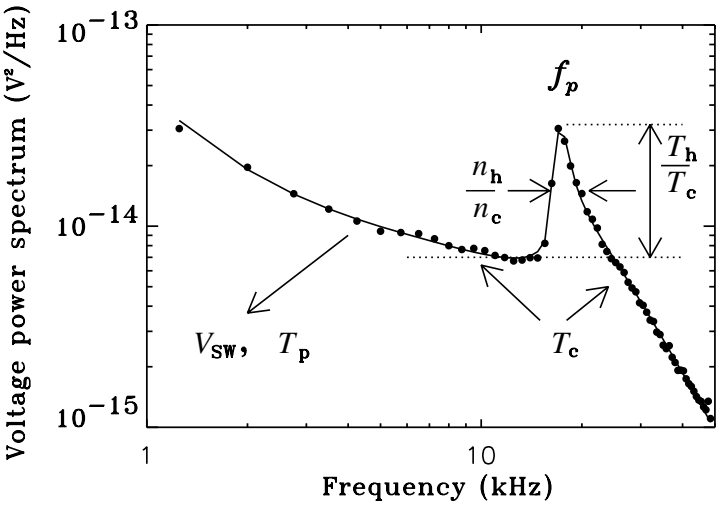

Fig. 5. Typical example of the thermal noise power spectrum measured in the solar wind. From [25]

in equilibrium with a black body. When immersed in a plasma, an antenna receives electrostatic waves that excite the plasma but do not propagate, in contrast to electromagnetic waves in the case of the black body. A local diagnostic is thus possible. This quasi-thermal noise is a function of the velocity distributions of the particles, and thus yields accurate values of the electron density (derived from the cutoff near the peak in a voltage power spectrum) and the thermal temperature from the shape of the spectrum. Figure 5 shows a typical example of the power spectrum measured in the solar wind on Ulysses, using the URAP radio receiver. The main feature of the spectrum is a peak located in the vicinity of the plasma frequency, which is the characteristic frequency of the plasma. From the cutoff position, it is possible to determine the electron density since $f_p \propto \sqrt{n_e}$. The shape of the spectrum yields the moments of the electron distributions, i.e., the halo and core electron density ratio and the halo and core electron temperature ratio. At low frequencies, the spectrum is due to the electrostatic fluctuations of the protons, which are Doppler-shifted by the solar wind speed. Issautier et al. extended the method, using this low-band frequency part to measure the solar wind speed and proton temperature [26].

The technique is routinely used on WIND, and Ulysses in the ecliptic plane at various heliocentric distances, as well as over a wide range of out-of-ecliptic latitudes [26]. The main advantage of the method is that it is nearly independent of the spacecraft potential and photoelectron perturbations[2] since the

[2] When particle analyzers are subjected to spacecraft charging effect, the electron parameters thus deduced could have an offset of more than 50% than the quasi-thermal noise determination.

volume sensed by the antenna is much larger than the spacecraft volume [27]. This method is complementary to particle analyzer technique and can be used to cross-check other plasma sensors. In a detailed comparison between these two methods, Issautier et al. [28] pointed out that particle analyzers provides reliable ion diagnostics in addition to suprathermal (halo) electron parameters and yields fundamental information on particle velocity distributions, whereas the improved quasi-thermal noise method accurately provides total electron density and core electron temperature.

2.2 Observations Near Solar Minimum

Over the 11-year sunspot cycle, the large-scale structure of the corona changes from a rather simple and well-ordered solar wind structure near the solar minimum (see, e.g., top of Fig. 6) to a complex and irregularly structured mixture of slow and intermediate speed flows near solar maximum (see, e.g., bottom of Fig. 6).

On the surface of the Sun, i.e. the photosphere, no sunspots are observed at solar minimum. The corona is essentially described by dipolar and quadrupolar components of the photospheric magnetic field, superimposed on the heliospheric current sheet (as schematically presented in the left panel of Fig. 7). It is generally aligned at lower latitudes, with no warps, and separates the two solar hemispheres of opposite polarity. The polar coronal holes from which the fast solar wind is supposed to originate are at their maximum size during solar minimum [17]. At the orbit of the Earth, there are mainly two types of wind: a fast wind flow of 800 km/s emanating from coronal holes, with a total electron density around 2 and 3 particles per cm^3, and 10% of helium particles compared to protons; in contrast, a typical slow wind flow, coming from the closed field lines near the Sun, has a speed around 400 km/s at 1 AU, a total electron density around 10 particles per cm^3 and a helium abundance which is reduced to 5% of that of the protons.

I will present two main results of the Ulysses observations which are directly linked to the theoretical part of this course. The reader will find a detailed report of the entire Ulysses heliospheric results at solar minimum published in a special book [31].

The Ulysses mission is devoted to explore the out-of-ecliptic region over the Sun (from 1.3 to 4.3 AU), over a wide range of latitudes (between 80^o S and 80^o N). Launched in October 1990, Ulysses reached the south polar pass in September 1994 and measures the solar wind from pole to pole over 10 months during the period close to the 1996 solar activity minimum. For the first time, the large-scale structure of the corona was studied. Ulysses confirmed that at high latitudes, the solar wind is a steady and stationary high-speed flow, with a mean value of 750 km/s [32], the electron density and core temperature appear to vary smoothly with very little fluctuations [33]. In contrast, in an equatorial band spanning roughly $\pm 20^o$ of latitude with respect to the solar equator, all parameters show large variations since Ulysses crosses seven

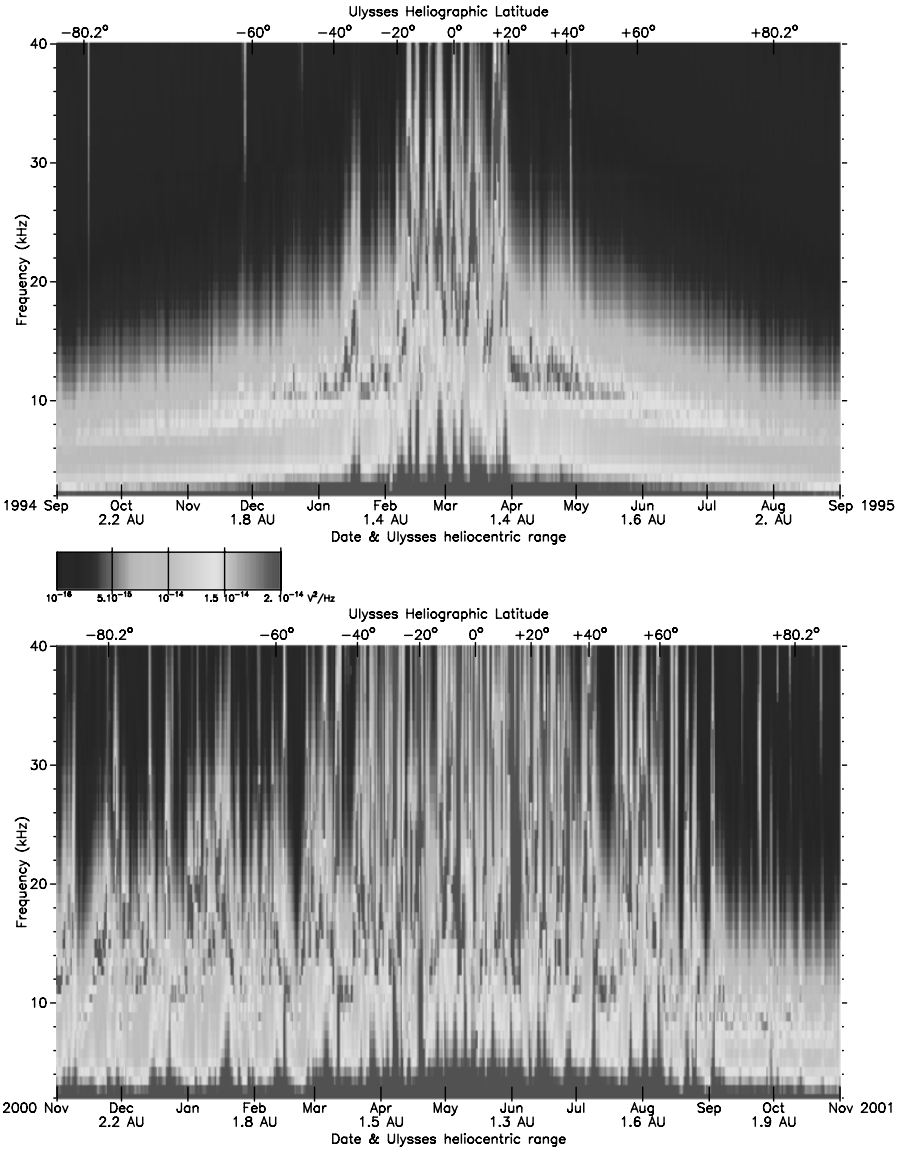

Fig. 6. Pole-to-pole radio spectrograms obtained during Ulysses fast latitude scans, near the 1996 solar minimum (*top*) and 2001 solar maximum (*bottom*). From [29]

times the warped and tilted heliospheric current sheet (HCS), as seen in the top panel of Fig. 6. The histograms of the plasma parameters, normalized to 1 AU, suggest several types of flows including (1) medium to high speed wind, which comes from equatorward extensions of the polar coronal holes; (2) HCS wind; and (3) compression zones due to fast–slow stream interactions [34].

The most interesting period is when Ulysses is embedded in the fast solar wind for several months at high latitudes (poleward 40°). Using the URAP radio receiver, it is possible to accurately derive the electron density and core temperature against the latitude and the radial distance. On average, the histogram of the density normalized to 1 AU from the Ulysses observations corresponds to one kind of wind, with an average density around 2.6 particles/cm^3, while the histogram of the core temperature, normalized to 1 AU, peaks at about 7.3×10^4 K. Both distributions are gaussian shaped, corresponding to a single wind flow. Because of the orbit of Ulysses, this gives a unique opportunity to derive the radial profile of the electron parameters of the steady-state fast solar wind without any arbitrary data selection to avoid bias. From the data sampled, Issautier et al. [26] found that the density varies as $r^{-2\pm0.01}$ with a good accuracy in the southern hemisphere. From the mass conservation and if one assumes a constant wind speed, which is the case for these high-latitude observations, the fast wind blows with a symmetric expansion. In addition, the core temperature varies as $r^{-0.64\pm0.03}$. The profile is thus roughly midway between adiabatic ($T \propto r^{-4/3}$) and isothermal ($T \propto cste$).

2.3 Observations Near Solar Maximum

In contrast to solar minimum, the large-scale structure of the corona is dramatically more complex during the rising solar cycle to solar maximum, as schematically seen in the right panel of Fig. 7. The heliospheric current sheet is tilted and warped, no longer centered near the equatorial plane [35] and, the HCS crossings extend to high latitudes of about 70°. With increasing solar activity, numerous coronal mass ejections occur while active regions are seen on the solar surface.

During the pole-to-pole journey of Ulysses between November 2000 to November 2001, different regimes of winds such as slow and intermediate winds from streamers are seen at all latitudes, in addition to sporadic fast wind flows from small coronal holes [36]. With the change of solar cycle, large polar coronal holes are replaced by small equatorward coronal holes [37]. Ulysses observes a unique long interval of fast wind around 750 km/s $\pm$ 50 km/s at high latitudes, above 72° N, nearly at the end of its second pass over the pole, as seen on the bottom panel of Fig. 6. From in situ quasi-thermal noise observations, the basic trend of the electron density variations with the heliocentric distance is analyzed [29]. Fitting the data set with a power law gives an index of -2.0 ± 0.1. In the same way, we can assume that the core temperature is only a function of the radial distance, and thus we can also fit it with a power law. In this high-speed flow the profile varies as $r^{-0.7\pm0.1}$

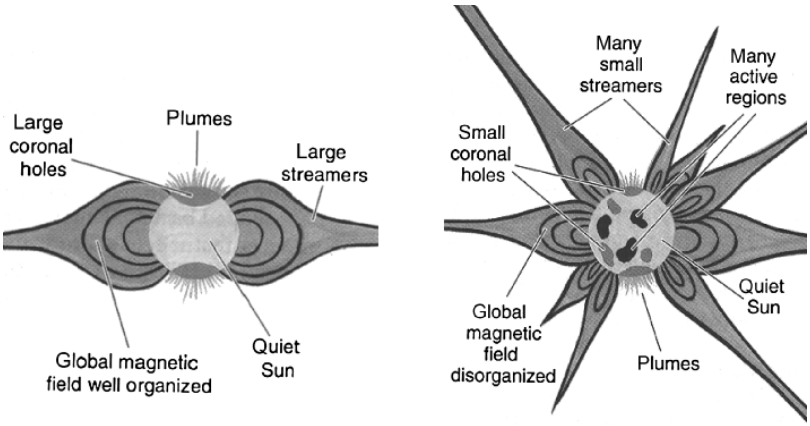

Fig. 7. A schematic view of the corona at solar minimum (*left panel*) and at solar maximum (*right panel*), adapted from [36]

between 1.76 and 2.25 AU, which is in good agreement with the index value found in the fast wind coming from the southern hemisphere around the 1996 solar minimum [38]. Radial profiles of electron parameters are displayed in Fig. 8. Moreover, the statistical properties of the high-speed wind from polar coronal holes reveal a single and stationary wind, with the same properties over the solar cycle 23 explored during the Ulysses mission [38].

What about the north–south asymmetry observed during the solar cycle 23? During solar maximum, the histograms of density obtained in both hemispheres lead to a slight asymmetry of 15%. On the other hand, there is no

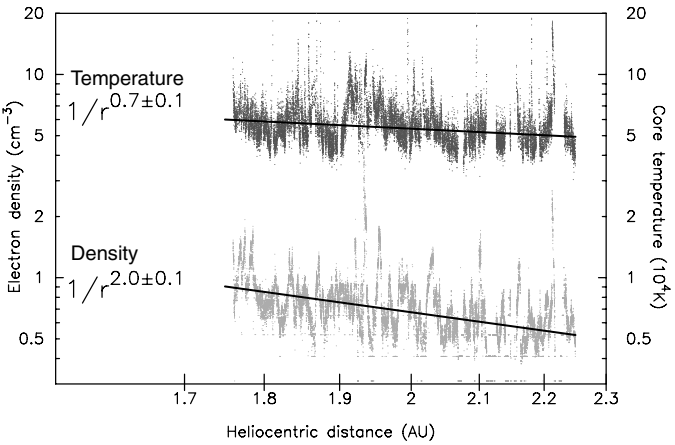

Fig. 8. Radial profiles of the electron density and thermal temperature derived from the URAP/Ulysses observations in the solar wind, near the 2001 solar maximum period, in the northern hemisphere. From [38]

significant asymmetry of the histograms of temperature [29]. At solar minimum the observed asymmetry of 10% in the electron density, temperature and magnetic field may be due to a genuine asymmetry of polar coronal holes [26] and/or to temporal variations; from the data acquired during the 2001 solar maximum the phenomena are much more difficult to understand. Nevertheless, the present asymmetry may also be due to a temporal variation since the solar activity slowly increases to solar maximum during the 10-month fast latitude scan. Over a solar cycle one can expect different number and/or sizes of coronal holes, as well as an enhancement of the number of CMEs, which may be different from one hemisphere to the other. Compared to the 2001 solar maximum, the solar wind is on average 15% less dense and 20% cooler than during the 1991 solar maximum, when Ulysses was in the ecliptic solar wind [29]. This may be due to some latitude effects and/or to genuine coronal effects, since the solar activity measured by the sunspots number is smaller in 2001 than in 1991.

Let us examine the core temperature T_c histogram (in white) from 80° S to 72° N, which is displayed in Fig. 9. We have also superposed in this figure the T_c distribution (in grey) of 27,000 measurements acquired in the polar coronal hole, discussed above. The shape of the white histogram clearly shows two distinct peaks. The first one corresponding to a cold population could be identified to the dilute density population, probably emanating from small coronal holes at various latitudes at solar maximum. Indeed, the grey histogram from the northern polar coronal hole fits fairly well the colder part of the white histogram that is found to be associated with the lowest densities [29]. The

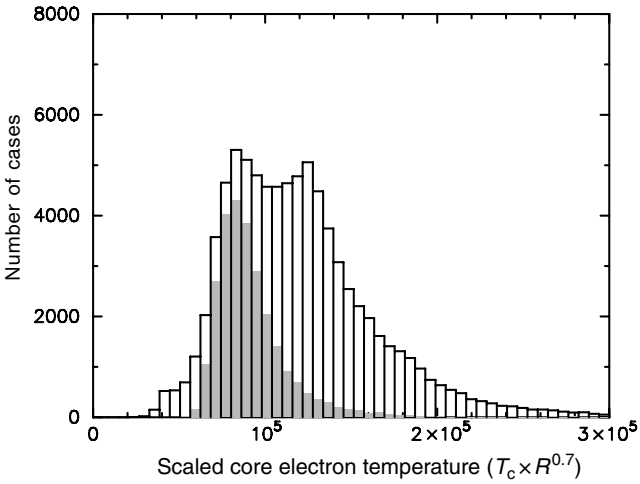

Fig. 9. Scaled core temperature distributions obtained at solar maximum during Ulysses' fast latitude scan from 80° S to 72° N (white histogram), and in the polar coronal hole beyond 72° N (grey histogram). Bin size is of 6,000 K. From [29]

second peak corresponding to hotter populations of the white histogram may be associated with interaction regions of fast and slow winds and/or to the vicinity of the HCS. With regard to purely high-speed wind observations, we conclude that the polar coronal holes have similar features at solar maximum and minimum. However, since Ulysses was probably not completely immersed in the polar coronal hole because of its limited size during solar maximum, the fast wind beyond 72° N is on average 5% denser and 20% hotter than during solar minimum [38]. Because of the small size of its source regions, this cool and dilute wind probably undergoes some interaction as it comes out from the Sun, in contrast to the wind coming from large polar coronal holes, which may flow out from the Sun with negligible interactions. Finally, it is important to note that composition measurements based on the study of the O^7/O^6 ratio [39] showed that the fast solar wind originates from cooler regions in the solar corona, which is consistent with our findings.

Balogh et al. [31] reviewed the radial component of the magnetic field normalized to 1 AU and averaged over solar rotations during the two fast latitude scans in 1994–95 and in 2000–01 of the Ulysses mission. In Fig. 10, one can see at solar minimum that the field is independent of the latitude and shows the same mean value (in magnitude) in both hemispheres, around 3.3 nT. In addition, the magnetic field is inward (negative) in the southern hemisphere and outward (positive) in the northern hemisphere. In contrast, near solar maximum, because of the highly tilted current sheet, both sectors of polarity are present at nearly all latitudes (see bottom panel of Fig. 10). The mean values are the same in the northern and southern hemispheres, and indeed in agreement with the mean value measured at the solar minimum in spite of the dramatic reconfiguration that takes place in the solar magnetic field.

Ulysses allows also to measure the relative abundance of ions in the solar wind. This enables to determine the profile of the electron temperature in the corona. From instruments flown in the solar wind, the electron temperature is obtained with the concept of "freezing-in temperature," measuring the charge state distribution of heavy ions (i.e., the relative abundance of ions with different charge states) as seen in Sect. 2.1.1. A model is used to convert the observed charge states at 1 AU into the equivalent coronal temperature. In the paper [16], the authors deduce the coronal temperature from oxygen charge states over the pole-to-pole passage at both solar minimum and maximum. They also show a close inverse correlation between the coronal temperature and the solar wind speed. For a low speed flow, the temperature is high up to 2×10^6 K whereas it is low around 10^6 K for a high-speed flow, independently of the solar cycle. This may reveal a fundamental relation between the property of the corona and the solar wind speed.

We finally conclude on the heliopause boundary, i.e., the terminal influence of the solar wind on the interstellar medium. For that, one uses the ion dynamic pressure of the solar wind $n_p \times m_p \times V^2 + 4m_p \times n_p \times V_\alpha^2$ from in situ measurements [40]. At the distance of the heliopause, R_{H}, which has

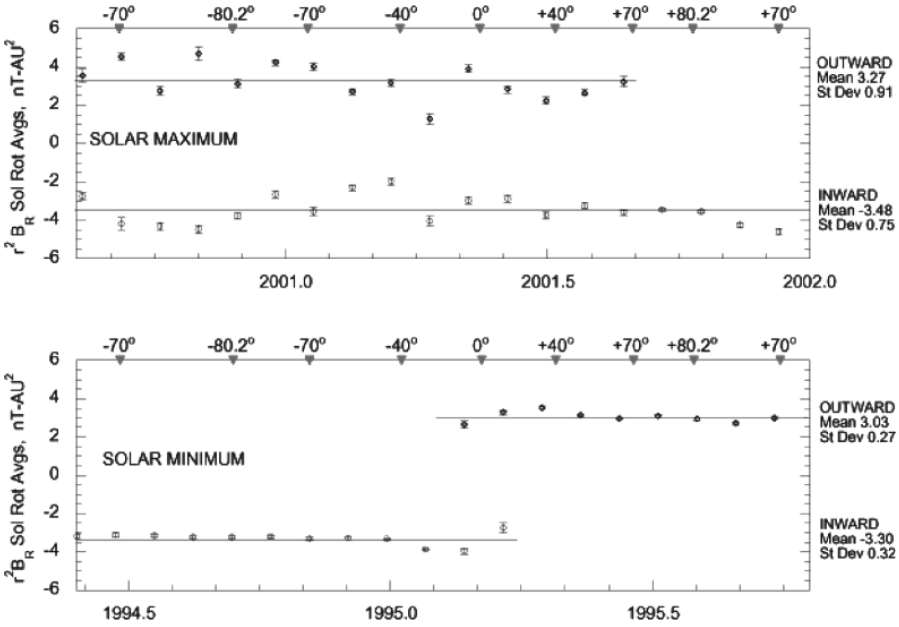

Fig. 10. Normalized radial magnetic field during Ulysses fast scans, at solar minimum and maximum. The data are averaged over solar rotations. From [31]

to be evaluated, there is a balance between the pressure of the interstellar medium $P_{\rm ISM}$ and the solar wind pressure $P_{\rm 1AU}$, scaled to 1 AU. Then $R_{\rm H} = (P_{\rm 1AU}/P_{\rm ISM})^{1/2}$. With $P_{\rm ISM} = 10^{-13}$ Pa, one can find the typical distance of the heliopause at $R_{\rm H} \simeq 140$ AU. Figure 11 displays the dynamic pressure against the latitude near solar minimum (solid line) and near solar maximum (dash-dotted line). One can see that in both cases, the pressure and thus the shape of the heliosphere are rather symmetric with a peanut-like shape. Both at minimum and at maximum in the fast solar wind the dynamic pressure is around 2.6 nPa whereas the value reaches 2.2 nPa in the slow solar wind. The dynamic pressure variation averaged over solar rotations is only 20% over the solar cycle, and is mainly due to the variation of the proportion of the two different kinds of winds. Note that the dynamic pressure does change with time and that the boundaries of the heliosphere may move in and out over tens of AU [42] as the Earth's bow shock does over a few Earth radii.

2.4 The Solar Wind on Small Scales

The problem of the energy dissipation in the solar wind is one of the major unsolved problems, which takes place more generally in all astrophysical turbulent collisionless plasmas. For such media, collisions are of small importance to thermalize the plasma and another efficient process should exist to transfer the energy contained in the large-scale motions to small-scale motions,

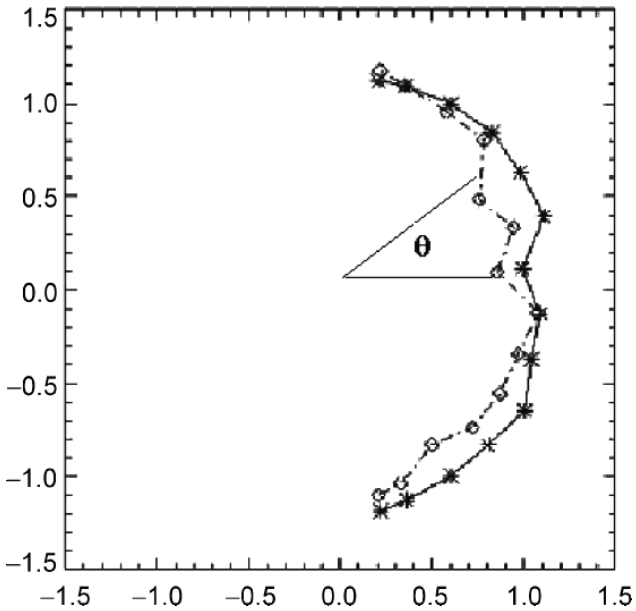

Fig. 11. Proton dynamic pressure, normalized to 1 AU, versus latitude near solar minimum (*solid line*) and near solar maximum (*dash-dotted line*). The data from SWOOPS instrument are averaged over a 27-day solar rotation, and the angle θ represents the latitude. From [41]

i.e., the so-called dissipative scales. Therefore, a nonlinear cascade of energy could take place from large to small scales. However, two questions remain. What is the nature of the turbulent cascade of the energy for collisionless plasmas ? What is the nature of the dissipative phenomena that replace the resistive or viscous dissipation as in classical fluids?

The solar wind is a supersonic and superalfvenic collisionless plasma. Its mean-free path is of the order of 1 AU. It is also turbulent since the different parameters (speed, magnetic field,...) have important fluctuations at different spatial and temporal scales. Likewise, the fluctuations of the magnetic field and the speed are $\delta B/B \approx \delta V/V \leq 0.5$. To understand the dissipation, one should explore simultaneously all these scales. In 2000, Salem et al. made the first global spectrum of the magnetic and electric fluctuations in the solar wind using different observations on board the WIND spacecraft [43]. The high temporal resolution of the WAVES instrument allows to explore for the first time the high frequency part of the spectrum. Figure 12 displays the global spectral density, for frequencies corresponding to the 27-day solar rotation period and to the electronic oscillations of the plasma. We can distinguish the MHD scales ranging from the low frequency part to the gyrofrequency of the ions f_{ci}, and beyond the kinetic scales. In the MHD regime, the fluctuations are changing with the expansion of the solar wind and its

speed structure (slow–fast speed flows). The fluctuations produced near the Sun propagate into the interplanetary medium while the characteristic time of the solar wind expansion is smaller than the interaction time of nonlinear fluctuations. At 1 AU it corresponds to frequencies smaller than 10^{-4} Hz. Moreover, the fluctuations interact with a nonlinear regime and produce a cascade of energy from large to small scales through the so-called *inertial domain*. Spectra have a power-law variation with a spectral index close to $-5/3$ predicted by Kolmogorov for the fluid turbulence. Near f_{ci} kinetic effects become important, and there is a link between the fluctuations and the particle motions. These wave–particle interactions are local phenomena. We often speak of *microturbulence*. Dissipation takes place through this microturbulence produced locally. One can see in Fig. 12 that the slope changes near f_b, which is the frequency f_{ci} Doppler-shifted with the $Alfvèn$ speed V_a, i.e. $f_b \sim f_{ci}(V/V_a)$ where V is the solar wind speed. Beyond f_b the magnetic energy does not dramatically decrease like in fluid turbulence where the viscous dissipation dominates, but one can see a cascade of energy decreasing as f^{-3}, which is faster than in the inertial domain. In addition, between f_b and f_{ce}, whisler waves are observed and may contribute to the regulation of the transport of the energy and heat in the solar wind, diffusing electrons, which could thus contribute to thermalize the electron distribution functions [43].

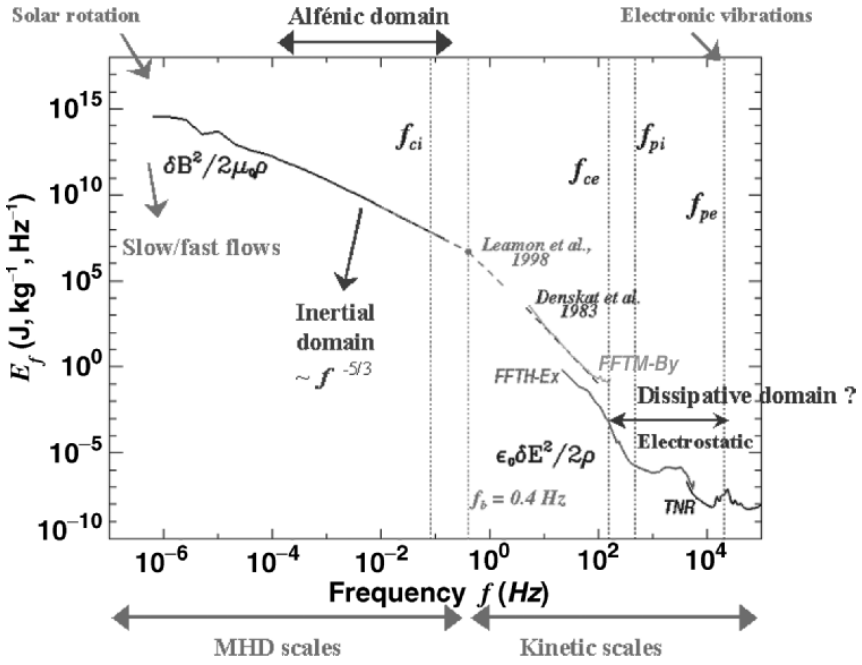

Fig. 12. Spectral density of magnetic energy versus the frequency, measured in the frame of the spacecraft WIND. From [43]

At f_{ce} the magnetic energy is dissipated by electron cyclotron damping. Beyond this frequency, the fluctuations become purely electrostatic and form a bump in the spectrum: it is the regime of ionic acoustic waves. Thanks to the high resolution of the Wind instruments, this part of the spectrum was analyzed for the first time by [44] and [45]. These authors pointed out that these waves are coherent waves, formed by wave packets and solitary structures. The ionic acoustic waves in the solar wind are coherent waves, which have recently been identified; their spatial repartition was studied by Salem et al. [46], thanks to the high temporal resolution of Wind and the wave form instrument. Although these waves are intermittent, they are nearly permanent phenomena in the solar wind. Moreover, double-layer structures have also been measured for the first time in the solar wind. Examples are displayed in Fig. 13. They were previously studied in the Earth auroral zone and in the magnetosphere of the Earth. These structures are stationary local charge separations, which take place over a few Debye lengths. They are associated to a potential jump of some millivolts. From the occurrence rate of these structures, Salem et al. [46] deduced that the associated potential from the corona to the Earth orbit is in the range 300–1000 V, a result compatible with the value necessary to ensure the global neutrality of the plasma. These structures could be another mechanism to possibly accelerate the particles along the magnetic field.

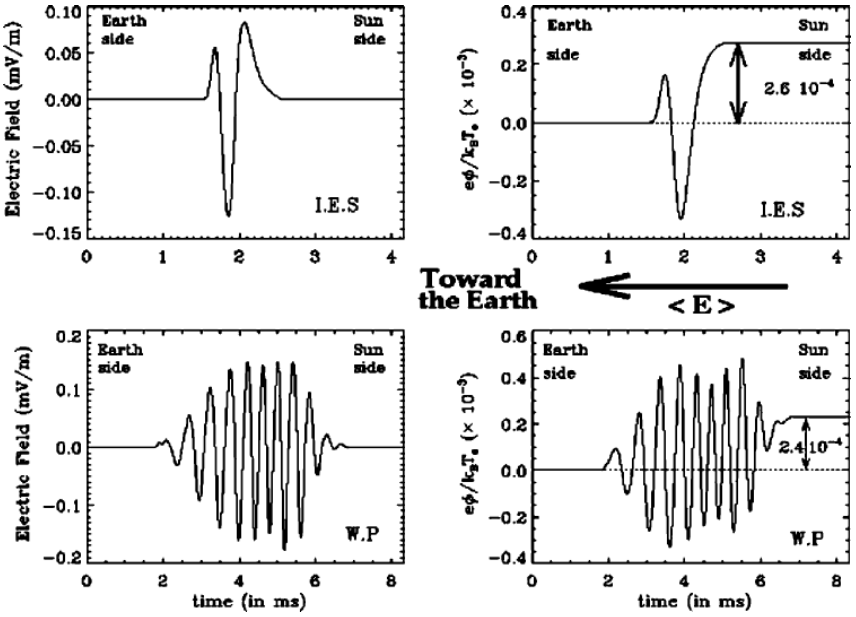

Fig. 13. Example of double layers and wave packet structures measured in the solar wind by WIND. From [45]

3 Theoretical Models

The heating of the corona and the acceleration of the solar wind are closely linked, and one should not model these two phenomena separately. There are two extreme approaches to solve the enigma of the heating and acceleration of the plasma. Since the mean-free path in the solar wind is of the order of the characteristic scale height (the density scale, for example), a fluid approach assumes that the plasma is in a thermodynamic equilibrium, i.e., the velocity distribution function is Maxwellian, thus the plasma is strongly collisional. It is then easy to deduce the macroscopic parameters of the solar wind, such as the density and the speed, assuming an ad hoc temperature profile. However, the solar wind, as most of the astrophysics plasmas, are not in thermodynamic equilibrium, which means that the velocity distribution functions are not Maxwellian [47]. The kinetic approach uses the Vlasov equation, thus implying no collisions, with any distribution function. In this latter case, one should represent self-consistently the properties of the different types of electron populations in the solar wind. Of course, the physics, of the solar wind is in between these two simplified approaches, and one should model the plasma, using a kinetic model with few collisions. The transport of the energy in a semicollisional plasma is the general and open question.

3.1 Fluid Approach: Basics of Parker's Model

There are several comprehensive text books on the fluid approach of Parker for the solar wind (see, e.g., [48, 49]). Here I will just give a short introduction. First, let us consider a stationary and neutral corona, made of electrons and protons, submitted to gravity and pressure, in a hydrostatic equilibrium. The balances of the forces are thus

$$\frac{\mathrm{d}P(r)}{\mathrm{d}r} = -\rho\frac{GM_*}{r^2} \tag{1}$$

where G is the gravitational constant, M_* the mass of the Sun, P the pressure, and ρ the mass density by unit volume, defined by $\rho = (m_p + m_e) \times n(r) \simeq m_p n(r)$, $n(r)$ being the number of particles per unit volume. If we assume for simplicity that the temperatures of the electrons and of the protons in the corona are equal to $T(r)$, the total pressure P of the plasma is the sum of the electron and proton pressures and can be written as

$$P(r) = 2n(r)k_\mathrm{B}T(r) \tag{2}$$

where k_B is the Boltzmann constant. Then, (1) becomes

$$\frac{dP(r)}{P(r)} = -\frac{GM_*m_p}{2k_\mathrm{B}T(r)}\frac{dr}{r^3} \tag{3}$$

which can be easily integrated as

$$P(r) = P_0 \exp\left[-\frac{GM_* m_p}{2k_\mathrm{B}} \int_{r_0}^{r} \frac{dx}{T(x)x^2}\right] \tag{4}$$

where P_0 is the pressure at the base of the corona. From this formula, a hydrostatic equilibrium of the atmosphere should imply that the pressure in the solar wind at large distances balances the pressure in the interstellar medium that is of the order of 10^{-13} Pa. This implies that the temperature has to vary as fast as $1/r$ to enable the solar wind pressure to drop to zero.

If we simply assume that the transfer of energy is purely due to thermal conduction, and that there is no heat flux sources, then

$$\nabla.(-\kappa \nabla T) = 0 \tag{5}$$

$$\kappa = 7.7 \times 10^7 T(r)^{5/2} \tag{6}$$

where κ is the thermal conductivity. Thus, this yields

$$T(r) = T_0 \left(\frac{r_0}{r}\right)^{2/7} \tag{7}$$

T_0 is the temperature of the corona.

Finally, we can obtain the variation of the solar wind pressure with the distance by

$$P(r) = P_0 \exp\left[-\frac{7}{5}\frac{GM_* m_p}{k_\mathrm{B} T_0 r_0}\left(1 - \left(\frac{r_0}{r}\right)^{5/7}\right)\right] \tag{8}$$

At infinity, with typical coronal parameters, i.e., $T_0 = 2.10^6$K, $n_0 = 10^6 \mathrm{cm}^{-3}$, $r_0 = 1.5\, R_\mathrm{s}$, the pressure has a finite value and is 10^5 larger than the pressure in the interstellar medium. Indeed, a hot static corona cannot be confined and the corona should expand [1]. Therefore the motion of the plasma has to be taken into account.

Following Parker's model, we write the conservation of both the mass and the momentum for spherical geometry.

$$\rho V r^2 = \text{const.} \tag{9}$$

$$m_p \left[\frac{dV(r)}{dt} + V(r)\frac{dV(r)}{dr}\right] = -\frac{GM_* m_p}{r^2} - \frac{1}{n(r)}\frac{dP(r)}{dr} \tag{10}$$

In the case of a stationary corona expanding at a speed V, neglecting the magnetic field, the viscosity and the solar rotation, (10) can be written as

$$\rho V(r)\frac{dV(r)}{dr} = -\rho\frac{GM_*}{r^2} - \frac{dP(r)}{dr} \tag{11}$$

In this case, we also assume a plasma composed of electrons and protons, with the same temperature $T(r)$. Then, replacing the pressure in (11) by (2) and substituting ρ by $m_p n(r)$, we obtain

$$\frac{1}{V(r)}\frac{dV(r)}{dr}\left[V(r)^2 - \frac{2k_{\rm B}T(r)}{m_p}\right] = -\frac{GM_*}{r^2} + \frac{4k_{\rm B}T(r)}{m_p r} - \frac{2k_{\rm B}}{m_p}\frac{dT(r)}{dr} \quad (12)$$

For simplicity, we choose an isothermal behavior of the temperature, i.e., $T(r)$ =const., so that the term $dT(r)/dr$ can be removed from (12). From this expression it is easy to show that a critical speed V_c and a critical distance r_c, as defined below, are solutions of (12).

$$V_c = \sqrt{\frac{2k_{\rm B}T}{m_p}} \quad (13)$$

$$r_c = \frac{GM_* m_p}{4k_{\rm B}T} \quad (14)$$

Figure 14 displays the set of solutions of the radial solar wind speed profile for a temperature decreasing slower than $1/r$. The heavy black line is the unique transonic solution where the speed is subsonic before r_c and supersonic beyond. This solution gives a pressure close to zero at infinity and an average speed of 350 km/s at 1 AU, as observed in the slow solar wind. This figure also shows that the acceleration of the solar wind occurs within a few solar radii. Recently, Patsourakos and vial [51] deduced the solar wind speed outflow of 67 km/s near one solar radius in the fast solar wind from the SOHO/SUMER experiment, using a combination of Doppler shift and Doppler dimming measurements.

The Parker fluid model cannot explain the fast wind flow of 800 km/s without ad hoc sources of energy. Because of the intrinsic nature of describing the solar wind with one fluid, the character of the suprathermal electrons is

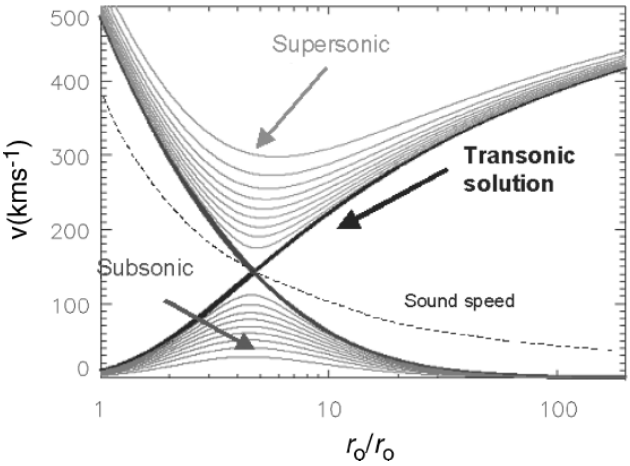

Fig. 14. Profile of the radial flow speed showing solutions from Parker's model. The dashed line is the sound speed. From [50]

not taken into account. However, bifluids or multifluids models have generalized the Parker's model (see, e.g., [52–55]). These kinds of models are not fully satisfactory since the macroscopic parameters do not fit well with the observations.

3.2 Exospheric Approach

Another class of model, based on the kinetic description of the plasma to explain the solar wind acceleration, was first developed by Chamberlain [57]. By analogy with the evaporation of neutral particles from a planetary exosphere [58], Chamberlain suggested that the radial expansion of the corona is the result of the thermal evaporation of the hot protons from the corona. His model, so-called "solar breeze", was not able, however, to produce a supersonic wind, and gave key parameters at 1 AU in disagreement with in situ observations and with Parker's model results. Kinetic models were thus suspected not to be applicable to solar wind physics. However, Lemaire and Schare [59] and Jockers [60] have independently shown that the kinetic approach yields relevant parameters as fluid models using the self-consistent electric field. This potential is higher than the Pannekoek–Rosseland potential, which is inappropriate in the case of the expanding solar corona. Indeed, to maintain the quasi-neutrality of the plasma for an expanding atmosphere using the Pannekoek–Rosseland potential, the electric flux of the electrons escaping the corona (which is proportional to the thermal speed of the electrons) is 43 times larger than the proton flux. Hence to equilibrate the fluxes and to have no net current, an electric potential of the order of 700 V has to be maintained in order to attract more electrons. The electric field associated to the latter potential will then "push" the protons and accelerate the wind to its supersonic regime [61].

The solar atmosphere can be described using the Boltzmann equation without collision (namely the Vlasov equation). Solutions are any constant of the motion. Hence, since the total energy for each species of particles is conserved, the total energy is a solution of the Vlasov equation. The energy that is conserved is the sum of the kinetic, gravitational, and electric potential energies:

$$E_{\text{total}} = \frac{1}{2}mv^2 - m\frac{GM_s}{r} + Ze\phi_{\text{E}}(r) = \text{const.} \tag{15}$$

where $\phi_{\text{E}}(r)$ is the electric potential, and Ze the charge of the particles.

Moreover, the magnetic momentum μ is conserved, since we considered gyration radius much smaller than the curvature of the magnetic field line. Hence, we have

$$\mu = \frac{mv_\perp^2}{2B(r)} = \text{const.} \tag{16}$$

where $v_\perp$ is the component of the speed perpendicular to the magnetic field lines.

Beyond the exobase radius r_0, the distance where the mean-free path is equal to the density scale height, the solar wind is assumed collisionless and described by the Vlasov equation. Taking an arbitrary velocity distribution function at the exobase, it is thus possible to know the evolution of this velocity distribution function at an altitude $r > r_0$ via the Liouville's theorem and thus deduce the moments of the distribution. Indeed, Liouville's theorem claims that the velocity distribution function is constant on the particle trajectory, and therefore the velocity distribution function f_0 at the exobase r_0 allows to derive the velocity distribution function f at any altitude $r > r_0$ for a given particle species.

$$f(r, v^2, v_\perp^2) = f_0(r_0, v_0^2, v_{0\perp}^2) \tag{17}$$

To begin, one can make two main assumptions in exospheric models: a radial magnetic field, i.e., $B(r) = B(r_0)r^2/r_0^2$ and a monotonous potential [61]. In the velocity space, different kinds of particle trajectories exist which are obtained from the resolution of (15) and (16). Hence, for electrons, there are two kinds of particles: those with enough energy to overcome the potential barrier (electrostatic and gravitational), namely the escaping electrons, and those without enough energy to escape from the exobase. The so-called ballistic and trapped particles are the nonescaping electrons. Indeed, the escaping speed for the electrons is obtained from (15). At the exobase, it is given by

$$v_{0e} \simeq \left(\frac{2e\phi_{\mathrm{E}}(r_0)}{m_e}\right)^{1/2} \tag{18}$$

since the gravitational energy is negligible for the electrons.

In contrast, protons have a different behavior; they all escape from the exobase, in the case of a monotonic potential. At the exobase, the escaping speed of the protons is given by

$$v_{0p} \simeq \left(\frac{2e}{m_p}\right)^{1/2} \left(\frac{GM_s m_p}{er_0} - \phi_{\mathrm{E}}(r_0)\right)^{1/2} \tag{19}$$

To calculate self-consistently the electric potential, one first imposes the equality of the proton flux and electron flux (flux from the escaping electrons) at the exobase. It yields the potential at r_0. Then, one can calculate the potential at the distance r from the equation of neutrality. The moments of the velocity distribution function are deduced. They depend on ϕ_{E} at any distance via Liouville's theorem. The second moment of the electron velocity distribution function gives the electron temperature. Analytical calculations at large distances lead to the temperature profile. For the first time, it is possible to predict the behavior of the temperature variation and to compare it with in situ observations [25]. The electron temperature is thus given by [62]

$$T_e/T_{0e} \simeq 1 + \left(\frac{m_p}{m_e}\right)^{5/6} \left(\frac{r_0}{r}\right)^{4/3} \tag{20}$$

The electron temperature is almost independent from the velocity distribution function chosen at the exobase. It is noteworthy that the two terms have the same order of magnitude at 1 AU and that explains that the temperature profile is flattened at large distances, as observed.

Moreover, the solar wind speed at large distances can also be calculated. In contrast to the temperature profile, the wind speed is dependent on the velocity distribution at the exobase. In a Maxwellian case, Meyer-Vernet and Issautier [62] confirmed analytically the wind speed of 350 km/s at 1 AU, for typical parameters of the corona at r_0. For a distribution with a suprathermal tail, like the Lorentzian distribution function,[3] the expression of the solar wind speed is

$$V_{\rm SW} \simeq v_{\rm the} \left(\frac{m_e}{m_p}\right)^{1/2} \left[\left[\frac{v_{\rm the}\sqrt{\pi} A_\kappa \kappa^{\kappa-1/2}}{v_{\rm thp} 4(\kappa-1)}\right]^{1/(\kappa-1)} - \frac{2 m_p G M_s}{r_0 m_e v_{\rm the}^2}\right]^{1/2} \tag{22}$$

where the dominant term is the first one, with the power index of $1/(\kappa-1)$. Therefore, the solar wind speed can be simplified to

$$V_{\rm SW} \propto v_{\rm the} \left(\frac{m_e}{m_p}\right)^{1/2} \left[\frac{v_{\rm the}}{v_{\rm thp}}\right]^{1/(\kappa-1)} \tag{23}$$

From this simplified expression, one can see that the solar wind speed at large distances increases when κ decreases, i.e., when the contribution of suprathermal particles increases. For typical corona conditions, an exobase of $r_0 \sim 4R_{\rm s}$ and $\kappa \sim 3$, the solar wind speed reaches 700 km/s. One can note that the solar wind speed depends directly on the velocity distribution at the exobase and on its proportion of suprathermal particles [62, 63]. When κ decreases, i.e., energetic particles become more important, the electron flux escaping from the Sun becomes larger, and the electric potential has to increase to balance the charge separation, which thus gives a larger solar wind speed.

It is important to note that we can take into account a spiral magnetic field, which is more realistic than the radial magnetic field. The temperature profile is then slightly changed [64].

In addition, to treat the birth of the fast solar wind coming from coronal holes, the exobase has to be taken below $4R_{\rm s}$. In this case, the total potential for the protons has to be generalized to a nonmonotonic potential. This

[3] Generalized Lorentzian distribution is defined by

$$f(v) = \frac{n_0}{2\pi} \frac{A_\kappa}{(\kappa v_{\rm th}^2)^{3/2}} \left[1 + \frac{v^2}{\kappa v_{\rm th}^2}\right]^{-(\kappa-1)} \tag{21}$$

where $v_{\rm th}$ is the thermal speed, and $A_\kappa = \Gamma(\kappa+1)/\Gamma(\kappa-1/2)\Gamma(3/2)$. When κ is small, the distribution tends to a power-law distribution, whereas when κ tends to infinity, the distribution becomes a Maxwellian.

potential is attractive from the exobase to a critical distance, $r_{\max}$, and then beyond that distance the potential becomes repulsive. Different kinds of protons are thus present, escaping and nonescaping protons that complicate the resolution of the model [65, 66].

Finally, we can discuss the existence of a kappa distribution in the corona. Up to now, we know that most of astrophysical plasmas are not in thermodynamic equilibrium and thus particle velocity distributions are not Maxwellian, but contain suprathermal tails. Generalized Lorentzian distributions, namely "Kappa" distributions, are useful tools to describe plasmas that are not in equilibrium and contain an excess of energetic particles. To justify the existence of "Kappa" distribution function, Treumann [30] and Leubnar [68] attempted to create an associate thermodynamic theory where "Kappa" distributions will be the equilibrium state.

3.3 Velocity Filtration Mechanism

Most of exospheric models use nonmaxwellian velocity distribution functions to explain fast solar wind speed. The pioneer work of Scudder was at this base [69] and could explain the heating of the corona by the presence of nonthermal distribution functions at the base of the corona. Indeed, if nonthermal distribution functions do exist at the exobase, the regions beyond the exobase are populated by these energetic particles, yielding an increase of the temperature with height, in contrast to the Maxwellian distribution function. The key point with the velocity filtration mechanism is indeed to produce such nonthermal distributions in the upper chromosphere and to maintain them in the transition region, where Coulomb collisions are not negligible and should a priori drive any distribution function toward a Maxwellian one. However, recent studies of Vinas et al. [70] point out that suprathermal electrons in a dense plasma, such as the chromosphere, can be produced, thus confirming Scudder's hypothesis. Moreover, to obtain compatible results of the electron temperature profile in the corona from both in situ ion charge state observations in the solar wind and remote sensing observations of the corona, Esser and Edgar [71] claim that non-maxwellian character of the electron distribution has to develop rapidly as a function of height and has to reach close to interplanetary properties within a few solar radii.

As a consequence, the classical heat flux (valid for collisional plasmas) given by Spitzer and Harm [72], which tends to compensate the temperature rise from the exobase to an upper region, is not dominant. If nonthermal distribution functions do exist in the corona, for a critical excess of suprathermal particle numbers, Dorelli and Scudder [73] and Landi and Pantellini [74] show that the heat flux does not obey to the classical heat flux law; in contrast, it is driven from cool regions to hot regions!

4 Final Remarks

Despite four decades of research on the solar corona and on the solar wind, our knowledge on these topics is still limited. The Sun is an ideal laboratory, thanks to its proximity. Indeed, in situ measurements can be performed, which are fundamental to understand the transport of the energy in the solar wind. It is why Solar Probe should be the key mission of the next decade [75], since it will give some basics on physical processes in semicollisional plasmas that could be applied for the study of other stars.

Acknowledgment

I thank Dr. J.-P. Rozelot for giving me the opportunity to present these lectures on the solar corona and the solar wind during the summer school of Oléron. Special thanks to Dr. Milan Maksimovic, Dr. Jean-Louis Steinberg, and Madeleine Steinberg for their suggestions and comments on the manuscript. I also thank Dr. Chadi Salem and Iannis Zouganelis for providing figures incorporated in this manuscript. This work was funded by the French CNRS and by CNES under the Ulysses program.

References

1. E.N. Parker: Astrophys. J. **128**, 664-684 (1958)
2. L. Biermann: *Kurze original milteilungen* (Naturwissenschaften, pp. 34–87, 1946)
3. K.I. Gringauz, V.V. Bezrukikh, V.D. Ozerov, R.E. Rybshinskiy: Sov. Phys. *Docklady*, English version, **5**, 361 (1960)
4. M. Neugebauer, C.W. Snyder: J. Geophys. Res. **71**, 4469 (1966)
5. A.K. Dupree: Winds from cool stars. In: *Solar Wind Eight*, ed by D. Winterhalter, J.T. Gosling, S.R. Habbal, W.S. Kurth, M. Neugebauer (AIP Conference Proceedings 382, Woodbury, New York, 1996) pp. 66–71
6. S. Grzedzielski, D.E. Page: *Physics of the Outer Heliosphere* (Pergamon Press, 1990)
7. V. Izmodenov, G. Gloeckler, Y. Malama: Geophys. Res. Lett. **30**(10), doi:10.1029/2002GL016127 (2003)
8. M. Maksimovic: 'Le vent solaire vu par Soho et Ulysse. In: *SF2A, Paris, France, June 24-June 29, 2002*
9. B. Edlèn: Zeitschrift Astrophys. **22**, 30 (1942)
10. A.J. Hundhausen: *Coronal Expansion and Solar Wind* (Springer-Verlag, Berlin, 1972)
11. R. Schwenn, E. Marsch: *Physics of the Inner Heliosphere I* (Springer-Verlag, Berlin 1990)
12. , M.C.E. Huber et al.: Astrophys. J. **194**, L115–L118 (1974)
13. C. David, A.H. Gabriel, F. Bely-Dubau, A. Fludra, P. Lemaire, and K. Wilhelm: Astron. Astrophys., **336**, L90–L94 (1998)

14. Y.-K. Ko, L.A. Fisk, J. Geiss, G. Gloeckler and M. Guhathakurta: Sol. Phys. **171**, 345–361 (1997)
15. A. Bürgi, J. Geiss: Sol. Phys. **103**, 347 (1986)
16. R. von Steiger, N.A. Schwdron, L.A. Fisk, J. Geiss, G. Gloeckler, S. Hefti,B. Wilken, R.F. Wimmer-Schweingruber, T.H. Zurbechen: J. Geophys. Res. **105**, 27,217 (2000)
17. S.R. Cranmer: Space Science Rev. **101**, 229–294 (2002)
18. S. Giordano, E. Antonucci, M.A. Dodero: Adv. Space Res. **25**, 1927–1930 (2000)
19. M.D. Montgomery, S.J. Bame, A.J. Hundhausen: J. Geophys. Res. **73**, 4999 (1968)
20. W.C. Feldman, J.R. Asbridge, S.J. Bame, M.D. Montgomery, S.P. Gary: J. Geophys. Res. **80**, 4181 (1975)
21. R.C.L. Grard: J. Geophys. Res. **78**, 2885 (1973)
22. C. Salem, J.-M. Bosqued, D.E. Larson, A. Mangeney, M. Maksimovic, C. Perche, R.P. Lin, J.-L. Bougeret: J. Geophys. Res. **106**, 21,710 (2001)
23. W.C. Feldman, E. Marsch: Kinetic phenomena in the solar wind. In: *Cosmic winds and the Heliophere*, ed by J.R. Jokipii, C.P. Sonett, and M.S. Giampapa (University of Arizona Press, Tuscon, 1997) pp. 617
24. N. Meyer-Vernet: J. Geophys. Res. **84**, 5373 (1979)
25. K. Issautier, M. Moncuquet, N. Meyer-Vernet, H. Hoang, R. Manning: Astrophys. Space Sci. **277**, 309–311 (2001b)
26. K. Issautier, N. Meyer-Vernet, M. Moncuquet, S. Hoang: J. Geophys. Res. **103**, 1969 (1998b)
27. N. Meyer-Vernet, S. Hoang, K. Issautier, M. Maksimovic, R. Manning, M. Moncuquet, R.G. Stone: 'Measuring plasma parameters with thermal noise spectroscopy. In: *Measurement Techniques in Space Plasmas: Fields,* ed by Borovsky et al. (Geophys. Monograph Series, **103** 1998) pp. 205–210
28. K. Issautier, R.M. Skoug, J.T. Gosling, S.P. Gary, D.J. McComas: J. Geophys. Res. **106**, 15, 665 (2001a)
29. K. Issautier, M. Moncuquet, S. Hoang: Solar Phys, **221**, 351–359 (2003)
30. R.A. Treumann: J. Physica Scripta **59,** 19 (1999)
31. A. Balogh, R.G. Marsden, E.J. Smith: *The Heliosphere Near Solar Minimum: The Ulysses Perspective* (Springer, Praxis Publishing Ltd., Chichester, UK, 2001)
32. Phillips et al.: Geophys. Res. Lett. **22**, 3301 (1995)
33. K. Issautier, N. Meyer-Vernet, M. Moncuquet, S. Hoang: J. Geophys. Res. **104**, 6691 (1998)
34. M. Neugebauer: Observations constraints on solar wind acceleration mechanisms. In: *Solar Wind Five*, ed by M. Neugebauer (NASA Conf Publ., CP-2280 1983) pp. 135–145
35. D.J. McComas et al.: Space Science Reviews **97**, 189 (2001)
36. D.J. McComas, H.A. Elliott, J.T. Gosling, D.B. Reisenfeld, R. M. Skoug, B.E. Goldstein, M. Neugebauer, A. Balogh: Geophys. Res. Lett. **29**(9), doi:10.1029/2001GL014164 (2002)
37. J.G. Luhmann, Y. Li, C.N. Arge, P.R. Gazis, R. Ulrich: J. Geophys. Res. **107**(8), doi:10.1029/2001JA007550 (2002)
38. K. Issautier, M. Moncuquet, S. Hoang: Large-scale structure of the polar solar wind at solar maximum: Ulysses/URAP observations. In: *Solar Wind Ten,* ed by M. Velli (AIP Conference Proceedings) **679**, 59–62 (2003)

39. J. Geiss, G. Gloeckler, R. von Steiger: Space Sci. Rev. **72,** 49 (1995)
40. D.J. McComas et al.: Geophys. Res. Lett. **30**(10), doi:1029/2003GL017136 (2003)
41. K. Issautier, S. Hoang, N. Meyer-Vernet, M. Moncuquet, D.J. McComas: 'The solar wind observed by Ulysses/URAP at solar maximum. In: *10th European Solar Physics Meeting, Prague, Czech Republic, 2002*
42. J.W. Belcher, A.J. Lazarus, R.L. McNutt, G.S. Gordon: J. Geophys. Res. **98**, 15, 177 (1993)
43. C. Salem: Ondes, turbulence et phénomènes dissipatifs dans le vent solaire à partir des observations de la sonde WIND. PhD Thesis, University P7, France (2000)
44. A. Mangeney, C. Salem, C. Lacombe, J.-L. Bougeret, C. Perche, R. Manning, P.J. Kellogg, K. Goetz, S.J. Monson, J.-M. Bosquet: Ann. Geophysicae **17**, 307-320 (1999)
45. C. Salem, A. Mangeney, J.-L. Bougeret: Coherent electrostatic nonlinear waves in collisionless space plasmas'. In: *Lecture Notes in Physics*, **536**, ed by T. Passot & P.L. Sulem (Springer-Verlag, 1999) pp. 251–268
46. C. Salem, C. Lacombe, A. Mangeney, P.J. Kellogg, J.-L. Bougeret: Weak double layers in the solar wind and their relation to the interplanetary electric field'. In: *Solar Wind Ten*, ed by M. Velli (AIP Proceedings), **679**, 513 (2003)
47. M. Maksimovic, V. Pierrard, P. Riley: Geophys. Res. Lett. **24**, 1151 (1997b)
48. L.M. Celnikier: *Basics of Cosmic Structures* (Edition Frontieres, Gif sur Yvette, France, 1989)
49. M.G. Kivelson, C.T. Russel: *Introduction to Space Physics* (Cambridge University Press, 1995)
50. I. Zouganelis: Modèle cinétique du vent solaire avec un potentiel non-monotone pour les protons. Master report, University P6, France (2002)
51. S. Patsourakos, J.-C. Vial: Astron. Astrophys. **359**, L1–L4 (2000)
52. E.N. Parker: Astrophys. J. **139**, 72, (1964)
53. F.L. Scarf, L.M. Noble: Astrophys. J. **141**, 1479–1491 (1965)
54. P.A. Sturrock, R.E. Hartle: Phys. Rev. Lett. **16**, 628–631 (1966)
55. C.L. Wolff, J.C. Brandt, R.G. Southwick: Astrophys. J. **165**, 181–194 (1971)
56. S.R. Habbal, R. Esser, M. Guhathakurta, R.R. Fisher: Geophys. Res. Lett. **22**, 1465–1468 (1995)
57. J.W. Chamberlain: Astrophys. J. **131**, 47–56, (1960)
58. J.H. Jeans: *The Dynamical Theory of Gases,* 4th ed (Cambridge University Press, New York, 1923)
59. J. Lemaire, M. Scherer: C.R.H. Acad. Sci. Ser. B **269,** 666–669 (1969)
60. K. Jockers: Astron. Astrophys. **6**, 219–239 (1970)
61. J. Lemaire, Scherer: J. Geophys. Res. **76,** 7479–7490 (1971)
62. Meyer-Vernet, N. and K. Issautier: J. Geophys. Res. **103,** 29, 705 (1998)
63. M. Maksimovic, V. Pierrard, J. Lemaire: Astron. Astrophys. **324**, 725 (1997a)
64. V. Pierrard, K. Issautier, N. Meyer-Vernet, J. Lemaire: Geophys. Res. Lett. **28,** 223 (2001)
65. H. Lamy, V. Pierrard, M. Maksimovic, J. Lemaire: J. Geophys. Res. **108**(8), doi:10.1029/2002JA009487 (2003)
66. I. Zouganelis, M. Maksimovic, N. Meyer-Vernet, H. Lamy, V. Pierrard: A new exospheric model of the solar wind acceleration: the transsonic solutions'. In: *Solar Wind Ten*, ed by M. Velli (AIP Proceedings), **679**, 315 (2003)

67. R. Woo, S.R. Habbal: American Scientist **90,** 532–539 (2002)
68. M.P. Leubner: Astrophys. Space Sci. **282**, 573–579 (2002)
69. J.D. Scudder: Astrophys. J. **398**, 299 (1992)
70. A.F. Viñas, H.K. Wong, A.J. Klimas: Astrophys. J. **528**, 509 (2000)
71. R. Esser, R. Edgar: Astrophys. J. **532,** L71 (2000)
72. L. Spitzer, R. Härm: Phys. Rev. **89**, 372 (1953)
73. J.C. Dorelli, J.J. Scudder: Geophys. Res. Lett. **26,** 3537 (1999)
74. S. Landi, F. Pantellini: Astron. Astrophys. **372**, 686–701 (2001)
75. D.M. Hassler: Solar probe: mission to the Sun. In: *Innovative Telescopes and Instrumentation for Solar Astrophysics,* ed by Stephen L. Keil, Sergey V. Avakyan (Proceedings of the SPIE, Vol. 4853, 2003) pp. 180–186
76. M. Neugebauer: The solar wind and heliospheric magnetic field in three-dimensions'. In: *The Heliosphere Near Solar Minimum: The Ulysses Perspective*, ed by A. Balogh, R. Marsden, and E.J. Smith (Springer-Praxis books in Astrophysics and Astronomy 2001) pp. 43–99

The Solar Spectrum in the UV, EUV, and X Ranges: Observations, Modelling, and Effects on the Earth Upper Atmosphere in the Frame of Space Weather

Jean Lilensten and Matthieu Kretzschmar

Laboratoire de Planétologie de Grenoble, Observatoire des Sciences de l'Univers de Grenoble, Bâtiment D de physique, B.P. 53, 38041 Grenoble cedex 9

Abstract. In this chapter, we introduce the way the energetic electromagnetic flux is emitted by the Sun, and we present how it creates an upper partly ionized layer in the Earth atmosphere.

1 Introduction

The Ultra Violet and X solar fluxes are certainly among the most important parameters to monitor and forecast space weather. They constitute the first and main source for the creation of the ionosphere. Any sudden variation of their intensities (due, for example, to a solar eruption) has an immediate effect on the ionospheric concentration, and therefore on parameters used for telecommunication system. They also affect the thermosphere, in particular through heating and expansion of the gas, with a direct application to orbitography. They also affect other layers of the Earth atmosphere through interactions with the terrestrial environment, and help to create short-time scale space weather and the longer term global climate. In particular,

- Variations of the total solar irradiance (TSI), ultraviolet (UV), far ultraviolet (FUV), extreme ultraviolet (EUV), and soft X-rays (XUV) solar irradiances are the fundamental forcing mechanisms to the terrestrial atmosphere, land, and oceans.
- UV solar irradiances below 300 nm are completely absorbed by molecular oxygen and ozone, and this radiation is both a dominant loss and source mechanism for stratospheric and lower mesospheric ozone. Ozone photochemistry is affected by Lyman-alpha (121.5 nm)[1] photons via the process of mesospheric water vapor dissociation, which produces catalytically active hydroxyl radicals.

[1] Not to be confused with Hα line, in the visible spectrum, at 656.3 nm (red).

J. Lilensten and M. Kretzschmar: *The Solar Spectrum in the UV, EUV, and X Ranges: Observations, Modelling, and Effects on the Earth Upper Atmosphere in the Frame of Space Weather*, Lect. Notes Phys. **699**, 53–91 (2006)
DOI 10.1007/3-540-33759-8_4

Solar UV control of the middle atmosphere may couple with the Earth's biosphere. It is still unclear if solar EUV and XUV variability that affects the Earth's near-space environment also couples with the biosphere. One solar–terrestrial coupling phenomenon may be active. Anthropogenic carbon dioxide and methane may be convectively transported upward from lower atmosphere layers and may have an effect upon the upper atmosphere hydrogen budget, cooling this region over long timescales.

1.1 Fast Description of a Highly Variable, But Badly Known (Until Now) Part of the Solar Spectrum

The solar spectrum has been first analyzed at the beginning of the 20th century, and was found to closely follow the Plank law, with a maximum spectral flux at about 460 nm, i.e., in the blue part of the visible spectrum. Inside this spectrum, known as the "blackbody spectrum," Fraunhofer could identify several absorption lines that helped to reveal the chemical composition of the Sun's chromosphere (Fig. 1).

It is not until 1931 that it started to be radioanalyzed. This started when Karl Jansky discovered the radio-emission of the Milky Way. In the late 30th and the beginning of the 40th, some experiments showed the presence of a strong solar radio emission correlated with the presence of sunspots. From these first observations and physics considerations, it was expected that the corona would be quite hot (reaching 10^9K) and therefore radiate in the UV and X ranges (see Table 1). Since these radiations are not observed at the surface of the Earth, it meant that they are absorbed in the atmosphere. The ionosphere was roughly known because of the radar observations. There were therefore clues about the origin of the ionosphere even before the space age. However, instruments designed to observe the hottest part of the spectrum were meant to flight, on rockets or earth-orbiting satellites to altitudes where the absorption is reduced. Thus, progress in this area had to await the arrival of the space age. Solar X-ray emission was observed for the first time by T.R. Burnight in a 1949 flight of a rocket.

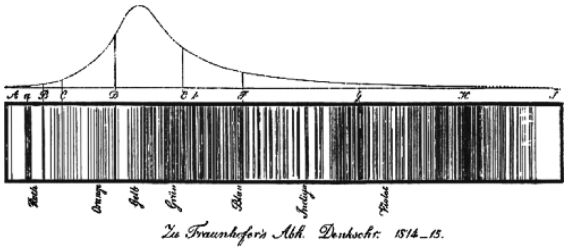

Fig. 1. Original Fraunhofer's spectrum (from [1]). der K. Denkschriften: Acad. Der Wissenschaften zu München, 1814–1815, pp. 193–226

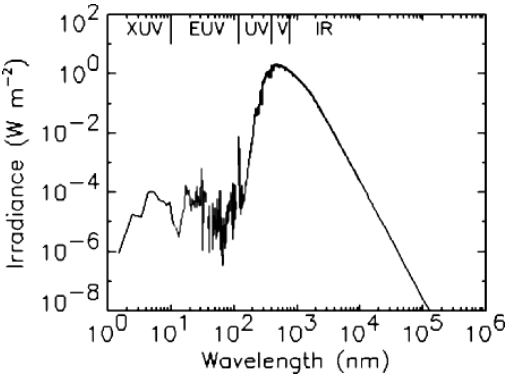

Fig. 2. Solar spectrum known as the reference 2000 spectrum [2]

We can now rely on different experiment to get a short description of this energetic part of the solar spectrum:

The continuum intensity decreases with decreasing wavelength beyond the violet and, at wavelengths less than 208.5 nm, bright emission lines start to appear. The solar continuum eventually fades to invisibility at wavelength of around 140 nm. There is a very bright emission line at 121.5 nm due to the excitation of hydrogen atoms in the chromosphere: it is the Lyman–α line. The X-rays depends on the solar flares still stronger than the UVs. In flares, the iron may be left with only 2 electrons, with X-ray emission corresponding to 20 10^6 K. Gamma rays, at the extreme short-wavelength end of the electromagnetic spectrum, were detected for the first time in 1972 with the OSO-7 spacecraft.

A reference spectrum has been assembled in Fig. 2, from Tobiska. One sees that there is a ratio 1/10000 between the highest value of the irradiance, in the visible part, and the EUV/XUV part of the spectrum. However, this last part is very energetic and has a strong influence on the space environment of the Earth.

The logarithmic scale in this figure does not allow distinguishing the multiple absorption lines in the visible–Near UV ranges. The observations made during the ATLAS 1 mission by the SOLSPEC spectrometer [3, 4] show into details the absorption by the solar atmosphere (Fig. 3), which were discovered by Joseph Fraunhofer in 1811. They allow characterizing the chemical composition since each line corresponds to the signature of a specific absorption by a given chemical element.

On the contrary, when examining the most energetic part of the spectrum, the obvious feature are emission lines (Fig. 4). We will discuss them in more detail in the next section, but it is obvious that many lines are very intense. Not surprisingly, the brightest emission is again the Lyman–α line at 121.5 nm.

The XUV–UV emissions are very variable. They are strongly related to magnetic activity of the Sun.

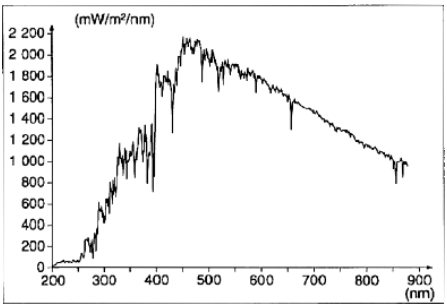

Fig. 3. The solar spectrum versus wavelength (From [5])

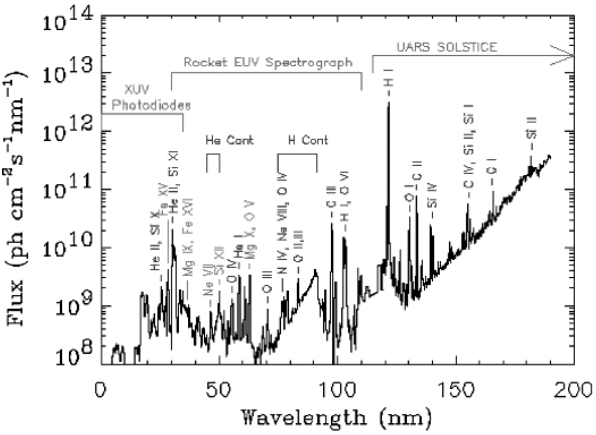

Fig. 4. Solar UV Irradiance Measurement Made on November 3, 1994, by the original SEE Prototype Instrument from a Sounding Rocket. The continuum at the longer wavelengths is from the solar photosphere. The many emission lines, which are more variable than the photospheric continuum, are from the solar chromosphere and corona [6, 7]

- Short-term variations (minutes to hours) are related to eruptive phenomena on the Sun.
- Intermediate-term variations, modulated by the 27-day rotation period of the Sun, are related to the appearance and disappearance of active regions, plages, and network on the solar disk.
- Finally, long-term variability is related to the 22-year magnetic field cycle of the Sun.

An accurate, long-term XUV-UV variation is still to be determined with satellite solar instruments.

Until 2002, there has been no permanent monitoring of the UV/EUV flux, because of technological limitations. Therefore, there is a serious lack of EUV/UV data of sufficient radiometric accuracy (<10%) as well as of

temporal coverage. As to the latter, there are no EUV (in the spectral range >10 nm and <110 nm) data sets available extending a full solar cycle. Spectrophotometric satellite survey EUV/UV observations were conducted since the 1960s. Following the end of the Atmospheric Explorer-E measurements in December 1980 [8], there have not been daily solar EUV irradiance measurements except for approximately 20 days during the 8-month San Marco 5 satellite mission [9]. Moreover, for wavelengths ¡110 nm no satellite spectrometer has been calibrated in-flight.

Therefore, modelers are left with the use of proxies for the thermosphere/ionosphere (T/I) models such as F10.7 (radio flux at 10.7 cm) or the magnesium line Mg II K (see below). They are used instead of the solar extreme ultraviolet (EUV/UV) radiation that is the primary energy source driving the T/I system. Since the solar radio emission F10.7 is generated by a variety of different physical processes localized in the solar photosphere, chromosphere, and corona, the correlation with the solar EUV/UV flux is not satisfying for modern requirements. Yet, T/I modellers and operations continue to use F10.7 for reasons of convenience and of lack on handy and accurate EUV/UV data. For special applications there have been developed numerous other proxies and they each have disadvantages as well.

In December 2001, a new instrument devoted to the observation of this part of the solar spectrum has been launched to space, onboard TIMED (NASA). The primary science objective of the 2-year TIMED mission is to understand the energy transfer into and out of the Mesosphere and Lower Thermosphere/Ionosphere (MLTI) region of the Earth's atmosphere, and the basic structures that result from the energy transfer into these regions. The Solar Extreme Ultraviolet Experiment (SEE) is composed of a spectrometer and a suite of photometers designed to measure solar ultraviolet radiation and the primary energy that is deposited into the MLTI atmospheric region. It studies the solar ultraviolet irradiance – how much it varies and how it affects the atmosphere; how much it heats the atmosphere and changes its composition. It also aims at understanding and establishing an index of the solar variabilities. Therefore, it fully falls into the subject of this chapter. Unfortunately, few SEE data have yet been published and this lecture will not take them into account. SEE is observing the Sun about three min per orbit while the Sun is in full view. When possible, it will view the sunset through the atmosphere, in order to determine the atmosphere's density. Data collected from SEE's observations of the Sun will show where the solar energy, or radiation, is coming from as a function of wavelength and how each wavelength varies with time (http://lasp.colorado.edu/see/).

1.2 Definition of the UV, EUV, and X Ranges (ISO)

The definitions of all the irradiances are not yet totally agreed upon. Table 1 gives the actual most agreed ranges. It is in agreement with the new ISO initiative [2].

Table 1. Irradiances ranges. The irradiances are defined from the wavelength range, not from the energy range. The energies and temperatures given here are approximated

Irradiance	Subdomain	$\Delta\lambda$	Energy (eV)	Associated Temperature (K)
Radio		>1.5 cm	$<8 \times 10^{-5}$	<0.2
Microwave		1 mm to 1.5 cm	8×10^{-5} to 1.25×10^{-3}	0.2–3
Microwave	W	3.3 mm	3.75×10^{-4}	1
Microwave	V	5 mm	2.5×10^{-4}	0.6
Microwave	Q	7.5 mm	1.65×10^{-4}	0.5
Microwave	Ka	10 mm	1.25×10^{-4}	0.4
Microwave	K	13.6 mm	9×10^{-5}	0.2
Infrared[a]		700 nm to 350,000 nm	10^{-3} to 1,8	2.7–4700
infrared	Near	700 nm to 5000 nm	0.25 to 1.8	630–4700
infrared	Mid [b]	5,000 nm to 25,000 nm	0.05–0.25	130–630
infrared	Far[b]	$>25,000$ nm	<0.05	<130
Visible		400 nm to 700 nm	1.8–3	4600–7700
Ultraviolet		30 nm to 400 nm	3–41	7700–10^6
Ultraviolet	A[c]	315 nm to 400 nm	3–4	7700–10^5
Ultraviolet	B[c]	280 nm to 315 nm	4–4.5	10^5
Ultraviolet	C[3]	100 nm to 280 nm	4.5–12.5	10^5–3×10^5
Ultraviolet	Near[d]	200 nm to 400 nm	3–6	70,000–140,000
Ultraviolet	Far[e]	120 nm to 200 nm	6–10	140,000–230,000
Ultraviolet	Extreme[e]	30 nm to 120 nm	10–41	230,000–10^6
X-rays[5]		0,005 nm to 30 nm	$41–2,5 \times 10^5$	10^6–6×10^9
X-rays	XUV or Soft[e]	1 nm to 30 nm	41–125	10^6–3×10^6
X-rays	Hard	0,005 nm to 1 nm	$125–2.5 \times 10^5$	3×10^6–6×10^9
γ		$<0,005$ nm	$>2.5 \times 10^5$	$>6 \times 10^9$

[a] The upper wavelength limit definition is not yet agreed upon. Sometimes considered as 10.000 or 200.000

[b] Sometimes 40.000 instead of 25.000

[c] Adopted range of the World Health Organisation (WHO) and the International Commission on Illumination

[d] Middle ultraviolet is sometimes considered as the range 200 nm to 300 nm

[e] Definition adopted in the aeronomy community. Other communities may consider 10 nm instead of 30 nm and 100 nm instead of 120 nm.

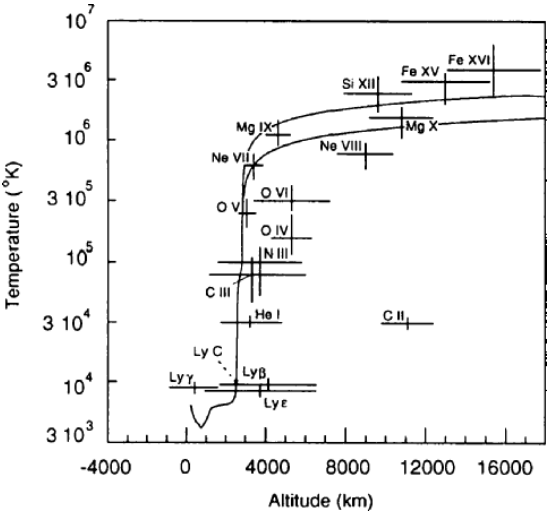

Fig. 5. Altitude of selected UV lines in the transition region and upper corona [10, 11]

From this table, it becomes clear that the observation of a given wavelength reveals a temperature at the site of emission. This is how the temperature of the corona has been determined. Figure 5 shows which lines have been used to explore the coronal temperature profile.

Finally, in Table 2, we give some prominent UV emission lines and their temperature of formation. It allows retrieving the temperature indicated in the figure above mentioned.

1.3 Goals of the Chapter

Here, we want to focus on two main points:

- To understand the physics of the solar emission, and the physics of the terrestrial absorption and
- To understand how this is linked to the space weather through physics.

We will consider only the irradiances that have an effect for space weather, i.e. UV, EUV, and soft X-rays.

The next (and second) part examines where these irradiances are coming from, and what physical process is involved. It then explores their variability versus the solar activity, and makes a point on the actual state in modelling. Among the large bibliography devoted to the Sun, this work makes special use of two very good books (to the opinion of the authors): in English: K.J.H. Phillips [12] in French: P. Lantos [11].

The third part deals with the physical effects of this solar spectrum on the earth. We show the ionization, excitation, dissociation, and heating rate processes, and explain the basics for a physical understanding. It also shows

Table 2. Reference UV lines in the solar corona

Name	Wavelength [nm]	Temperature [K]
Fe IX	17.1	900,000
Fe X	17.48	1,100,000
Fe XI	18.04	1,300,000
Fe XII	19.5	1,500,000
Fe XIV	21.9	1,800,000
Fe XV	23.4	2,000,000
Ni XVII	24.9	2,500,000
Fe XVI	25.1	2,200,000
He II	25.6	50,000
Fe XVI	26.3	2,200,000
Fe XIV	26.5	1,800,000
Fe XV	28.4	2,000,000
He II	30.4	50,000
Fe XVI	33.5	2,200,000
Mg IX	36.8	1,000,000
Ne VII	46.5	500,000
O IV	55.4	160,000
Mg X	62.5	1,100,000
C III	99.7	70,000
O VI	103.2	320,000
C III	117.6	70,000
Si III	120.6	30,000
H I (Ly-A)	121.5	20,000
N V	124.0	200,000
C II	133.5	20,000
Si IV	139.4	60,000
Si IV	140.3	60,000
Si II	153.3	14,000
C IV	155.0	110,000
He II	164.0	50,000
C I	165.7	<10000
C I	167.0	<10000
Si II	180.8	14,000
Si II	181.7	14,000

some effects relating to space weather, both in the thermosphere through the drag and in the ionosphere through electronic content variations.

2 First Part: Observations (Sun)

2.1 The UV/EUV/XUV Solar Spectrum Origin

At the considered temperatures, the source function cannot be described by the blackbody radiation function, and there is no local thermodynamic equilibrium. The core of the UV lines is formed above the height of the temperature minimum, where the local value of temperature, i.e., that describing

the speeds of atoms, ions, and electrons, may be quite different from that characterizing the radiation in which the atoms and ions in the chromosphere are immersed. The source function can no longer be considered equal to the Plank function, but must be evaluated taking the individual atomic processes that are involved in forming the line. In other words, Table 1 is not sufficient to retrieve the corresponding temperature of formation of a line from its wavelength, and Table 2 must be used instead. However, the UV spectrum is formed at relatively low temperatures, i.e., in the chromosphere and in the transition region.

The atomic processes that create line photons result in an *emission coefficient*. The atomic processes that destroy line photons result in an *absorption coefficient*. The *source function* is defined as the emission coefficient divided by the absorption coefficient. In the following paragraph, we will present these processes. We will *not* present the processes that govern the broadening and splitting of the spectral lines, although they are quite important in the solar physics. However, they are not necessary to understand the effect of these lines on the Earth atmosphere, in the frame of space weather.

2.2 Near UV Emission Process: Electronic Transition

In the near UV range, one finds some distinct lines such as: H (line δ) at 410.2 nm, Ca^+(line H) at 396.8 nm, Ca^- (line K) at 393.4 nm, Fe (line M) at 373.5 nm, Mg at 285.2 nm, Mg^+ (line h) at 280.2 nm, and Mg^+ (line k) at 279.5 nm. All these lines are refereed in the Fraunhofer spectrum and are of chromospheric origin. The first phenomenon to consider is the collisions. Collisions can both create and destroy photons. They can result in the excitation of the electrons, followed by spontaneous transition and light emission, or to the energy transfer through desexcitation without photon emission.

The radiation governed by these phenomena is called "collisionnal," in contrast to the "photoelectric" process. In this latter one, photons of the photospheric radiation field likewise create new photons or destroy them through the excitation or de-excitation of atoms, mainly hydrogen. Finally, the scattering process occurs when the line photons are repeatedly absorbed and reemitted in different directions by atoms. The scattering is "coherent" if the scattered photons have identical energies and "incoherent" if there are slight changes in their energies, owing to the motion of the absorbing and reemitting atoms. The incoherent mode is more generally the case. The effect of these is neither to add nor to take away line photons: the two processes merely give rise to a diffusion of the line photons.

Recent UV data obtained from the UVSP experiment on board the Solar Maximum Mission satellite in the 184.5- to 232.5-nm spectral range, SOLSPEC (ATLAS 1 mission) and SUSIM (UARS) spectrometers, allowed to gather the absolute solar irradiance with an accuracy of 10% in the 184.5- to 232.5-nm spectral range with a spectral resolution of 0.01 nm (Fig. 6: [13]).

In the UV range, one finds the hydrogen Lyman series, which includes the Ly-α line at 121.5 nm, Ly-β at 102.5 nm, Ly-γ at 97.2 nm... These lines are

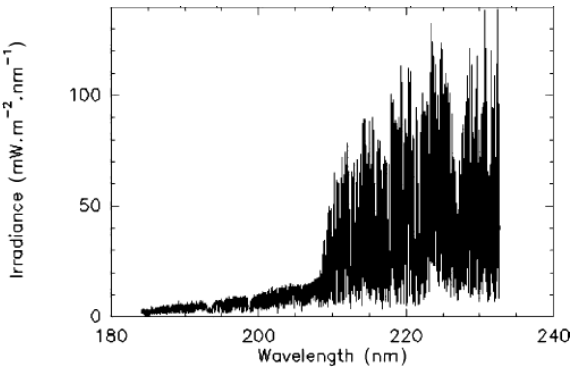

Fig. 6. High spectral resolution solar irradiance in the 184.5- to 232.5-nm range from the SOLSPEC and UVSP spectrometers [13]. The accuracy is 10%, the spectral range 184.5–232.5 nm, the spectral resolution 0.01 nm and the spatial resolution is 3 arcsec

typical electronic lines, in which the electron goes from ground state ($n = 1$) to higher radius. Ly-α corresponds to $n = 2$ toward $n = 1$, Ly-β $n = 3$ to $n = 1$, Ly-γ $n = 4$ to $n = 1$.

The energy gained through collisions or photon absorption may exceed the ionization threshold. This is the case in the chromosphere for Ca. However, at such temperatures, calcium atoms re almost all in the singly ionized state Ca^+ (or Ca II), with the single outer electron in a 4s orbit (H line). The 4p orbit may eventually be also reached (K line). Ca II lines are collisionally controlled. Since this line is bright and observable from the ground, daily observations are performed, in particular at Big Bear Solar observatory (Fig. 7).

Two other Fraunhofer lines in the near UV are important. They are both due to singly ionized magnesium, at wavelengths of 280.2 nm (Mg II h line) and 279.5 nm (Mg II k line). The electron transitions involved are similar to those for the Ca II H and K lines, and they are also collisionally controlled. These lines have given rise to an abundant literature and many observational projects. This observation has given birth to a solar index suitable for use as a proxy for the solar ultraviolet irradiances. It starts with the observation that the profile of the Mg II spectrum exhibits two wings, one originating in the upper chromosphere that exhibits solar ultraviolet variations and the other, in the upper photosphere, which is insensitive to solar variations (Fig. 8). The Mg II index core-to-wing ratio was first developed from Nimbus-7 SBUV spectral scan irradiance data by Heath and Schlesinger [14]. It is calculated by taking the ratio of the irradiance at the core of the Mg II absorption feature at 280 nm to the average irradiance in the wings of the Mg II feature at approximately 276 and 283 nm. By taking a ratio with the nearby wing irradiances, which are generated in the upper photosphere and are relatively insensitive to solar variations, the Mg II index is unaffected by most temporal and spectral changes in instrument response.

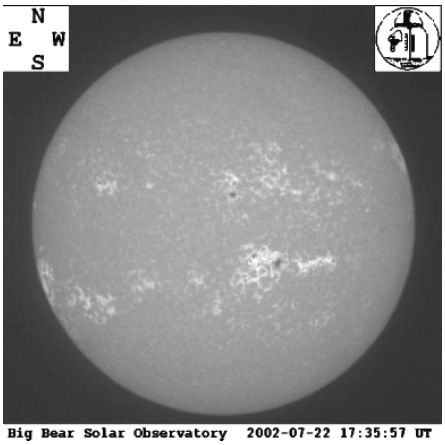

Fig. 7. Whole disc spectroheliogram in the core of the Ca II K line. The chromospheric network, marked by the coarse bright mottles, shows more clearly than in the HA spectroheliogram, as do the active regions, but the filaments are barely visible (Big Bear Observatory, picture taken with Kodak Megaplus 1.4i digital CCD camera with Daystar filter bandpass of 1.5 Å)

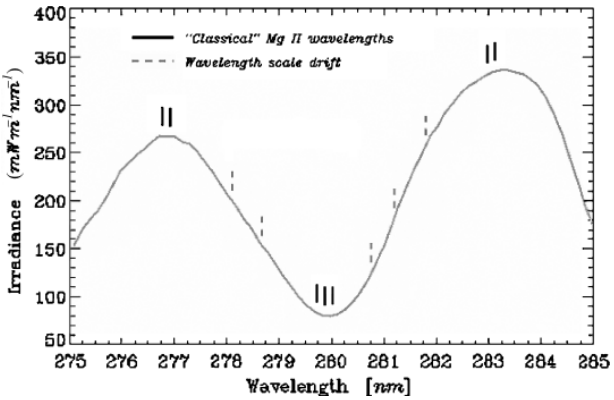

Fig. 8. SBUV / 2 discrete MgII k spectrum [15]

Finally, the He II line at 30,4 nm is currently observed by the EIT/SOHO filters [16]. It is emitted at 50,000 K, and therefore constitutes a picture of the chromosphere. This can be seen in Fig. 9.

2.3 UV to XUV Emission Processes: Free–Free and Free–Bound Processes

When we deal with UV and EUV emission processes, we no longer face atoms or singly charged ions, but multiple charged ions. One sees from Tables 1 and 2 and from Fig. 5 that we now face high-temperature zones of the solar atmosphere, i.e., the coronal radiation. The ion may be in any state, ground or excited. On top of electron excitation seen above, several processes compete.

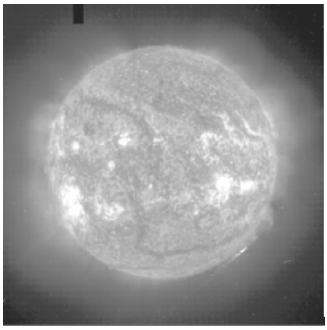

Fig. 9. The Sun observed in the He II emission line by the EIT instrument onboard SOHO, July 24, 2002 (The SOHO EIT Consortium; SOHO is a joint ESA-NASA program)

The collision with an electron creates an additional ionization if the incident electron has energy larger than the threshold (above typically 12 eV). We then get an ionization ($X^{+m} + e \rightarrow X^{+m+1} + 2e^-$). The ion can be left in an excited state, and goes to state of smaller energy with emission of a photon. We can also have a recombination ($X^{+m} + e \rightarrow X^{+m-1}$) with the emission of a photon. This is then refereed to as a radiative recombination. The impact with an electron may also leave the ion in such an excited state that it autoionizes after a short period of time ($X^{+m^*} \rightarrow X^{+m+1} + e^-$). This excitation can be an electronic recombination ($X^{+m} + e \rightarrow X^{+m-1^*}$). After autoionization, the ion is left in a ground state. Some of these processes can also occur with proton collisions or with photoabsorption. These processes are, however, of very small influence. Finally, the charge transfer with the abundant hydrogen can leave the ion in an excited state from which a photon is emitted ($X^{+m} + H \rightarrow X^{+m-1^*} + H^+$).

The radiative recombination involves the transfer of a free electron to a captured electron. It is called a "free–bound" process. Another process may create UV to X light, the "free–free" one. In this case, an electron is accelerated or decelerated through interaction with a Colombian potential due to an ion. This velocity change produces a glow called free–free since the electron is not captured, or *Bremsstrahlung* (the word is German for braking radiation). These two last phenomena are responsible for the "continuum": all the frequencies are excited, creating a continuous baseground for the solar spectrum. The other origin of the continuum is the recombination of electrons with the bare nuclei of carbon and oxygen.

The physics involved depend on many parameters, such as the relative abundance of each element, the ionization ratio, excitation ratio. In Fig. 10, we show the ionisation ratio for the oxygen and iron ions. The ionisation state is shown with the spectroscopic notation for the oxygen (O II = O^+) and with the ionisation degree for the iron (9 = Fe IX) (from [17, 18].

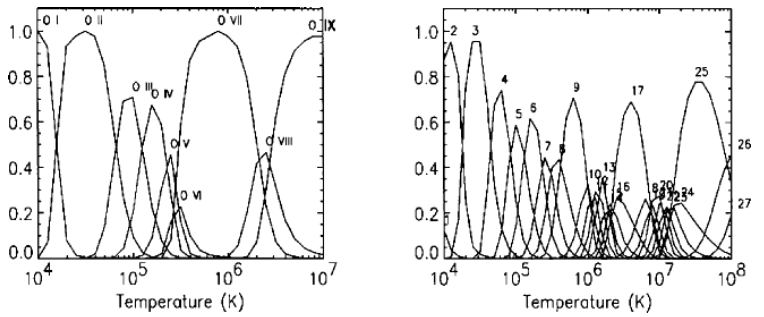

Fig. 10. Ionization ratio for oxygen (*left*) and iron (*right*) versus temperature

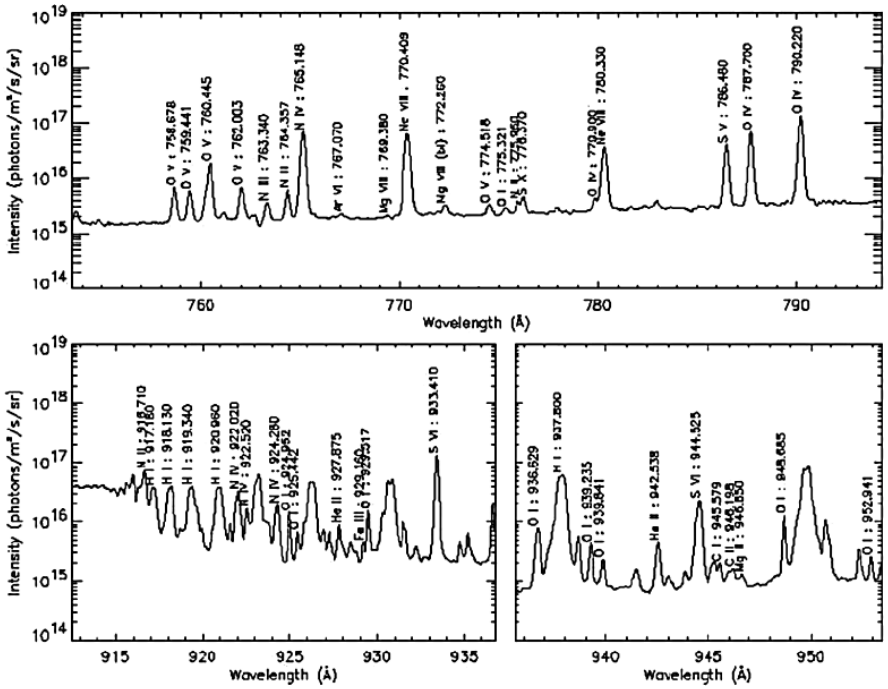

Fig. 11. Reference spectrum assembled from the SUMER data

The SUMER instrument [19] onboard SOHO allowed to gather a full EUV spectrum assembled in Fig. 11. The SOHO/SUMER instrument is a normal incidence spectrometer with two alternates detectors working in UV wavelength, from 500 Å to 1,610 Å. Spectral resolution along the slit has an average value of 1 arcsec and spectra resolution about 0.044 Å.

On top of the continuum, several lines are worth to be examined.[2]

[2] The two following paragraphs are greatly inspired from [12].

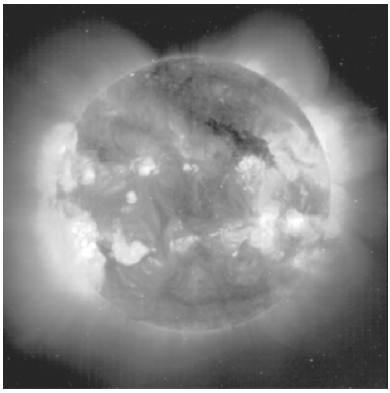

Fig. 12. The Sun observed in the Fe XV emission line by the EIT instrument onboard SOHO, July 24, 2002 (The SOHO EIT Consortium; SOHO is a joint ESA-NASA program)

In the X-ray emission, two resonance lines in the Fe XIV spectrum, at 5.90 and 5.96 nm, are emitted from the 3p (C) ground state to the 4d (A) state. Over the sunspot regions, the lower corona temperature is enhanced up to 4×10^6 K This results in an additional ionization of iron, especially Fe XV and Fe XVII, which have bright emissions at 28.4 and 1.7/1.5 nm, respectively. This has been the basis for one of the EIT/SOHO filters [16], which observes the corona at 28.4 nm (but also Fe IX/X at 17,1 nm, Fe XII at 19,5 nm, and He II at 30,4 nm). Such an picture may be seen in Fig. 12. The actives regions, where the temperature is enhanced, appear as bright regions while the coronal zones look darker.

In the XUV range, one also finds other lines. The resonance lines of helium-like ions of light elements are represented, such as carbon (C V) at 4.03 nm, oxygen (O VII) at 2.16 nm, and neon (Ne IX) at 1.345 nm. Similarly, there are lines of hydrogen-like ions, equivalent to the Lyman lines of hydrogen itself at UV wavelengths: the "Lyman α" lines of hydrogen-like carbon (C VI) at 3.37 nm and oxygen (O VIII) at 1.90 nm.

In the EUV range, several intense lines are due to lithium-like ions. Lithium has three electrons, with the outer in the $n = 2$ orbit. Excitation may take it from a 2-s suborbit to a 2p, and de-excitation back to 2s results in two closely spaced lines forming a doublet. The lithium-like carbon (C IV) doublet at 155 nm is emitted at transition region temperatures. The lithium-like oxygen (O VI) doublet is at 103.2 nm and 103.8 nm, and originates in the coronal region. The lithium-like magnesium (Mg X) is at 61.0 nm and 62.5 nm, and the silicon (Si XII) is at 49.9 nm and 52.1 nm.

Fe IX/X at 17,1 nm, which is also observed by EIT, is due to a 3p–3d transition. A view of the Sun at this wavelength is shown in Fig. 13. We now observe the Sun at a temperature of 10^6 K.

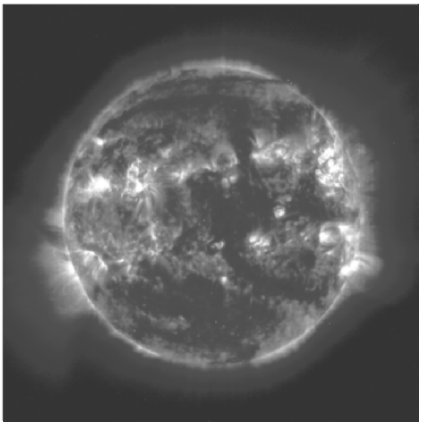

Fig. 13. The Sun observed in the Fe X emission line by the EIT instrument onboard SOHO, July 24, 2002 (The SOHO EIT Consortium; SOHO is a joint ESA-NASA program)

2.4 The UV/EUV/XUV Solar Spectrum Variability

Figure 14 shows the variation of the solar spectrum over a solar cycle versus the wavelengths. One sees that this variability is very small in the visible range (less than 0.1%), and quite small in the IR part (less than 1%). The picture is totally different in the UV range, where a doubling of the intensity may be observed. In the following, we study these variations.

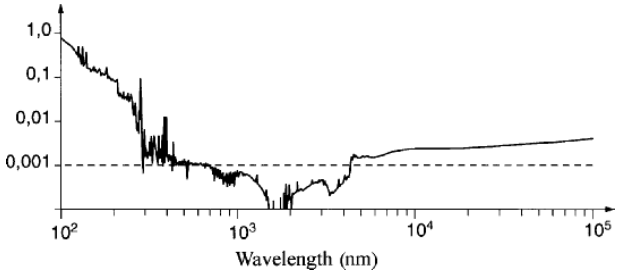

Fig. 14. The solar spectrum variability over a solar cycle versus wavelength (from [5, 20])

2.5 UV Radiance Variability

The observation of the Ca K line allows to figure out the solar variability of the chromosphere. This is regularly performed at the Big Bear Solar Observatory, where the CaII K-line indices (called BBSO daily CaII K index) have been

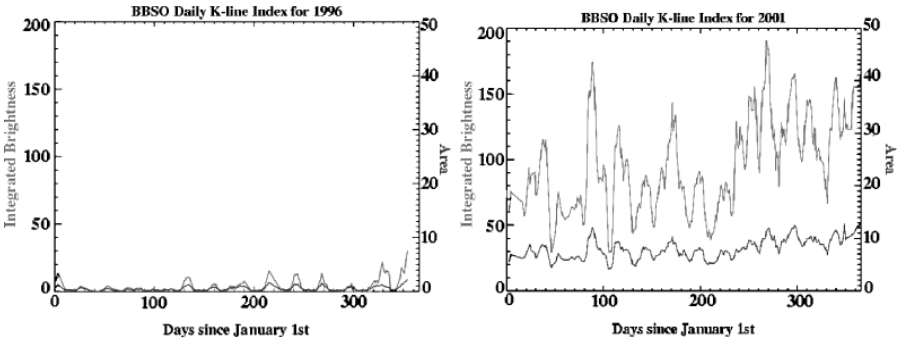

Fig. 15. Big Bear Solar Observatory (BBSO) daily CaII K index. The left panel shows a period of low solar activity (1996) and the right panel a period of strong solar activity (2001) (http://www.bbso.njit.edu/Research/Cak/). The upper index in each panel is the integrated brightness above 7.5% of the central disk brightness; the bottom index is the corresponding area

calculated every day since late 1995. It is shown in Fig. 15. We present below daily indices of excess K-line brightness and area.

From these curves, one sees that the integrated brightness can vary from unity to values up to about 200. This shows a two-order magnitude of this UV line within the cycle, which is a witness of the variability of the near UV range.

Multiple instruments have produced Mg II index data sets during the last two decades. Mg II index data sets from different instruments typically differ in absolute value due to differences in resolution, wavelength selection, and derivation method. However, there is excellent agreement in the response to solar variations [21–25]. Data from four separate instruments are shown in Fig. 16 (http://ssbuv.gsfc.nasa.gov/solar.html#HS86). Here the individual measurements are presented as "dots" and the heavy lines represent 27-day running averages of the daily data. Nimbus-7 SBUV Mg II data derived from spectral scan irradiance measurements are discussed by Heath and Schlesinger [14], and a data set covering November 1978 to February 1987 is available on line (*pub/solar/sbuv*). NOAA-9 and NOAA-11 spectral scan Mg II index data have also been created beginning in March 1985 and February 1989, respectively, and were used in various publications [15, 23, 26, 27]. Beginning in May 1986 with NOAA-9, the SBUV/2 instruments made daily measurements of the Mg II line in the discrete operating mode, which provides improved S/N and wavelength scale stability. "Classical" discrete Mg II index data, using the wavelength positions proposed by Heath and Schlesinger [14], have been discussed by Donnelly [28], DeLand and Cebula [23], and Cebula and DeLand [22]. Other instruments currently producing Mg II index data include UARS SUSIM [29], UARS SOLSTICE [24] and Global Ozone Mapping Experiment [30].

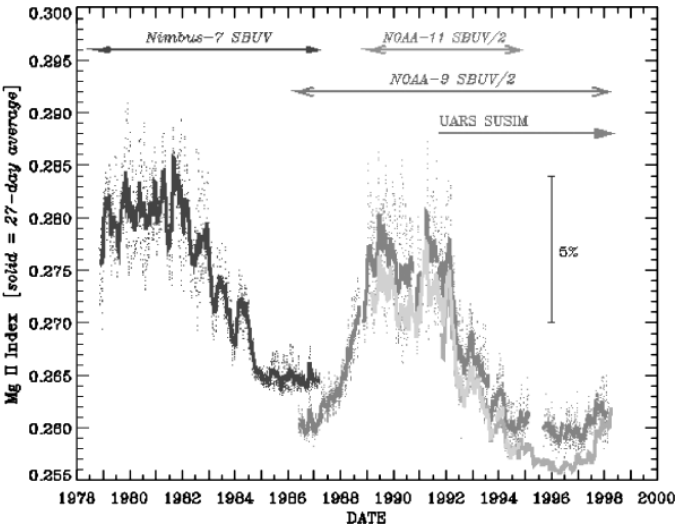

Fig. 16. Variation of the Mg II solar index over 3 solar cycles (21–23) from different measurements (http://ssbuv.gsfc.nasa.gov/solar.html#HS86)

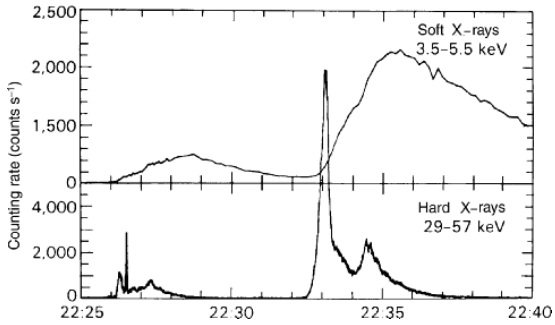

Fig. 17. Time profiles in hard and soft X-rays (from [12])

2.6 EUV/XUV Radiance Variability

This variability is of two kinds. The first one is depending on sporadic explosive events (flares, CMEs, eruptions) and the second one is depending on the full disc activity.

Sporadic events result in a general enhancement of the EUV flux. This is due to the enhancement of the temperature and to the fact that electrons are accelerated in the eruptive events. Therefore, the free–free process is enhanced, and the emission gets larger, by factors that can reach a few hundreds. This is shown in Fig. 17. It shows the time variations of soft and hard X-rays for a flare on November 5, 1980. Time is indicated in minutes, and measurements were made onboard the Solar Maximum Mission (NASA). One sees that the

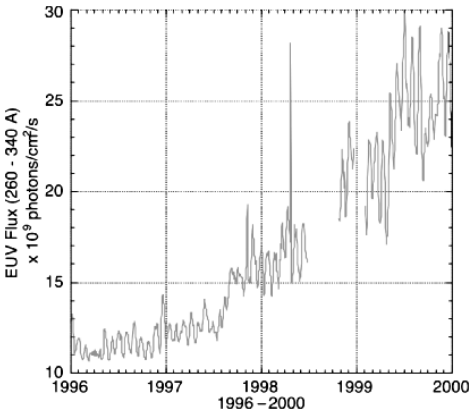

Fig. 18. CELIAS/SEM experiment on the Solar Heliospheric Observatory (SOHO) spacecraft (SOHO is a joint ESA/NASA mission)

impulsive phase of the flare is particularly seen in hard X-rays, while the soft X-rays are enhanced during the expansion phase. The hard X-rays exhibit short bursts at the onset of each soft X-rays enhancement.

The variability depending of the global solar activity can be seen in Fig. 18. It comes from the SEM instrument onboard SOHO [31]. The Solar Extreme Ultraviolet Monitor (SEM) is a transmission grating spectrometer designed to measure the absolute solar EUV flux in the aluminum bandpass region (17–70 nm) at the central order and ± 4 nm about the 30.4 HEII line at the ± first orders (http://www.usc.edu/dept/space_science/sem.htm).

Here, the EUV flux integrated over the spectral range 26–34 nm is plotted over 4 years. 1996 was a period of minimum activity, while the activity was close to its maximum at the end of 2000 (the maximum has been reached in February 2001). One sees that the flux has been multiplied by a factor larger than 2. The large peak in 1998 corresponds to the so-called "Bastille Day event," a large CME occurring on July 14. The oscillations correspond to the solar 27-day rotation. The data gap in 1998 is due to the loss of the spacecraft.

2.7 The UV/EUV/XUV Solar Spectrum Modelling

In the expectation of SEE-TIMED data, most of the current EUV/XUV models rely on few experiments taken onboard the Dynamics Explorer missions [8] and rocket launches. Hinteregger [31] and Hinteregger et al. [32] gave a first representation of Solar EUV fluxes for aeronomical applications. A first reference flux SC#21REF was assembled from measurements performed in July 1976 (F10.7 = 70) and given in 1659 wavelengths. An extrapolation model (SERF 1) allows estimating the flux during other periods of solar activity.

Torr and Torr [33, 34] proposed two reference fluxes for aeronomy called F79050N (F10.7 = 243) and SC#REFW (F10.7 = 68). The UV spectrum was

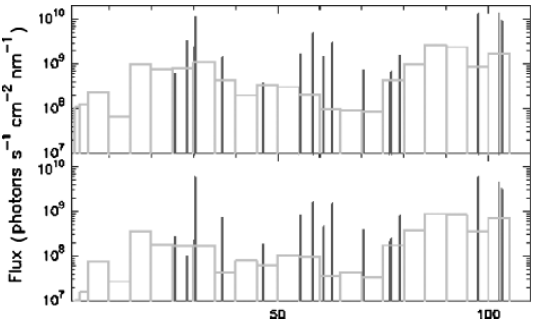

Fig. 19. Reference fluxes proposed by Torr and Torr [34] in 37 boxes. The upper panel shows the flux F79050N (F10.7 = 243) and the bottom panel shows the flux SC#21REFW (F10.7 = 68). The abscissa is the wavelength in nm

divided in 37 bins. Some correspond to the following intense spectral lines: He^{+} and Si^{9+} at 25,63 nm; Fe^{14+} at 28,415 nm; Si^{10+} at 30,331 nm; He^{+} at 30,378/,nm; Mg^{10+} at 36,807 nm; Ne^{6+} at 46,522 nm; O^{5+} at 55,437 nm; He at 58,433 nm; O^{3+}, Mg^{9+} at 60,976 nm; O^{4+} at 62,973 nm; O^{++} at 70,331 nm; N^{3+} at 76,515 nm; Ne^{7+} at 77,041 nm; O^{3+} at 78,936 nm; C^{++} at 97,702 nm; H at 102,572 nm (Lyman β) and finally O^{5+} at 103,191 nm. The Lyman α line at 121,565 nm does not show up because it is not energetic enough to ionize the terrestrial ionozphere. The remaining boxes are representing the mixing of close lines and the continuum. Such a flux is shown in Fig. 19. This work revealed to be extremely useful. One of its qualities was that the authors proposed the corresponding absorption and ionisation cross sections for the major thermospheric species.

Its main limitation is that the measurements do not allow reaching a good estimate of the flux variability for different solar activity conditions. Since then, several authors developed their codes to take better advantage of the AE database. Among them, two must be emphasized.

- Tobiska [35–37] developed a model called EUV, which takes data from other sources into account: SME, OSO; AEROS; rockets and ground-based facilities. This model takes into account the solar emission zone of each line, through a parameter. It proposes a formula to retrieve a solar flux from the gift of the decimetric index and its average. A new version, SOLAR2000, has been recently developed. It uses a new input parameter named E10.7, computed from a previous version of the code [38].
- The second improved model is EUVAC [39]. Its main difference with previous models is the reference flux chosen, and the interpolation formula. The coronal flux is also constrained to be at most 80% of the total.

These models are very important for aeronomic computation. They allow developing a fairly good physics. However, they cannot properly take into account the variability at different wavelengths. Indeed, specific full measure-

ments (e.g., onboard the space shuttle) clearly show that there is no linear variation with the decimetric index. On the contrary, some lines of the solar flux may increase with solar activity or decrease, sometimes drastically.

Finally, Warren et al. [40, 41] have undertaken a radically different approach. They combined a spectral emission line database, solar emission measure distributions, and estimates from ground-based solar images of the fraction of the Sun covered by the various types of activity to synthesize the irradiance. The goal was to give a way to estimate the irradiance from EUV line emission formed in the upper chromosphere and lower transition region from the Ca II K-line through the model. On the basis of this approach, they could derive the emission measure from an average spectrum of the quiet solar disk measured with the Harvard instrument on Skylab and compilations of atomic data ([41] paper I). The irradiance spectrum from 50 to 1200 A was then computed for the quiet Sun, with the contributions of optically thick emission lines and continua included empirically. A comparison with the empirical models described above indicates relatively good agreement among fluxes of emission lines formed in the solar chromosphere and transition region. A factor of typically 2 is found with the fluxes for coronal emission lines.

Models of the Earth's ionosphere and upper atmosphere rely on the solar 10.7-cm radio flux as a surrogate or proxy of the solar short wavelength radiative input. The variation in the 10.7-cm radio flux, however, originates in active regions. Recent studies show that a significant contribution to the short wavelength radiation emission levels comes from the dispersed fields of active regions and weak network. This component of solar activity is not well represented by the 10.7-cm flux. The Ca II K index and He I 1083-nm equivalent width include contributions from active regions, as well as the weaker magnetic structures distributed over the entire surface of the Sun. However, better estimates of the short wavelength radiative emission can be realized by using solar atmospheric models for different activity structures, such as sunspots, plages, active regions, and the network. In addition, understanding the physical basis for the variability and improving the development of reliable proxies are valuable.

The most promising research directed at this problem involves combining semi-empirical atmospheric models. These models fit the spectra of observed spatially resolved solar features. They use databases of line and continuum spectra computed in local thermodynamic equilibrium (LTE) and non-LTE, as appropriate. They analyze the distribution on the solar disk of specific activity features from observations. This procedure yields a synthetic disk image, full-disk spectra, and the absolute full-disk irradiance in selected spectral bands. At the present time, the solar flux models are limited to lines formed at temperatures less than 10^5 K, that is to the chromosphere up to the lower boundary of the transition region. Comparisons of the calculated Lyman alpha irradiance, for example, with that measured by the UARS satellite show an agreement to within about 10%, indicating the potential of this analysis approach.

In the frame of space weather, several questions have to be addressed: what is the contribution of each different zone of the Sun to the global flux? Can we find one index, a mixing of several indexes, or a selection of thin lines (to be monitored) allowing to determine the flux on top of the Earth atmosphere with a much better precision than the decimetric index (and its mean)? Can we forecast the solar flux hours in advance?

3 Second Part: Atmospheric Effects (Earth)

Figure 20 shows that when measured from the sea level, the solar spectrum exhibits a shape quite different from the one studied earlier. In this figure, we show the origin of the absorption in the visible and IR part of the spectrum. This total absorption is such that the total energy at sea level is 1111 $\mathrm{W\,m^{-2}}$ while it is about 1366 $\mathrm{W\,m^{-2}}$ above the atmosphere perpendicularly to the sun. However, a feature immediately shows up: the total extinction of the EU/EUV/XUV part of the spectrum.

This extinction is due to absorption by ozone, molecular oxygen, atomic oxygen, and molecular nitrogen through four main processes: ionization, excitation, dissociation, and excitation. The species responsible for the absorption in the UV/EUV/XUV range are shown in Fig. 21. The photoionization is most efficient above 150 km, and filters the light down to about 80 km. The main

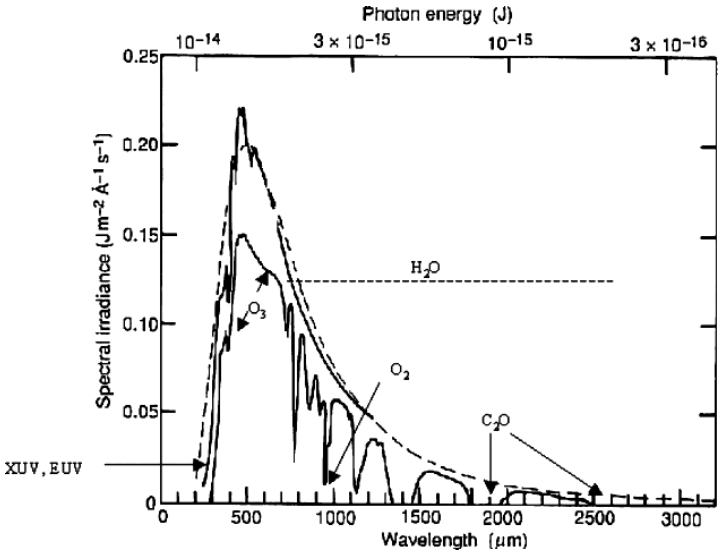

Fig. 20. The solar spectrum at Earth. The responsible for the different absorptions are indicated. The upper full line represents the solar irradiation outside the Earth atmosphere. The lower full line represents the sea-level irradiation in very clear atmosphere. The *dashed line* is the curve for black body at 5,800 K

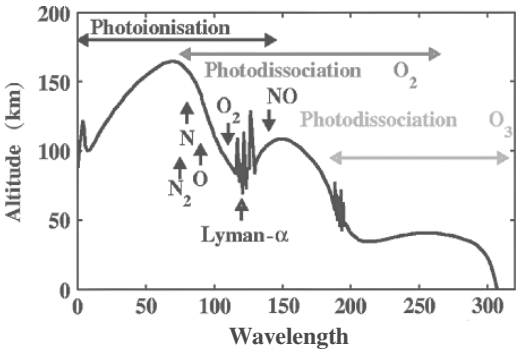

Fig. 21. Penetration of solar ultraviolet and soft X-ray emission in the Earth's atmosphere as a function of wavelength, with principal absorbing gases indicated

species involved are O_2, N_2, and O. Between 70 and 280 nm, the photodissociation of N_2, and O_2 becomes an important or preponderant process. It filters the light down to low altitude, i.e., about 20 km. The near UV is mostly absorbed by dissociation of ozone with a maximum of efficiency around 40 km.

To understand the way this absorption works, and in the frame of this school, it may be not necessary to present the recent sophisticated approach to the creation of the ionosphere. We will present here a theory first proposed by S. Chapman as early as 1931. This theory gave many very good results, and has the advantage of being easily coded.

3.1 Physical Effects

The Chapman Theory

We examine the influence of a monochromatic beam $\Im_\infty$ [photons m^{-2} s^{-1}] on top of the atmosphere. This beam crosses the atmosphere along a straight line, and is continuously absorbed. Let us call s the distance along the trajectory of the beam in the atmosphere. At a given altitude z, the incident beam is absorbed proportionally to the density of the neutral gas $n(z)$, proportionally to the absorption cross section σ_a, and to the incident flux $\Im(s)$ at this point:

$$d\Im(s) = -\Im(s)\sigma_a n(z) ds \tag{1}$$

This equation considers two altitude, z and s. The problem that Chapman had was to link the two. Lets call χ the solar zenith angle. It depends on the day, hour, altitude, and geographic coordinates. This geometry is shown in Fig. 22 in the case of a plane planet, dream of a fool scientist of the middle age.

In this simple case, the relationship between s and z is straightforward:

$$ds = \frac{dz}{\cos\chi} \tag{2}$$

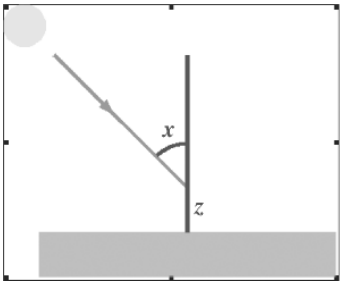

Fig. 22. Propagation of an electromagnetic beam in the atmosphere of an "artificial" flat plane planet (from [42])

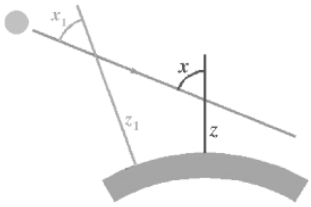

Fig. 23. Propagation of an electromagnetic beam in a more realistic atmosphere (from [42])

However, many experiments as well as theoretical considerations have proven that the planets are usually closer to a sphere than to a plane. In this case, we face a slightly different problem, shown in Fig. 23: the verticals are not parallel, and the solar angles therefore depend on the geographical location.

However, the Sun is as distant to the point $(z\ ,\ \chi)$ as to the point $(z_1\ ,\ \chi_1)$. One can therefore write the simple equation:

$$(R_T + z_l)\sin\chi_l = (R_T + z)\sin\chi \tag{3}$$

where R_T represents the earth radius. From (2) written in $(z_1\ ,\ \chi_1)$, we can deduce

$$ds = \frac{dz_1}{\sqrt{1 - \left(\frac{R_\tau + z}{R_\tau + z_1}\right)^2 \sin^2\chi}} \tag{4}$$

Equation (4) reduces to (2) when the solar zenith angle is smaller than 60°. We usually note $\sec\chi(z_1)$ the square root of the above expression:

$$\sec\chi(z_1) = \frac{1}{\sqrt{1 - \left(\frac{R_\tau + z}{R_\tau + z_1}\right)^2 \sin^2\chi}} \tag{5}$$

We can then simply express the relationship between s and z through

$$ds = \sec\chi(z_1)dz_1 \tag{6}$$

And therefore, the variation of the solar flux versus the altitude becomes

$$\Im(z_1) = -\Im(z_1)\sigma_a n(z_1) \sec\chi(z_1) dz_1 \tag{7}$$

Many attempts have been made to define a still more accurate formulation (in particular, when χ is close to or larger than 90°) [43–45]. In a generic manner, any new formulation is called a "Chapman" function, and usually noted Ch (x, χ). Nowadays, it is not necessary anymore to reach an exact formulation because the correct value can be numerically computed. However, to keep in mind the problem of the geometric projection, (7) is still written as

$$\Im(z_1) = -\Im(z_1)\sigma_a n(z_1) \mathrm{Ch}(z_1.\chi) dz_1 \tag{8}$$

The next problem that Chapman had was to characterize the neutral atmosphere without having access to space experiment data. The usual way to consider the atmospheric gas is to write the hydrostatic equilibrium, which allows to define the scale height $H_\mathrm{n}{=}\frac{K_\mathrm{B}T}{\mathrm{mg}}$, where k_B is the Boltzmann constant, m the mass of the considered particle (or the mean mass of the air), T its temperature, and g the gravity. Chapman considered an isothermal atmosphere with a single species. Its density varies with altitude, but is independent of the latitude as well as the longitude. In the altitude range that we consider here, we neglect the variation of the gravity. The density decreases exponentially as

$$n(z) = n_n^o \, e^{-\frac{z-z_0}{H_n}} \tag{9}$$

where z_o is the reference altitude where $n = n^{o,n}$. With these assumptions, one can integrate (8):

$$\mathrm{In}\frac{\Im_\infty}{\Im(z)} = \sigma_a n_n^o \int_z^\infty \sec\chi(z_1) e^{-\frac{z_1-z_0}{H_n}} dz_1 \tag{10}$$

At small angles, $\sec\chi(z) = \frac{1}{\cos\chi}$ and this becomes

$$\mathrm{In}\ \frac{\Im_\infty}{\Im(z)} = \sigma_a n_n^o \frac{H_n}{\cos\chi} e^{-\frac{z-z_0}{H_n}} \tag{11}$$

We define the optical depth τ as being

$$\tau = \sigma_a n_n^o \frac{H_n}{\cos\chi} e^{-\frac{z-z_0}{H_n}} \tag{12}$$

so that we finally can write the intensity of the beam at altitude z as a simple Berr–Lambert law:

$$\Im(z) = \Im_\infty e^{-\tau} \tag{13}$$

The altitude at which $\tau = 1$ defines the penetrating depth of the beam.

Once the intensity is computed, it was possible to examine the effect on the atmosphere. The absorption cross section σ_a is the sum of the ionization

cross section σ_i, the excitation cross section σ_{exc}, and the dissociation cross section σ_{dis}. Lets call p any of these 3 processes. In the atmosphere, almost all the ionizations create single charged ions. The electron production rate is then simply

$$P(z) = \sigma_i n(z) \Im(z) \tag{14}$$

Or

$$P(z) = \sigma_i n_n(z) e^{-\tau} \Im_\infty \tag{15}$$

At low solar angle, one gets

$$p(z) = \sigma_i n_n^o \exp\left\{ -\frac{z - z_o}{H_n} - \frac{\sigma_a n_n^o H_n}{\cos\chi} e^{-\frac{z-z_o}{H_n}} \right\} \Im_\infty \tag{16}$$

which becomes with (12)

$$P(z) = \frac{\xi \cos\chi}{H_n} \Im_\infty \tau e^{-\tau} \tag{17}$$

The reference altitude z_o is usually chosen as the altitude at which the optical depth equals 1 when the Sun is at zenith. For a zenithal Sun ($\chi = 0$), we can then write

$$\sigma_a n_n^o H_n = 1 \tag{18}$$

so that the production becomes

$$P(z) = P_o \exp\left\{ 1 - \frac{z - z_o}{H_n} - \frac{1}{\cos\chi} e^{-\frac{z-z_0}{H_n}} \right\} \tag{19}$$

where P_o is the maximum ion production for a zenithal Sun. This relation defines a production called the "Chapman production function." When normalized to P_o, this function is represented in Fig. 24. One sees that the maximum increases and its altitude decreases when the Sun goes from large zenith angles to zenithal position.

Above the altitude of the maximum, we have $\frac{z-z_0}{H_n} \gg 1$ so that the production becomes

$$P(z) = P_o e^{-\frac{z-z_o}{H_n}} \tag{20}$$

It decreases as an exponential function of the scale height of the neutral species. Once the production is computed, Chapman had still to retrieve the electron density. A simple chemical model considers only the electronic recombination. It turns out that such a model is relatively correct between 90 km and 200 km. This recombination is described by a efficiency coefficient α. The loss L is

$$L = -\alpha n_e^2 \tag{21}$$

At photoequilibrium, the losses equal the production so that the electron density can be deduced from

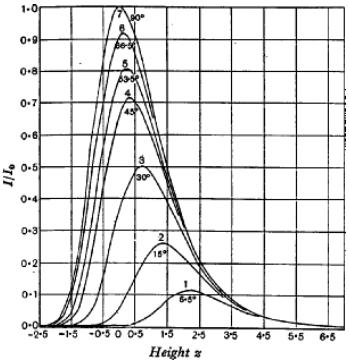

Fig. 1. Ion-production at noon for various values of (θ + δ)

Fig. 24. Chapman production fonction normalized versus altitude $((z - z_0)/H_n)$at different solar zenith angles. This is the original plot published by Chapman in 1931. The convention for the zenith angle was the opposite of today's convention, with 90° being the angle at zenith [46, 47]

$$n_e(z) = \sqrt{\frac{P_o}{\alpha}} \exp \frac{1}{2} \left\{ 1 - \frac{z - z_o}{H_n} - \frac{1}{\cos \chi} e^{-\frac{z - z_0}{H_n}} \right\} \tag{22}$$

This (quite) simple equation defines an atmospheric layer where there is permanently a population of ions and electrons. This layer does not fully reproduce the exact ionosphere, and is referred to as the "Chapman layer." However, it explains many features of the measurements. It explains, for example, why the maximum of electron density depends on the local time. This maximum is reached when $\tau = 1$. Its value is therefore

$$n_e^{\max} = \sqrt{\frac{\xi \cos \chi}{\alpha e H_n} \Im_\infty} \tag{23}$$

At a given solar zenithal angle, the altitude of the maximum is given by

$$\frac{dP(z)}{dz} = 0 \tag{24}$$

From (19), it comes

$$\cos \chi = e^{-\frac{z - z_0}{H_n}} \tag{25}$$

or

$$z = z_o + H_n \log(\cos \chi) \tag{26}$$

The altitude of the maximum therefore varies in the same direction than the solar zenith angle as in Fig. 24.

Limitations of the Chapman Theory

This theory has proven to be very useful and allows getting a rough idea of the ionosphere. However, the ionosphere is not as simple as a single electron

production layer. To describe fully its formation, it is necessary to make more realistic assumptions and to develop a theory on the basis of transport phenomena. Such a theory will not be developed here, because it is not necessary in the frame of space weather. Readers can refer to Lilensten [48, 49] or to Schunk and Nagy [50]. The following points have to be addressed in a full approach:

The neutral atmosphere has to be considered as a multicomponent atmosphere. It varies versus the solar UV flux studied in the first part of this chapter. Most of the present models use F10.7 or Mg II as proxies. MSIS [51] is the most commonly used in the research thermospheric community. The Drag Temperature Model (DTM, [52, 53]) is used and developed by the French space agency CNES. They are based on a large set of data, physics and statistics. However, no statistical model can reproduce exactly the true ionosphere at a given time because several sources of variations are very variable. Figure 25 shows the vertical profiles of the neutral atmosphere between ground and 600 km from the MSIS model. It represents the atmosphere at 45° of north latitude, at the beginning of April. The left panel shows the particle densities and the right panel shows the temperature. The full lines correspond to a low solar activity (F10.7 = 80) and the dashed lines to a strong solar activity (F10.7 = 300). One sees that the exospheric temperature increases from 880 K to 1580 K while the neutral densities are enhanced above about 100 km by factors of 100 at 600 km.

- The Chapman theory considers only constant cross sections. In reality, the photoabsorption cross sections are strongly dependent on the wavelength, as shown in Fig. 26.

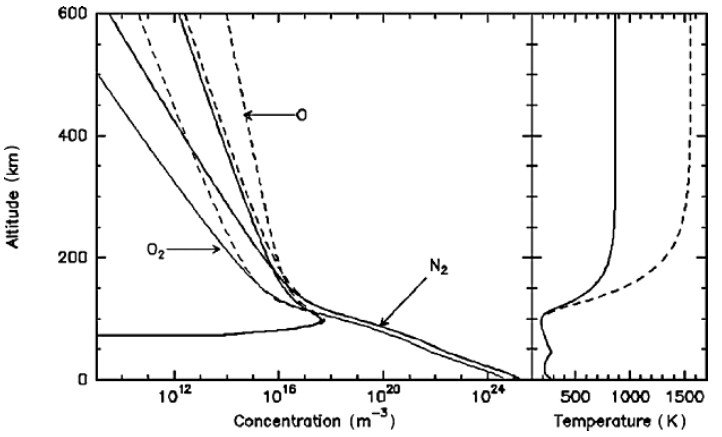

Fig. 25. Vertical profile of the neutral atmosphere from the MSIS model

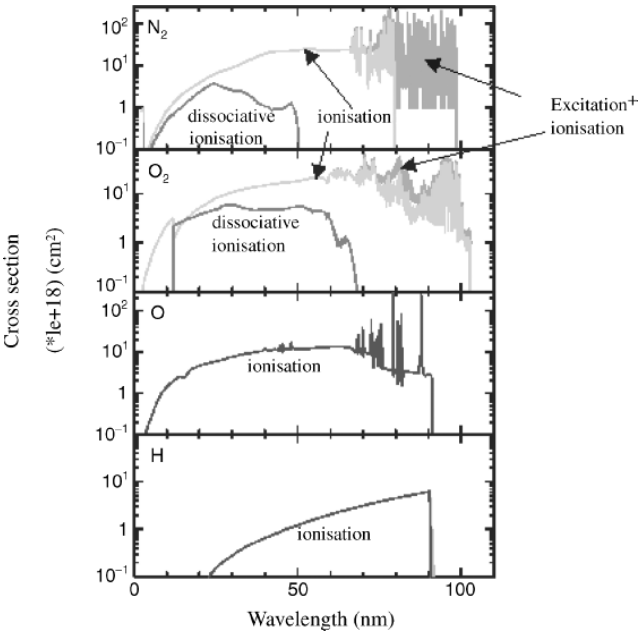

Fig. 26. Absorption cross sections (y axis) versus the incident wavelength (x axis) in nm

- The Chapman theory does not consider the variations of the solar flux at each wavelength. This has been studied in the first part of this chapter.
- One must also take into account the fact that the photoelectrons created by solar photoionization are themselves energetic particles. They create a secondary production through collisions, which is of the order of 30% of the primary one above about 180 km, but may reach three times the primary one below this altitude [54].

The full theory allows to compute the electron flux at each altitude, as well as the electron and ions production (N_2^+, O_2^+, O^+, N^+, H^+ et He^+). In the frame of space weather, the ion composition is not an important parameter. However, in view of the first part of this chapter, it is interesting to indicate that the EUV continuum contributes to approximately 50% of the electron production, the other 50% coming from the discrete lines (Fig. 27).

In Fig. 28, we have plotted the effect that each of the line referred in the Torr model (see above) has on the electron production in the atmosphere.

The values of the productions depend, of course, on the solar activity. However, it is obvious that the Lyman-β (102,572 nm) plays the preponderant role around 100 km, since it creates by itself about 40% of the line production (and therefore about 20% of the total production). Between 150 and 400 km, He II is responsible for about 20% of the line production. The other important lines are HeI and CIII.

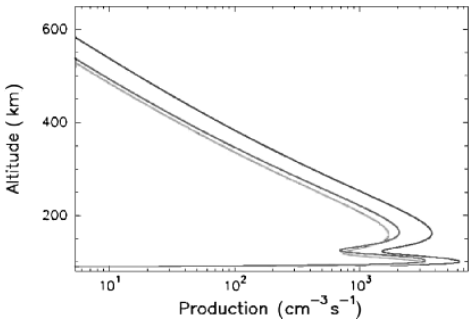

Fig. 27. Electron production due to the continuum (lowest production at upper altitude) and sum of the discrete lines. The sum of the two productions is also plotted

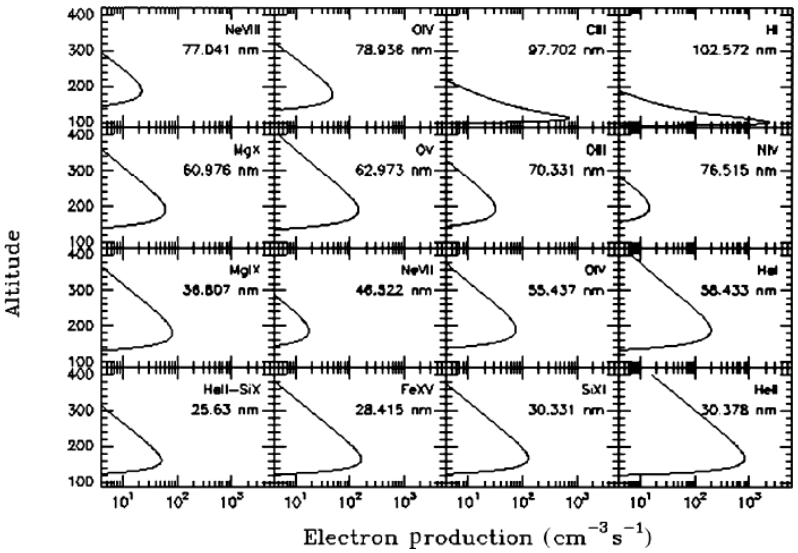

Fig. 28. Electron production due to the separate EUV lines for a mean solar activity

This electron and ion production has several consequences important in the frame of space weather:

– When the electrons produced have energies smaller than about 10%, friction with the neutral atmosphere produces heating. This heating rate is balanced by several cooling rates of chemical or physical origins. The physical cooling rates can be inelastic (collisions) or elastic. This latter case concerns mostly the rotational and vibrational excitations of N_2 and O_2, the fine structure excitation of O, the electronic excitation of all the neutral constituents. The balance results in an enhancement of the temperature up to the values shown in Fig. 25 and in a dilatation of the neutral atmosphere. Because

of the large temperatures, the neutral atmosphere at altitude above about 80 km is called the thermosphere. Finally, the transport of the particles has to be taken into account in the energy budget of the atmosphere.

– Chemical reactions among the neutral atmosphere, the electrons, and the ions result in the existence of a permanent population of ions and electrons. This part of the atmosphere is called the ionosphere so that the atmosphere at upper altitude is the sum of two mixed components, the thermosphere and the ionosphere. The ionosphere has been divided in different regions summarized in Table 3. The chemical scheme around 120 km is represented in Fig. 29. It creates the ion NO^+, which becomes the major ion around 160 km, while the NO neutral parent is only a very minor constituent of the the-mosphere. Finally, the diffusion process and the thermal velocities have also to be taken into account in a full model of the thermosphere.

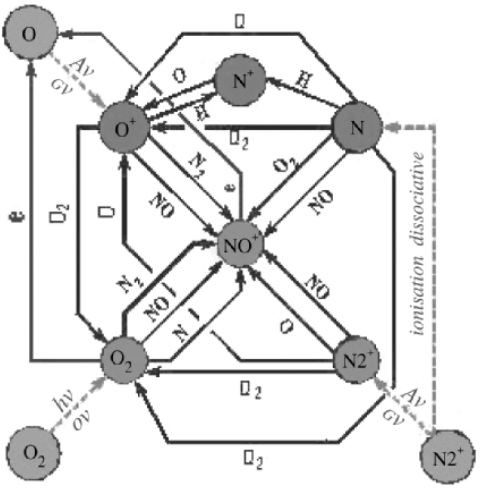

Fig. 29. Ion chemistry in the ionosphere; hν stands for photoionization

The main characteristics of the ionosphere are summarized in Table 3.

Two other effects of the EUV on the atmosphere are worth to be mentioned here.

– *Dissociation*: Effects in the thermosphere and in the ozone layer (EUV, UV). The ozone problem is only to be mentioned, since it is discussed in another chapter.
– *Excitation*: The atmosphere is left in possible excited states through electronic collisions and/or photoexcitation. This results in particular in two bright airglows from the atomic oxygen: the green line (557.7 nm) which peaks around 100 km and the red line (630 nm) which peaks around 250 km.

Table 3. The different regions of the ionosphere

Altitude (km)	75	100	150	200	400	800	1200	3000
Région	D	E	F1	F2		F sup		
n_n [m^{-3}]	10^{21}	10^{18}	510^{16}	810^{15}	10^{14}	10^{12}	210^{11}	10^{10}
n_e/n_n	10^{-12}	310^{-9}	410^{-6}	10^{-4}	410^{-3}	410^{-2}	10^{-1}	1
T_e	200	200	600	1500	2500	3000	3200	3500
T_i	200	200	700	800	1000	2500	3000	3400
λ_D [cm] (Debye)	3	$0,6$	$0,4$	$0,3$	$0,5$	$1,7$	$2,7$	$4,4$
λ_{Ne} [cm] (lpm)	3	310^2	$6,410^4$	410^5	310^7	310^9	$1,610^{10}$	310^{11}
v_e [cm.s^{-1}]	110^7	110^7	210^7	$2,510^7$	310^7	$3,510^7$	$3,710^7$	410^7
λ_{Be} [cm] (Larmor)	$1,2$	$1,2$	$2,5$	$3,3$	$4,3$	$6,4$	$8,0$	$16,2$
ν_e[s^{-1}] (gyrofréq.)	$1,3\ 10^7$	$1,3\ 10^7$	$1,3\ 10^7$	$1,2\ 10^7$	$1,1\ 10^7$	$8,7\ 10^5$	$7,4\ 10^5$	$3,9\ 10^5$
ν_{ne}[s^{-1}] (coll.)		10^5	10^3	130	20			
v_i [cm.s^{-1}]	310^4	410^4	810^4	$1,210^5$	$1,410^5$	210^5	410^5	110^6
λ_{Bi} [cm] (Larmor)	$3,510^2$	$2,810^2$	$4,010^2$	$5,110^2$	$6,210^2$	$6,610^2$	$6,310^2$	$8,610^2$
ν_i[s^{-1}] (gyrofréq.)	$13,6$	$22,7$	$31,8$	$37,4$	$35,9$	$48,2$	101	$1,910^2$
ν_{ni}[s^{-1}] (coll.)		610^3	30	4	$0,5$			

3.2 Some Effects Relating to Space Weather

The Drag: A Thermospheric Process

When an object (spacecraft, debris ...) travels through an atmosphere, it experiences a drag force in a direction opposite to the direction of its motion. In a first simple approach, this drag force is given by

$$D = \frac{1}{2}\rho v^2 A\mathrm{Cd} \tag{27}$$

where r is the thermospheric density, v the satellite speed, A the satellite cross-sectional area and Cd is a drag coefficient of the order of 2.

The reduction in the period P due to atmospheric drag is given by

$$\frac{\mathrm{d}p}{\mathrm{d}t} = -3\pi a\rho\frac{A\mathrm{Cd}}{m} \tag{28}$$

where a is the semimajor axis and m the mass of the satellite.

The evaluation of the drag force is conditioned by the knowledge of the thermosphere density. This usually comes from a model. The sources of variations of the thermosphere are mainly X-rays and EUV fluxes, particle precipitation, and E fields. The physical processes involved are photoabsorption, particle collisions, Joule heating, and frictional heating. For space weather,

the main consequences (among other phenomena) are a dilatation of the thermosphere: density may increase by a factor of 10 at the altitude of the International Space Station.

It is of prime importance to realize that most of the perturbation sources are badly known, monitored, predicted, and modelled. It is the case for X-rays and EUV fluxes [34, 36, 37, 39, 41] and for particle precipitation [55]. Thanks to the Superdarn facility, the knowledge of the electric field has been improved in the recent years (http://superdarn.jhuapl.edu/map/index.html). However, this measurement depends on the presence of irregularities in the ionosphere. When there is no irregularities, a model is used to fill the gaps. A second limitation is that the Superdarn facility covers 18 MLT, and there is a need for global coverage. Finally, Superdarn is in several aspects a research tool, and for being used in Space Weather, data accessibility must still be improved.

It is therefore not surprising that the models fail in reproducing the real-time atmosphere, especially at high latitude and during magnetic perturbations. This implies a large uncertainty on the position of the spacecraft, summarised in Table 4.

Since the actual goal is to reach a precision of 20 km after 24 h, there is a necessity of a permanent monitoring and adjustment of the drag equation through neutral atmosphere models. Several methods are used.

Table 4. Uncertainties (in km) on the position of a LEO after x days of initial time for uncertainties on the thermosphere density of 5%, 10%, 15%, and 20% [56]

Days since epoch	± 5%	± 10%	± 15%	± 20%
1	5	22	33	43
2	46	91	137	182
5	280	559	839	1120
10	1261	2516	3750	5000

A "Proxy" Approach

Use of indices: Do remain basic data in Space Weather. Several exist to monitor the solar activity and the EUV flux variation or the geomagnetic activity at different scales. They are still impossible to bypass for long-term studies. Better indices with better space and time coverage are needed in several applications. To keep long records (past and future) of geophysical evolution, any Space Weather program should continue the monitoring of the main indices.

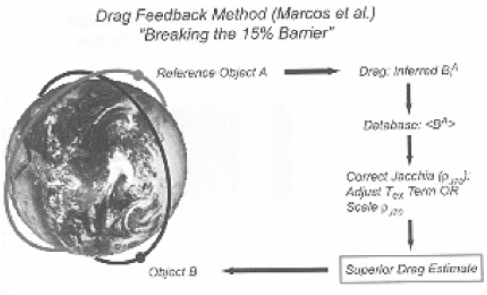

Fig. 30. Technological approach to estimate the thermospheric drag [56]

A "Technological" Approach

An example is given in Fig. 30 (from Marcos et al., reported in [56]). Here, a reference object is used to estimate the thermospheric drag, which then feeds the drag equation for the other spacecrafts.

"Physical" Approaches

The physical approaches consist in feeding the models with observations. The observations are of different kinds

UV airglow monitoring [56]: A spacecraft observes the airglow over a large scale. The thermosphere is adjusted in glow model until computation fits the observations. This is a ground operation, made in the US in the 55th squadron for Space Weather.

Temperature monitoring: Here, the neutral exospheric temperature is measured and compared to the exospheric temperature given by empirical models.

The adjustment is made directly on the models, without the necessity of an additional modelling (like the airglow in the example above). The total density is then extracted from the model to calculate the drag force. Since the end of 1991, the Earth' s upper atmosphere winds and temperatures are observed by the Wind Imaging Interferometer (WINDII) onboard the Upper Atmosphere Research Satellite (UARS) [58, 59]. Figure 31 [57, 60] displays temperature measurements along successive orbits for a very active day of the WIND II data base (February 26, 1992, ap = 65). The 3 h ap values corresponding to each orbit are indicated on the figure with the orbit number: they range from 22 for orbit 6 to 207 for orbits 11 and 12. A corresponding dramatic increase of the northern auroral latitude temperatures is observed. This increase is also present at lower latitudes, but it starts only for orbit 12. This corresponds to a time delay greater than 3 h with the auroral latitude increase. At 20° south latitude, the observed increase in temperature is already very large.

The bottom panel shows the corresponding MSIS-90 temperatures. What is important to note is that the variations of the model temperatures agree

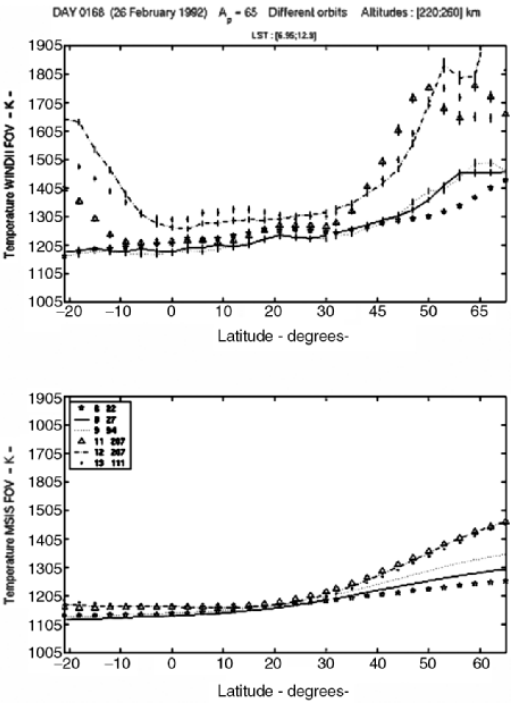

Fig. 31. Latitude/local time variations of the temperature measured by the WINDII interferometer onboard the UARS spacecraft, averaged between 220 and 260 km altitude, for 6 orbits on February 26, 1992. The *upper panel* shows WINDII temperatures, while the *bottom panel* shows the MSIS-90 ones [57]

qualitatively with the observations but not at all quantitatively. Such a behavior is common for each magnetic active day of the database. The temperature variations associated to magnetic activity are always underestimated, while the temperature variations associated to solar activity are much better estimated as shown in [57].

This approach is still very promising, but necessitates an improvement of the empirical models to better reproduce the atmospheric variations due to magnetic activity. The use of the two proxies F10.7 and kp (or ap) is not sufficient to reach this goal (Lathuillère, personal communication).

Use of the ionosphere as a tracer of the thermosphere: In this case, one may use ionospheric profiles measured by incoherent scatter radars [61] or integrated parameters such as the Total Electron Content [42]. In Fig. 32, one shows such an example. The Total Electron Content has been fitted by an ionospheric model where the oxygen density is multiplied by a factor f. The advantage of this method is that it requires routinely measurements (TEC are obtained in real time and at a planetary scale through GPS constellation spacecraft). The disadvantage is that it requires an ionospheric model, which

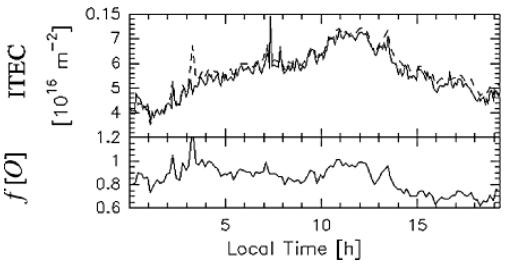

Fig. 32. The *upper panel* shows the ITEC (i.e., total electron content integrated up an altitude lower than the upper boundary of the ionosphere, here up to 500 km) by the EISCAT incoherent scatter radar in Tromso (full line). The *dashed line* is the fit obtained when a correction factor $f[O]$ is used in the neutral atmosphere model [42]

also depends on other parameters (solar EUV and particle precipitation). Finally, the fit of a single integrated parameter such as the TEC does not give a unique solution, and the method must be improved with the use of a second type of observation.

Combined methods are, of course, possible, such as incoherent scatter, plus visible airglow (red and green lines of the atomic oxygen) [62].

Telecommunication and Positioning: Ionospheric Processes

When a wave crosses through the ionosphere, it experiences several phenomena: scattering, absorption, faraday rotation [63]... Its wave number is related to the pulsation of the wave through the optical index. The optical index is a complex number, which is a function of the plasma pulsation, the collision frequency, and the pulsation of the wave. Therefore, it is strongly dependent on the electron density and also on the thermospheric composition.

The sources of variation of the ionosphere are the same as for the thermosphere, i.e., X-rays and EUV fluxes, particle precipitation, and E fields. An additional source is the physical link with the exosphere, in particular with the protonosphere. The physical processes involved are slightly different. They are photo-ionization, particle collision ionization, currents, and frictional heating. They result (among other phenomena) in rapid variations and creations of small-scale disturbances (blobs, patches, and scintillations...). Then, the models (physical, profilers, TEC derived from GPS...) fail in reproducing the real-time ionosphere, especially at high latitude and during solar events [42, 64, 65]. Like for the thermosphere, there is a necessity of a permanent monitoring and adjustment of the equations. The strategies are the same: Proxy, physical (topside sounders...). However, the ionosphere is somehow more accessible from ground than the thermosphere, which offers some additional opportunity to calibrate the models. As an example, we show thereafter a comparison between the EISCAT incoherent radar electron density profiles, and the results of a model. Developed under the auspices of the

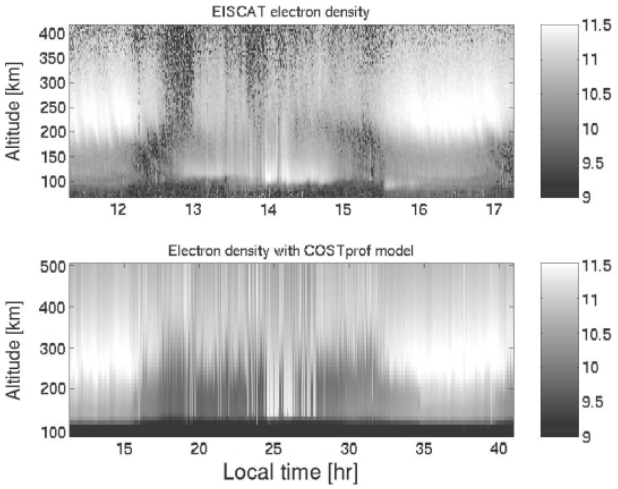

Fig. 33. Comparison between the electron density profiles obtained by the EISCAT incoherent radar (*top panel*) and the profiler COSTprof (*bottom panel*) [67]

European action COST 251, the European profiler COSTprof [66] has been fed here with NmF2 and hmF2 deduced from EISCAT measurements (Fig. 33).

In a large scale, this approach would necessitate a network of ionosondes.

Space Weather Versus Classical Weather

These domains are the subjects of specific papers in these proceedings, and are cited here only to recall that the Earth atmosphere can hardly be spitted in independent layers.

Geophysical and historical records show that mankind already experienced several climatic or meteorological changes. Several phenomena contribute to these changes. Some may be related to space weather:

- Impact of the solar constant and solar energy [68, 69]
- Impact of the cosmic rays: condensation nucleus [70–72]
- Impact of the greenhouse gazes: falling sky theory [73]
- Impact of upper lightning: red sprites, blue jets, elves [74].

The two last at least may be directly related to the thermospheric and ionospheric processes.

References

1. der K. Denkschriften: Acad. Der Wissenschaften su München, 1814–1815, pp. 193–226

2. J.R. Tobiska: Space environment (natural and artificial) – process for determining solar irradiances, ISO/TC/20/SC 14 N 184, WD 21348 (2002)
3. G. Thuiller, M. Hersé, P.C. Simon, D. Labs, H. Mandel, D. Gillotay: *Solar Phys.* **171**, 283–302 (1997)
4. G. Thuiller, M. Hersé, P.C. Simon, D. Labs, H. Mandel, D. Gillotay, T. Foujols: *Solar Phys.* **177**, 41–61 (1998)
5. E. Nesme-Ribes, G. Thuillier: Histoire solaire et climatique, ed Belin pour la science, ISBN 2 7011 1966 9 (2000)
6. T.N. Woods, S. Bailey, S.C. Solomon, G.J. Rottman: *SPIE Proce.* **1745**, 140–148 (1992)
7. S.M. Bailey, T.N. Woods, L.R. Canfield, R. Korde, C.A. Barth, S.C. Solomon, G.J. Rottman: *Solar Phys.* (in press)
8. H.E. Hinteregger, D.E. Bedo, and J.E. Manson: *Radio Sci.* **8**, 349–354 (1973)
9. G. Schmidtke, T.N. Woods, J. Worden, G.J. Rottman, H. Doll, C. Wita, S.C. Solomon, Solar EUV irradiance from the San Marco ASSI – A reference spectrum, *Geoph. Res. Lett.*, **19**, 2175–2178, (1992)
10. S.W. Simon, P.H. Seagraves, R. Tousey, J.D. Purcell, R.W. Noyers: *Solar Phys.* **39** (1974)
11. P. Lantos: Le soleil en face, Masson ed., ISBN 2 225 83054 1 (1997)
12. K.J.H Phillips: *Guide to the Sun* (Cambridge University Press, ISBN 0 521 39788 X, 1995)
13. A. Tartag, Y. Bénilan, D. Samain, G. Thuillier, P. Bruston: *Solar Phys.* **201**, 253–269 (2001)
14. D.F. Heath, B.M. Schlesinger: *J. Geophys. Res.* **91**, 8672–8682 (1986)
15. R.P. Cebula, M.T. DeLand, B.M. Schlesinger: *J. Geophys. Res.* **97**, 11613–11620 (1992)
16. Delaboudinière et al. (27 authors): *Solar Phys.* **162**, 291 (1996)
17. M. Arnaud, J.C. Raymond: *Astroph. J.* 394–406 (1992)
18. M. Arnaud, R. Rothenflug: *Astronomy Astroph.* **60**, 425–457 (1985)
19. K. Wilhelm, W. Curdt, E. Marsch, U. Schühle, P. Lemaire, A. Gabriel, J.C. Vial, M. Grewing, M.C.E. Huber, S.D. Jordan, A.I. Poland, R.J. Thomas, M. Kühne, J.G. Timothy, D.M. Hassler, O.H.W. Siegmund: *Solar Phys.* **162**, 189–231 (1995)
20. J.M. Pap, C. Fröhlich: *J. Atmospheric Solar–Terrestrial Phys.* **61**, 15–24 (1999)
21. L.A. Hall, G.P. Anderson: *Ann. Geophys.* **6**, 531–534 (1988)
22. R.P. Cebula, M.T. DeLand: *Solar Phys.* **177**, 117–132 (1998)
23. M.T. DeLand, R.P. Cebula: *Solar Phys.* **152**, 61–68 (1994a)
24. G. De Toma, O.R. White, B.G. Knapp, G.J. Rottman, T.N. Woods: *J. Geophys. Res.* **102**, 2597–2610 (1997)
25. O.R. White, G. de Toma, G.J. Rottman, T.N. Woods, B.G. Knapp: *Solar Phys.* **177**, 89–103 (1998)
26. M.T. DeLand, R.P. Cebula: *J. Geophys. Res.*, **98**, 12809-12823, (1993)
27. M.T. DeLand, R.P. Cebula: Changes in photochemically significant solar UV spectral irradiance as estimated by the composite Mg II index and scale factors *Ozone in the Troposphere and Stratosphere* ed by R. D. Hudson (NASA CP-3266, 1994b) pp. 927–930
28. R.F. Donnelly: *Adv. Space Res.* **8**, 777–780 (1988)
29. L.E. Floyd, P.A. Reiser, P.C. Crane, L.C. Herring, D.K. Prinz, G.E. Brueckner: *Solar Phys.* **177**, 79–87 (1998)

30. M. Weber, J.P. Burrows, R.P. Cebula: *Solar Phys.* **177**, 63–77 (1998)
31. H.E. Hinteregger: *Adv. Space Res.* **1**, 39–52 (1981)
32. H.E. Hinteregger, F. Katsura: *Geophys. Res. Lett.* **8**, 1147–1150 (1981)
33. M.R. Torr, D.J. Torr: *Geoph. Res. Lett.* **6**, 771–774 (1979)
34. M.R. Torr, D.J. Torr: *J. Geophys. Res.* **90**, 6675–6678 (1985)
35. W.K. Tobiska: *J. Atmos. Terr. Phys.*, **53**, 1005–1018 (1991)
36. J.R. Tobiska, Eparvier, EUV 97: *Sol. Phys.* **177**, 147–159 (1998)
37. J.R. Tobiska, Eparvier: *Geoph. Res. Lett.* **6**, 771–774 (1998)
38. Tobiska et al.: (2000)
39. P.G. Richard, Fennelly, D.J. Torr: *J. Geophys. Res.* **99**, 8981–8992 (1994)
40. H.P. Warren, J.T. Mariska, J. Lean, W. Marquette, A. Johannesson: *Geoph. Res. Lett.* **23**, 2207–2210 (1996)
41. H.P. Warren, J.T. Mariska, J. Lean: *J. Geoph. Res.* **103**, 12077–12089 (1998)
42. J. Lilensten, P.L. Blelly: *JASTP* (2002)
43. S. Chapman: *Res. Notes* (1953)
44. Smithe and Smith: *J. Geophys. Res.* **77**, 3592–3597 (1972)
45. A.E.S. Green, Lindenmeyer, Griggs: Molecular absorption in planetary atmosphere, *J. Geophys. Res.* **69**, 493–504 (1964)
46. S. Chapman: *Proc. Phys. Soc.* **43**, 26–45 (1931)
47. S. Chapman: *Proc. Phys. Soc.* **43**, 483–501 (1931)
48. J. Lilensten: Kinetic/fluid approaches coupling: application to the Dynamics of the high latitude ionosphere, ERCA vol 3, 317–336, C. Boutron ed., EdP Sciences (1999)
49. J. Lilensten et, P.L. Blelly, Du Soleil à la Terre, aéronomie et météorologie de l'espace: collection Grenoble Sciences, EDP Sciences, ISBN 2 86883 467 1, (2000)
50. R.W. Schunk, A.F. Nagy: *Ionospheres* (Cambridge University Press, ISBN 521 63237 4, 2000)
51. A.E. Hedin: *J. Geophys. Res.* **96**, 1159 (1991)
52. F. Barlier, C. Berger, J.L. Falin, G. Kockarts, G. Thuillier: *Ann. Geophysicae* **34**, 9–24 (1978)
53. C. Berger, R. Biancale, M. Ill, F. Barlier: *J. Geodesy* **72** (1998)
54. J. Lilensten, W. Kofman, J. Wisemberg, E.S. Oran, C.R. DeVore: *Ann. Geophysicæ* **7**, 83–90 (1989)
55. D.A. Hardy, M.S. Gussenhoven, E. Holeman: *J. Geophys. Res.* **90**, A5, 4229–4248 (1985)
56. A.C. Nicholas, J.M. Picone, S.E. Thonnard, R.R. Meier, K.F. Dymond, D.P. Drob: *JASTP* 1317–1326 (2000)
57. C. Lathuillère, W. Gault, B. Lamballais, Y.J. Rochon, B. Solheim: *Ann. Geophys.* **20**, 203–212 (2002)
58. C.A. Reber, C.E. Trevathan, R.J. McNeal, M.R. Luther: *J. Geophys. Res.* **98**, 10643–10647 (1993)
59. G.G. Shepherd, G. Thuillier, W.A. Gault, B.H. Solheim, C. Hersom, J-F. Brun, P. Charlot, D.-L. Desaulniers, W.F.J. Evans, F. Girod, D. Harvie, E.J. Llewellyn, R.P. Lowe, I. Powell, Y. Rochon, W.E. Ward, R.H. Wiens, J. Wimperis: *J. Geophys. Res.* **98**, 10725–10750 (1993)
60. C. Lathuillère, Thermospheric neutral response to geomagnetic activity: an overview of the results obtained by the WINDII experiment onboard UARS, SOLSPA proceedings, (2002)
61. P-L Blelly, J. Lilensten, A. Robineau, J. Fontanari, D. Alcaydé: *Ann. Geophysicæ* **14**, 1375–1390 (1996)

62. O. Witasse, J. Lilensten, C. Lathuillere, P.L. Blelly: *J. Geophys. Res.* **104**, 24639–24655 (1999)
63. J.L. Leroy, La polarisation de la lumière et: l'observation astronomique, Gordon and Breach ed., ISBN 90 5699 **111** 6 (1998)
64. N. Jakowski, S. Schlüter, E. Sardon: *J. Atmos. Sol-Terr. Phys* **61**, 299–307 (1999)
65. N. Lunt, L. Kersley, G.J. Bailey: *Radio Sci.* **34**, 735–732 (1999)
66. G. Hochegger, B. Nava, S.M. Radicella, R. Leitinger: *Phys. Chem. Earth'* **25**, 307–310 (2000)
67. Lilenslen and Cander: (2002)
68. E. Friis-Cristensen, K. Lassen: *Science* (1991)
69. K. Lassen, E. Friis-Cristensen: *J. Atmospheric Terrestrial Phys.* **57** (8), 835–845 (1995)
70. H. Svensmark, E. Friis-Christensen: *J. Atmospheric Solar–Terrestrial Phys.* **59**, 1225–1232 (1997)
71. H. Svensmark, E. Friis-Christensen: *J. Atmospheric Solar–Terrestrial Phys.* **62**, 79–80 (1999)
72. H. Svensmark, Cosmic: Rays and Earth's Climate, *Space Sci. Rev.* **93**, 155–166 (2000)
73. R.G. Roble, R.E. Dickinson: *Geoph. Res. Lett.* **16**, 1441–1444 (1989)
74. D.D. Sentman, E.M. Wescott, D.L. Osborne, D.L. Hampton, M.J. Heavner: *Geophys. Res. Lett.* **22**(10), 1205–1208 (1995)
75. L.A. Frank, J.D. Craven, R.L. Rairden: *Adv. Space Res.* **5**, No. 4, 53–68 (1985)
76. T.N. Woods, G.J. Rottman, S.M. Bailey, S.C. Solomon, J. Worden: *Solar Phys.* **177**, 133–146 (1998)
77. B. Zolesi, Lj.R. Cander: *Adv. Space Res.* (in press)
78. P. Bochsler: The CELIAS experiment on board the SOHO spacecraft, In: *Procedings of the IVth International Seminar: Manufacturing of Scientific Space Instrumentation*, ed. by V.M. Balebanov (Academy of Sciences, Space Research Institute, Frunze, 1989) pp. 137–147

Earth Radiation Belts

Sébastien Bourdarie and Daniel Boscher

ONERA/DESP, BP 4025, 2. Av. E. Belin, 31055 Toulouse Cedex 04, France

Abstract. The effects induced by the space environment on space vehicles and astronauts no longer need to be demonstrated. The nature of this environment varies greatly between low orbits and higher orbits such as the geostationary orbit and beyond. In this chapter, we attempt to describe the space environment relative to ionizing particles. To do this, we give a description of the radiation belts. The dynamics in then detailed with two different time scale: the solar cycle time scale and the storm time scale.

1 Introduction

Before the space era, the only manifestation of the presence of radiations in space was the deformation of the ionized tail of comets caused by the solar wind, the aurora borealis whose origin was not well understood, and the ionization of air, secondary cosmic-ray showers, and the isotopes (carbon 14, for example) produced by cosmic radiation. We had to wait until the beginning of the space conquest to discover in 1958 the presence around the Earth of very high energy charged particles (Van Allen belts). Since then, it has become evident that the space environment is a highly aggressive medium. Indeed, beyond the natural protection provided by the Earth's atmosphere, various types of radiation can be encountered. Their characteristics (energy and nature), their origins, and their distributions in space are extremely variable. This environment degrades electronic systems and on-board equipment in particular and creates radiobiological hazards during manned flights.

Based on several tens of years of the space adventure, a detailed analysis of the problems on satellites shows that the part due to the space environment is not negligible. It appears that the malfunctionings are due to problems linked to the space environment (9–21%), electronic problems (6–16%), design problems (11–25%), quality problems (1–8%), other problems (11–33%), and problems that are still unexplained (19–53%) [1]. It is clear that the unexplained problems are linked problems either to the space environment, or

S. Bourdarie and D. Boscher: *Earth Radiation Belts*, Lect. Notes Phys. **699**, 93–118 (2006)
DOI 10.1007/3-540-33759-8_5

to the electronics, or to the design, or to the quality or otherwise but the information collected on the ground is not sufficient to define the origin of the problem. The space environment is largely responsible for about 20% of the anomalies occurring on satellites and a better mastery of that environment could increase only the average lifetime of space vehicles.

This finding naturally leads to a detailed study of the space environment and of the effects that it induces on space vehicles and astronauts. The nature of this environment varies very greatly between low orbits and the higher altitudes such as the geostationary orbit and beyond. Among its components, we examine only the ionizing charged particles here, that is to say the particles trapped in the radiation belts, and the solar flare and cosmic radiation particles. From the point of view of the effects, the degradations will differ according to the energy of the particles, to their nature, and to the satellite's orbit. The degradations and disturbances induced by radiating space in the materials and the electronic components are phenomena that have been studied for many years. Two categories of effects should be noted:

- the cumulative effects such as the aging of thermal control coatings, of the optics, and electronics and the erosion of materials;
- the sporadic effects such as noises in the detectors and optics, singular events in highly integrated electronic circuits and electrostatic discharges.

The increasingly frequent presence of man in space and the projects such as the distant and long-duration missions (Lunar base, flight to Mars, etc.) pose the problem of the biological effects induced, essentially in the long term, by high-energy radiations. Radiations can have two possible types of biological effects:

- immediate, permanent, or delayed nonstochastic effects (destruction or modification of cells), the speed with which the symptoms appear and their seriousness increase in proportion to the exposure to the radiations;
- stochastic effects, associated with the modifications to the cells, whose probability of appearing in the long term increases in proportion to the irradiation (cancers, leukemia, genetic effects).

2 The Earth's Magnetosphere

The Earth's magnetosphere can be seen as a natural cavity in the interplanetary medium in which the Earth is relatively well protected against external influences. It is compressed on the solar side and highly drawn out on the antisolar side. In this structure, at the level of the poles, two horns, flaring out toward space offer the particles from the interplanetary medium a possibility of penetrating into the upper atmosphere. Close to the Earth, the charged particles present in the magnetosphere can be trapped by the magnetic field and form the radiation belts.

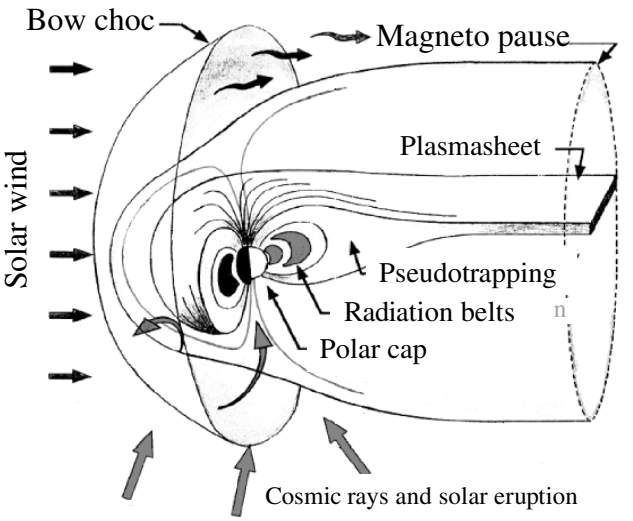

Fig. 1. The Earth's magnetosphere

In the magnetosphere, the radiation belts occupy only a relatively restricted internal region (Fig. 1). The region closest to the Earth is well known and constant over time: this is the upper atmosphere. The external limit, however, is poorly defined and depends on the conditions in the solar wind through the magnetic field as we will see later on. They therefore extend from the upper atmosphere (some hundreds of kilometer) up to geostationary orbit and beyond.

3 The Magnetic Field

In the Earth's magnetosphere, the magnetic field is the sum of two terms, one of internal (main component) and the other of external origin. The internal magnetic field is probably due to the convection movements in the core of the planet; in addition to this main term, there is the permanent residual field of the Earth's crust. At the zero order the field can be considered to be dipolar. The corresponding field lines are shown in Fig. 2. However the single dipolar approximation is not rigorous. It is then more appropriate to take an off-center and tilted dipolar magnetic field as approximation. This gives a dipole whose center is not at the center of the Earth and whose axis is not parallel to the Earth's rotation axis (Fig. 3). The result of this geometry of the magnetic field is an anomaly, a zone in which the field is weaker. This region is situated at the level of Brazil, and is known as the South Atlantic Anomaly. Other, more realistic, models of the internal field exist, the old models such as Jensen and Cain 60 [2], GSFC 12/66, and the International Geophysical Reference Field model (IGRF) [3]. These models consider the

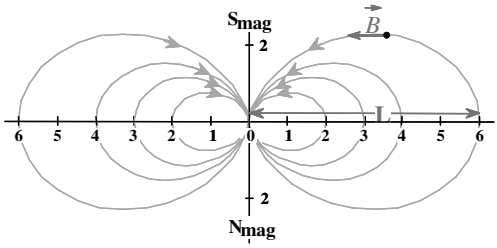

Fig. 2. Dipolar magnetic field lines

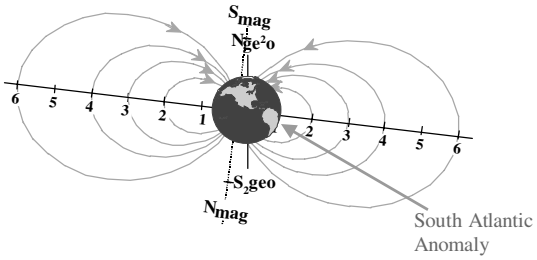

Fig. 3. Dipolar magnetic field titled and off-center with respect to Earth

terms of a multipolar higher order. The potential, V, is then a development in series based on Gauss spherical harmonic coefficients, g_m^n, h_m^n. The general form is then given by

$$V = a \sum_{n=1}^{N} \sum_{m=1}^{M} \left(\frac{a}{r}\right)^{n+1} [g_n^m \cos m\phi + h_n^m \sin m\phi] P_n^m \cos\theta$$

$$\mathbf{B} = -gr\mathbf{a}dV$$

It is important to note that the Earth's field is subject to long-term changes (secular drifts), in particular the South Atlantic Anomaly is drifting south-eastward. At the present time, we note

– a decrease in the intensity of 27 nT/an (0.05% a year),
– a drift of the axis, resulting in a westward rotation of the southern end of the dipole (0.014° a year) and an increase in the shift toward the West Pacific close to 3 km a year.

An iso-contour cartography (with a constant B modulus) for a given altitude makes it possible to see the South Atlantic Anomaly and its drift over time (Fig. 4).

So, up to a distance of some Earth radii, 5 to 6, the magnetic field is close to a dipolar field and the magnetosphere is more or less in revolution. Beyond that distance, the external fields become less and less negligible and contribute to the deformation of the dipolar internal field. These external

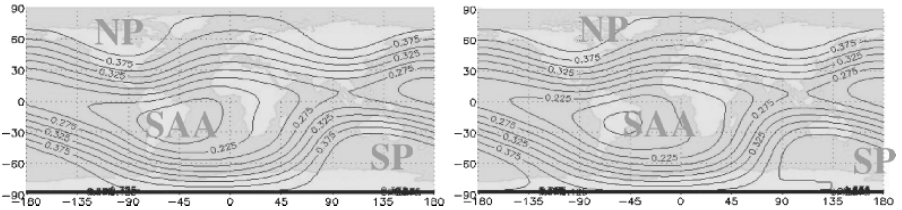

Fig. 4. Iso-contour of the Earth's magnetic field at an altitude of 800 km in 1965 on the left and in 2000 on the right deduced from the IGRF model (NP for "North Pole", SP for "South Pole" and SAA for "South Atlantic Anomaly"). The eastward and Southward drift of the South Atlantic Anomaly can be seen

fields are the sum of several components: the compression on the day side and the blast in the antisolar direction, forming the tail of the magnetosphere. Several models of external field exist, we can mention, for example, the models of Tsyganenko 1982 [4], 1989 [5] (Fig. 5), 1996 [6], Olson-Pfitzer [7,8], and Alexeev [9]. These latter – the sum of the fields transported by the solar wind and induced by the currents in the magnetosphere – are subject to rapid variations. Indeed, the variations in the interplanetary environment have an impact on the magnetosphere. The fluctuations in the speed of the solar wind

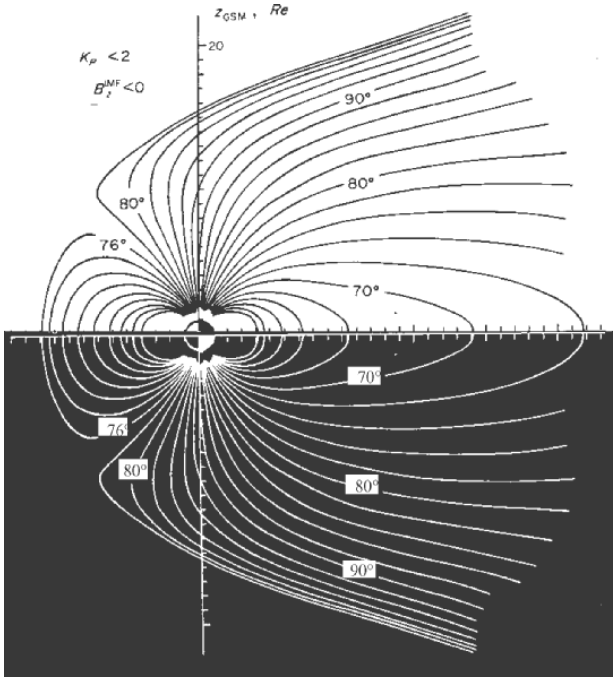

Fig. 5. Earth's magnetic field, external component. Tsyganenko 1982 model

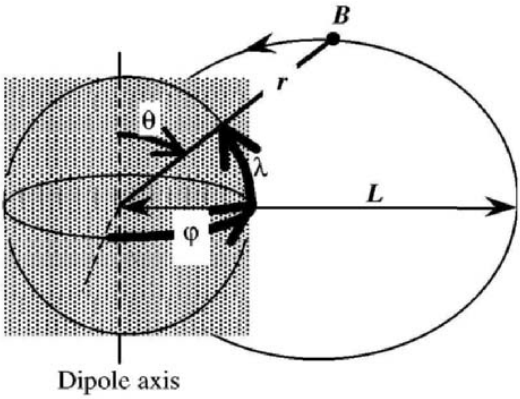

Fig. 6. Magnetic coordinates

(400–1,000 km/s) and therefore of the energy transported are, depending on the orientation of the interplanetary magnetic field, more or less well transferred to the magnetosphere, increasing the instabilities of the external magnetic field. For example, the compression of the subsolar zone may be sufficient to place a geostationary satellite temporarily beyond the magnetopause; likewise, during these geomagnetic storms injections of high-energy particles are observed in the radiation belts.

To understand and reproduce the dynamics of the charged particles present in the magnetosphere, it is common to define magnetic coordinates (Fig. 6). r is the distance from the center of the dipole to the point under consideration, θ its colatitude, λ its latitude, and φ its magnetic longitude. A field line (or force line) is defined by the McIlwain parameter, L [10], approximately equal (only true with a dipolar field) to the distance (expressed in planet radii), from the center of the planet to the intersection point of that force line with the magnetic equatorial plane. A point on a force line is defined by the B parameter, modulus of the magnetic field at the point under consideration. B and L then represent a coordinates system linked to the model of the magnetic field under consideration.

4 Charged Particles Motion

All charged particles immersed in an electromagnetic field will be subject to the Lorentz force: $\mathbf{F} = q\,(\mathbf{v} \wedge \mathbf{B} + \mathbf{E})$ where q is the particle's charge, $\mathbf{v}$ its speed, $\mathbf{B}$ the magnetic field, and $\mathbf{E}$ the electric field. If the magnetic field is very strong and the energy of the particles is great (and therefore their speed too) then the effect of the electric field can be ignored and the Lorentz force is reduced to $\mathbf{F} \approx q\,(\mathbf{v} \wedge \mathbf{B})$. We then speak of particles trapped by the Earth's magnetic field. Their movement is completely linked to the topology

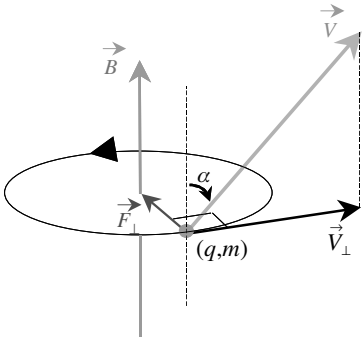

Fig. 7. Gyration movement of a charged particle around a magnetic field line

of the magnetic field. These particles represent the radiation belts or Van Allen belts. These conditions are met for particles whose energy is higher than about 10 keV and in zones close to the Earth where the magnetic field is great. Under these special conditions, the movement of the high-energy particles can be broken down into three basic periodic movements.

4.1 Gyration

A charged particle immersed in a magnetic field will have a rotation movement around the field line. This movement is called gyration (Fig. 7). It is then possible to define some magnitudes relative to this movement:

- The Larmor radius, $r_L = \frac{mv_\perp}{qB}$, where m is the relativistic mass of the particle, $v_\perp$ the component perpendicular to the magnetic field of the particle speed, q its charge, and B the modulus of the magnetic field;
- The relativistic magnetic moment, $\mu = \frac{mv_\perp^2}{2B} = \text{constant}$

4.2 Bounce

If a particle has one component of its speed parallel to the magnetic field, then it will move along the field line (Fig. 8). When making any movement the particles keep their relativistic magnetic moment, μ constant [11]. So, since the magnetic moment has to remain constant, the particle which moves from the equator (point where the magnetic field is weakest along the field line) toward the higher latitudes will see an increasingly strong magnetic field. It is necessary that the perpendicular component of the speed should increase in order for μ to remain constant. This will be possible until the perpendicular speed is equal to the particle's total speed, the parallel speed then being null. At this particular point the particle stops, it is at its mirror point. A weak force due to the gradient of the magnetic field enables this particle to go backward to its other mirror point situated in the other hemisphere. The particle therefore

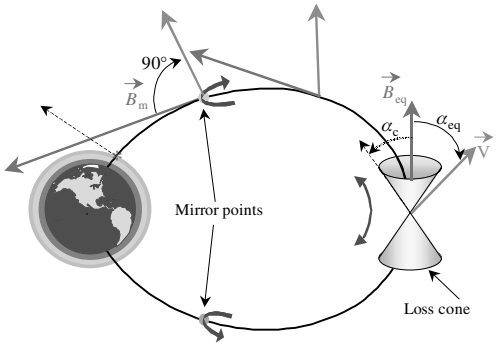

Fig. 8. Bounce movement of a charged particle between its two mirror points

has a back-and-forth movement between its two mirror points; this is the bounce movement.

It is possible to define the angle that the particle's speed vector must have with respect to the magnetic field when it crosses the equator such that its mirror point is in the upper atmosphere. The particle is then lost and will not be able to come back. This allows us to define a loss cone, that is to say if the speed vector is within the cone, then the particle cannot bounce and will be lost.

4.3 Drift

In order to simplify the problem, we place ourselves on the magnetic equator (Fig. 9). Since the magnetic field of the planets has a radial gradient, the gyration cannot take place in a constant Larmor radius. Indeed, the magnetic field along a gyration becomes stronger if the particle approaches the planet, the Larmor radius is then smaller and therefore the radius of the trajectory's curve is also smaller. The particle will thus be able to move away from the planet, the magnetic field will be weaker and therefore the Larmor radius and the radius of the trajectory's curve will be greater. The particle therefore does not go through a simple circle but along a more complex trajectory. This movement breaks down into a simple gyration (circular) and a rotation movement around the planet: this is the drift movement.

A charged particle submitted to these three basic [12] and periodic movements then moves through torus shaped surfaces around the Earth, which are commonly called drift shells (Fig. 10). The periods associated with each of these basic movements for a 3 MeV electron at $L = 3$ are respectively 2.14 10^{-4} s, 0.19 s, and 504 s. The disparity between the periods is very great, a factor of the order of 1,000 should be noted between each of them going from the gyration movement to the drift movement.

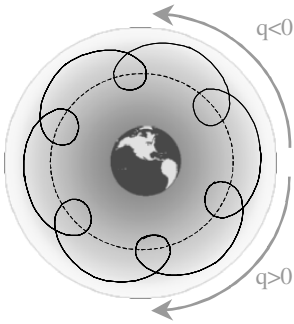

Fig. 9. Drift movement for an equatorial charged particle (which does not bounce $\alpha_{\text{eq}} = 90°$)

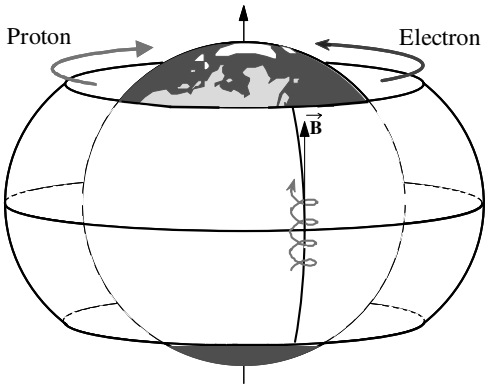

Fig. 10. Composition of a charged particle's three periodic movements: gyration, bounce, and drift. The particle then follows a torus surface called a drift shell

5 The Radiation Belts

5.1 Description

The magnetic field in the vicinity of the Earth becomes such that all relativistic charged particles are trapped and their movement is then quasi-periodic. These special conditions are thus favorable to the accumulation of high-energy–charged particles in certain regions of space that creates the radiation belts. Given the trajectories of the particles, the radiation belts have a toroidal shape that surrounds the Earth. The Earth's atmosphere is the lower limit of the radiation belts since it causes the loss of all the trapped particles. The upper limit, however, is less clear and is defined by the minimum intensity in the presence of disturbances of the magnetic field such that the particles are always trapped.

Discovered during the first space missions by J. Van Allen, the particles trapped in the radiation belts (or Van Allen belts) are essentially protons and

Table 1. Characteristics of the Earth's radiation belts

	Particle	Energy	Extension (Earth radii)
Earth	e-	1 keV–30 MeV	1–10
	p+	1 keV–100 MeV	1–7

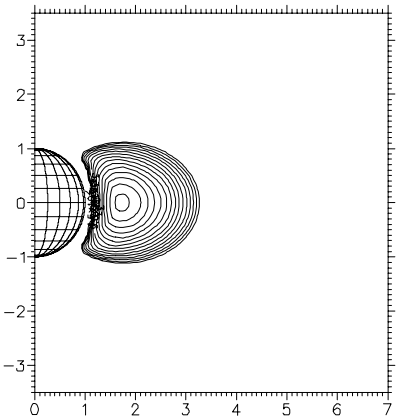

Fig. 11. Proton radiation belt

electrons. The energy ranges commonly encountered go from some keV up to some tens or even hundreds of MeV. Table 1 summarizes the properties of the Earth's radiation belts.

A view of the radiation belts is given in the following figures. A single maximum is observed for the proton belt (Fig. 11) for a value of L that depends on the energy ($L = 1.7$ for 10 MeV protons); the flows are very stable there and the maximum energies can reach between some MeV and some hundreds of MeV depending on the position.

The electrons belt is more complex (Fig. 12) and has two maximums, respectively, corresponding to the internal and external zones:

– the first one centered on $L = 1.4$ extends up to $L = 2.8$; the electron populations are relatively stable there and can reach maximum energy levels of the order of 10 or even 30 MeV;
– the second one, centered on $L = 5$, extends from $L = 2.8$ to $L = 10$; the electron flows there are much more variable and the energy levels can be as high as 7 MeV.

At zero order the radiation belts can be considered to be symmetrical in longitude in a region going from the Earth's surface up to the geostationary orbit, that is to say as long as the magnetic field can be equated with a dipole. However, as demonstrated in paragraph 3, at high altitudes, the field differs from a dipole and the belts are no longer in revolution. At the level of the geostationary orbit, the fluxes of high-energy particles (electrons between

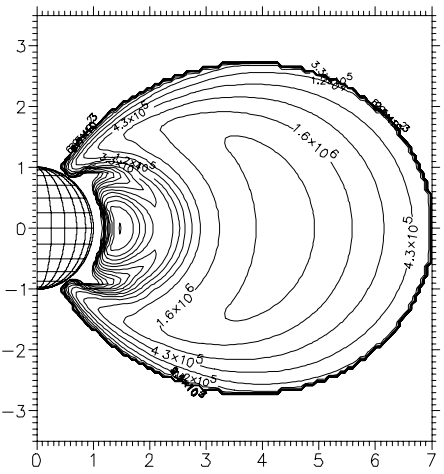

Fig. 12. Electron radiation belt

100 keV and some MeV and protons between 100 keV and 1 MeV) then have a maximum on the day side and a minimum on the night side. We then speak of day–night asymmetry (Fig. 13) due to the topology of the magnetic field (external).

5.2 The South Atlantic Anomaly

Since the Earth's dipole is tilted and off-centered by 500 km toward the West Pacific, the radiation belt (protons and electrons) descends to a low altitude over the South Atlantic, the populations of charged particles are attached to

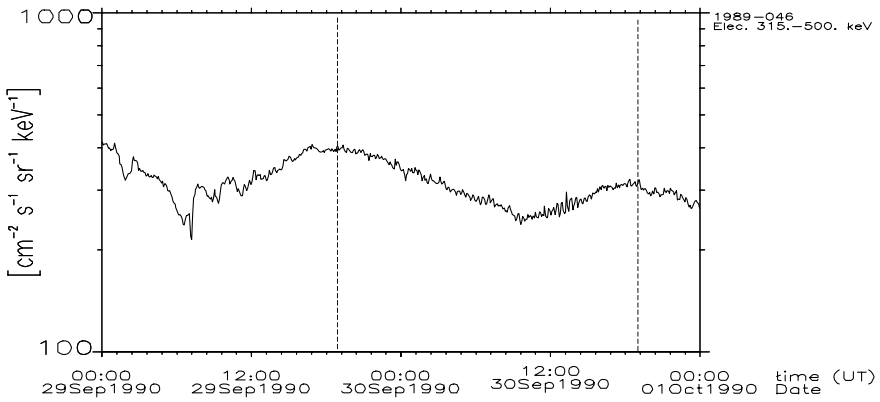

Fig. 13. Electron fluxes with an energy level between 315 and 500 keV in geostationary orbit measured by Los Alamos National Laboratory (NM-USA) satellite 1989-046. The *dotted lines* represent the passage of the satellite at local midday

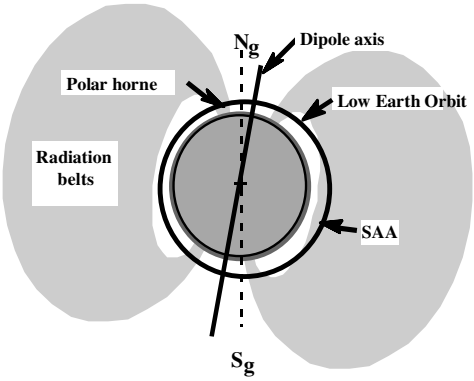

Fig. 14. Environment in low orbit

the magnetic field. A satellite in low orbit (LEO, Low Earth Orbit) will thus be exposed only to radiations on certain fractions of the orbit as far as the trapped particles are concerned when passing through (Fig. 14):

– the polar horns (electrons below 1,000 km, electrons and protons above that altitude),
– the South Atlantic Anomaly (protons and electrons at all altitudes).

As can be seen in Fig. 15, the position of Kourou, close to the SAA, means that the launcher's trajectory passes through a zone with a great flux of rapid trapped protons when being injected into geostationary transfer orbit. This must be taken into account when designing the on-board electronics that may be sensitive to the singular effects induced by protons.

5.3 Dynamics of the Radiation Belts

Given the measurements of the trapped particles in the Earth's environment, it is now certain that a static view of the radiation belts is obsolete. The American CRRES satellite in the early 1990s clearly evidenced the extreme dynamics of the trapped electrons and protons. As stated earlier, the radiation belts are linked to the existence of the Earth's magnetic field and the populations of particles are the result of an equilibrium between:

– the sources, injections from the tail of the magnetosphere and creations by nuclear reactions between atoms in the upper atmosphere and rapid ions (solar or cosmic),
– the losses by precipitation in the upper atmosphere or by charge exchange with the exospheric atoms and molecules.

These various terms can vary over time and are highly dependent on the magnetic field; any transient disturbances and time drifts of the magnetic field

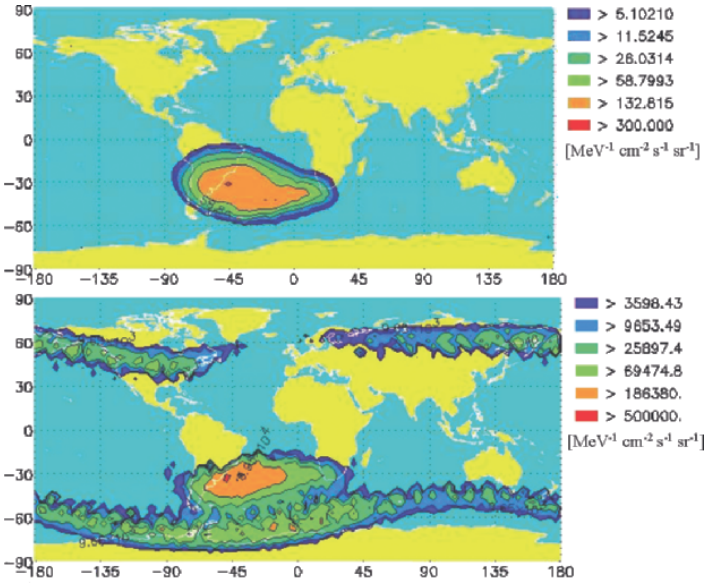

Fig. 15. Iso-flux curves for 9.4 MeV protons (*top*) and for 460 keV electrons (*bottom*) measured by the SPICA detector on the Argentinean SAC-C satellite at an altitude of 710 km

result in rapid fluctuations (substorms and magnetic storms) and long-term variations of the fluxes in the belt.

It is therefore judicious to look at the dynamics of belts at different time scales as a function of the effect (of the degradation) that you want to study. If you are interested only in the cumulative effects such as the dose effects then variations on the scale of the minute (substorm) or of the week (storm) serve no purpose. However, the variations on the solar cycle scale will be fundamental. On the contrary; in the case of studies on charging environments, the time scales go from some hours to some days, and the dynamics of the belts must be described on the scale of the substorm (surface charge) or of the magnetic storm (surface and internal charge).

Dynamics on the Scale of the Solar Cycle

Protons

The proton radiation belt (high-energy component >10 MeV) varies slowly as a function of the solar cycle [13]. The flux levels are at their highest when the solar cycle is at its lowest and vice versa. This is the result of two physical processes that condition the dynamics of the protons, the absorption of the protons by the upper atmosphere on the one hand and the modulation of the CRAND source (Cosmic Ray Albedo Neutron Decay) on the other hand.

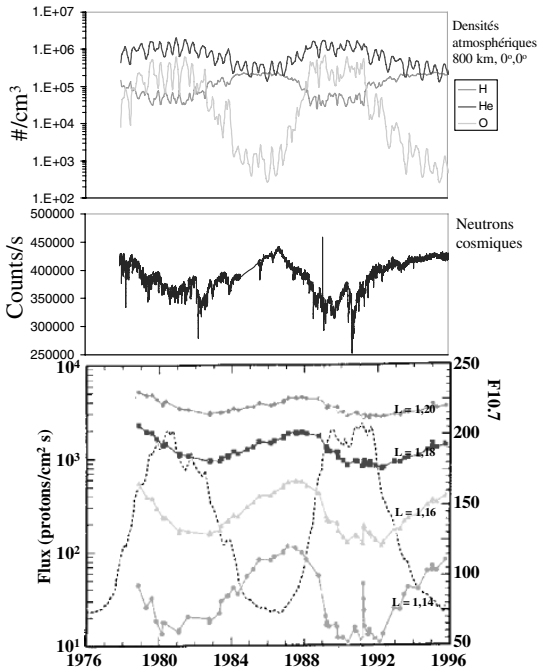

Fig. 16. Changes in the portion fluxes at low atitudes (*bottom*), in the cosmic radiation (*middle*), and atmospheric densities (*top*) as a function of the solar cycle

Indeed when the solar cycle is at its maximum, the upper atmosphere is heated up and the densities at constant altitude increase. It can then be understood that the losses of trapped protons induced by the charge exchange increase when the solar cycle is at its maximum. However, when the solar cycle is at its maximum, the fluxes of cosmic radiation fall because of the intense solar activity and the source is reduced. The balance is shown in Fig. 16.

Another important characteristic of low altitude proton fluxes is an overall decrease in the fluxes from one cycle to the next. The comparison of the fluxes from one solar minimum to the next shown in Fig. 16 very clearly illustrates this slow variation. It is because of the secular drift of the Earth's magnetic field. At the present time this poses problems for forecasting the low-altitude proton fluxes from one cycle to the next.

Electrons

The variations in the electron belt are above all known in the external zone, and the geostationary orbit is very well documented in particular [14,15]. In geostationary orbit (Fig. 17), the fluxes of electrons are at their lowest when the solar cycle is at its highest and are at their highest 3 or 4 years after the top of the cycle (just before the solar cycle is at its lowest). This

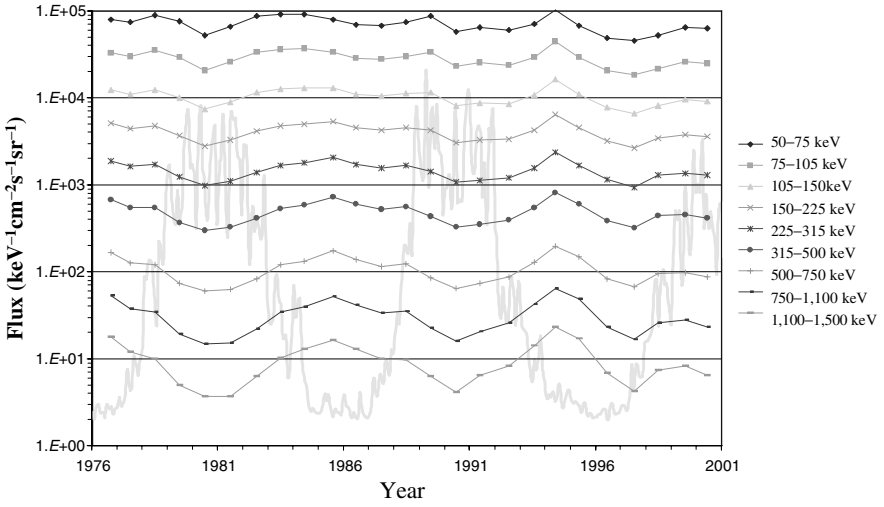

Fig. 17. Electron fluxes at geostationary orbit as a function of the solar cycle

modulation as a function of the radio-solar flow (F10.7) at 10.7 cm shows that the amplitude is all the greater if we examine the high energies (MeV and above). However, at low energy levels (some hundreds of keV) the modulation is virtually inexistent. The strong fluxes of electrons are linked to the presence of coronal holes on the surface of the sun, which in turn involve intense and long-duration magnetic storms at the level of the Earth's magnetosphere (see the next paragraph).

Even if the charge phenomena on satellites are induced by instantaneous fluxes of electrons, it is nevertheless possible to use this curve to define the unfavorable periods that lead to surface or internal charging. Surface charging can appear at any moment during the solar cycle, since the low-energy electrons involved in this process are not modulated by the solar activity. As for the internal charge, it will preferably appear some years after the maximum of the solar cycle when the coronal holes have an influence on the Earth's environment.

Dynamics on the Scale of the Magnetic Storm

Proton

The low-energy protons (some tens to some hundreds of keV) are very sensitive to magnetic storms. The fluxes of particles therefore follow the Earth's magnetic activity in a region going from $L = 2$ to $L = 6$ with time scales going from a minute to several hours. A view from the CRRES satellite (MEB instrument) makes it possible to view 14 months' dynamics of the belt of

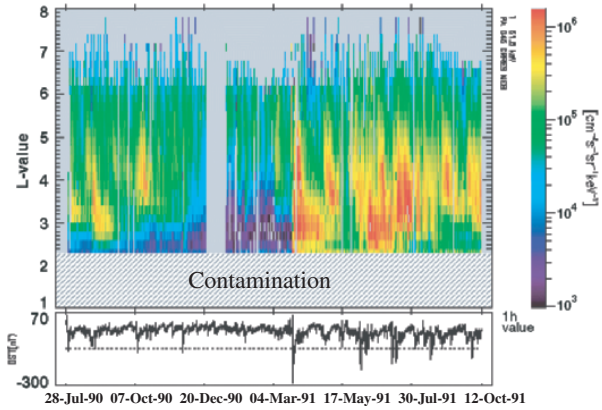

Fig. 18. Flux of 62 keV protons measured by the MEB detector on CRRES for 14 months

62 keV protons (Fig. 18) in various different regions (the satellite crosses the magnetic field lines close to the equator) [16, 17].

At higher energy levels (several tens of MeV) the belt is generally very stable but major events can dramatically change the flux levels in intermediate regions of the radiation belts [18]. In fact, if there is a solar flare in progress when a very intense magnetic storm is building up then the solar particles can be trapped and thus significantly increase the fluxes of trapped particles in a region between $L = 2$ and 2.5 [19]. The example of the event in March 1991 is striking (Fig. 19).

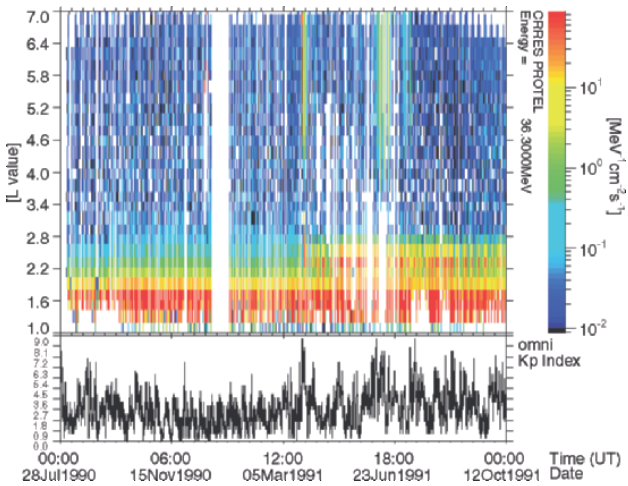

Fig. 19. Flux of 36.3 MeV protons measured by the PROTEL detector on CRRES for 14 months

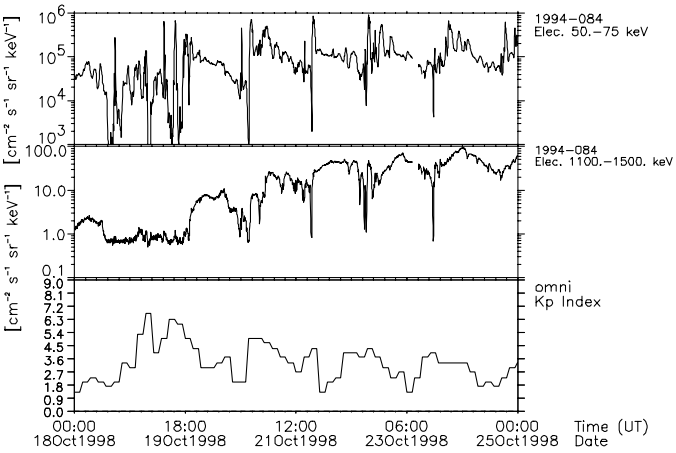

Fig. 20. Flux of 50–75 keV (*top*), 1.1–1.5 MeV (*middle*) electrons in geostationary orbit and magnetic activity Kp (*bottom*) as a function of time

Electrons

To better understand the environmental conditions that lead to charging phenomena on satellites, the dynamics of the electrons will have to be controlled during major magnetic storms. According to the observations made in geostationary orbit, the low-energy electrons (which induce surface charges) appear right from the first instants of the disturbance whereas the higher energy electrons (which induce the internal charge) are detected some days after the beginning of the event (Fig. 20).

A distinction can also be made between various different classes of events [20] (Fig. 21): (1) storms where the magnetic activity index Kp is high (up to 8 or 9) but which do not last long (less than 1 day) and which do not produce any or only a few high-energy electrons in geostationary orbit (Fig. 21 on the left) and (2) the storms where the magnetic activity index Kp is moderate (up to 6 or 7) but which last longer (several days) and which produce large quantities of high-energy electrons in geostationary orbit (Fig. 21 in the middle). The most surprising thing is that in the second case the storms where the magnetic activity index oscillates between 2 and 4 for several days produce nearly as many high-energy electrons in geostationary orbit as a more violent storm with a Kp of 6 (Fig. 21 on the right).

To understand the electron acceleration phenomena, we must examine in detail the physical processes that affect the dynamics of these particles. The low-energy electrons are first of all transported from the tail of the magnetosphere toward the inside of the radiation belts by an increase in the radial diffusion at the beginning of the storm. As they come closer to the Earth, they

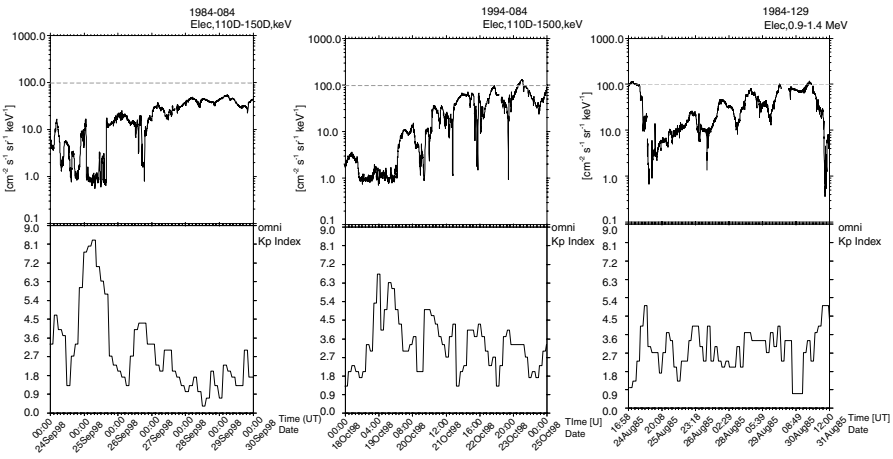

Fig. 21. Comarison of the consequences of three magnetic storms on the fluxes of 1.1–1.5 MeV electrons in geostationary orbit for three different levels of activity

see an increasingly strong magnetic field and, under the effect of the Lorentz force, they drift around the Earth firstly in the night–morning sector. In the vicinity of the plasmapause ($\sim L = 4$), these electrons are submitted not only to radial diffusion but also to the wave–particle interaction. The combination of the two leads to a slow but continuous acceleration of the electrons. A large proportion of these electrons (now at high energy levels) will diffuse radially toward the internal zone of the radiation belts. There, they will be globally lost by precipitation in the loss cone due to the wave–particle interaction that is then preponderant [21]. However, a small proportion of the high-energy electrons will be able to diffuse from the plasmapause toward the exterior of the belt and finally reach the geostationary orbit. This acceleration mechanism makes it possible to explain, in particular, the delay between the low-energy electrons and the high-energy electrons in geostationary orbit.

Events such as these are very frequent, the CRRES period makes it possible to view the dynamics of the electrons for 14 months still with the major storm of March 1991 (Fig. 22).

The Salammbô Models

Since the 1990s, ONERA/DESP has been developing physical models of the proton and electron radiation belts, called the Salammbô codes. At the present time, these codes represent a family of models (Saalmmbô 4D, Salammbô 3D, and Salammbô 2D) which provide a more or less well-refined description of the belts as a function of what one wants to reproduce and of the desired resolution of the result [17, 19, 21–23].

These models make it possible to describe the dynamics of the proton and electron belts with energy levels of 10 keV–300 MeV and 10 keV–10 MeV,

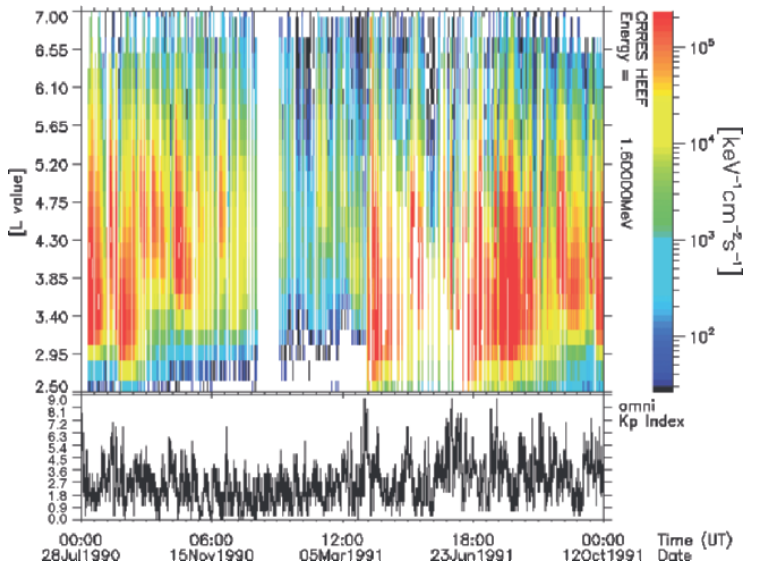

Fig. 22. Flux of 1.6 MeV electrons measured by the HEEF detector on CRRES for 14 months

respectively, in the region going from $L = 1$ to 7 with a time resolution of between 1 minute and several hours. The inputs to these models are the magnetic activity indexes Kp and Dst and a boundary condition deduced from geostationary measurements.

At present these models make it possible to understand the dynamics of the charged particles trapped subsequent to magnetic storms of variable intensities. Notably, the creation of the second proton belt seen by CRRES has been reproduced, as have the effects of long and short magnetic storms on the external belts of electrons.

In the future, this model should make it possible to define the conditions required to obtain a worst case for radiation belts. It also offers the possibility of validating, or not, the representativeness of the measurements and even of extrapolating measurements over time. Finally, another application of the model is to interpolate and extrapolate the measurements in order to reconstruct a complete and dynamic cartography of the radiation belts.

6 The Sources of Energetic Particles Outside the Magnetosphere

6.1 Solar Flares

Particular transient events occur that disturb on-board systems in space. This concerns solar flares. The exact composition of the particles produced by

solar flares are not yet well known. The most harmful particles produced are protons and sometimes heavy ions (He, O, C, Fe ...). Although the protons always represent the majority among the ions, certain flares are accompanied by emissions of heavy ions whose spectrums, charge states, and relative abundances are variable from one event to another, and are therefore difficult to model.

These emissions last between some hours and some days (Fig. 23). The spectrums, which vary greatly from one flare to the next and during the event itself, can extend up to energy levels as high as some hundreds of MeV. The time profiles very often show a sudden increase of the instantaneous fluxes in the vicinity of the flare's peak (see, for example, early afternoon of October 20, 1989), this corresponds to an acceleration caused by a shock wave (usually linked to a coronal mass ejection) in the interplanetary medium. The fluence associated with a flare can be as high as some 10^{10} protons/cm^2 with an energy level higher than 10 MeV during major events.

Since the flares are linked to spots on the surface of the sun, they are not distributed evenly through the solar cycle. The result is that during solar maximums the proton and ion events are very numerous (Fig. 24), and can be produced by several successive flares. However, isolated but very intense flares sometimes appear during solar minimums (e.g., August 1972). These events occur at random and it is impossible, with the knowledge we currently have, to predict their date and seriousness in the long term.

6.2 Cosmic Rays

Galactic Cosmic Rays

The origin of cosmic rays lies outside the solar system. It comes from very distant galactic and extragalactic point sources. It is propagated through-

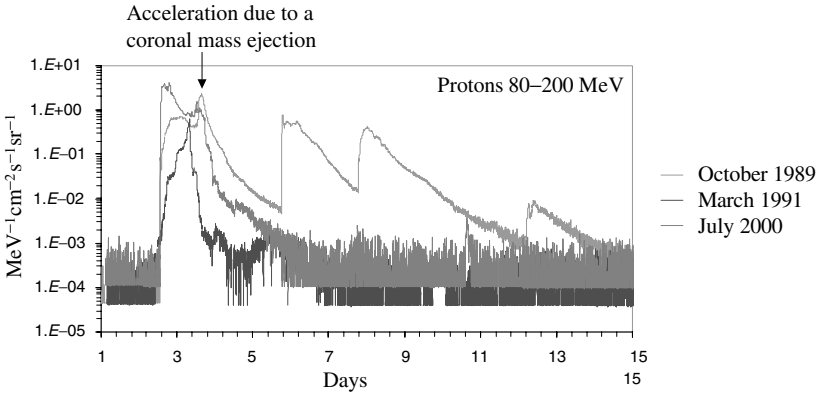

Fig. 23. Comparison of the time profile of three major flares for protons with energy lavels comprised between 80 and 200 MeV measured by the GOES satellites

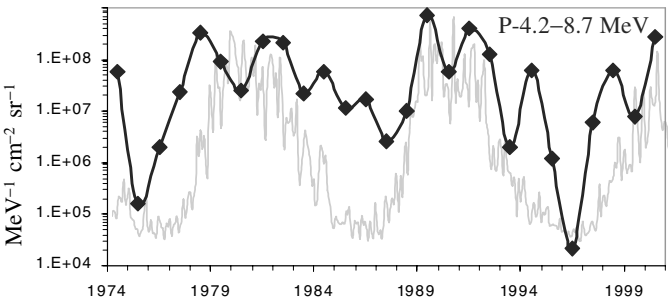

Fig. 24. Distribution of flares with protons with energy levels of 4.2–8.7 MeV seen at the level of the Earth's orbit as a function of the solar cycle shown in pale color in the background (cycle 21, 22, and the begining of 23 are shown). The total number of particles is at its highest during the solar maximum, whetever the energy level

out space that is not occupied by dense matter. The interactions with matter (approximately 7 g/cm^2 of interstellar gas), shock waves, and interstellar electromagnetic fields scatter and accelerate these particles that, at the level of the solar system, have isotropic angular distributions and are completely ionized. The cosmic rays represent a continuous background of ions whose energy levels can be very high. They can reach several thousands of GeV (significantly higher than those observed in most solar flares). Beyond some GeV/nucleon, the energy distributions, $\Phi\ (E)$, are described well by a law of the type: $\Phi(E/A, Z) = k(Z)(E/A)^{-\tau}$, where A, Z, E, respectively, designate the mass, the atomic number, and the energy of the ion, and τ, the spectral index, is close to 2.7. Its composition is practically the same as that of the local galactic matter such as it is known in the solar system. It consists approximately of 83% protons, 13% helium (^{4}He ion), 3% electrons, and 1% heavy ions. However, two zones of enrichment in light elements (Li; Be; B) and in medium nucleii (Se; V; Cr; Mn) are observed and attributed to the nuclear interactions with the interstellar matter.

In the solar system the ions from the cosmic rays are deviated by the turbulent magnetic field transported by the solar wind. These large-scale distributions for the slowest ions increase with the field, resulting in a modulation of the fluxes at low energy levels by the solar activity. The fluxes of cosmic ions are then at their maximum during the minimum levels of solar activity, and vice versa. The measurements made by the Pioneer and Voyager satellites have demonstrated that the fluxes of cosmic particles are not very dependent on the distance from the sun. The radial gradient between 0.3 and 40 AU is less than 10% per AU, or even 0% at the solar maximum between 0.3 and 30 AU. As for the variations in latitude, they are also very low, of the order 0.5% per degree.

Anomalous Cosmic Rays

In the interplanetary medium, certain ions stand out clearly from the galactic cosmic rays due to their state of charging (these ions have lost only one peripheral electron), their energy (approximately comprised between 50 and 100 MeV/nucleon) and their composition (essentially He, N, O, Ne, and Ar). The origin of this so-called anomalous component is assumed to be the low-energy neutral atoms that remain in the interstellar medium due to their high ionizing potential. These chargeless particles are not deviated by the interplanetary magnetic field and penetrate into the solar system, the heliosphere. As they approach the sun, these atoms are finally ionized after an electron is torn off by a photo-electric effect or at the time of a collision with the interplanetary matter. Accelerated by shock waves, they can reach energy levels of some tens of MeV/nucleons, in the interplanetary medium.

The radial and latidudinal variations of the anomalous component of the cosmic radiation are slightly higher than those in the previous case, the values measured being respectively 15% per AU and 3–6% per degree. Given their energy levels and their abundance, these particles have only a slight effect on satellites.

6.3 Magnetospheric Shielding

The charged particles of external origin (cosmic and solar flare ions) are deviated by the Earth's magnetic field (Fig. 25). These particles, which are propagated in the interplanetary medium where the magnetic field is of some nanoteslas, rapidly see the magnetic field increase to several thousands of nanoteslas. They are then submitted to the Lorentz force linked to the planet's magnetic field, $\mathbf{F} \approx q\,(\mathbf{v} \wedge \mathbf{B})$. Still because of the magnetic field's radial gradient, the particle heads toward the Earth while beginning a gyration, and then the curve radius of its trajectory decreases significantly. The particle then moves away from the planet while continuing to gyrate. The curve radius of its trajectory then becomes so large that the particle escapes from the influence of the Earth. It simply passes by. It is evident that, given the dependence of the Larmor radius on the particle's energy (speed) and on the magnetic field, the higher the level of the particle's energy, the more a strong magnetic field will be required to make it deviate. It is possible to define a limit below which the particles that come directly from the solar wind cannot penetrate, this being a function of their energy level. We then speak of magnetospheric shielding.

In order for an ion (of atomic weight A and charge Ze) to be able to penetrate the magnetosphere to a certain depth, it must have a rigidity R greater than a cutoff threshold R_{c}given by Boscher et al. [24]:

$$R = \frac{1}{z}\sqrt{E^2 + 2E_o E}$$

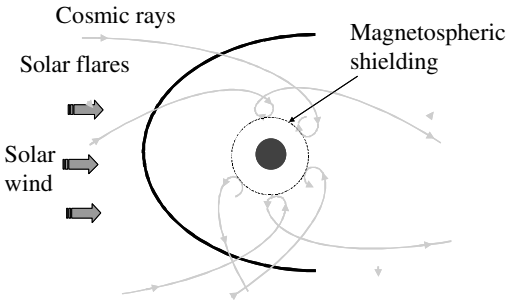

Fig. 25. Trajectory of the very high energy solar or cosmic particles when passing in the vincity of the Earth, evidencing the magnetospheric shielding

where A is the atomic number, Z the ion's charge, E its energy and E_o its energy at rest.

Since the cutoff rigidity R_c cancels out at the highest geomagnetic latitudes, the magnetospheric shielding is negligible at the level of the magnetic poles (in the polar cusp regions). An example is given in the case of the Earth in the approximation of the dipolar field in Fig. 26. It is obvious that if a magnetic storm (consequence of a disturbance that comes from the sun) occurs, the magnetospheric shielding will be modified, in particular it will be lowered and the particles will then be able, in this way, to reach regions closer to the Earth. A magnetospheric shielding calculation in magnetic storm conditions can be considered to be a worst case.

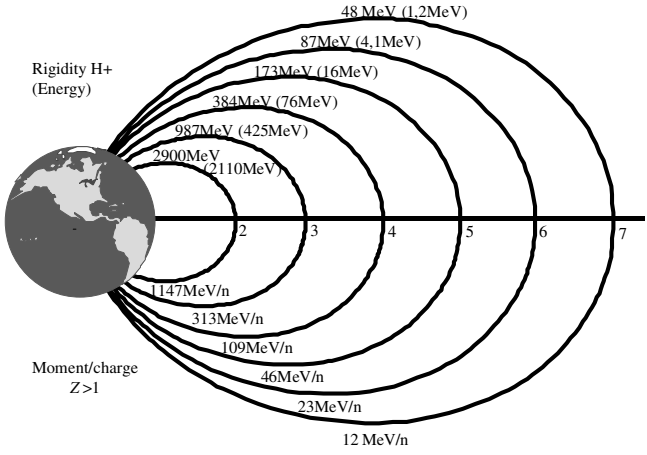

Fig. 26. Magnetospheric shielding – rigidity (or energy in parenthesis) as a function of L

7 Sensitivity of Orbits to the Radiations

It is clear that, given the distribution of the high–energy–charged particles in the radiation belts and the magnetospheric shielding to protect against solar or cosmic particles, the environment close to satellites is highly dependent on the orbit. Here we propose to give a rapid overview of this environment on the basis of the AP8, AE8, and JPL91 models for low orbits, 800 km 98°, and 30°, 1,400 km, circular and geostationary orbit 20,000 km 55°.

A projection of each of these orbits in a meridian plane is shown in Fig. 27 to appreciate the belt regions passed through by each of the satellites. It can immediately be seen that the high-altitude orbits are not subjected to the fluxes of high-energy trapped protons. However, these orbits are constraining from the relativistic electron viewpoint.

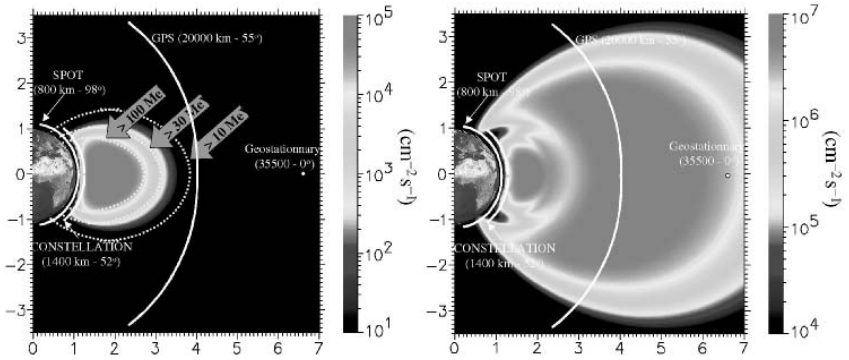

Fig. 27. Projection of the various orbits in a meridian plane with, in the background, omnidirectional integrated fluxes of protons with energy levels higher than 10 MeV (AP8 MIN) on the left and of electrons with energy levels higher than 500 keV (AE8 MIN) on the right. The red arrows on the left-hand diagram indicate the solar or cosmic protons with the fields line where they are stopped

If we look, in greater detail, at the differences from one orbit to another (Fig. 28) it can be seen, from the point of view of the protons, that the high orbits (35,000 and 20,000 km) are not very sensitive to the trapped protons but, on the other hand, they are not protected by the magnetospheric shielding, hence the presence of solar protons. In low orbit the situation is not the same, the trapped protons are not negligible whatever their level of energy. However, if a low orbit is greatly tilted then the presence of solar protons will be great, but there are virtually none for slightly tilted orbits, which are naturally protected by the magnetospheric shielding. As for the electrons, as it has been stated earlier, the high orbits are greatly exposed.

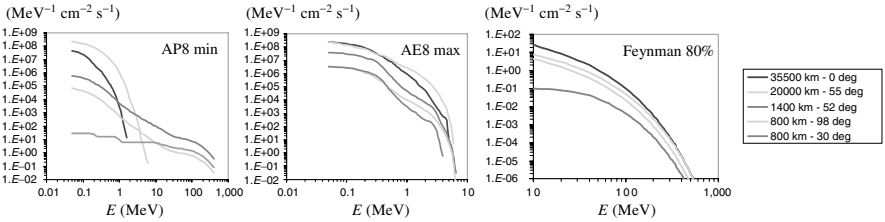

Fig. 28. Omnidirectional differential flux spectrum for trapped protons (AP8 min) on the left, for trapped electrons (AE8 max) in the center and for solar protons (Feynman 80%) on the right

References

1. Space Flight Environment, V, n04, Sept–Oct 1994
2. J.C. Cain, S.J. Hendricks, R.A. Langel, W.V. Hudson: J. Geomag. Geoelectr. **19**, 335–355 (1967)
3. D.C. Jensen, J.C. Cain: J. Geophys. Res. **67**, 3568 (1962)
4. N.A. Tsyganenko: Planet. Space Sci. **35**, 1347–1358 (1987)
5. N.A. Tsyganenko: Planet. Space Sci. **37**, 5–20 (1989)
6. N.A. Tsyganenko, D.P. Stern: J. Geophys. Res. **101**, 27187–27198 (1996)
7. W.P. Olson, K.A. Pfitzer: Magnetospheric magnetic field modeling, Annual Scientific Report, AFOR Contract No. F44620-75-C-0033 (1977)
8. K.A. Pfitzer, W.P. Olson: *EOS* **69**, 426 (1988)
9. I.I. Alexeev, E.S. Belenkaya, R.C. Clauer J. Geophys. Res. **105**, 21119–21127 (2000)
10. C.E. McIlwain: J. Geophys. Res. **66**, 3681–3691 (1961)
11. J. Bourrieau, J.P. David: Levy léon, Environnement spatial
12. T.G. Northrop, Interscience tracts on physics and astronomy, 1963
13. S.L. Huston, K.A. Pfitzer, Space environment effects: Low altitude trapped radiation model, NASA/CR 1998 208593 (1998)
14. D.N. Baker, J.B. Blake, R.W. Klebesadel, P.R. Higbie: J. Geophys. Res. **91**, 4265 (1986)
15. G.D. Reeves, Geophys. Res. Lett. **25**, 1817–1820 (1998)
16. R.H.W. Friedel, A. Korth, Geophys. Res. Lett. **22**, 1853–1856 (1995)
17. D. Boscher, S.A. Bourdarie, R.H.W. Friedel, A. Korth, Geophys. Res. Lett. **25**, 4129–4132 (1998)
18. M.S. Gussenhoven, E.G. Mullen, D.H. Brautigam, IEEE Trans. Nucl. Sci. **43**, 2 (1996)
19. A. Vacaresse, D. Boscher, S. Bourdarie, M. Blanc, J.A. Sauvaud, J. Geophys. Res. **104**, 28601 (1999)
20. K.L. McAdams, G.D. Reeves, R.H.W. Friedel, T.E. Cayton, J. Geophys. Res. **106**, 10869–10882 (2001)
21. D. Bosche, S.A. Bourdarie, R. Thorne, R. Abel, Adv. Space Res. **26**, 163 (2000)
22. S. Bourdarie, D. Boscher, T. Beutier, J.-A. Sauvaud, M. Blanc, J. Geophys. Res. **101**, 27171 (1996)

23. S. Bourdarie, D. Boscher, T. Beutier, J.-A. Sauvaud, M. Blanc, J. Geophys. Res. **102**, 17541 (1997)
24. M.A. Shea, D.F. Smart, A world grid of calculated cosmic ray cutoff vertical rigidities for 1980.0, 18th International Cosmic Ray Conference, conference papers, (1983)

Radio Emissions from the Sun and the Interplanetary Medium

Monique Pick

LESIA, UMR CNRS 8109, Observatoire de Paris, Place Janssen, Meudon 92195, France

Abstract. The Sun is a radio emitter in a large spectral domain from submillimeter to kilometer wavelengths. Observations at different wavelengths sample different heights in the solar atmosphere, with longer wavelengths referring to higher heights above the photosphere. This review focuses on a few topics related to the physics of the Sun–Earth system. Section 2 summarizes the general context of radio wave propagation and radio emissions. The limits of the shortest and longest wavelengths that can be observed from ground are fixed, respectively, by the transparency of the Earth's atmosphere and by the frequency cutoff of the ionosphere. Satellite observations extend the observable radio spectrum. Radio emissions result from thermal and nonthermal mechanisms. Section 3 summarizes the radio thermal observations of the Sun. The thermal emission is produced by thermal bremsstrahlung and also by gyro resonance emission of the electrons in the presence of a magnetic field (mainly in the microwave domain). Thermal emissions originate from regions with distinct physical parameters, and their detection will depend on the observing frequency. The different classes of radio bursts are presented in Sect. 4. They have distinct spectral characteristics and can last from a fraction of second to several hours; this section focuses more particularly on radio bursts that are produced by accelerated electron beams propagating along the magnetic field or by shocks. The impact on technologies of solar radio bursts is briefly discussed in Sect. 5. Observations of radio bursts reveal various forms of activity and acceleration processes that are associated sometimes to large-scale eruptive phenomena that include flares, filament eruptions, Coronal Mass Ejections (CMEs), and shocks. CMEs are the most spectacular large-scale manifestations occurring at the Sun. Radio observations of CME events are presented in Sect. 5. It is shown that radio imaging and spectral observations provide signatures on the initial steps and development of CMEs. The last section concludes that radio observations offer significant insights to understand solar activity, its link with the interplanetary medium, and the consequence on the Sun–Earth system.

1 Introduction

The Sun is a strong radio emitter in a large spectral domain from submillimeter to kilometer wavelengths. Radio observations provide powerful diagnostics

M. Pick: *Radio Emissions from the Sun and the Interplanetary Medium*, Lect. Notes Phys. **699**, 119–142 (2006)
DOI 10.1007/3-540-33759-8_6

on the solar atmosphere and on dynamical phenomena occurring in the solar corona and in the interplanetary medium. Observations at different wavelengths sample different heights in the solar atmosphere, with longer wavelengths referring to higher heights above the photosphere. Therefore, a given event and its related effects can, in principle, be probed from the bottom of the corona to a large distance in the interplanetary medium, beyond the Earth orbit.

Observations are made by radiometers and spectrographs that measure the total flux. Spatially resolved observations are obtained by radio interferometers; radio heliographs are solar dedicated instruments that provide full images of the Sun.

I do not intend here to describe all the topics in which radio astronomy techniques have widely contributed to solar studies. I have rather selected few areas related to the physics of the Sun–Earth system. Excellent reviews were written. The list is long and only a few of them are mentionned here: Kundu [1] Kruger [2]; Solar radio physics [3]; Melrose and McPhédran [4]; Benz [5]; Bastian et al. [6] Aschwanden [7].

2 The General Context of Radio Wave Propagation and Emission

Radio waves can propagate only in a medium where the refractive index is real. The refractive index n for a plasma, neglecting the magnetic field, is $n^2 = 1 - {f_p}^2/f^2$, where f_p and f are, respectively, the plasma and observing frequencies. The electronic density N_e, thus the plasma frequency $f_p \sim {N_e}^2$ of the solar atmosphere, decreases monotonically with increasing altitude; therefore, for each frequency, there is an altitude below that propagation does not take place and the range of heights above the photosphere that is observable by a radio telescope is determined by its frequency window. This is illustrated in Figs. 1 and 2. At 1AU, the plasma frequency is 30 kHz.

In an isotropic medium, the radiation path is determined by the Snell-Descartes law:

$$n \sin \alpha = \text{constant}$$

where α is the angle of propagation relative to the gradient of the refractive index. For increasing index of refraction, as is the case for radiation propagating from the Sun to the Earth, the radiation is refracted toward the direction of the gradient as illustrated in Fig. 3.

Moreover, fluctuations in the refractive index, because of coronal inhomogeneities, cause multipath propagation between the source and the observer. This effect modifies the observed properties of the radio sources, introduces an angular broadening, and therefore prevents very high angular observations of radio emissions. Finally, the limits of the shortest and longest wavelengths that can be observed from ground are fixed, respectively, by the transparency

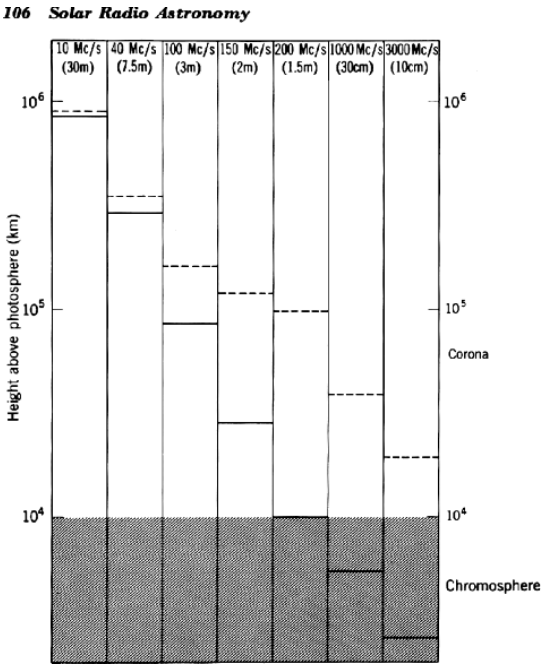

Fig. 1. Levels of zero refractive index in the solar atmosphere in the field-free case and above a large sunspot (3,000 gauss); they also represent the innermost levels from which radiation can escape. *Full line*: the only level in the free-field case as well as the ordinary level (quasi-transverse case) above a sunspot. *Broken line*: the extraordinary level above a sunspot (from [8])

of the Earth's atmosphere and by the frequency cutoff of the ionosphere; indeed, below approximately 10 MHz, which is the plasma frequency of the ionosphere, the radio waves cannot propagate down to the ground. Satellite observations extend the observable radio spectrum.

Radio emissions result from thermal and nonthermal mechanisms. For thermal emissions, the "source" function, B_f is given by the Planck function (Rayleigh–Jeans limit):

$$B_f = k_\mathrm{b} T f^2/c^2$$

where k_b is the Boltzman constant, T the temperature, f the frequency, and c the speed of light.

For nonthermal emissions, an effective temperature T_eff can be similarly defined:

$$B_f = k_\mathrm{b} T_\mathrm{eff} f^2/c^2$$

Spatially resolved observations are limited in angular resolution to a solid angle Ω. The intensity I is defined as the received power emitted per unit area, unit frequency, and unit solid angle:

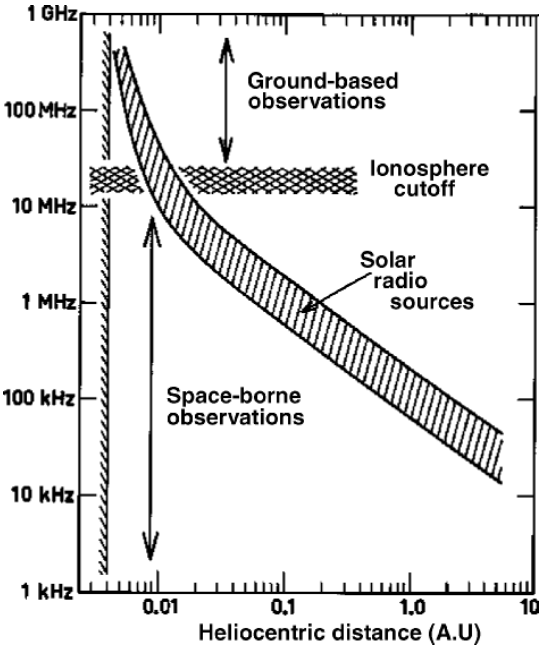

Fig. 2. Variation of the plasma frequency versus altitude in the corona and the interplanetary medium (courtesy of J.L. Bougeret)

$$I_f = k_\mathrm{b} T_\mathrm{b} f^2/c^2$$

where T_b is called the brightness temperature and defined by the above formula.

T_b and $\mathrm{T_{eff}}$ (or T) are related by the radiative transfer equation:

$$dT_\mathrm{b}/d\tau = -T_\mathrm{b} + T_\mathrm{eff}$$

where, $d\tau = kdr$ is the optical depth, k the absorption coefficient of electromagnetic waves, and r the distance along the line of sight.

If T (or T_eff) is constant (e.g., for the quiet corona):

$$T_\mathrm{b} = T(1 - (\exp - \tau))$$

For an optically thick source, $T_\mathrm{b} = T$; for an optically thin source $\tau \ll 1$, $T_\mathrm{b} \sim \tau T$ (e.g. emission of some coronal structures).

The flux of a radio source is the power received per unit surface and unit frequency. It is expressed in solar flux unit (sfu $= 10^{-22}$ $\mathrm{Wm^{-2}\,Hz^{-1}} = 10^4$ Jansky).

In the presence of a magnetic field and in the case of the "cold plasma approximation," two modes of propagation exist, the extraordinary, x, and the ordinary, o, modes (see Fig. 1). The polarization characteristics of the

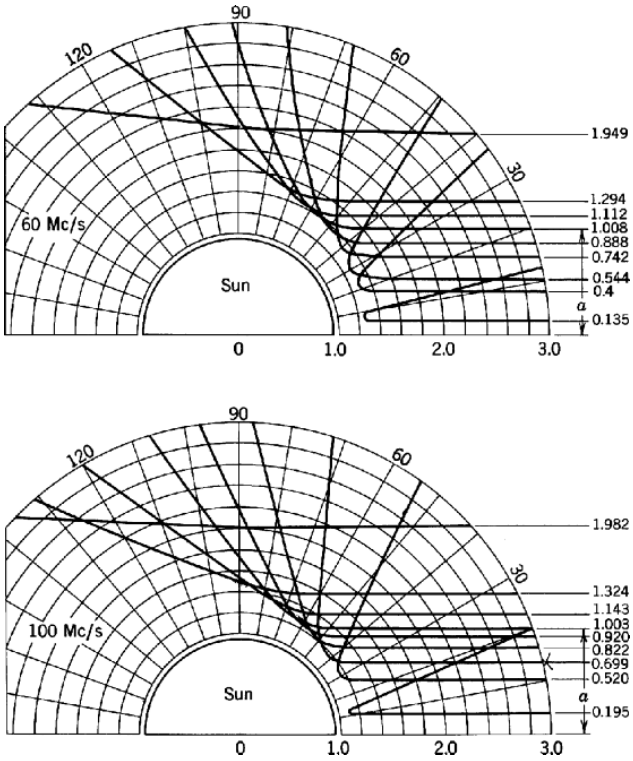

Fig. 3. Ray trajectories in the solar atmosphere for 60 and 100 MHz. The radial scale is in units of 705,000 km (=photospheric radius + 7,650 km). The numbers on the curves give the dimension α in the same unit (from [23])

observed radio waves are determined by the emission mechanism and/or by the propagation conditions. In general, the two electromagnetic modes propagate independently (weak mode coupling) and, if the radiation travels through a region in which the longitudinal component of the magnetic field changes sign, so does the orientation of the circular polarization. Note that this is not the case under strong mode coupling conditions.

3 Thermal Emission from the Sun

Radio observations of the Sun probes its atmosphere at different altitudes; thermal emissions originate from regions with distinct physical parameters and their intensity varies in time. The origin of this slowly varying component (SVC), which is superimposed over the emission of the steady Sun, depends on the frequency of observation.

3.1 Microwave Domain

In the microwave domain, low temperature plasmas in the corona, such as dark filaments, are detected as absorbing objects on the disk and as emitting ones above the limb. Above the active regions, the emission is produced by thermal bremsstrahlung (or free–free emission), resulting from the Coulomb interaction between the plasma electrons and the corresponding ions, and by gyro resonance emission of the electrons in the presence of a magnetic field. Thermal gyro emission resonance [24, 43] results from thermal electrons spiraling along coronal magnetic field lines and is emitted at low harmonics of the local electron gyro frequency ($f = sf_{\mathrm{b}}$) where $s = 1, 2, 3$, and $f_{\mathrm{b}} = 2.8 \times 10^6 \mathrm{B}$. Above the active regions, the enhanced magnetic field strength increases the gyro frequency and the gyro resonance emission can be the dominant thermal radiation process between approximately 3 and 15 GHz. The magnetic field does not exceed a few hundred Gauss in the faculae but, it can reach values up to few thousand Gauss in the sunspot regions. Above 15 GHz, free–free emission will dominate for all regions with magnetic fields below 2,000 Gauss (this value corresponds to the third harmonic of the gyro frequency). An image of the Sun at 17 GHz, seen by the Nobeyama Radio Heliograph (NoRH, [33]), is displayed in Fig. 4.

Note that at 2.8 GHz (10 cm) (flux measurement at this frequency is used as an index of solar activity) the emission above active regions is a combination of the "faculae" (bremsstrahlung) and of the "sunspot" (gyroresonance) components. Note also that an occasional contribution of nonthermal emission in some limited areas of the active regions cannot be excluded [19].

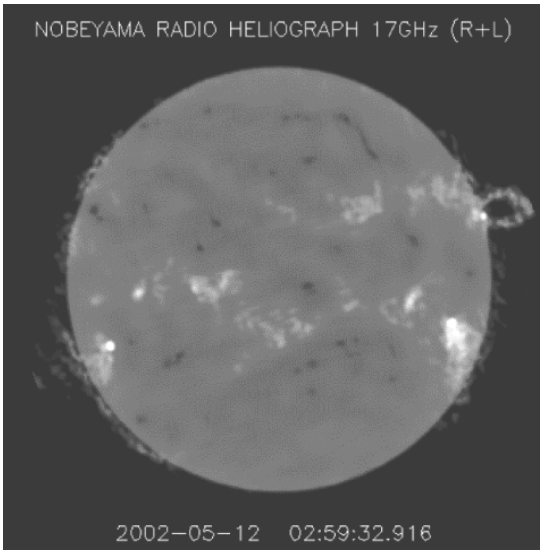

Fig. 4. The Sun seen at 17 GHz by the Nobeyama Radioheliograph

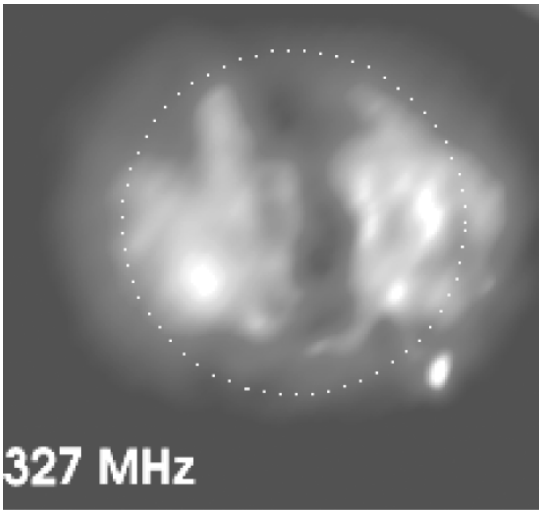

Fig. 5. The corona seen at 327 MHz on October 14, 2000, by the Nanay Radio Heliograph. Note, in particular, the presence of a coronal hole extended in latitude

It is important to point out that spatially resolved observations of the polarization provide local coronal magnetic field measurements. Quantitative and accurate measurements of this magnetic field bring strong constraints on the calculation of magnetic fields extrapolated from measured photospheric fields.

3.2 Decimeter–Meter Domain

Below 0.5 GHz, at metric wavelengths, the thermal emissio originates from higher in the corona, where the magnetic field does not exceed a few Gauss, and at these wavelengths, the SVC will be sensitive to large-scale structures of the corona, including coronal holes, arches, and streamer belt. These emissions are unpolarized. Radio imaging allows, for example, to follow the evolution of the coronal holes that are the source of high velocity solar wind streams detected in the interplanetary medium. An image of the corona seen at 327 MHz, seen by the Nançay Radio Heliograph (NRH, [27]), is shown in Fig. 5.

4 Solar Radio Bursts

A large variety of radio bursts have been reported in the literature; they present distinct spectral characteristics and can last from a fraction of a second to several hours. They have been historically classified into several morphological types. Radio emission offers many diagnostic tools to address questions such as energy release, particle acceleration, and transport. Radio bursts are not necessarily associated with flares.

4.1 Emission Mechanisms

Radio emission produced by nonthermal electrons is attributed to incoherent gyro synchrotron emission and to coherent plasma emission. Their relative contribution depends upon the observing frequency. Gyro synchrotron emission, which is proportional to the number of radiating electrons, usually dominates at frequency above about 3 GHz. This emission provides diagnostics on the ambient plasma, on the energy range of radiating electrons and on their evolution. Coherent plasma emission (electrons radiating in phase) most often dominates at frequencies below 3 GHz and is caused by plasma instabilities driving various modes that produce observable electromagnetic radio waves. Classification of these radio bursts and their relation with emission mechanisms remain arbitrary in many respects. One can however identify the radio bursts due to (i) the traveling of electron beams or shocks through the corona, then through the interplanetary medium; (ii) trapped electrons in coronal loops; and (iii) regions of coronal reconnection or restructuring.

4.2 Electron Beams

Particularly important are the radio bursts produced by electron beams along the magnetic field; these bursts contain many pieces of information on the electron acceleration, injection, and propagation mechanisms, on the beam characteristics and on the medium itself.

Type III bursts are due to electron beams propagating along open magnetic field lines and exciting Langmuir waves at the local plasma frequency of the corona which, in turn, produce a radio emission at the fundamental or at the second harmonic of the plasma frequency. These beams travel through the corona at speeds of a fraction of the light velocity. Because the density (thus the plasma frequency) decreases outward from the Sun, the emission drifts rapidly from high to lower frequencies as shown in Fig. 6. When streams propagate along a coronal loop, a U or J shape is observed on spectrograms (f, t) as illustrated in Fig. 7. Other streams travel through the interplanetary medium; interplanetary kilometric type III bursts (IP) can be detected by experiments aboard space missions. Figure 8 illustrates the progression of an IP type III burst, the in situ detection of the Langmuir waves and of the electron beams. Directional measurements, based on the analysis of the spin modulation of the receiver signal are used to find the source location of IP type III bursts. The source locations projected on the ecliptic plane follow an Archimedean spiral [12].

Radio observations, in the *dm–m* wavelength range, also provide pieces of information on the acceleration region of the electron beams. Type III bursts above 1 GHz generally have a downward motion in the corona. At lower frequencies, typically 0.4–1 GHz, pairs of type III bursts drifting in opposite directions are observed. An example is shown in Fig. 9. In the spectrum, the frequency location of the change from upward to downward moving beams

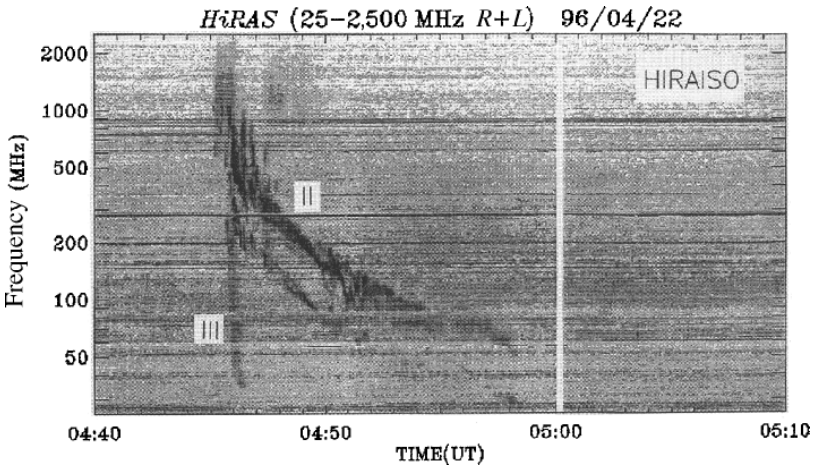

Fig. 6. Dynamical spectrum of April 22, 1996, event from Hiraiso Terrestrial Research Center: type III and type II bursts emitted in the corona (after [21])

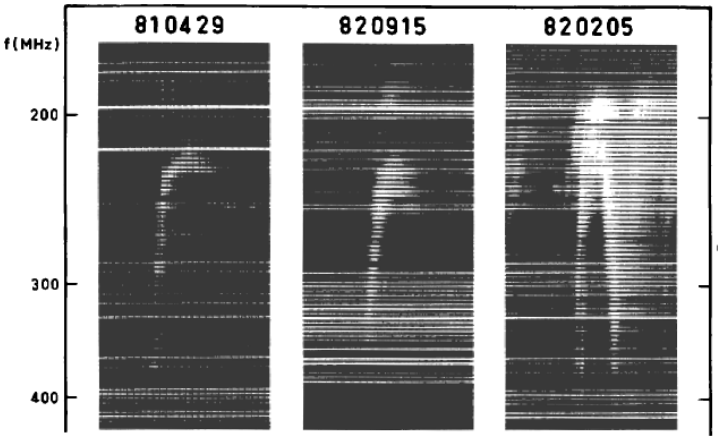

Fig. 7. Dynamic spectrum displayed on film for three type U bursts (from [39])

corresponds to the region of electron acceleration. Another information is given by narrow frequency spikes that are observed just above the starting frequency of type III bursts; these spikes are closely related to the acceleration region (Fig. 10). Radio bursts produced by electron beams are often produced during the impulsive phase of solar flares. It will be seen in Sect. 4.4 how the observation of radio emission produced by electron beams has contributed to the understanding and development of flare models.

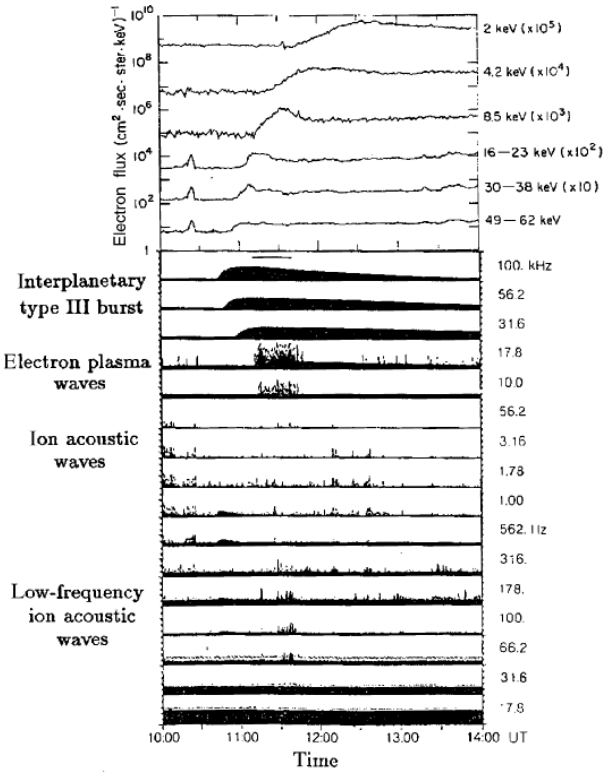

Fig. 8. Electron flux and waves observed by the ISEE3 satellite at the Lagrangian point L1 between the Sun and the Earth. The *top panel* shows nonthermal electrons in different energy channels. The slower electrons arrive later. The four upper channels in the *bottom panel* show an interplanetary type III burst and its drift in frequency. When the type III burst is detected at the local plasma frequency, near the 17.8 kHz channel, Langmuir electron plasma waves are also detected at the same time. Comparison between top and bottom panels shows that these waves are excited by electrons with energy of approximately 8.5 keV. Ion acoustic waves are also detected during this event (after [28])

4.3 Shocks

Type II bursts are caused by electrons accelerated by shocks at the local plasma frequency and/or at its harmonics. Two types of shocks are considered to produce the type II bursts: the coronal shocks that generate metric type II bursts (Fig. 6) and the Coronal Mass Ejection (CME) driven shocks that generate IP type II bursts. Figure 11 shows an IP type II burst measured by the WAVES radiospectrograph aboard the WIND spacecraft [15]. Metric type II bursts are associated with flares and most often vanish before reaching the high corona. The general finding is that they are produced by blast coronal waves. Indeed, they are associated with Hα Moreton waves that were

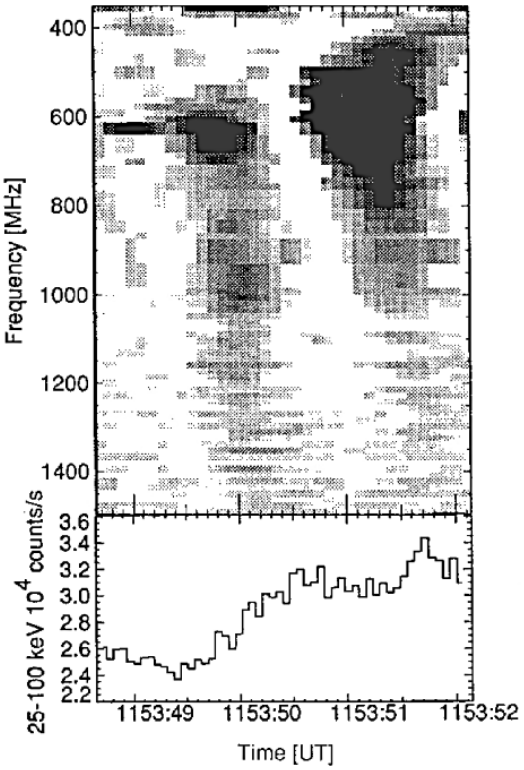

Fig. 9. *Top*: radio flux density of solar type III emission observed by the Zurich spectrometer. Two reverse slope bursts mark two downgoing beams. The second is accompanied by a simultaneous upgoing beam ($f \leq 550$ MHz). *Bottom*: hard X-ray counting rate measured by BATSE on the GRO satellite (from [8])

discovered by Moreton and Ramsey [32]. Moreton waves travel away from the flare region with speeds ranging from a few hundred to a few thousand kilometers per second. They are interpreted as the chromospheric trace of MHD coronal waves.

IP type II bursts are excited by CME-driven shocks formed, most often, at an altitude above 1 solar radius. Figure 8 shows that IP type II bursts are confined in an instantaneous narrow frequency band. Metric and IP type II bursts, when observed together, have distinct drift rates and distinct locations.

4.4 Radio Emission During Flares and Large-Scale Disturbances

During flares, a large part of the energy release is initially converted into energetic electrons and ions. The plasma is heated and particles are accelerated to relativistic energies on a short-time scale. A large flare may require the acceleration of 10^{37} electron $\sec^{-1}$ to energies >20 keV within tens of seconds.

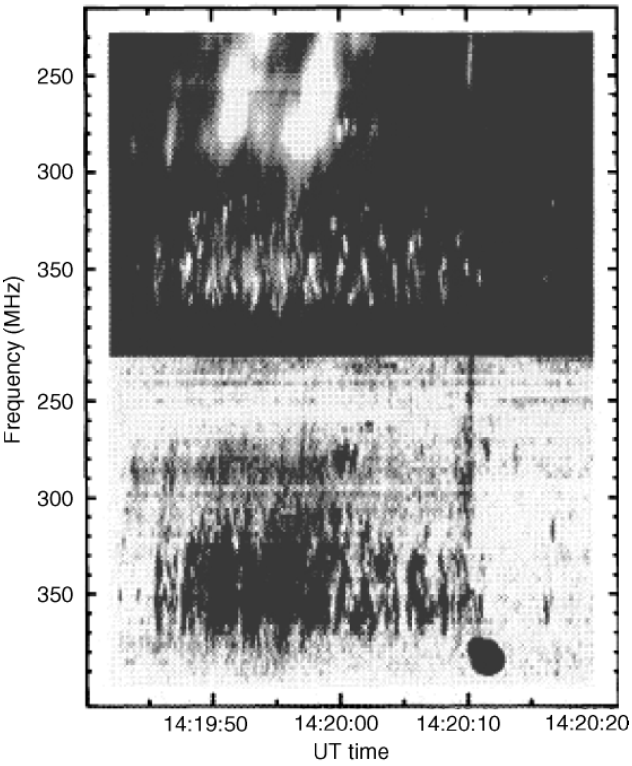

Fig. 10. Spectrogram of metric spikes (above 325 MHz) and type III bursts (below 325 MHz) observed on January 1, 1981, by the Ikarus, spectrometer near Zurich (Switzerland) *Top*: enhanced total flux density. *Bottom*: degree of polarization, left circular polarization, is dark (from [13])

Synchrotron or gyro synchrotron emission of electrons is observed even in the smallest flares. Synchrotron emission produced by MeV electrons dominates at frequencies >3 GHz. Microwaves, Soft (SXR), and hard (HXR) radiations are spatially and temporally correlated: they are produced by the same population of electrons accelerated and partly trapped in loop systems. SXR emission (heated plasma) is produced in coronal magnetic loops. The dominant sources of HXR emission are located in conjugate magnetic foot points in the low corona. Microwave emission is produced in the entire volume accessible to nonthermal electrons (e.g. [6]). Figure 12 shows a schematic representation of a flare model derived from radio observations of electron beams and from X-ray observations.

Radio emission associated with flares at metric and decimetric wavelengths corresponds to a wide variety of bursts. Broadband incoherent gyro synchrotron radiation and coherent plasma radiation are both commonly observed in this frequency range. Radio observations, and also, occasionally, gamma-ray

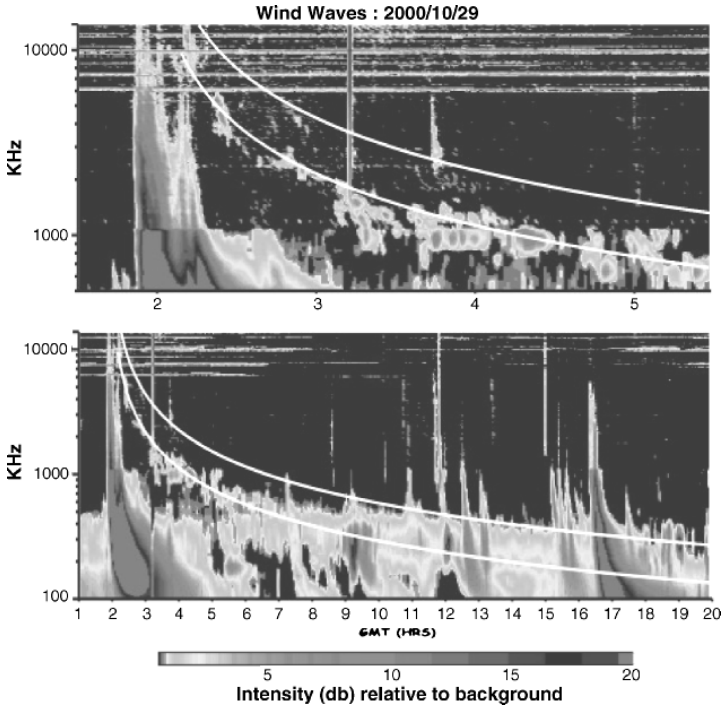

Fig. 11. Dynamic spectrum from the WAVES experiment on Wind. The interplanetary type II burst can be seen as the slow frequency-drifting structure. The two *solid curves* indicate calculated profiles of the plasma-frequency fundamental and harmonic radiation that would be produced by the shock at the initial shock speed of 800 kms^1 and constant acceleration of 1.25 ms^2 (from [41])

observations (e.g., [25]), revealed that this sequence of flare acceleration in the low corona can be followed by time extended acceleration, lasting from tens of minutes to hours. Figure 13 gives a simplified overview on the radio bursts associated with flares and of the subsequent activity. After the flare episode has taken place, energetic electrons produce type IV radio bursts that are broadband continua. Moving type IV bursts are produced by electrons radiating in ascending arches, whereas stationary type IV bursts are observed for several hours and, then, evolve gradually into noise storms. Noise storms are the most common form of activity at metric and decametre wavelengths; narrowband, spiky type I bursts (type III at longer wave lengths) are superposed to the continuum. Noise storms are produced by supra-thermal electrons accelerated continuously over time scales of hours or days. Noise storm activity is often detected in the absence of large-flares.

Finally, the current understanding of this complex zoology is that these various forms of activity and acceleration processes are associated to large-scale eruptive phenomena that include flares, filament eruptions, CMEs and

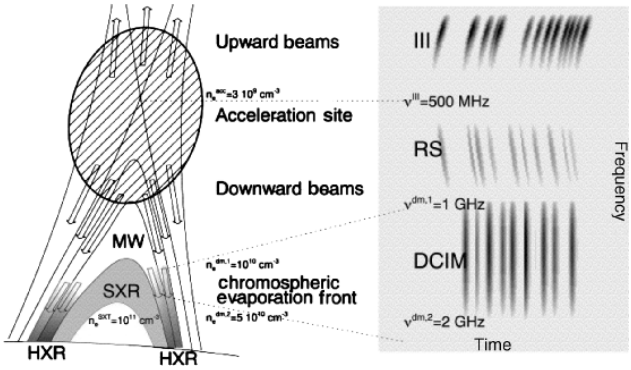

Fig. 12. *Left panel*: diagram of a flare model envisioning magnetic reconnection and chromosphere evaporation processes. *Right panel*: a dynamic radio spectrum with radio bursts indicated in a frequency versus time diagram. The acceleration site is located at the cusp from where electron beams are accelerated in upward (type III) and downward directions (reverse bursts). Downward-precipitating electron beams can be traced as decimetric bursts with almost infinite rate in the 1–2 GHz range (from [9])

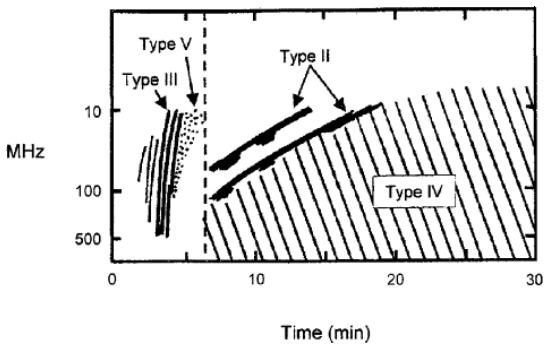

Fig. 13. Idealized sketch of a complete radio event [42]. *Left of the broken vertical line*: impulsive phase of the flare, described in Fig. 12

shocks. These phenomena often occur simultaneously and are due to a fast release of the magnetically stored energy through the breaking of the coronal magnetic field structure. This coincidence emphasizes the difficulty of understanding the link between solar processes and Solar Energetic Particle events (SEP) measured in the interplanetary medium.

5 Impact on Technologies of Solar Radio Bursts

The effects of solar activity on technologies were firmly recognized more than one century ago and have, since this period, hugely expanded with

the increasing complexity of those technologies. The interference of solar radio bursts with radar systems was discovered during the Second World War (1942). These radio bursts can affect various systems, as for example, a reduction in received Global Positioning Satellite (GPS) signals, resulting in a degradation of the signal acquisition (see for a review Lanzerotti, pp. 1–14, in [20]).

As shown in the previous sections, variations in solar radio noise levels, that are driven by the physical emitting mechanisms, are strongly dependent on frequency and can attain very large amplitudes, many dB above the quiet Sun. Consequently, the prediction of solar radio bursts that might produce interference in radio receiving systems will depend on the operating frequency. For this purpose, a few recent investigations have been made on the amplitude distribution of solar radio bursts [10, 34, 35], analyzed 412 solar radio bursts, recorded over 2 years, in the microwave range 1.2–1.8 GHz. They found that the probability for solar interference for systems operating at $f > 2.6$ GHz, with a noise level $\eta = 1$ is low, but that it increases significantly at frequencies $f < 2.6$ GHz and also for systems with higher sensitivity $\eta < 1$.

The yearly dependence and the 11-year solar cycle effect on the daily number of burst events, for events with peak flux densities $>10^3$ and $>10^4$ SFU, were reported by Lanzerotti, 2004; this is illustrated in Fig. 14. Three frequency bands, 1–2 , 2–4 , 4–10 GHz, are shown in this figure. However, whereas the impacts of radio events on technologies are now widely recognized, the effects have not yet been precisely quantified. Lanzerotti (2004), assuming a solar level of 10^3 SFU as a context "threshold," derived from Fig. 14 that about one event of this size can be expected at least every 10–20 days, with a larger occurrence rate at the solar cycle maximum. He concluded that the chances for interference at a given cell site by an event with peak flux density $>10^3$ SFU would be a few times per year.

6 Radio Signatures of Coronal and Interplanetary Coronal Mass Ejections

Coronal Mass Ejections (CMEs) are the most spectacular large-scale manifestations of activity occurring at the Sun. They correspond to the destabilization of a large portion of the corona. 10^{14}–10^{16} g of matter are ejected into the heliosphere with speeds ranging from 100 to 2000 km/s. Typical CMEs seen by coronagraphs span about 50° in angular extent with a few outstanding events reaching angular extents greater than 100°. CMEs are often associated with eruptive prominences (EP) or disappearing filaments on the solar disk. In that case, the CMEs contain three distinct regions: a bright compression front that surrounds a dark cavity and a bright core inside. The bright core is formed by the material ejected from the cool and dense prominence. CMEs have frequently a much more complex structure than the one just described:

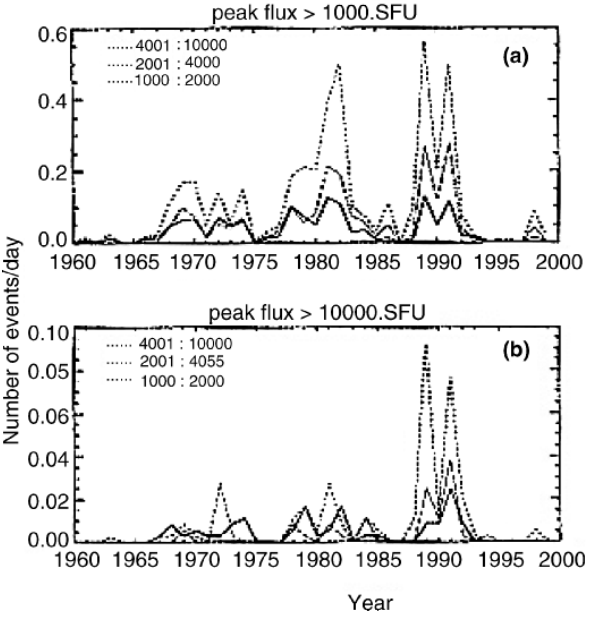

Fig. 14. Total number of events per day as a function of time in years (**a**) for peak flux $> 10^3$ SFU and (**b**) $> 10^4$ SFU. The frequency ranges are 1–2, 2–4, and 4–120 GHz (from Lanzerotti, in [20])

they involve multiple magnetic flux systems and neutral lines. As already mentioned, CMEs and flares can be produced jointly but it is now well established that there is no causal relationship between these two phenomena. CMEs can also drive interplanetary shocks (type II bursts) that together with Earth-directed CMEs can produce large transient interplanetary and geomagnetic disturbances (Sect. 6.3). Therefore, their study is very important for understanding and predicting Space Weather conditions. CMEs were most often observed by white-light orbiting coronagraphs which occult the solar disk and which cannot observe their initiation and early stages of development. Since 1996, the LASCO instrument (Large Angular Spectrometric Coronagraph) aboard the SOHO mission has provided for the first time a large field of view from 1.1 to approximately 30 solar radii [17]. Combined radio/EUV/LASCO observations have led to new insights on the physics of CMEs.

Radio telescopes can observe both the solar disk and the corona out to a few solar radii with a high cadence (<1 s), while the cadence of CME observations made by space-borne instruments is severely limited. Radio observations are sensitive to different aspects of CMEs depending on the selected wavelength domain.

Figure 15 shows the evolution of a prominence observed in radio, at microwave lengths, which was associated with a CME. Prominences have a low

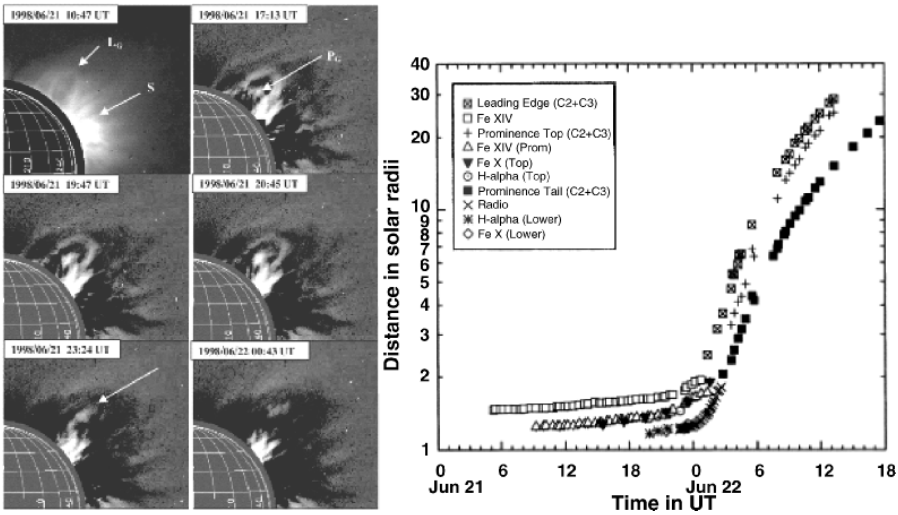

Fig. 15. *Left panel*: Time-lapse images taken by LASCO-C1 coronagraph in Fe XIV emission line. The field of view is 1.1-3 Rs. All the images shown here have been substracted from a reference image taken before the occurrence of the CME, except the one at 10:47 UT. The image at 10:47 UT is an online image with a nearby continuum and is given in order to show the bright streamer adjacent to the CME. *Right panel*: plot of height versus time (on log scale) for different features of the CME, viz, the leading edge, the prominence top and the tail, as measured from the images obtained at different wavelengths by various instruments. (from [40])

temperature (8000°), a high density ($\sim 10^{10}$–10^{11} cm^{-3}) and are optically thick at microwave frequencies. The prominence first exhibited a progressive evolution then, during the eruption, it heats up and expands rapidly. Prominences are likely to become CME cores. At decimeter wavelengths, observations of filament eruptions showed that both the filament and the precursor to the white light CME cavity can be detected. There is a clear continuity between the radio thermal depression observed in the low corona, which is identified to the filament cavity, and the corresponding CME when they are observed together [44].

Meter activity is often observed in association with CMEs and in the absence of flares; a close spatial and temporal relationship exists between noise storm enhancements and white light transient activity such as CMEs or additional material in the corona at the vicinity of the radio source [26]. The origin of this nonthermal activity is due to emerging magnetic loops interacting with overlying loops and leading to coronal magnetic reconfiguration. In the presence of flares, strong radio bursts are observed over a broad frequency range. This is discussed in the next section.

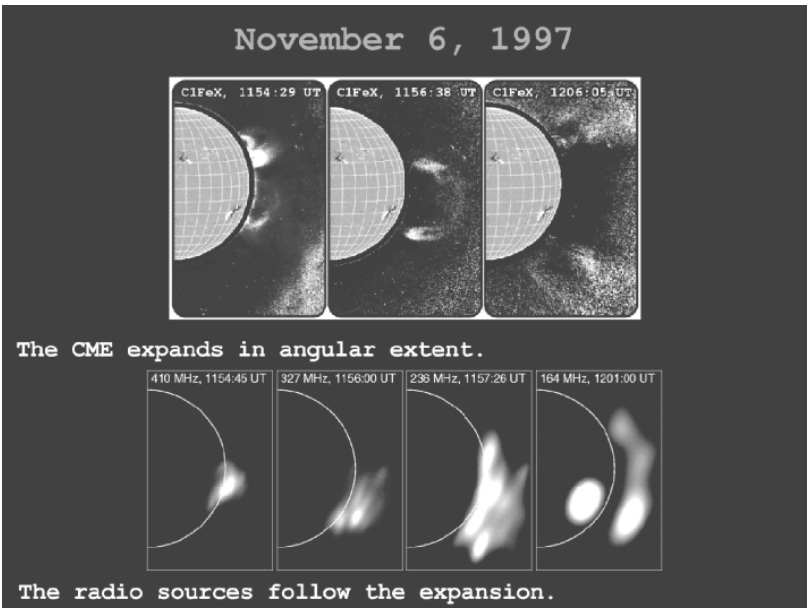

Fig. 16. November 6, 1997. *Top*: radio images at distinct frequencies which show that the emission expanded progressively from the vicinity of the flare region toward the northern hemisphere. *Bottom*: composite image of a LASCO-C2 coronagraph image with a radio image at 164 MHz (after [29])

6.1 Flare/CME Events: Lift-off and Angular Spread in the Corona

Radio imaging of fast flare CME events shows that many of them originate from a rather small coronal region, in the vicinity of the flare site and expand by successive magnetic interactions at progressively larger distances from the flare site; signatures of these interactions are detected by bursts of nonthermal origin, in the dm–m wavelength domain. CMEs reach their full extent in the low corona (below 2Rs) on a time scale of a few minutes. This time scale corresponds to disturbances with speeds of 1,000 km/s which were identified with coronal type II bursts by on-the-disk observations. An important conclusion of these studies is that tracing the space time evolution of the metric emission, with a temporal cadence of typically 10s, easily allows to follow the opening of CMEs. This is illustrated, for both a limb and an on-disk event, in Figs. 16 and 17 for a limb event [29] and in Fig. 18 for an on-disk event [38]. Figure 17 displays two plots showing the space time evolution of the limb event observed by the NRH at 164 MHz: by integrating the NRH solar images in the north–south and east–west directions respectively, one obtains two dimensional scans that, when displayed in sequence, provide the evolution of the radio emission. This figure exhibits a clear radio signature of the progression in latitude of the CME event and the corresponding speed of the disturbance

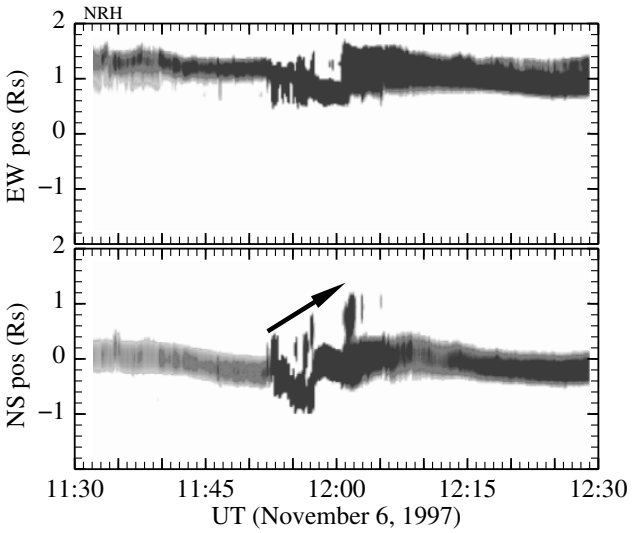

Fig. 17. November 6, 1997: two one-dimensional plots along east–west *top* and north–south *bottom* directions showing the space-time evolution of the event at 164 MHz (from [37])

can be easily estimated [37]. However, this result cannot be generalized; other flare/CME events show, indeed, that they can span over 90° in so short a time that it is incompatible with the preceding scenario. These events suggest that large interconnecting loops are ejected together. The triggering of these events could be caused by coronal reconnection at a magnetic null point leading to the destabilization of the system and the ejection of large interconnecting loops [30].

6.2 Direct Radio CME Imaging

For events associated with flaring regions located behind the limb, faint emissions can be detected over the solar limb and directly compared to white light coronagraph emissions. Radio loops can be detected behind the CME front. The emission is nonthermal gyrosynchrotron from electrons with energy of a few MeV. These observations, presently rather rare, are important as they allow to obtain precise pieces of information on the CME structures such as constraints on the thermal plasma density [11]. An example is displayed in Fig. 19.

6.3 Interplanetary Coronal Mass Ejections

It is well established that large, nonrecurrent geomagnetic storms are caused by interplanetary shocks and Interplanetary Coronal Mass Ejections (ICMEs).

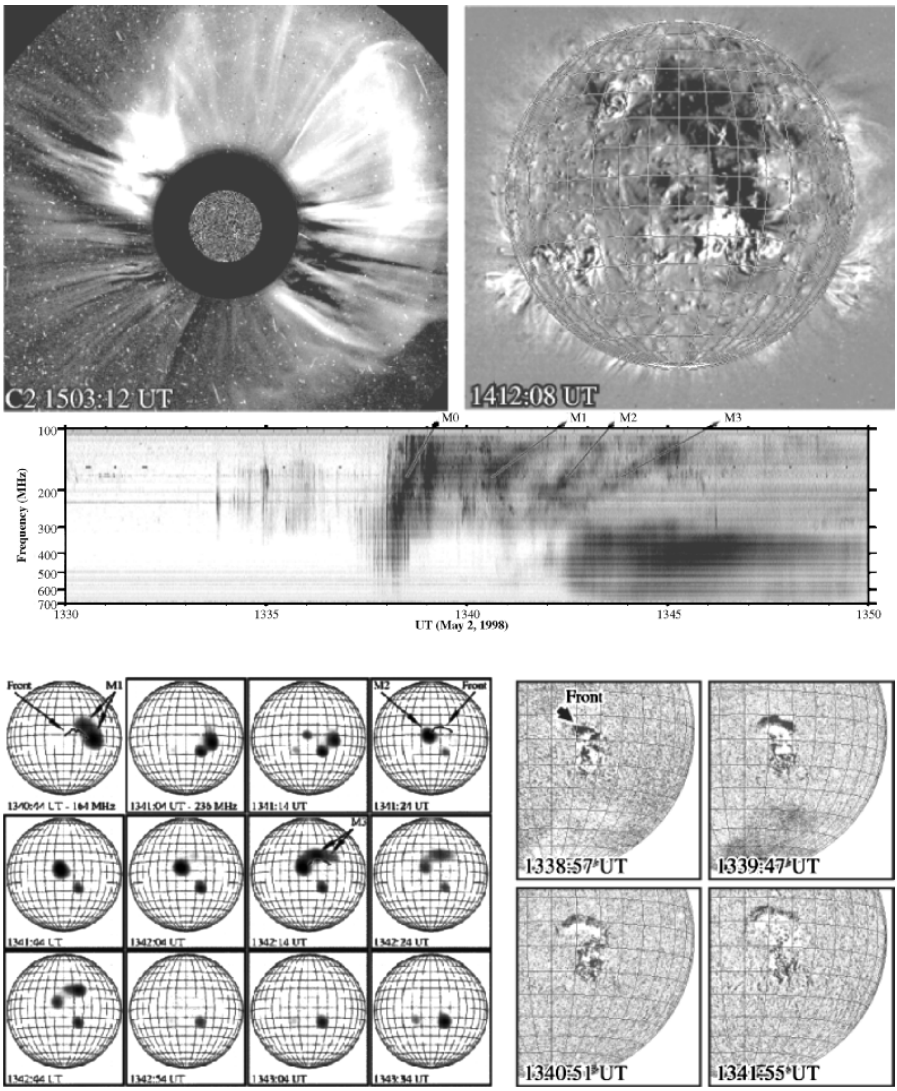

Fig. 18. May 2, 1998. *Upper panel, left*: SOHO LASCO Coronagraph image showing the halo CME. *Upper panel right*; SOHO EIT at 195 Å showing the EIT dimming region. *Middle panel*: Artemis IV radio spectra. The spectral drifting sources are labeled M0 for the one in the flash phase and M1, M2, M3 for the type II-like emission. *Lower panel, right*: running difference of Kanzelhohe Hα images showing the moving wave front (marked by an arrow in the first difference image). *Lower panel, left*: Nancay Radio heliograph images at 164 and 236 MHz showing the location of the sources labeled M1, M2, M3 at selected times (adapted from [38])

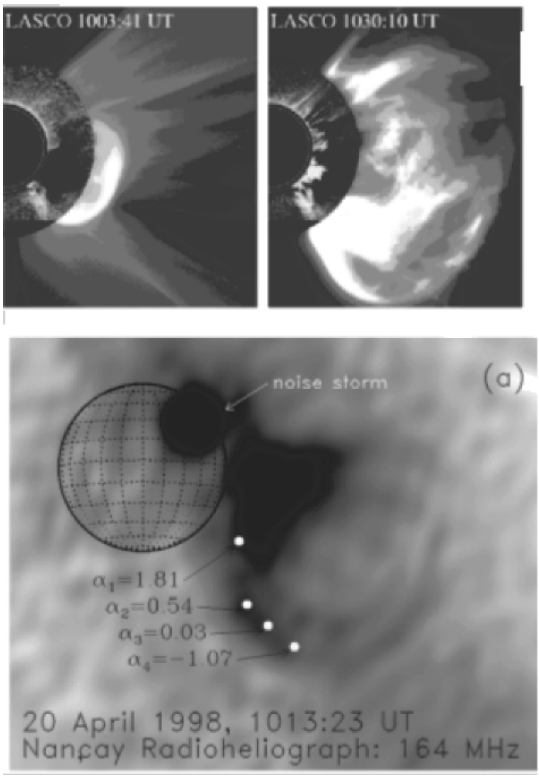

Fig. 19. April 20, 1998: *Upper panel*: Composite LASCO SOHO coronagraph images (C1 and C2) showing the images of a CME. *Lower panel*: Snapshot map of the corresponding radio CME at 164 MHz at 10:13 UT; the brightness of the radio image is saturated in the low corona; the emission is gyrosynchrotron. Numbers on the same figure correspond to spectral index measured at four locations and not discussed here (from [11])

ICMEs, observed in the solar wind, most often include an IP shock preceding a turbulent plasma sheath and an ejecta. The term "magnetic cloud" refers to ICMEs for which ejecta are characterized by a smooth and continuous rotation of the magnetic field (flux rope), [16]. Many CMEs do not produce large disturbances in the solar wind. Moreover, it is often difficult to make a unique association between ICMEs and CMEs. One underlines the importance of on-disk solar observations to identify the solar events and their solar origin that will produce the solar wind disturbances propagating out and reaching the Earth after a transit time of 2–4 days.

Propagating interplanetary disturbances are distorded by the slow and fast solar winds. Interactions between fast and slow CMEs have been identified by long-wavelength radio and white light observations; during these interactions, intense continua are detected, as shown in Fig. 20.

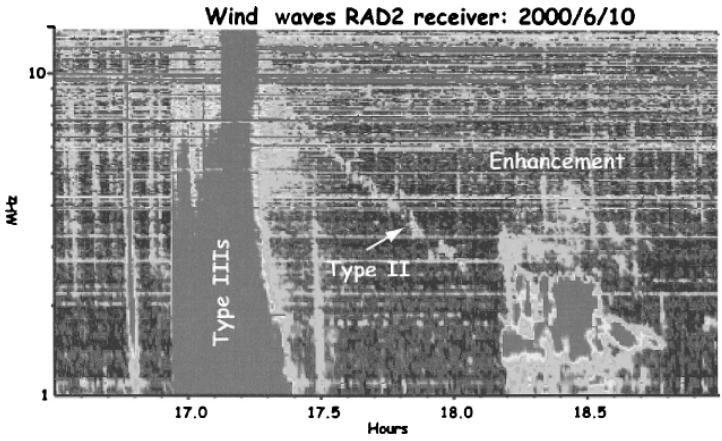

Fig. 20. Example of an hectometric interplanetary type II burst observed by the Wind/WAVES spectrograph in the 1–14 MHz range. The thin dashed feature is a type II burst. A bright emission is detected between 18.12 and 18.48 UT (from [22])

7 Concluding Remarks: Importance of Radio Observations for Understanding the Sun–Earth System

From the work discussed in the previous sections, one can derive several key areas where radio observations offer significant insights to understand solar activity, its link with the interplanetary medium, and the consequences on the Sun–Earth system. These observations are important to:

- Probe a given event and its related effects from the bottom of the corona to large distances in the interplanetary medium.
- Establish the link between activity on the Sun's surface and the resulting evolution of the corona, the origin of electron acceleration, transport in the corona and then in the interplanetary medium.
- Provide key parameters characterizing the coupling between the corona and the interplanetary medium through constant monitoring of the solar atmosphere at different altitudes; initiate synoptic studies of filaments, active regions, coronal holes, and streamer belts. One important goal is, for instance, to investigate the relationship between the space and time evolution of coronal holes and that of fast solar wind streams associated with geomagnetic activity.
- Detect the onset of CMEs, visualize their development in the corona, identify those that are Earth-directed, track their progression through the interplanetary medium, and then predict space Earth conditions. Orientation and magnetic polarity of filaments associated with CME occurrence often determine the sign of the transverse B_z component of the interplanetary magnetic field [14]. The probability of reconnection between the IP and

magnetospheric magnetic fields will depend on the sign of B_z. Severe geomagnetic storms are produced when these two fields reconnect.

Many synoptic studies that modern telescopes can easily achieve are still needed to define, in an operational way, the parameters that will be necessary for Space Weather applications. Ground-based instruments have the potentiality of giving information in areas where space-based instruments cannot. But, to achieve this goal, one of the most obvious needs is to develop multifrequency radio imaging of the Sun at different locations. Also, radio spectral data that contribute in obtaining a complete specification of the radio bursts are necessary. Although many sophisticated radio spectrographs have been constructed at different locations, no adequate spectral coverage is still achieved. The situation certainly needs to be improved.

In conclusion, I would like to stress the importance for Space Weather applications of

- continuous radio patrols at various frequencies to predict their effects on various systems;
- radio multifrequency imaging observations, which, obtained at high cadence, allow accurate and prompt vizualisation of the on-the-disk development of fast halo CMEs and an estimate of their angular expansion. Their probability to reach the Earth environment can be, in principle, easily predicted.

The author thanks Alain Kerdraon and the referee for helpful comments, and J.P. Rozelot and O. Malandraki for a careful reading of the manuscript.

References

1. M.R. Kundu: *Solar Radioastronomy* (Intersience Publishers, a division of John Wiley and Sons, New York, 1965)
2. A. Kruger: *Introduction to Solar Radio Astronomy and Radio Physics* (D. Reidel, Dordrecht, the Netherlands, 1979)
3. Solar Radio Physics: ed by D.J. McLean, N.R. Labrum (Cambridge University Press, 1985)
4. D.B. Melrose, R.C. McPhedran: *Electromagnetic Processes in Dispersive Media* (Cambridge Unversity Press, Cambridge, UK, 1991)
5. A.O. Benz: In *Plasma Astrophysics*, vol. **184** (Kluwer Academic Publishers, Dordrrecht, the Netherlands 1993)
6. T.S. Bastian, A.O. Benz, D.E. Gary: Annu. Rev. Astron. Astrophys., **36**, 131–188. (1998)
7. M.J. Aschwanden: Space Sci. Rev. **101**, 1–2 (2002)
8. M.J. Aschwanden, A.O. Benz, R.A. Schwartz: ApJ **417**, 790 (1993)
9. M.J. Aschwanden, A.O. Benz: ApJ **480**, 825–39 (1997)
10. B. Bala, L.J. Lanzerotti, D.E. Gary, D.J. Thomson: Radio Science **37**, 2 (2002)
11. T.S. Bastian, M. Pick, D. Kerdraon, D. Maia, A. Vourlidas: ApJ **20**, L 65–69 (2001)

12. M.M. Baumback, W.S. Kurth, D.A. Gurnett: Solar Phys. **48**, 361–380 (1976)
13. A.O. Benz, A. Csillaghy, M.J. Aschwanden: Astron. Astrophys. **309**, 291–300 (1996)
14. V. Bothmer, D.M. Rust: Geophys. Monogr. **99**, 139–146 (1999)
15. J.L. Bougeret, M.L. Kaiser, P.J. Kellog et al.: Space Sci. Rev. **71**, 231–263 (1995)
16. L. Burlaga, E. Sittler, F. Mariani, R. Schwenn: J. Geophys. Res. **86**, 6673–6684 (1981)
17. G.E. Brueckner, 14 coauthors: Solar Phys. **162**, 357–402 (1995)
18. H.V. Cane, Jr. N.R. Sheeley, R.A. Howard: J. Geophys. Res. **92**, 9869–9874 (1987)
19. F. Drago-Chiuderi, C. Alissandrakis, M. Hagyard: Solar Phys **112**, 89 (1987)
20. D.E. Gary, C.U. Keller: *Solar and Space Weather Radiophysics - Current Status and Future Developments*, ed. by Dale E. Gary, Center for Solar-Terrestrial Research, New Jersey Institute of Technology, Newark, NJ., USA; Christoph U. Keller, National Solar Observatory, Tucson, AZ, USA ASTROPHYSICS AND SPACE SCIENCE LIBRARY Vol. 314 (Kluwer Academic Publishers, Dordrecht, 2004)
21. N. Gopalswamy, 8 coauthors: J. Geophys. Res. **105**, A1, 307–316 (1998)
22. N. Gopalswamy, S. Yashiro, M.L. Kaiser, R.A. Howard, J.L. Bougeret: ApJ (Lett.) **548**, L 91–94 (2001)
23. J.C. Jaeger, K.C. Westfold: Aust. J. Sci. Res. **A2**, 322 (1949)
24. T. Kakinuma, G. Swarup: ApJ **39**, 5 (1962)
25. G. Kanbach, 9 coauthors: Astron. Astrophys. **97**, 349–353 (1983)
26. A. Kerdraon, M. Pick, G. Trottet: ApJ (Lett.), **265**, L 19 (1983)
27. A. Kerdraon, J.M. Delouis: In: *Coronal Physics from Radio and Space Observations*, vol. **483** ed by G. Trottet (Springer, Berlin 1997) pp. 192–201.
28. R.P. Lin, W.K. Levedahl, W. Lotko, D.A. Gurnett, F.L. Scarf: ApJ **308**, 954 (1986)
29. D. Maia, A. Vourlidas, M. Pick, R. Howard, R. Schwenn, A. Magalhaes: J. Geophys. Res. **104**, 12, 57 (1999)
30. D. Maia, G. Aulanier, S.J. Wang, M. Pick, J.M. Malherbe, J.P. Delaboudinière: Astron. Astrophys., in press (2003)
31. C. Marqué, P. Lantos, J.P. Delaboudiniere: Astron. Astrophys. **387**, 317–325 (2002)
32. G.E. Moreton, H.E. Ramsey: PASP **72**, 428, 357 (1960)
33. H. Nakajima, 26 coauthors: Proc. IEEE **82**, 705 (1994)
34. G.M. Nita, D.E. Gary, L.J. Gary, D.J. Thomson: ApJ **570**, 423 (2002)
35. G.M. Nita, D.E. Gary, J. Lee: ApJ **605**, 528 (2004)
36. J.L. Pawsey, S.F. Smerd: *Solar Radio Emission, the Sun* ed by G.P. Kuiper (University of Chicago Press, Chicago, 1953)
37. M. Pick, D. Maia, Marqué.: Advances in Space Res., in press (2003)
38. S.D. Pohjolainen, 9 coauthors.: ApJ **556**, 421–431 (2001)
39. M. Poquerusse, J.L. Bougeret, C. Caroubalos: Astron. and Astrophys. **136**, 10–16 (1984)
40. N. Srivastava, R. Schwenn, B. Inhester, S.F. Martin, Y. Hanaoka: ApJ **534**, 468–481 (2000)
41. J. Torsti, 5 authors: ApJ **573**, 1, L59–L63 (2002)
42. J.P. Wild, S.F. Smerd, A.A. Weiss: Ann. Rev. Astron. Astrophys. **1**, 291 (1963)
43. V.V. Zheleznyakov: Soviet Astron. **6**, 3 (1962)
44. Marque et al.: (2002)

The Sun, The Earth, and the Space Weather

F. Portier-Fozzani and Team Nina[1]

Le Neptune E1, Boite a Lettres 146, 8 Quai des Docks, F-06300 Nice On leave from: STEREO Team, Max Planck Institut fur Aeronomie, Max Planck Strasse 2, 37191 Katlenburg-Lindau, Germany
fabrice.3DSun@free.fr

Abstract. Determining when GPS gives false positioning due to Space Weather consequences has been one of the aims in a study done by Team Nina 2002 during the Alpbach Summer School. For that, TEC maps (Total Electron Contents of the Earth atmosphere at a certain position) must be derived because the precision is invert proportional to the number of particles along the line of sight for satellites. These maps are sensible to the fluctuations day/night but also particles injections coming from the solar corona via Coronal Mass Ejections (CMEs) or Coronal Holes (CHs). Also a 3D prevision of which structures could erupt toward the magnetosphere are needed for these aspects of Space Weather. We first present the SOHO mission and its European data base MEDOC at IAS. SOHO has 12 instruments including a EUV imageur EIT and 3 coronagraphs LASCO. Densities and temperatures can be measured by SOHO/EIT wavelength ratios and the spectroscopic CHIANTI code. SOHO/EIT has observed CMEs evolution in projection. If the CMEs are coming toward the Earth, magnetosphere perturbations can be observed. The understanding and the forecasting need 3D observations and interpretations of such structures. As the solar corona is optically thin, thus the intensity is

[1] Team Nina was formed at Alpbach Summer School 2002 by F Portier-Fozzani (Max Planck Institute fuer Aeronomie, Germany), P. Puhl-Quinn (Max-Planck-Institut fur extraterrestrische Physik, Garching, Germany), M. Grill (Lancaster University, UK), G. Kleindienst (University Braunschweig, Germany), C. Siponen (University of Turku, Finland), N. Partamies (Nokia, Finland), E. Huttunen (University of Helsinki, Finland), S. Apatenkov (Department of Geophysics, Institute of Physics, St. Petersburg State University, Russia), S. Kiehas (University of Graz, Austria), B. Luethi (Space Research & Planetary Sciences, University of Bern, Switzerland), D. Martini (Geophysical Department of Hungarian Academy of Science, Hungary), A. Sarkar (Univ. Goettingen, Germany), A. Asnes (University of Bergen, Norway), S. Mühlbachler (Academy of Science, Austria), T. Sahla (Univ. of Turku, Finland), S. Schäfer (University Braunschweig, Germany), A. Blagau (Max-Planck-Institut fuer Plasmaphysik, Germany), M. Haberreiter (World Radiation Center, Davos, Switzerland), S. Heidicke (Hochschule Aachen, Germany), V. Sterken (Delft University of Technology, Netherlands), T. Thibert (Université de Liège, Belgium), and tutor: Nina von Krusenstierna (aerotechtelub, SAAB Group Company, Sweden).

F. Portier-Fozzani and T. Nina: *Thr Sun, The Earth and the Space Weather*, Lect. Notes Phys. **699**, 143–164 (2006)
DOI 10.1007/3-540-33759-8_7

deduced from the emission measure integrated along the line of sight. This integration creates uncertainties when we want to determine precisely structures morphology and geometrical parameters. Portier-Fozzani [4, 5] has shown that the classical stereo methods do not work directly. Tomography methods would be the most appropriate for optical thin material, but because of the low number of different view angles, these methods cannot be applied easily. Meanwhile, by introducing constraints to stereographics methods such as the geometrical shape of the object (example: loops = circle, plumes = conics,...), it is possible to derive some geometrical parameters. Afterward, the physical coherence of this model purely observational is checked. Thus in Aschwanden et al. (APJ. 515–842 (1999)), we could measure from a more sophisticated method the geometrical parameters of loops. From the EIT image ratio, physical parameters of potential loops are determined. Considering the possibilities of small deformations, Portier-Fozzani, Demoulin et al. (Sp. Sci. Rev. **97**, 51–54 (2001)) took into account that the loops could be twisted. They measured that in an emerging active region, loops appear first twisted and detwist as they expand. This result, if we assume that magnetic helicity has to be conserved [44], gives important stability criteria in function of the size and the twist degrees for coronal loops. Then we describe the future observations that the STEREO/SECCHI Mission will made. It is two satellites separating themselves from 22.5° per year. That will improve stereovision reconstruction that is actually limited to the high temporal dynamic of structures as CMEs involved in Space Weather.

1 Introduction

The Sun–Earth relations are still a subject of research. Meanwhile some criteria are known for alert and Space Weather predictions.

In a first paragraph, we present the data available for Space Weather with examples at the MEDOC Center. In a second paragraph, we present prediction's methods and an example of magnetic disturbances consequences for the user point of view. The Earth atmosphere when receiving the impact can have storms and aurora. Disturbance thus created have consequences for satellite transmissions Global Positioning Systems (GPS) can be out of order because of such storms. During the Alpbach Summer School, a group of people have derived examples of Space Weather service. The main aim was to define alerts and area of fiability of the data obtained by the GPS. It could be very important while for building bridge or reservoir, the precision needs to be few millimeters to avoid any breaking accident of the building structures. Also, because of the possible sudden uncertainties, GPS are not recognized by civil planes for automatic positioning.

Finally, in the third part we explain what could be for the future 3D inputs for a better knowledge of the relation Sun to Earth. We also summarize quickly what are the image processing techniques that 3D coronal specialists are building taking into account the big specificity of the optical thickness of the solar corona.

2 Data Available and MEDOC Center

2.1 SOHO and the MEDOC

The SOHO satellite has been launched in December 1995 and is operated since January 1996. A complete description of the satellite is given by Poland in Domingo, Fleck & Poland, 1995. The satellite is around the L1 Lagrange point, which gives a similar view angle as the Earth with possibility of operating 24 hours per day. It includes different types of instruments that observe the solar interior up to the solar corona. In the context of Space Weather, EUV imageur such as EIT, coronagraphs such as LASCO, and magnetic field measurement for extrapolation modelling such as MDI are the main useful tools. In Orsay (France), the European center MEDOC (Multi-Experiment Data Operations Center for SOHO) receives and archives the data from the satellite. It has the support of many institutions including ESA, and twice a year the satellite is directly controlled from there (the "MEDOC Campaign") giving the opportunities to all Europeans to lead directly there their scientific objectives. A Web page describes completely the center (cf. http://www.medoc-ias.u-psud.fr/). At the Experiment Analysis Facilities, it is possible to use real-time data of all instruments to derive the Space Weather from multiwavelengths observations.

2.2 Correct Use of Multiwavelength Observations

Determination of different area of interests is the first step for Space Weather prediction. As we will derive in the second part, people must beware about active regions loops (ARLs) and sigmoids, twisted filaments, and coronal holes (CHs).

Active region loops can be seen on coronal EUV images (with EIT or CDS for example). These loops correspond to coronal structures where the plasma is frozen by the closed magnetic field over a bipolar (or multipolar) area. On SOHO/EIT, loops can appear differently depending on the wavelength [1].

Usually they appear more distinctly with the transition region line (Fe IX/X, 171 Å, the blue "images") and with the regular coronal line (Fe XII, 195Å, "the green images") than the hotter line (Fe XV, 284Å, "the yellow images"). Note also that same kind of comparisons can be made also with the instruments of the TRACE satellite. Comparing wavelength observations of the same structure can give with the atomic CHIANTI code, information concerning temperatures and densities along and across structures [2–5] (Fig. 1). The importance of the twist and the shear in such structures can give them the aspect of sigmoids ([4, 5] and Fig. 2) in which instabilities such as kink waves can be developed [6]. Sudden detwisting of active region loops correlated to flares and eruption have been derived [7, 8].

Filament channel because of their lower temperature (outside the eruptive time) can be seen on SOHO/EIT 195 usually as an emission depression that

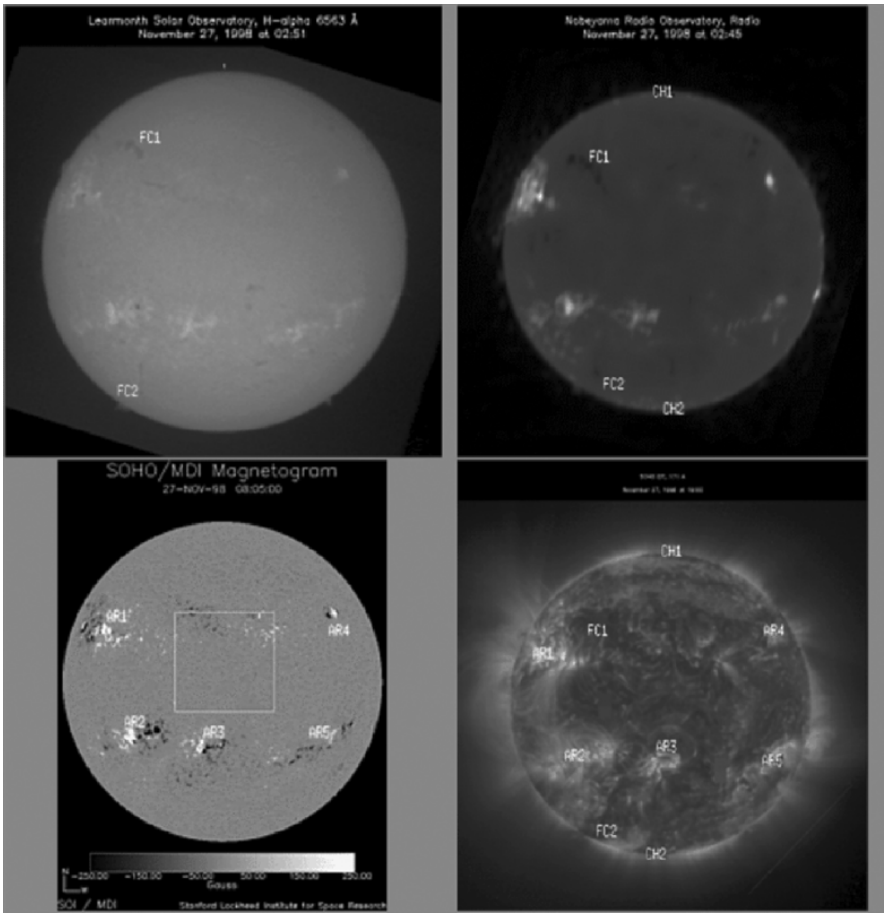

Fig. 1. Multiwavelength observations are useful to determine the nature of the observed structure. *Top left*: H_α disk image; *top right*: Radio observations; *bottom left*: Magnetogram; *bottom right*: EUV coronal image. Example of structures discriminations which appear dark on SOHO/EIT images: Filament Channel -FC- and Coronal Holes -CH- [4, 5]. Coronal Holes are the source of one type of perturbations of the magnetosphere

follows the neutral line. To be sure about areas definition, it is needed to compare with several instruments and Halpha disk images that trace filament. The complete scenario for filament eruption is not completely understood [9] but the nonsymmetries of the structure play a major role in their development. Portier-Fozzani and Noens [28] have shown how the twist degrees decrease while the filament is ejected into the Coronal Mass Ejections. These two results are compatible with the conservation of the magnetic helicity because the degree of twist is transfered into the size of the structure. Thus for the

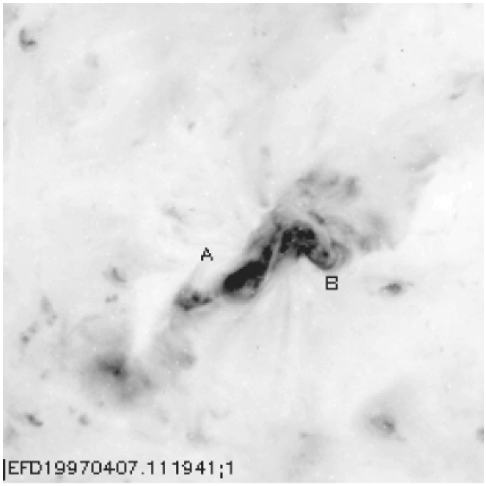

Fig. 2. Example of a sigmoid seen on the disk before an eruption (April 4, 1997; SOHO/EIT 195 Å zoomed with a reversed look up table image). Sigmoids are active region loops sheared or half turn twisted, which are supposed to support filaments. Filament eruptions lead to magnetospheric disturbances if the CMEs are directed toward the Earth and if the magnetic field of the cloud (Bz) is opposite to the Earth magnetic protection ([42], EGU)

case of solar loops for example the stabilized loops after emergence have been measured to follow such law [29]. Bothmer [12] derives the relationship conservation with the interstellar medium.

Coronal holes are unipolar open magnetic field. They can be derived from the magnetograms of SOHO/MDI. Also, and more easily for the observers they can be seen as a dark area on SOHO/EIT transition or coronal lines if it is together seen as a brightness on radio observations of Nobeyama at 87 GHz [4, 20, 41]. The steady fast solar wind originates on open magnetic field lines in coronal holes, which may last for many solar rotations [26] and infers to the Earth when connected through the Parker Spiral.

Thus the main structures that we need for the derivation of the Space Weather are determined. In the next paragraph, from an example of user application, we will derive what to do and what do we need for that kind of Space Weather forecasting.

3 Better GPS Reliability by Space Weather Analysis

3.1 Introduction

We derive here an application of interest for forecasting in the context of Space Weather with a scheme of alert. Geomagnetic storms threaten the integrity of satellite navigation (SN) systems. Because the existing systems are

unable to fully correct the ionospheric delay during severe Space Weather conditions, users of single-frequency SN receivers, such as non-military GPS, experience loss of accuracy in the calculation of their position. A concept called GLOTEC, developed during the Alpbach Summer School 2002, could increase the integrity of satellite navigation systems by

- providing improved ionospheric delay corrections and
- providing an early warning system based on reliable forecasts of geomagnetic storm activity.

In this chapter we mainly summarize the work concerning the prediction while the complete project was also consisting in 3 parts in charge of the Space Weather Prediction Center, the Space Weather Data Center and the Operative Space Weather Mission, respectively.

Satellite Navigation systems use triangulations to calculate the position of a receiver. The integrity and continuity of SN systems are of vital importance for the modern world. Continuity and integrity are affected when one or more satellites become unavailable or unreliable. There are many reasons why this can happen, but one that can be dealt with, is contents and variations in composition of the ionosphere, which lies between the satellite and the receiver. Depending on what you are using, the positioning for this can have more or less severe consequences.

Anyone using a SN solution is potentially affected by the problem of EM (emission measure) signal transmission through the ionosphere. Whether you are laying a road or simply out for a walk in the woods, you might suddenly be without the positioning information on which you are relying.

3.2 Background on Existing SN Systems

The GPS and Galileo systems consist of fleets of positioning satellites (24 for GPS and 27 for Galileo) that transmit signals to receivers on the ground. They send their position and time information. The similarities and differences between the two systems are summarized in Table 1.

For users of single-frequency SN receivers, the "Best of All Possible Worlds" situation would be to have contact with at least three of these positioning satellites and to receive their information unaltered. In reality, there are obstacles of three forms:

1. the incorrect satellite ephemerids which introduce errors in the satellite positioning for the user point of view,
2. the poor geometry of the satellites constellation, and
3. the plasma regions variable between satellites and receivers.

Ionospheric delays (possibly causing errors on the order of 60 m) are by far the largest effects that compromise integrity and continuity of SN systems. The left side of Fig. 3 illustrates these effects. They are caused by refraction

Table 1. Comparing properties of Satellite Navigation Systems. MEO signifies Medium Earth Orbits

Nb. of sat.	GPS 24+3 spares	Galileo 27+3 spares	Glonass 24
Orbits (inclination) (height)	6 MEO 55° 20,200 km	3 MEO 56° 23,616 km	3 MEO 64.8° 25,510 km
accuracy (95%) horizontal vertical	 22 m 27.7 m	 4 m 7.7 m	 ? ?
remarks	5–8 sat. visible	Coverage up to 75 N interoperable with GPS and GLONASS	

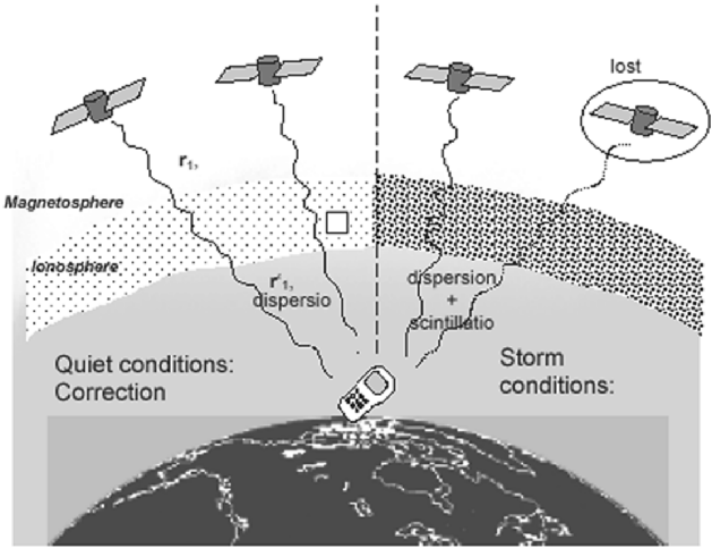

Fig. 3. Summary of all transmission definition conditions for a receiver of satellite navigation

and dispersion in the atmosphere. To correct for ionospheric delays, a critical parameter, known as Total Electron Content (TEC) must be broadcast to single-frequency receivers. There exist many quiet-time models for TEC, such as NeQuick. TEC values can also be directly calculated on an ionospheric grid produced by an ensemble of reference stations (known as SBAS [Satellite Based Augmentation Systems]).

Under severe geomagnetic storm conditions, the ionosphere becomes a more dynamic and turbulent environment, as illustrated on the right-hand side of Fig. 3. In addition, to dispersion and refraction, a phenomenon known as scintillations can severely affect the incoming signal. While TEC

variations in the ionosphere affect positioning for single-frequency receivers, TEC gradients and irregularities compromise integrity. Scintillations and Faraday rotation in the ionosphere can even interrupt continuity and availability of the SN system. In existing SN systems, nothing is currently done about a warning system for these severe conditions.

3.3 The Challenge: Improving the Integrity and Continuity of SN Systems During Geomagnetic Storm Conditions

Different kinds of users can be interested by such kind of Space Weather application system. GLOTEC main users will be the owners of single-frequency SN system receivers. GLOTEC secondary costumers will be Space Weather scientists who will need our data products to study how TEC is affected by geomagnetic storm activity.

Our primary goal is to provide a warning system that will warn users of potentially compromised position information due to severe Space Weather. In addition, improved measurement of the critical TEC parameter will be provided to both our primary and secondary users.

To accomplish this, GLOTEC has three major active components: The Data Center, The Prediction Center, and the Space Segment.

3.4 The Data Center

Overview of Information Flow

The figure below illustrates the GLOTEC flow of information. The GLOTEC Data Center is responsible for interfaces with the following segments: The Space Segment, the Prediction Center, the various sources of existing Solar–Terrestrial (ST) data, the Primary User, and the Secondary User (Fig. 4).

For the Space Segment interface, the data center ultimately receives the raw telemetry data stream from both the L1-situated spacecraft (i.e., B_{sw}, n_{sw}, and v_{sw}) and the TEC fleet (i.e., $TEC(t, \theta, \phi)$). These spacecraft, as well as the telemetry scheme are described below in the Space Segment section.

The Data Center transfers data from the Space Segment, as well as other sources of ST data to the Prediction Center. As indicated in the above diagram, these other sources of ST data are from varied sources and will have a variety of formats. Care is taken to meet the temporal and spatial resolutions required by Prediction Center. The output products of the Prediction Center are then broadcast to the primary user through the Data Center. This broadcasting procedure is described below.

The GLOTEC Data Center is also responsible for the production of the real-time TEC, which is ultimately broadcast to our primary users. This data processing is a rather detailed task and is described in the following section. The Data Center will also provide GLOTEC archival TEC and ST data for use in relation with the Space Weather scientists.

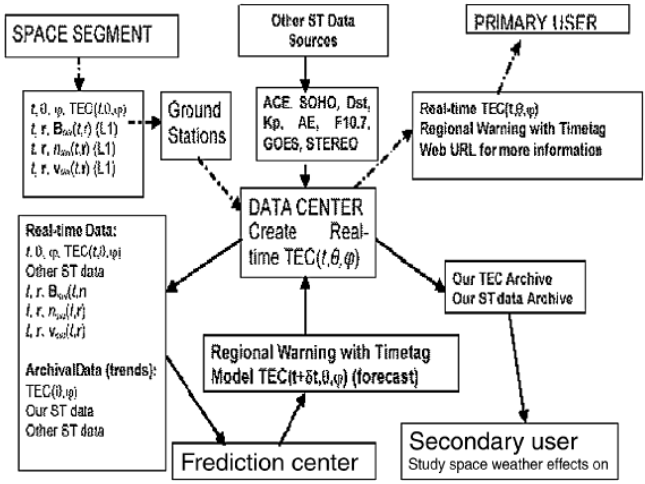

Fig. 4. Chart of GLOTEC center

3.5 Production of the Real-Time TEC

The procedure for production of near real-time global TEC maps will consist of a combination of direct measurements and two different TEC models. One model (NeQuick) will provide TEC values for the quiet time ionosphere, while the second model will provide corrections for the stormy ionosphere. Initially the storm time model (STORM) will be fairly simple, but this is likely to be greatly improved in the future (e.g., from the work of our prediction group). The quiet time ionosphere model will generally have small errors. The global TEC map will be made from fitting the modelled TEC map to the measured values and such a map will be produced every 5 min to be distributed to the customers. Even if 5 min are shorter than the global updating for the TEC map, this temporal frequency allows to take into account an equal amount of relatively recent TEC measurements together with previous measures weighted for completing the coverage.

Descriptions of the Models

STORM

An empirical Storm time ionospheric correction model, based on measurements from a long list of ionosonde stations covering latitudes from 83.2 N to 78.8 S. So far this has been developed only for f0F2, but we will assume that a TEC-model (which is proposed) will be available before our mission is operable. The model currently operates in real time, with hourly updates, but once again we assume that this will be improved in the near future (by ourselves if necessary). The error of this model is estimated by comparing the

model results with true ionosonde measurements and should be satisfactory for providing error bars for different locations

The input needed for this model to work is the hourly Ap for the last 30 h.

NeQuick

A quiet time model that improves previous models significantly. The inputs are the statistical database and the sunspot number (R12) estimated from the 10.7 cm solar radio flux (F10.7). The TEC model will be a sum of the two models. STORM will contribute only during active times. The routine for obtaining a global TEC is a fitting of the model TEC to the true (directly measured) TEC. During quiet times this method will provide high-quality TEC values. For storm times, values qualities could be highly variable. However, as long as we can provide satisfactory error estimates, the user will know that his position calculated could be wrong, which is the aim of this project.

Error Estimate

The error at a given point will be based on several factors. For a TEC value at time t_o the error will depend on

- density of true measurements in the region,
- time tag of nearby true measurement (large distance in time will increase error),
- the error provided by the models, and
- it is also possible to get in estimate of the accuracy of the model TEC by comparing the model with true values where these exist. The adjustment in error should, however, not be based on agreement in isolated points but rather on agreement over larger regions.

3.6 Prediction and Warning of Compromised Position Information by the Prediction Center: Using Smileys Happy ":-)", Medium ":-!" or Sad ":-("

Positioning systems are affected by magnetic storms and substorms. To obtain a reliable positioning service, we must globally monitor the variation of the particle densities in the ionosphere that act as a perturbation term in communications. GLOTEC will provide real-time TEC map and eventually scintillation indexes.

Magnetic storms and substorms will be predicted. GLOTEC is going to provide its customers with warnings at 1.5 days and at 1 h that the position that they will obtain from global positioning system satellites signals (such as GPS or Galileo) might be not accurate. End of alert's service will also be available.

Because of the information to be received by the user must be understood easily, we decided to provide alert systems on the basis of smileys (as the people exchange on the Internet by e-mails).

Responsibilities

Because of the instruments present on the Sun Earth L1 Lagrangian measurement point, warning problem messages are guaranteed 1 h before.

When SOHO/EIT and SOHO/LASCO/C2 or STEREO/SECCHI data will be available, we guarantee additional global warning at least 1 day before.

3.7 Basic Description and Functionality

Description of the TEC (Total Electron Content)

The total electron content (TEC in 10^{16} electrons/m^2) is the number of electrons in a column of one square meter cross section along a path from a satellite to a ground receiver through the ionosphere (Fig. 5). TEC varies by latitude and daytime (Fig. 6). In the daytime, the Sun's ultraviolet radiation usually produces more plasma (and, therefore, TEC) at middle latitudes than in higher latitudes. At night, the auroral ionosphere in high latitudes often has more plasma than the midlatitude ionosphere. TEC maps are produced in real-time by mapping GPS observables collected from 25 ground stations. In fact, accurate information on TEC is essential for satellite navigation systems. Information on TEC provides a valuable tool for investigating global and regional ionospheric structures. These maps are also used to monitor ionospheric weather, and to nowcast ionospheric storms that often occur responding to activities in solar wind and Earth's magnetosphere as well as thermosphere.

Description of the Scintillation

A signal between satellite and the receiver could exhibit temporal fluctuations of intensity and phase because of turbulence and irregularities of electron density. This phenomenon is called scintillation. Phase scintillation induces frequency shift, and when this shift exceeds the phase lock loop bandwidth, the signal is lost. Scintillations are strong at high latitudes, weak at middle

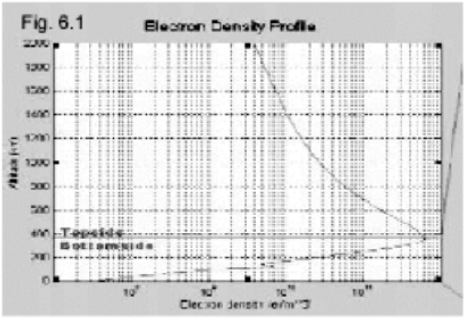

Fig. 5. TEC profile (adapted from the literature)

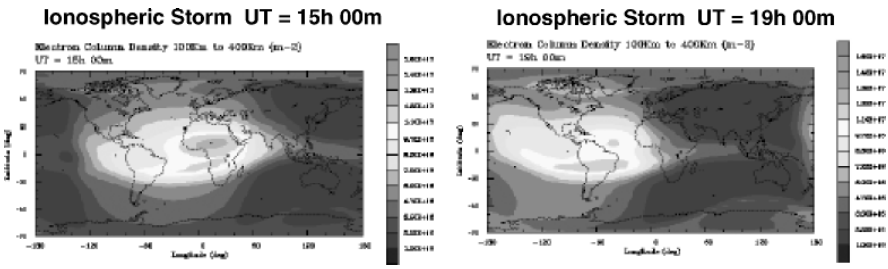

Fig. 6. Daily variation of the TEC (adapted from the literature)

latitudes, and intense in the equatorial region. During solar maximum period, the maximum value is attained at all latitudes when the ionosphere (F region) ionizes. The magnitude of scintillations during the solar minimum period is greatly reduced mainly because of decreased background ionization density. At high latitudes, scintillations are found to be associated with large-scale plasma structures. Polar scintillation is more conspicuous in winter when solar ionization radiation does not smooth out the irregularities. In the equatorial region, at the time of the sunset, the ionospheric conductivity integrated along the magnetic field line changes rather abruptly across the sunset line or the terminator. Large-scale plasma bubbles are formed in the bottom side of the ionosphere and rise to great heights. These irregularities cause intense dense L-band (1-20dB) scintillation. It decays shortly after midnight. The trigger mechanisms that make space time variability of scintillation are unresolved ([10] and reference herein). Empirical scintillation model WMBOD is available and could be used to forecast the scintillation.

3.8 Physical Description of the Phenomena Involved

Flares are ejecting high-energy particles that reach the L1 point about 1 h later (seen as CCD snow on solar image instruments of SOHO). When concentrating to the effects concerning TEC, the main influence on the Earth is Polar Cap Absorption. Often quasi-simultaneously, CMEs are expanding. If they are oriented toward the Earth, they reach the L1 point. If the z component of the IMF measured by the ACE satellite (Advanced Composition Explorer, cf. http://www.srl.caltech.edu/ACE/) points southward and reaches a certain value in a given time, together with some evolution of some plasma parameters v, n, Tp, it will create a magnetic storm as it reaches the Earth. Classical timescale for a shock to travel from the Sun to the Earth is 80 h (from 40 to 120 h, based on Schwenn et al. [34]) (Fig. 7).

Baumjohann and Treumann (1997) derived the equations that describe the magnetic ring current, substorms, and storms. Particles trapped in the dipole magnetic field are submitted to a drift that creates a ring current. At certain time more particles than usual are injected from the tail into the ring

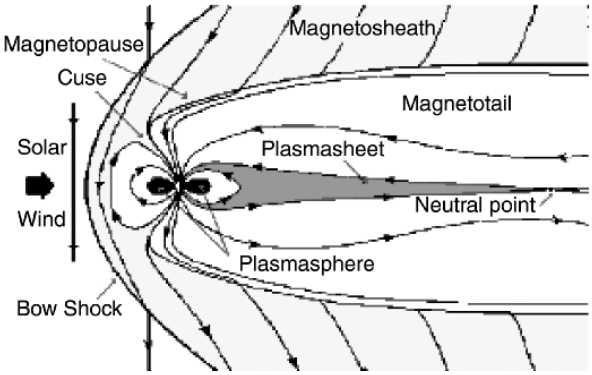

Fig. 7. The Earth environment (adapted from the literature)

current, creating additional depression in near equatorial region. When the depression is large, it is called a magnetic storm and had two different phases:

1. For some hours or days, an enhanced electric field injects lots of particles into the inner magnetosphere.
2. After a day or two, the injection rate goes back to normal and ring current can lose particle by charge exchange and pitch angle scattering.

Another important aspect in Earth Magnetic Disturbances is due to Auroral electrojets, when particles precipitating in the auroral oval are causing significant ionization and increase the conductivity. The Auroral Electrojet (AE) index, which is a measure of global auroral electrojet activity, is based on readings of the northward magnetic disturbance from 12 observatories. The amount of dayside magnetic flux merged per unit time depends on the number of southward oriented interplanetary field lines which get into contact with the Earth's magnetopause during a given time interval. According to the actual theory [14], the magnetic flux rope of a CME directed toward the Earth might create these disturbances (Fig. 8).

A magnetic substorm starts when the dayside merging rate is distinctively enhanced. The flux eroded on the dayside magnetopause is transported into the tail, and then after reconnections, the AE index increases. The period of enhanced convection and loading of the tail with magnetic flux corresponds to substorm growth phase. During that period (around 1 h), the main effect concerning TEC on the Earth is increasing Auroral ionization. After that, the tail releases the surplus of energy (the substorm onset) and thus starts the expansion phase. For 30–60 min. auroral arc, plasmoid ejections, occurred. After that for about 1 or 2 h the aurora fade (recovery phase).

So the main features during storms and substorms that can affect the ionosphere are

- auroral precipitations (Joule heating and Currents),

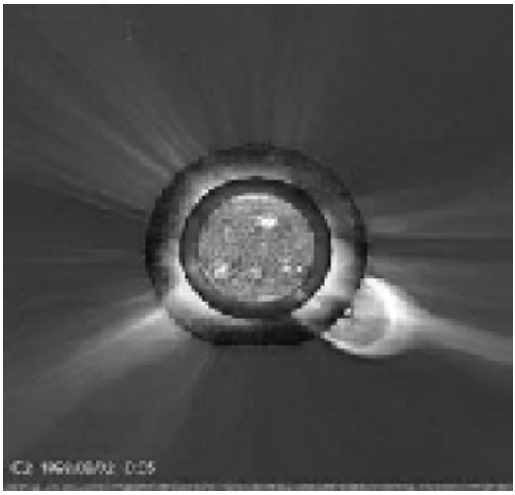

Fig. 8. Composite image of EIT and LASCO showing a CME limb formation

- potential drop across the polar cap, which leads to plasma drift from aurora regions, and
- ring current decay (precipitation in midlatitudes, heating of ionosphere by energetic neutral particles after recharging in the ring current).

Change in the global convection in the ionosphere leads to

- Change in the TEC (Fig. 6 shows the daily evolution)
- Scintillation.

Description of the System

The prediction will be done including two different timescales:

1. *CME or Flare warning:* To determine the projected speed of a Halo CME, we will use a temporal sequence of SOHO/LASCO coronagraph. To know whether the observed CME is frontside, we need disk observations. CMEs are often associated with flares and filaments, at so-called "disparition brusques." The flare level is determined from GOES with X-ray flux measurements. The SOHO/EIT images provide us the location of the flare (the figure to the left is a composite SOHO/EIT and LASCO image of a CME). Their timing resolution is around 12 min, and we estimate that a CME can first be seen on LASCO 1 h after the emission (derived from [1, 21]). Synoptic images are taken at least four times a day [22], so in the worst case the alert of a CME could be given 33 h before the arrival on Earth. To determine the direction of the expansion and the eventual time impact on the Earth, the solar rotation can be used (assuming the conservation of

the main plain direction) with stereoscopic techniques on EUV images together with a time velocity derived from the coronagraphs (Portier-Fozzani et al., 2001). STEREO/SECCHI could be also used in a later phase of the mission for including the 3D aspect of a CME [23].

2. Storm and substorm alert: The Earth is divided in three regions: High Latitude (HL) regions in northern and southern hemisphere and Low Latitude (LL) region. Substorm and storm warnings are given to regions most affected by the activity.

- Substorms: Using (IMF) magnetic field and solar wind velocity measurements from ACE spacecraft at L1, we calculate the epsilon parameter $\epsilon = 10^7 \times V \times B^2 \sin^4(\theta/2) \times l_0^2$, where V = solar wind speed, B = magnitude of the solar wind magnetic field, θ = IMF clock angle, and l_0 = empirical parameter = $7R_e$). When $\mu > 10^{11}W$ and IMF $Bz < 0$ for at least 20 min the substorm warning smiley " :-(" is given to the midnight sector (18:00–02:00 Magnetic Local Time) of the HL region (warning smiley ":-!" for $\pm 2h$) for the next 2 h.
- Storms: The Dst value determined by Burton (1975) is: $\frac{dD_{st}}{dt} = a\epsilon - \frac{D_{st}}{\tau_R}$ according to the solar wind measurements from the L1 point with $\epsilon = 10^7 V B^2 \sin^4(\theta/2) l_0^2$,
  The storm warning level is $Dst < -50nT$ and the warning is given separately for the main and recovery phases.
  (a) During a main phase of the storm we give warning smiley ":-("for 16:00–08:00 MLT sector of the HL region (warning smiley ":-!" for $\pm 2h$), and warning smiley ":-!" for the LL region for the next 6 h.
  If $Dst < -100nT$, warning smiley ":-(" is given everywhere.
  (b) During a recovery phase, the warning smiley ":-(" goes to the midnight sector of the HL region, and warning smiley ":-!" to the LL region for the next 3 h.

Note that the Auroral Oval location model is based on the auroral AL indexes (and not Kp).

The future will consist in improving the modelling of the ionosphere during storm and substorm conditions. There are no current models that can make any long-term prediction of ionospheric disturbances. The only thing which is used currently is models that can predict quiet time future this is for example NeQuick, of which the only input is f10,7 (Radio Flux). For storm conditions the only thing that can be done currently is making a warning that something might happen, and this only with a very poor time estimate of when the possible storm will hit Earth. So a general warning can be sent out, but unfortunately with very large uncertainty partly because we do not know for sure whether a storm actually will occur, and in the case a storm occurs how it will evolve, how severe it will be and where the effect will be largest. Today measurements at the L1 point allows us certain predictions of a storm occurrences, but there is only around 1 h before the storm hits the Earth.

One of the aims of future models should be to increase the amount of warning time from 1 h, preferably up to 3 days.

3.9 Space Segment Component

To provide a reliable TEC-Map of the Earth 16 Satellites orbiting in four different orbits can be launched to complete the GLOTEC system. Team Nina 2002 proposed to use the polarization of signal to determine the TEC overseas. There have been some other propositions to be able to do the measurement outside the place where the ground network is dense. It was proposed to

- **use the SAR in land such as in Africa:** For place in the world where there are not a lot of calibration GPS stations, we planned to use the SAR (Synthesis Aperture Radar) to calibrate the TEC. Measurement is done with two frequencies and with some calibration point we can deduce TEC over the whole area [32].
- **to use the phone satellite for high latitude measurement:** Calibration is done while measuring the difference phase of a simultaneous signal sent on phone satellite and thus the TEC can be measured between all possible connecting phone satellites [32]. Association with phone companies in exchange of providing them the availability of their network is planned.

Moreover, SOHO/EIT imageur and SOHO/LASCO coronagraph, in addition of the equivalent of an ACE Bz measurement, are needed in the Lagrangian point L1 to be able to have relevant data for the Space Weather.

4 The Future for Space Weather and Solar Physics: The Corona in 3D

4.1 The Motivation

As we have seen in the previous paragraph, knowing the solar corona and the dynamic in three dimensions is needed to build Space Weather forecast. The sigmoids and when they are going to erupt, the emergence of new active regions, the border of coronal holes are different parts of the puzzle which play a role in the Sun-to-Earth interaction. Portier-Fozzani et al. [29] have built a method that is able to measure degree of twist and thus the 3D geometry for coronal loops. An automatization of the method for being able to complete statistics and verify the expected relation between asymmetries and flares is under investigation ([42], COSPAR).

4.2 Nonclassical Material

The optical thickness of the corona introduces uncertainties that classical 3D inversion methods are not able to deal with directly. Tomography [23] would be the best to apply because of the optical thickness of the solar corona. But, because of the lack of view angles, models must be introduced, which makes the inversion depending on a lot of the magnetic extrapolations. With two satellites (like it will be in the future with STEREO) or using the solar rotation to observe with two different view angles static coronal structures, it should be possible to adapt stereoscopic techniques to our structures [43]. Portier-Fozzani [32] proposed to adapt a geometric matching model and to deduce 3D parameters with stereo techniques (Fig. 9). It has been successfully used to measure the physics for some loops. Automatization of the method by searching structures with level set methods are under construction.

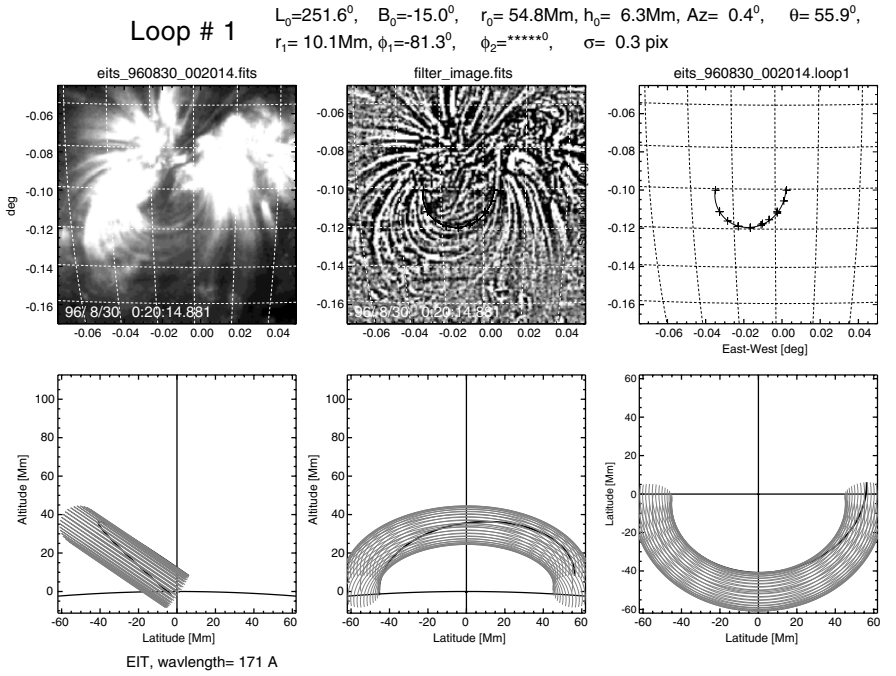

Fig. 9. Example of loops parameters measurement from stereoscopic methods (adapted from [29]

4.3 Adapting Stereoscopic Reconstruction

Stereoscopy is based on human vision where the depth information of scene is seek from two or more images. In agreement with the review of Pollefeys [27], the main steps of stereo reconstruction are

1. the choice of an appropriate input sequence,
2. extract structures from each images,
3. match the features,
4. make the projective reconstruction, and
5. rebuild a 3D model for the objects.

Extracting information from images (which mean relating the intensities measured by a camera with a representation of the world) are a major task in computer vision. Without any preprocessing, a computer can display only an image at a pixel level (intensities represent a low level of an image, for example a piece of blue) while the human is used to think at a symbolic level (high level) of interpretation (recognizes directly a lake, for example). This relation between images intensities (and shape deduced from it) and knowledge on the object (representation) has to be built explicitly for working in computer vision.

From a numerical image, primitive shapes are extracted. A sum of representative objects (icons) is then obtained and parameters are derived. Thus a structural representation (hierarchy with trees, leaves, ...) would lead to an interpretation (from model) and thus the description of the scene. The scene description and the definition of what are the similar structures improve the objects matching. A matching method must be used first while relations between points in different images cannot be uniquely defined from geometrical arguments only. For example, on the Sun, a filament can be morphologically described as pieces of wires when twisted, and the matching between images should be made over the whole structure.

When the position of the two satellites is known, we have a relationship between a point on each of the image and the optical centers (Fig. 10). Epipolar geometry tells us with its transformations where to look in a second image a structure extracted from a first image (Fig. 11). But because structures are optically thin, illuminations can change from one image to the next. Thus it is needed to include a recognition step before the matching based on the iconic level. If we do that at a pixel level, the correlation between the epipolar line could have several solutions that are not easy to separate between ghost and true solutions.

Structure correlations are done to obtain unicity of the matching. 3D inversions obtained from the dense positioning measurement of each points in the image pair.

Automatizations of stereoscopic coronal methods are the main actual challenge. Difficulties encountered come from structures definitions to be taken into account in the possible matching.

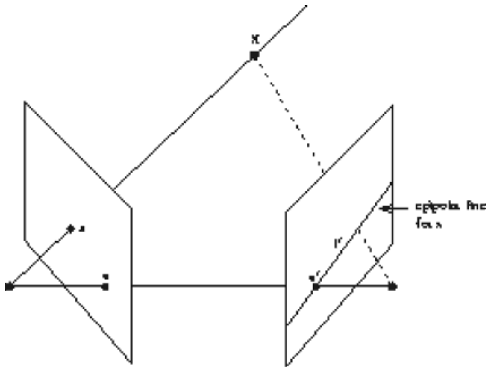

Fig. 10. Epipolar geometry defined by the two different view angles used in stereoscopic techniques

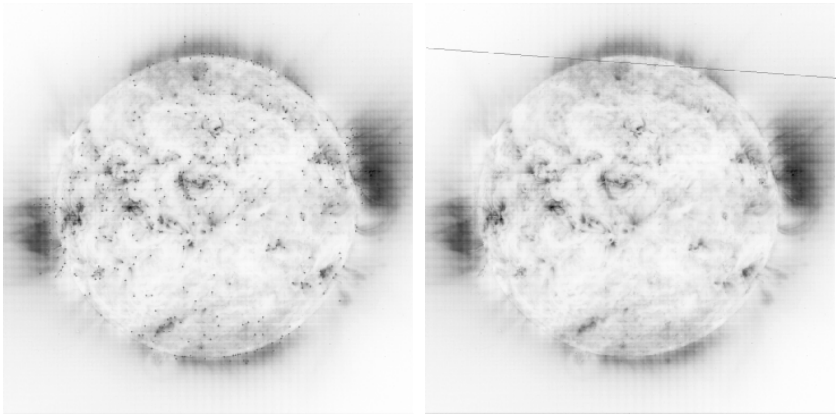

Fig. 11. The structures have to be matched on the epipolar line from the stereoscopic pair of images: The point P1 on image 1 corresponds to a point that lies on the epipolar line ep1 on the image 2 (cf. Fig. 10)

4.4 STEREO/SECCHI

The Sun Earth Connection Coronal and Heliospheric Investigation (SECCHI) on the Solar Terrestrial Relations Observatory (STEREO) mission is a suite of remote sensing instruments consisting of two white light coronagraphs, an extreme ultraviolet (EUV) imager, and a heliospheric imager. SECCHI will observe coronal mass ejections (CMEs) from their birth at the Sun, through the corona to their impact at Earth. Since each STEREO spacecraft will drift away from the Earth at the rate of 22° per year, 3D coronal structures and CMEs headed toward Earth will be clearly imaged and thus the dynamic of the Sun will be taken into account in 3D for Space Weather Forecasting. This

international mission led by the NRL (Naval Research Laboratory, Washington DC, USA) is planned to be launched in 2005.

4.5 Conclusion for 3D Coronal Perspectives

Measurement of solar coronal structures are needed to be able to have good understanding of the physics and to build efficient Space Weather forecasting. 3D classical image processing has shown the difficulties to observe or rebuild the solar corona in three dimensions. New methods are built from multiscale vision model (for the structure extraction) using the epipolar geometry (for the matching). With new satellites such as STEREO, we could expect to take the 3D dynamic into account which is the major step for Space Weather prediction.

5 Conclusion

In this chapter we have defined what kind of data are useful for Space Weather. The MEDOC Center provides SOHO data that are needed for the forecasting. An example in the user point of view called GLOTEC (GLObal TEC map variation warning) has been derived. It consists for the users of GPS (Global Positioning Systems) to be able to know when their positions derived are not correct. It allows also to warn problems such as satellite transmissions default due to Space Weather storm activities, etc. Finally, we present what kind of 3D techniques for the solar corona are going to be useful for good forecasting. The STEREO mission – launch July 2006 provide simultaneously two different view angles that let us into account the dynamic of the solar corona. Other permanent missions will be needed to have a good data coverage needed for Space Weather forecasting as we have for terrestrial weather forecast.

References

1. J.-P. Delaboudinière et al.: Solar Phys. **162**, 291–312 (1995)
2. W.M. Neupert, J. Newmark, J.-P. Delaboudinière, B.J. Thompson, R.C. Catura, J.D. Moses, J.B. Gurman, F. Portier-Fozzani, A.H. Gabriel, G. Artzner, F. Clette, P. Cugnon, A.J. Maucherat, J.M.; Defise, C. Jamar, P. Rochus, K.P. Dere, R.A. Howard, D.J. Michels, S. Freeland, J.R. Lemen, R.A. Stern: Solar Physics, v. 183, Issue 2, pp. 305–321 (1998)
3. M.J. Aschwanden, J.S. Newmark, J.P. Delaboudiniére, W.M. Neupert, J.A. Klimchuk, G.A. Gary, F. Portier-Fozzani, A. Zucker: APJ 515–842 (1999)
4. F. Portier-Fozzani: Etude de la couronne solaire en 3D et de son évolution avec SOHO/EIT, PhD Thesis, UNSA, France; Also Available at: http://www.linmpi.mpg.de/˜fabrice/ (1999a)
5. F. Portier-Fozzani: ESA SP446, pp. 549–554 (1999b)

6. Heliospheric Plasma Physics: An Introduction Space Solar Physics: Theoretical and Observational Issues in the Context of the SOHO Mission: Proceedings of a summer school, held in Orsay, France, 1–13 September 1997. Edited by Jean Claude Vial, Karine Bocchialini, and Patrick Boumier. Berlin; New York: Springer, c1998. Also Lecture Notes in Physics, v. 507., p. 217
7. F. Portier-Fozzani, B. Inhester et al.: In: *Imaging and Stereovision Techniques* from SOHO to STEREO, STEREO Meeting (Paris, 2002)
8. F. Portier-Fozzani, B. Inhester, T. Papadopoulo, A. Bijaoui, I. Fermin, B. Vandame, E. Aristidi: *3D observations of the magnetic corona from SOHO to STEREO*, EGS Meeting, Nice (2002)
9. G. Aulanier, B. Schmieder: A&A **386**, 1106–1122 (2002)
10. S. Basu, K.H. Groves: Space Weather, Geophys Monogr. **125** (1996)
11. Baumjohann and Treumann: In: *Basic Space Plasma Physics* (Imperial College Press, UK, 1997)
12. V. Bothmer: "Source of magnetic helicity over the solar cycle", ISCS Conf., ESA Pub., (2003), in press
13. V. Domingo, B. Fleck, A.I. Poland: "The SOHO Mission: an Overview" Solar Physics, v. **162**, pp. 1–37 (1995)
14. J. Krall, J. Chen, R.A. Howard, B.J. Thompson: "Three-Dimensional Structure of Flux-Rope CME's: Theory and Observation", American Astronomical Society, SPD meeting 32, Augest 2001 (2000)
15. O. Faugeras: In: *3D Computer Vision: a Geometric Viewpoint* (MIT Press, USA, 1993)
16. O. Faugeras, Q.T. Luong & S. Maybank: *Computer Vision—ECCV,* Lecture Notes in Computer Science 588, (Springer-Verlag, 1992), pp. 321–334
17. T.S. Fuller-Rowell, M.V. Codrescu, R.J. Moffett, S. Quegan: J. Geophys. Res. **101**, 2343–2353 (1996)
18. T.S. Fuller-Rowell, E.A. Aranjo-Pradere, Codnescu: Advance Space Research **25** (1), 139–146 (2000)
19. T.S. Fuller-Rowell: Available at http://www.sel.noaa.gov/storm/PAPERS/AGU-monogra.html (2002)
20. N. Gopalswamy, K. Shibasaki, M. Salem: Journal of Astrophysics and Astronomy, **21** 413 (2000)
21. R. Howard, D. Moses: Proc. SPIE, **4139**, 259–283 (2000)
22. D. Moses et al.: Solar Physics, v. **175**, Issue 2, pp. 571–599 (1997)
23. B. Inhester, F. Portier-Fozzani: In: *Applying Spectroscopy and Tomography to Corona Observations*, STEREO Meeting (Paris)
24. B. Inhester et al.: 2001, internal note
25. Inhester et al.: 2001, the 3D Nice 2001 Meeting
26. Marsch: 2001, IAU Symposium 203, PASP Conf. Ser. p. 447
27. M. Pollefeys : "3D Modeling from Images", ECCV (2000)
28. F. Portier-Fozzani, J.C. Noens: 3D Structures & dynamic of the solar corona: inputs from stereovision technics and joined Ground Based and Space Observations for the development of Space Weather: 2003, Semaine de l'Astrophysique Française, meeting held in Bordeaux, France, June 16–20, (2003). Eds.: F. Combes, D. Barret and T. Contini. EdP-Sciences, Conference Series, p. 45
29. F. Portier-Fozzani, B. Vandame, A. Bijaoui, A.J. Maucherat & EIT Team: Sol. Phys. **201**(2), 271–287 (2001)
30. F. Portier-Fozzani, M. Aschwanden, P. Démoulin, W. Neupert, Team EIT: Solar Physics, v. 203, Issue 2, pp. 289–308 (2001)

31. F. Portier-Fozzani, B. Inhester: Sp. Sci. Rev. **97**, 51–54 (2001)
32. F. Portier-Fozzani: Internal Report for the Alpbach Summer School (2002)
33. M. Proesmans, L. Van Gool, A. Oosterlinck: Comp.Vision ECCV94, Lecture Notes (1994)
34. R. Schwenn, A. Dal Lago, W.D. Gonzalez, E. Huttunen, C.O. St.Cyr, S.P. Plunkett: In: *A Tool for Improved Space Weather Predictions: The CME Expansion Speed*, AGU Meeting (2001)
35. SOHO site http://sohowww.nascom.nasa.gov
36. J.-L. Starck, F. Murtagh, A. Bijaoui: In: *Image processing and Data Analysis. The Multiscale Approach* (Cambridge University Press, UK, 1998)
37. STEREO SECCHI site http://projects.nrl.navy.mil/secchi/index.html
38. TEC site http://www.windows.ucar.edu/cgi-bin/realtime/spaceweather/ionosphere_movie.html
39. Trucco and Verri: In: *Introductory Techniques for 3D Computer Vision,* (Prentice Hall, N J, 1998)
40. Yair Weiss: ICCV, *8th International Conference on computer vision,* (IEEE computer Society, 2001) pp. 68–75
41. S. Pohjolainen, F. Portier-Fozzani, D. Ragaigne: Astronomy and Astrophysics Supplement, v. 143, pp. 227–263 (2000). "Comparison of 87 GHz solar polar structures with EUV and soft X-ray emission"
42. F. Portier-Fozzani, T. Papadopoulo, I. Fermin, A. Bijaoui, and Stereo/Secchi 3D Team, 2004, invited talk, 35th COSPAR Scientific Assembly. Held 18–25 July 2004, in Paris, France., p. 2259, "3D Observations techniques for the solar corona"
43. F. Portier-Fozzani, B. Inhester, T. Papadopoulo, A. Bijaoui, M. Aschwanden, 2002, In: Proceedings of the Second Solar Cycle and Space Weather Euroconference, 24–29 September 2001, Vico Equense, Italy. Editor: Huguette Sawaya-Lacoste. ESA SP-477, Noordwijk: ESA Publications Division, ISBN 92-9092-749-6, 2002, pp. 159–162, "3D coronal observations with the solar cycle"
44. P. Démoulin, M. A. Berger: Sol. Phys., v. 215, Issue 2, pp. 203–215 (2003). "Magnetic Energy and Helicity Fluxes at the Photospheric Level"

Index

Lecture Notes in Physics

For information about earlier volumes
please contact your bookseller or Springer
LNP Online archive: springerlink.com

Vol.653: E. Papantonoupoulos (Ed.), The Physics of the Early Universe

Vol.654: G. Cassinelli, A. Levrero, E. de Vito, P. J. Lahti (Eds.), Theory and Application to the Galileo Group

Vol.655: M. Shillor, M. Sofonea, J. J. Telega, Models and Analysis of Quasistatic Contact

Vol.656: K. Scherer, H. Fichtner, B. Heber, U. Mall (Eds.), Space Weather

Vol.657: J. Gemmer, M. Michel, G. Mahler (Eds.), Quantum Thermodynamics

Vol.658: K. Busch, A. Powell, C. Röthig, G. Schön, J. Weissmüller (Eds.), Functional Nanostructures

Vol.659: E. Bick, F. D. Steffen (Eds.), Topology and Geometry in Physics

Vol.660: A. N. Gorban, I. V. Karlin, Invariant Manifolds for Physical and Chemical Kinetics

Vol.661: N. Akhmediev, A. Ankiewicz (Eds.) Dissipative Solitons

Vol.662: U. Carow-Watamura, Y. Maeda, S. Watamura (Eds.), Quantum Field Theory and Noncommutative Geometry

Vol.663: A. Kalloniatis, D. Leinweber, A. Williams (Eds.), Lattice Hadron Physics

Vol.664: R. Wielebinski, R. Beck (Eds.), Cosmic Magnetic Fields

Vol.665: V. Martinez (Ed.), Data Analysis in Cosmology

Vol.666: D. Britz, Digital Simulation in Electrochemistry

Vol.667: W. D. Heiss (Ed.), Quantum Dots: a Doorway to Nanoscale Physics

Vol.668: H. Ocampo, S. Paycha, A. Vargas (Eds.), Geometric and Topological Methods for Quantum Field Theory

Vol.669: G. Amelino-Camelia, J. Kowalski-Glikman (Eds.), Planck Scale Effects in Astrophysics and Cosmology

Vol.670: A. Dinklage, G. Marx, T. Klinger, L. Schweikhard (Eds.), Plasma Physics

Vol.671: J.-R. Chazottes, B. Fernandez (Eds.), Dynamics of Coupled Map Lattices and of Related Spatially Extended Systems

Vol.672: R. Kh. Zeytounian, Topics in Hyposonic Flow Theory

Vol.673: C. Bona, C. Palenzula-Luque, Elements of Numerical Relativity

Vol.674: A. G. Hunt, Percolation Theory for Flow in Porous Media

Vol.675: M. Kröger, Models for Polymeric and Anisotropic Liquids

Vol.676: I. Galanakis, P. H. Dederichs (Eds.), Half-metallic Alloys

Vol.677: A. Loiseau, P. Launois, P. Petit, S. Roche, J.-P. Salvetat (Eds.), Understanding Carbon Nanotubes

Vol.678: M. Donath, W. Nolting (Eds.), Local-Moment Ferromagnets

Vol.679: A. Das, B. K. Chakrabarti (Eds.), Quantum Annealing and Related Optimization Methods

Vol.680: G. Cuniberti, G. Fagas, K. Richter (Eds.), Introducing Molecular Electronics

Vol.681: A. Llor, Statistical Hydrodynamic Models for Developed Mixing Instability Flows

Vol.682: J. Souchay (Ed.), Dynamics of Extended Celestial Bodies and Rings

Vol.683: R. Dvorak, F. Freistetter, J. Kurths (Eds.), Chaos and Stability in Planetary Systems

Vol.684: J. Dolinšek, M. Vilfan, S. Žumer (Eds.), Novel NMR and EPR Techniques

Vol.685: C. Klein, O. Richter, Ernst Equation and Riemann Surfaces

Vol.686: A. D. Yaghjian, Relativistic Dynamics of a Charged Sphere

Vol.687: J. W. LaBelle, R. A. Treumann (Eds.), Geospace Electromagnetic Waves and Radiation

Vol.688: M. C. Miguel, J. M. Rubi (Eds.), Jamming, Yielding, and Irreversible Deformation in Condensed Matter

Vol.689: W. Pötz, J. Fabian, U. Hohenester (Eds.), Quantum Coherence

Vol.690: J. Asch, A. Joye (Eds.), Mathematical Physics of Quantum Mechanics

Vol.691: S. S. Abdullaev, Construction of Mappings for Hamiltonian Systems and Their Applications

Vol.692: J. Frauendiener, D. J. W. Giulini, V. Perlick (Eds.), Analytical and Numerical Approaches to Mathematical Relativity

Vol.693: D. Alloin, R. Johnson, P. Lira (Eds.), Physics of Active Galactic Nuclei at all Scales

Vol.694: H. Schwoerer, J. Magill, B. Beleites (Eds.), Lasers and Nuclei

Vol.695: J. Dereziński, H. Siedentop (Eds.), Large Coulomb Systems

Vol.696: K.-S. Choi, J. E. Kim, Quarks and Leptons From Orbifolded Superstring

Vol.697: E. Beaurepaire, H. Bulou, F. Scheurer, J.-P. Kappler (Eds.), Magnetism: A Synchrotron Radiation Approach

Vol.698: S. Bellucci (Ed.), Supersymmetric Mechanics – Vol. 1

Vol.699: J.-P. Rozelot (Ed.), Solar and Heliospheric Origins of Space Weather Phenomena